NASA CONTRACTOR REPORT 166137

VOLUME 1

A STUDY OF A VTOL THRUSTING EJECTOR IN LOW SPEED FLIGHT

BY V. R. STEWART

March 1981

Prepared under contract NAS2-10494 By

ROCKWELL INTERNATIONAL CORPORATION

Columbus, Ohio

for

NASA

AMES RESEARCH CENTER

NATIONAL AERONAUTICS AND SPACE ADMINISTRATION

NASA CONTRACTOR REPORT 166137

VOLUME 1

A STUDY OF A VTOL THRUSTING EJECTOR IN LOW SPEED FLIGHT

BY V. R. STEWART

March 1981

Prepared under contract NAS2-10494 By

ROCKWELL INTERNATIONAL CORPORATION

Columbus, Ohio

for

NASA

AMES RESEARCH CENTER

NATIONAL AERONAUTICS AND SPACE ADMINISTRATION

FOREWORD

This report presents the results of an experimental investigation of V/STOL thrust augmenter wings in flight at slow forward speeds. Two rectangular wing planforms of differing relative chord lengths were tested. The augmenters were positioned in the aft portion of the wing so as to produce increases in circulation lift. Two blown flap configurations were also tested for comparison.

Surface pressures as well as total forces and moments were obtained on the semispan models at two flap deflections and a range of momentum coefficients. The results are compared with predictions made by use of Spence's jet flap theory.

Volume 2 contains tabulation of (1) surveys at the pressure augmenter exit, (2) downwash surveys downstream of the wing, and (3) all force and moment data acquired during the test.

CONTENTS

LIST OF ILLUSTRATIONS

LIST OF TABLES

A STUDY OF A VTOL THRUSTING EJECTOR IN LOW SPEED FLIGHT

By Vearl R. Stewart
Rockwell International
North American Aircraft Division
Columbus, Ohio

SUMMARY

Results are presented of a wind tunnel test to quantify the performance of a VTOL Thrust Augmenter Wing (TAW) and a comparable blown flap configuration during low speed flight. The objectives of the study were to obtain a systematic and comparable set of data and to determine the ability of Spence's jet flap theory to predict the aerodynamic effects of the TAW. The ability of the theory to adequately predict the characteristics can be increased by correctly utilizing the individual components of the theory; therefore a secondary objective of this study was to break out the components making up the jet flap theory, and where possible, to better define those components. The data obtained from the test portion of the study included longitudinal forces and moments, surface static pressures, augmenter exit surveys, and downstream flow field surveys.

Results of the study indicate that jet flap theory when modified to account for the TAW components is able to predict the characteristics with a reasonable accuracy. The modifications are: (1) increase jet momentum coefficient (C_μ) in the theory by the thrust augmentation (ϕ), i.e., C_μ becomes ϕC_μ; (2) account for augmenter inlet momentum (ram drag) in the drag and pitching moment equations; and (3) account for increased wing aspect ratio due to the endplate required to close out the augmenter. Based on augmenter exit surveys, it appears that forward speed has no appreciable effect on thrust augmentation ratio or entrainment of this type of augmenter.

INTRODUCTION

Ejectors provide a means of increasing the engine thrust as well as a means for deflecting the thrust in a direction to provide lift and/or control for a V/STOL vehicle. Several studies have shown augmentation values of 1.6 to 2.0 at static conditions, References (1) to (4). Ejectors can be utilized in several possible configuration arrangements. One such configurational arrangement is the thrust augmenter wing (TAW) concept. In this concept the augmenter is located in the wing trailing edge and is capable of deflection from full down (for vertical flight) to angles approaching the wing plane (for transition). An example of a TAW concept for VTOL is the Navy/Rockwell XFV-12A (see Reference (5)).

Most of the test data obtained to this date on TAW concepts have been very configuration-oriented and not complete enough for broad design or analysis application. In general, those data are not sufficiently

general or detailed to allow the designer to determine the component inputs into loads and to prepare stability and control estimates for general configuration concepts. An understanding of the component loads breakdown, the flow field characteristics, and the effect of forward speed on these parameters is needed.

In order to gain this understanding, data have been obtained from test of a model with the necessary instrumentation at speed conditions representative of transition to conventional flight. A TAW configuration was tested with two chord lengths of the wing, and similar tests were made with the augmenter rearward components removed to form a more conventional blown or jet flap.

The results of these tests are analyzed with regard to overall aerodynamic performance and are compared to Spence's jet flap theory of Reference (6), as presented by McCormick (Reference (7)).

SYMBOLS

AR	-	Wing Aspect Ratio - see Table I	
A_E	-	Augmenter Exit Area Perpendicular to Mean Angle	cm^2 (inches^2)
A_j	-	Nozzle Exit Area	cm^2 (inches^2)
$b_w/2$	-	Wing Semispan	cm (inches)
$\bar{c}_w$	-	Wing Mean Aerodynamic Chord	
C_f/c	-	Flap Chord to Wing Chord Ratio	
C_L	-	Lift Coefficient, $Lift/qS_R$	
C_D	-	Drag Coefficient, $Drag/qS_R$	
$C_{D_{Ram}}$	-	Augmente[illegible] Secondary Flow	
C_M	-	Pitching Moment Coefficient, $Pitching\ Moment/qS_R\bar{c}_w$	
C_μ	-	Momentum Coefficient, $\dot{M}_j V_j/qS_R$	
D	-	Throat Width	meters (feet)
F	-	3-D Correction Factor, Function of AR and ϕC_μ	
K_1	-	Induced Drag Correction Factor for Taper	
K_2	-	Induced Drag Correction Factor for Part Span Flaps	
K_b	-	Lift Correction Factor for Part Span Flaps	
M	-	Mach number	
$\dot{M}_p$	-	Primary (nozzle) Mass Flow	kg/sec. (slugs/sec.)
$\dot{M}_s$	-	Secondary (entrained) Mass Flow of Augmenter	kg/sec. (slugs/sec.)
$\dot{M}_T$	-	Total Mass Flow, $\dot{M}_p + \dot{M}_s$	kg/sec. (slugs/sec.)
P	-	Pressure	pascals (pounds/in.^{2})
P_a	-	Atmospheric Pressure	pascals (pounds/in.^{2})
P_S	-	Static Pressure	pascals (pounds/in.^{2})
P_T	-	Total Pressure	pascals (pounds/in.^{2})
P_R	-	Pressure Ratio, P_T/P_a	
q	-	Freestream Dynamic Pressure, $\frac{1}{2}\rho V_\infty^2$	newtons/meter^2 (pounds/ft^2)
q_h	-	Dynamic Pressure at Tail Location	newtons/meter^2 (pounds/ft^2)

r	-	Thrust Recovery Factor	
S_R	-	Reference Wing Area	meters^2 (feet^2)
t	-	Wing Thickness	cm (inches)
t	-	Temperature	K° (R°)
T	-	Thrust	newtons (pounds)
t_o	-	Total Temperature	K° (R°)
V	-	Velocity	meters/sec (feet/sec.)
V_∞	-	Freestream Velocity	meters/sec (feet/sec.)
V_j	-	Nozzle Jet Velocity	meters/sec (feet/sec.)
X	-	Horizontal Dimension, Positive Aft	meters (feet)
Y	-	Lateral Dimension from Plane of Symmetry, Positive Right	meters (feet)
Z	-	Vertical Dimension from WRP, Positive Up	meters (feet)
λ	-	Taper Ratio	
ϕ	-	Thrust Augmentation Ratio	$\frac{\text{Augmented Thrust}}{\text{Isentropic Thrust}}$
ρ	-	Air Density	Kg/meter (slugs/ft)
α	-	Angle of Attack	degrees
θ	-	Thrust Angle	degrees
ϵ	-	Downwash Angle	degrees
δ_F	-	Mean Flap Angle Measured from WRP	degrees
δ_{CB}	-	Centerbody Angle Measured from WRP	degrees
δ_{FWD}	-	Nose Flap Angle Measured from WRP	degrees
δ_{AFT}	-	Aft Flap Angle Measured from WRP	degrees
δ_D	-	Diffuser Half Angle Measured from Mean Angle	degrees

MODEL AND APPARATUS

Model Description

The model tested was a floor mounted semispan model representing an unswept, untapered augmenter wing configuration and is shown (Figure 1) mounted in the 4.27 x 4.88 meter (14 x 16 feet) test section of the Rockwell International Columbus wind tunnel facility. The model was tested at mean flap deflections representative of STOL or transition operation.

The wing cross-section and augmenter are shown in Figure 2. An overall model sketch and dimensions are presented in Figure 3a. The augmenter has two Coanda slot nozzles and a hypermixing centerbody nozzle. Figure 3b presents a sketch of the centerbody nozzle. The centerbody has an external hinge arrangement to allow the jet to be located at the centerline of the throat at mean deflections of 90 degrees (vertical flight mode) and yet to close for cruise flight. The model nozzle gaps are arranged such that the flow split from the three nozzles is: each Coanda approximately 25 percent and the centerbody 48 percent with 2 percent applied on the end walls for control of flow attachment.

The augmenter consists of a fixed nose section with a hinged lower surface flap, a hinged centerbody and an aft flap. The nose section flap and the centerbody retract to provide the airfoil section. The nose section flap leading edge is tangent to the forward circular Coanda radius at all flap angles. The surfaces open to provide the augmenter wing. Several angle relationships are important to the discussion. The mean angle (δ_F) of the augmenter is the average angle of the inside surfaces of the nose flap and aft flaps. The thrust angle (θ) is the balance-measured thrust angle at static tunnel conditions, and the diffuser angle (δ_D) is the variation of the inside surface from the mean angle, positive for positive diffusion. The centerbody angle (δ_{CB}) was fixed for maximum static augmentation ratio and was 70 degrees at $\theta = 40°$ and 60 degrees at $\theta = 30°$. All angles (except δ_D) are measured from the wing reference plane. Figure 3c presents the augmenter nomenclature.

The basic augmenter wing model has a relatively short leading edge ahead of the augmenter throat. A modification to the wing chord was achieved by adding a chord extension of .254 meters (10 inches) ahead of the basic wing. The two chord lengths chosen would be representative of those which might be used in a thrust augmenter wing (TAW) configuration. Although no attempt was made to match other variables, such as, surface thickness and throat width to flap length, the chord lengths chosen for this study are closely representative of the Rockwell XFV-12A TAW. The short chord could be considered to represent the canard while the longer chord is representative of the nose lengths associated with the XFV-12A wing geometry.

The configuration was modified to provide a jet flap configuration by removal of the aft flap and centerbody of the basic model. Thereby, four separate configurations were tested. These are shown in Figure 4,

and are two TAW configurations with flap chord to wing chord ratios of 0.40 (Augmenter 1) and 0.28 (Augmenter 2) and two jet flap configurations with flap chord to wing chord ratios of 0.61 (Jet Flap 1) and 0.365 (Jet Flap 2). The TAW C_f/C_w ratio is based on aft flap length and the respective wing chord lengths. The model geometry of the four configurations tested is shown in Table 1.

Instrumentation

The model instrumentation consisted of a five component force balance, instrumented air supply system, surface pressure instrumentation, and flow field pressure survey apparatus. An external five component post balance was used to measure normal force, axial force, pitching moment, rolling moment, and yawing moment. The rolling and yawing moment data from a semispan model such as this are utilized primarily as a diagnostic and are not presented. Normal, axial, and pitching moment data were transferred to stability axis reference system and are presented.

The surface pressure instrumentation consisted of one chordwise row of taps on the upper and lower surface and one spanwise row of taps on the upper surface. Pressure data and the instrumentation locations are presented in detail in Appendix C.

A traversing survey rig was developed and used to survey both the augmenter exit and the flow field in the area of the horizontal tail locations. The exit survey was accomplished with a rake of three pitot-static tubes (Figure 5). The exit was traversed at several stations. Data were recorded by individual transducers for each of the six pressures. The downwash survey was made with United Sensor five hole directional probes. The probes are accurate to approximately 40 degrees angle. Figure 5 shows the downwash survey rig. Surveys were made in both vertical and spanwise directions.

Test Procedure

The test was conducted in the 4.27 x 4.88 meter V/STOL test section of the Rockwell International wind tunnel located at Columbus, Ohio. The V/STOL test section can be operated at speeds of zero to 80 knots. The semispan model described in the preceding sections was mounted on a five component post balance. Figure 6 shows the schematic installation of the model, balance, and air supply.

The high pressure air for the nozzles crosses the balance through a trombone pipe arrangement. This air supply system results in a small hose tare which is accounted for in the data reduction. The balance was calibrated with the hoses in place. The calibration change for hose pressure was checked during the balance calibration. A separate balance calibration matrix was required for the hoses pressurized or nonpressurized.

The tests were conducted in three phases. The primary portion conducted was a force and surface pressure test. The balance data and sur-

Table 1 Model Geometry

Wing: (Basic)

Section: t/c	17% Supercritical L.E. Radius = 2.54 cm (1.0 in.)
Taper:	1.0
Span: $b_w/2$	152.22 cm (59.93 inches)
Chord: $\bar{c}_w$	57.46 cm (22.62 inches)
Twist:	none
Incidence:	none
$S_w/2$	.875 m^2 (9.414 ft^2), AR = 5.3

Trailing Edge Flap:

Chord:	39.4% $\bar{c}_w$ = 20.12 cm (7.92 inches)
Span: $b_{AF}/2$	117.93 cm (46.43 inches) (full span outboard of fuselage)
Hinge:	.60 x/c
Deflections:	30^o, 40^o
Nozzle:	.191 cm (.075 inches) Gap
Flaperon Extension (E):	6.43 cm (2.53 inches)

Lower Surface Flap:

Span: $b_{PF}/2$	117.93 cm (46.43 inches)
Deflections:	30^o, 40^o
Nozzle:	.191 cm (.075 inches) Gap

Centerbody:

Span:	117.93 cm (46.43 inches)
Deflections:	Variable position, 0^o through 90^o
Nozzle:	Hypermixing, gap = .38 cm (.15 inches)

Fuselage:

Approximate .2 scale Type "A" TAW Semi-Span Transport Model

Reference Geometry:

	Augmenter 1	Augmenter 2	Jet Flap 1	Jet Flap 2
Span				
(Total) cm(In.)	152.22(59.93)	152.22(59.93)	152.22(59.93)	152.22(59.93)
(Exp.) cm(In.)	117.93(46.43)	117.93(46.43)	117.93(46.43)	117.93(46.43)
Chord				
(Undeflected) cm(In.)	57.46(22.62)	82.86(32.62)	37.67(14.83)	63.07(24.83)
Area $m^2(ft^2)$	.875(9.414)	1.261(13.576)	.574(6.172)	.961(10.334)
Aspect Ratio				
(Total)	5.3	3.67	8.08	4.83
Center of Gravity (x/c)	0.430	0.605	0.655	0.790

face pressure data were obtained through a range of angles of attack from -12 degrees to 20 degrees for each of the four configurations discussed at various levels of blowing coefficients and thrust deflection angles. Thrust deflection angles were maintained at approximately 30 degrees and 40 degrees for all testing. The thrust deflection angle was determined from measured forces at static (zero forward speed) conditions. Effect of forward speed on thrust deflection angle was not investigated.

The second test portion consisted of a series of augmenter exit surveys to investigate the effects of forward speed on the augmentation ratio and secondary mass flow of the system.

The third portion of the test consisted of a downwash survey behind the augmenter and jet flap configurations. Fibure 5b shows the setup for the downwash survey. The measurements were made at several heights, span stations, and at three longitudinal positions behind the wing.

Data Reduction

The data are presented in the standard engineering coefficients about the stability axis system shown in Figure 7. Heyson wall corrections and solid blockage corrections have been included in the coefficients. A discussion of Heyson corrections can be found in References (8) to (11). The pitching moment coefficients are referenced to the center of the augmenter for all configurations including the jet flap configurations, see Figure 2. This moment center was held constant for all configurations tested for purposes of data comparisons of the induced load centers. The aft center of gravity results in a very unstable configuration in certain cases, particularly the jet flap configurations; reference c.g. locations are shown in Table 1. The surface pressures have been integrated and compared to balance forces.

Augmenter exit surveys were recorded as total and static pressures. Examples are presented in Appendix A.

Downwash surveys were reduced to angle and dynamic pressure ratios and are presented as a function of position.

Blowing moment coefficient was changed by variation of both nozzle pressure ratio and tunnel speed to provide the desired levels for the force testing; however, during the exit survey and downwash tests, the nozzle pressure ratio was maintained at a pressure ratio of 1.5 for all surveys to provide a direct basis for comparison of velocity effects. The low level of $P_R = 1.5$ was chosen because of limitations in stiffness of the surveying mechanism. Higher pressure ratio would have required considerably higher tunnel speeds and would have more than doubled the forces acting on the rake.

The thrust utilized in calculation of blowing momentum coefficient and augmentation ratio is the ideal nozzle thrust for each pressure ratio tested.

$$\text{Thrust} = \dot{M}_p V_j ; \quad C_\mu = \frac{\text{Thrust}}{qS}$$

Mass flow was measured by calibrated venturis located upstream of the model pressure control valves.

TEST RESULTS

General

The TAW was tested at thrust angles of 30 and 40 degrees and at diffusion angles of 0, 8, and 16 degrees for both nose lengths. The diffuser angle variation has two effects on the augmenter characteristics. At a constant mean angle, reducing the diffuser angle reduces the static augmentation ratio (ϕ) and increases the thrust angle. In order to provide data more useful in comparison and to facilitate data analysis, the thrust angle change was kept constant by simultaneous changes to diffuser angle and mean angle. The variation of static augmentation ratio (ϕ) with diffuser angle is shown in Figure 8. A second order change in ϕ was noted with pressure ratio (see Figures 9 and 10).

It is felt the pressure ratio effect is a corner flow separation problem and will be eliminated with forward speed. Previous data obtained on this model at other conditions have shown that although a small change in ϕ is noted at static conditions, the data may be compared as a function of C_μ. These data are presented in Reference (4) and are reproduced in Figures 11 and 12.

The basic lift, drag, and pitching moment data for the Augmenter 1 configuration at the diffuser angles of 0, 8, and 16 degrees are presented in Figures 13, 14, and 15, respectively, for 40 degree thrust angle and in Figures 16, 17, and 18 for the 30 degree thrust angle. The Augmenter 2 data are presented in Figures 19 to 24 for the same conditions. Jet flap data are presented in Figures 25 and 26 for the Jet Flap 1 and in Figure 27 for the Jet Flap 2. Figure 28 presents the data for the basic wing with no flap deflection and two chord lengths.

The augmenter data for both nose lengths show that as the augmentation ratio is increased by larger diffuser angle deflection, the entrainment, lift, and stall angle increase. At diffuser half angles of 8 and 16 degrees, the circulation lift buildup is similar to jet flap results, large lift changes for low values of C_μ. The pitching moment becomes more positive as the entrainment increases, indicating a forward lift center as well as the augmenter inlet momentum effect. Diffuser angles of zero degrees have a different characteristic. Low augmentation values are obtained at $\delta_D = 0$; the augmentation ratio is less than 1.0; therefore the mass entrainment is also lower. This results in reduced circulation lift at the lower levels of C_μ. With the diffuser open to 8 or 16 degrees, providing for reasonable augmentation level, the augmenter configurations do not show stall below 20 degree angle of attack. The jet flap configurations stalled at angles of attack of approximately 16 degrees for C_μ of 1.0 and 2.0, but did not show stall at angles of attack up to 23 degrees with $C_\mu = 4.0$. The stall angles are readily apparent in the lift coefficient vs angle of attack.

Effect of Diffuser Angle

The augmentation ratio of any augmenter increases with the diffusion of the augmenter until the diffuser angles become large enough to induce wall separation. The effect of the diffuser angle on augmentation ratio at static tunnel conditions was shown in Figure 8. The diffuser angle also has an effect on the aerodynamic characteristics at forward speed. Lift data are presented in Figure 29 as a function of C_μ for both augmenter configurations. The data show considerable spread at a given C_μ with greatly reduced lift for the lower diffuser angles. Figure 30 presents the same data as a function of ϕC_μ or gross C_μ. The data show better correlation here, indicating that circulation lift is more of a function of the gross thrust of the augmenter; however, some discrepancies are still to be noted, particularly with the short chord augmenter. The diffuser angle of 16 degrees gives the maximum augmentation level obtainable with this particular augmenter configuration; thus, the augmenter is entraining the maximum amount of secondary air at this condition. As the entrainment is reduced through the closing of the diffuser, the external flow separates from the aft surfaces of the centerbody and aft flap, thereby reducing the circulation about the airfoil and resulting in the reduced lift coefficients seen in the data. The correlating parameter chosen for this report is C_μ or ϕC_μ. The parameters involving velocity ratios have been developed and may be of interest. The data necessary to compute various velocities can be found in the tabulated data, Appendix C.

Pitching moment and drag coefficients are also significantly affected by diffuser angle; however, here the effect of ram drag contributes a large portion to the apparent effect of diffuser angle. The variations of drag coefficient are presented in Figures 31 and 32 as a function of C_μ and ϕC_μ, respectively. Again, better correlation is shown with ϕC_μ, but the separation effects discussed for the circulation lift are apparent at low values of ϕC_μ. It would appear that if a TAW configuration could be developed such that the separation at low C_μ levels does not occur, ϕC_μ will be a suitable parameter for data correlation.

Pitching moment coefficients for Augmenters 1 and 2 at $\alpha = 0$ are presented in Figure 33. These data are presented at an angle of attack of zero and as a function of C_μ only. Correlation on ϕC_μ is no better than C_μ due to the ram drag input into the moments. As will be discussed in the following sections, the effective ram drag arm is shown to be a function of the blowing coefficient, C_μ. The ram drag moment arm acts at some percentage of the stream tube of the entrained air. As C_μ increases, the stream tube of the entrained air also increases in area. The analysis shows that much of the increase in size is above the wing; therefore, the position of the apparent location of the pitching moment force shifts upward. The surface pressure, as will be discussed in the wing component lift distribution section, shows the induced pressures to be concentrated on the leading edge section at all blowing coefficients.

Effect of Forward Speed

The effect of forward speed on the augmenter characteristics is seen in several parameters. The major items of interest at forward speed are circulation lift, induced drag, augmentation ratio, and secondary mass flow which results in ram drag. The pitching moment coefficient also varies with forward speed but is a result of the combination of the above major items. The circulation lift generated by the augmenter is the sum of the angle of attack lift, flap lift, and to the lift induced by blowing through the augmenter. Induced drag is the result of circulation lift. Investigation of forward speed effects on augmentation ratio and ram drag were broadened in this study to include a pressure survey of the augmenter exit at several conditions. Previous analyses had attempted to obtain a wind-on augmentation by solving the jet flap drag equation,

$$C_D = -r\phi C_\mu + C_{D_0} + C_{D_i} + C_{D_{Ram}}$$

$$= -r\phi C_\mu + C_{D_0} + \frac{K_1 C_L^2}{\pi AR + 2\phi C_\mu} + \frac{K_2 C_L^2}{\pi AR + 2\phi C_\mu} + \frac{\dot{M}_s V_\infty}{qS} \qquad \text{(Eq. 1)}$$

This procedure indicated a sizable increase in augmentation ratio (ϕ) with forward speed.

The exit pressure surveys (Appendix A) taken do not show an increase in mass flow or augmentation ratio due to forward speed and, in fact, show a decrease in local thrust at a blowing coefficient of 2.0. Figure 34 presents the average exit thrust from the exit survey indicating a reduction in ϕ as the speed increases. The data are shown as a function of C_μ. Since the survey data are for a constant primary pressure ratio of 1.5, the momentum coefficient (C_μ) is directly proportional to T/V^2. The mass flow is less consistent than thrust and indicates variations of ±10% (see Figure 35) compared to,

$$\frac{\dot{M}_s}{\dot{M}_p} = \left(\sqrt{\phi \frac{A_{exit}}{A_{jet}}} - 1\right)\sqrt{\frac{t}{t_o}} \qquad \text{(Eq. 2)}$$

Due to the variations encountered in the survey results combined with the force data, it is concluded, in practice, that no significant wind effects can be attributed to the augmentation ratio or mass flow. The jet flap theory drag equation shown earlier has several other variables which are not firmly established and which may be a factor in the apparent ϕ increase. The major items are thrust recovery (r), C_{D_0}, the induced

drag, span factor, K_1 and K_2, as well as the effective aspect ratio of wing endplate. These individual items will be discussed in a following report section entitled, Jet Flap Theory Comparison.

Downwash Survey

The flow field behind the TAW and the jet flap was measured by use of a United Sensor calibrated five-hole probe. Survey locations are shown in Figure 3. The probe has been calibrated to yield both angle of attack (downwash) and sideslip as well as dynamic pressure. For purposes of this test only angle of downwash and dynamic pressure were of interest since the entire flow field was behind the wing and no cross-flows were experienced. Figures 36 and 37 show the variation of the dynamic pressure ratio q_h/q for the augmenter. Figures 38 and 39 present comparable data for the jet flap. The data show that the q_h/q is relatively uniform for the region surveyed at constant blowing conditions. With blowing off ($C_\mu = 0$), the data show a wake behind the wing. The free stream q is obtained at heights of approximately 1/2 $\bar{c}$ above the wing plane. With blowing on, the value of q_h/q_∞ is .8 to .95. The accuracy of the total pressure measurements is ±5% to ±10% so that while the absolute levels indicated are not adequately defined, the trends are probably correct.

The five-hole probe is arranged as shown:

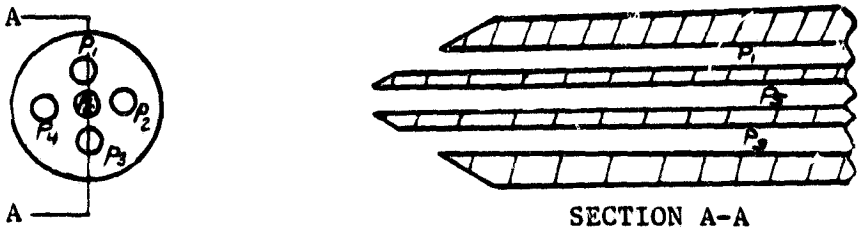

SECTION A-A

The total pressure is a function of pressure 5 and the static pressures an average of pressures 1 to 4. The NACAL V/STOL tunnel is not vented to the atmosphere, and the total pressure in the test section may be as much as 1 psi above atmospheric pressure during tests; therefore, it can be seen that the dynamic pressure measurements are a small percentage of the total pressure reading. All pressures are referenced to atmospheric.

$$q = P_T - P_S$$

At a tunnel velocity of 50 knots, $q = 8.5$ lbs/ft^2 = .059 lbs/in^2, P_S was approximately .45 psi above the reference pressure; therefore, the q_h is obtained from

$$q = P_T - P_S$$

$$= 14.809 - 14.750 = .059$$

Small errors in either the static or total pressure measurements can result in sizable q_h errors. Assuming a 1% error in P_T would result in an 8.6% error in q_h.

The measurement of angles is a function of pressure ratios, and large errors are less likely to be encountered. Sample results for the downwash angle are presented in Figures 40 and 41 for the TAW configuration. Large downwash angles of 20 to 25 degrees are shown in the wing plane with blowing. These levels reduce to 10 to 15 degrees as the test location is moved above the wing plane. The downwash angle is 5 to 10 degrees with no blowing. Longitudinal displacement does not materially affect the downwash angles.

The jet flap downwash angles for the same conditions are presented in Figures 42 and 43. At this fuselage station the downwash angles are reduced due to the increased longitudinal distance from the trailing edge. Moving forward to compensate for the forward shift of the wing trailing edge results in increased downwash angles (see Figures 44 and 45).

The complete downwash survey results are presented in Appendix B.

Surface Pressure Distributions

Surface static pressures were obtained at a midspan station for all configurations tested. Figures 46 to 49 present chordwise pressure distributions at an angle of attack of zero for the range of blowing coefficients tested. For Augmenters 1 and 2 (Figures 46 and 47) the diffuser angle is 8° and mean angle is 30°. For Jet Flap configurations 1 and 2 (Figures 48 and 49) the flap angle is 30°. As expected, there is a significant increase in the nose section lift due to the increasing blowing rates. The greatest effect of blowing, however, is on the blown flap surfaces. The aft flap of the augmenters experiences a downward load due to reduced pressures in the augmenter.

The effect of change in angle of attack is shown in Figure 50 for Augmenter 1 and in Figure 51 for Jet Flap 1. The data show an increase in the negative pressure coefficient near the leading edge with increasing angle of attack but little effect in the pressure at the forward flap knee or on the pressure centerbody and aft flap in the augmenter. For a given value of C_μ and α, the augmenter configuration has greater suction on the airfoil nose than does the jet flap and less peak suction near the flap, thus indicating an increase in circulation lift due to thrust augmentation.

The effect of diffuser angle for Augmenter 1, shown in Figure 52 for $\alpha = 0$ and in Figure 53 for $\alpha = 8°$, is similar to the effect of increased blowing shown in Figure 46. Increase in diffuser angle increases the entrainment and augmentation ratio. Therefore, it produces a change in pressures similar to that of increasing C_μ. A reduction in leading edge suction can be seen at $\delta_D = 0$ indicating the stall discussed earlier.

A direct comparison of the pressure distributions of Augmenters 1 and 2 is shown in Figures 54 and 55 for $\alpha = 0$ and 12°, respectively, and in Figures 56 and 57 for the jet flap configurations. The data show the same general results for the two nose lengths with greater leading edge suction indicated on the short nose.

Wing Component Lift Distribution

The surface pressure distributions show that most of the circulation lift buildup occurs on the wing nose. Figure 58 presents the lift breakout of the Augmenter 1 configuration. The sectional lift coefficient was obtained from integration of the surface pressures presented in Appendix C for the configurations tested. The lift component is made up of the pressures on the three augmenter surfaces plus the lift component of the nozzle thrusts; in this case only the aft and centerbody nozzle thrust contribute to the lift since the forward nozzle ejects in the thrust direction. The sketch below shows the component breakdown.

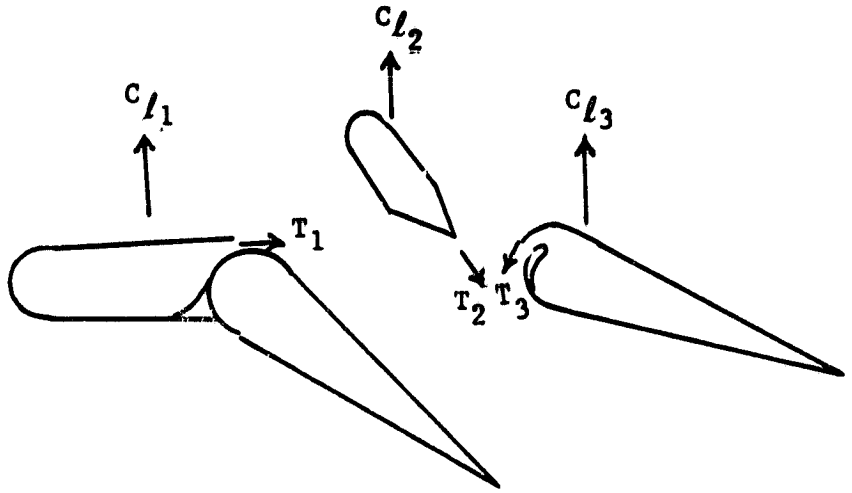

The lift breakdown can be written as

(Eq. 3)

$$C_\ell = C_{\ell_1} + C_{\ell_2} + C_{\ell_3} + \frac{T_1 \sin(\theta_1 + \alpha)}{qS} + \frac{T_2 \sin(\theta_2 + \alpha)}{qS} + \frac{T_3 \sin(\theta_3 + \alpha)}{qS}$$

where

C_ℓ = Integrated surface pressure loads
T = nozzle thrust
θ = nozzle angle
α = angle of attack

The term T/qS is the blowing coefficient (C_μ) for each nozzle; therefore the lift equation can be written as

$$C_\ell = C_{\ell_1} + C_{\ell_2} + C_{\ell_3} + C_{\mu_1} \sin(\theta_1 + \alpha) + C_{\mu_2} \sin(\theta_2 + \alpha) + C_{\mu_3} \sin(\theta_3 + \alpha) \quad \text{(Eq. 4)}$$

The pressure data show that within the range of C_μ tested most of the lift is carried on the nose section with generally small negative lift on the centerbody and aft flap and a positive lift increment due to the thrust angle. The negative lift on the centerbody is the result of the down facing portion becoming adjacent to the large negative pressure field in the throat of the augmenter. The aft surface negative lift forces are caused by the negative pressures within the augmenter overcoming the upper surface negative pressures resulting from the deflection of the streamlines.

Comparison of the integrated surface pressures with the overall force data is shown in Figure 59 for Augmenter 1. The section lift coefficients have been adjusted to a three-dimensional value by the jet flap correction factor discussed in Reference (7). The values of the 3-D correction factor for the augmenters tested are presented in Figure 60. The F values were computed utilizing an effective aspect ratio to compensate for the endplate effect of the augmenter endwall. The effective aspect ratio was determined from the lift curve slopes of the configurations with the augmenters closed. The basic wing lift characteristics were presented in Figure 28a.

JET FLAP THEORY COMPARISON

Lift

Estimates of TAW STOL characteristics have been made by use of the jet flap theory summarized in Reference (7). The data obtained during this study on TAW and jet flap configurations have added to the data bank, and it is now possible to present a one to one comparison. The theory provides corrections for 3-D effects by the following equation:

$$F(AR, C_\mu) = \frac{AR + 2C_\mu/\pi}{AR + 2 + 0.604\, C_\mu^{\frac{1}{2}} \text{ to } .876\, C_\mu} \quad \text{(Eq. 5)}$$

The 3-D corrections from Reference (7) are presented in Figure 61 for several aspect ratios. The F values utilized in the analysis of the two augmenter configurations tested during this study were presented in Figure 60.

The span correction factor K_b can be obtained from Figure 62.

The data from the tests are shown in Figure 63 reduced to a 2-D lift ($\partial C_\ell / \partial \delta$) as a function of flap chord/wing chord (C_f/C_w). Excellent agreement is seen for both the jet flap and TAW characteristics. The reference chord for the TAW is the aft flap section.

The C_{ℓ_α} ($C_f/c = 1.0$) has less consistent agreement, particularly with the jet flap configurations. The jet flap apparently has carryover lift on the fuselage approximately equal to the wing loading; in other words $K_b = 1.0$. The TAW does not indicate as much carryover and does in fact agree well with jet flap theory for the 100% chord jet flap theory. A possible reason for this is the reduced lifting area of the TAW configuration compared to the jet flap configuration. The centerbody of the TAW is nearly vertical and presents little lift surface to the pressures. Most of the circulation lift increments are carried on the section ahead of the augmenter and little change is noted due to angle of attack on the centerbody or aft surface of the TAW configurations. It should be noted that the agreement between jet flap theory and the TAW shown in Figure 63 is with the maximum diffuser angle of 16 degrees, the maximum entrainment as well as peak ϕ point. Reductions of diffuser deflection will reduce the circulation lift as discussed earlier and the agreement of the lower levels of C_μ will not hold.

Figure 64 shows the effect of C_μ on the lift for the TAW and Figure 65 shows the same variable for the jet flap. The slope of C_L vs C_μ at high values of C_μ should be equivalent to the blowing coefficient times the sine of the thrust angle in the case of the jet flap and $\phi C_\mu \sin \theta$ for the TAW. The data show that from $C_\mu = 2.0$ to $C_\mu = 4.0$, this relationship holds. At lower C_μ levels the blowing rate is insufficient to fully attach the flow and the rate of change of C_L with C_μ is higher. At high angles of attack the slope exceeds $C_\mu \sin \theta$ since $C_\mu = 2.0$ was not sufficient to fully attach the flow.

Drag

The force in the longitudinal axis is composed of the jet thrust, profile drag, the induced drag, and in the case of the augmenter, a ram drag term. Jet flap theory accounts for these terms as follows:

$$C_D = -rC_\mu + \frac{K_1 C_L^2}{\pi AR + 2C_\mu} + \frac{K_2 \Delta C_L^2}{\pi AR + 2C_\mu} + C_{D_0} \qquad \text{(Eq. 6)}$$

The terms are defined as:

C_L Total lift coefficient

r Thrust recovery factor

K_1 Induced drag factor due to nonelliptical load

K_2 Induced drag factor due to part span flap

ΔC_L Lift due to flaps

C_{D_0} Drag $\alpha = 0$; $C_\mu = 0$

Modifying this to fit the TAW gives:

$$C_D = -r\phi C_\mu + \frac{K_1 C_L^2}{\pi AR + 2\phi C_\mu} + \frac{K_2 \Delta C_L^2}{\pi AR + 2\phi C_\mu} + C_{D_{Ram}} + C_{D_0} \quad \text{(Eq. 7)}$$

where

ϕ Augmentation Ratio

$C_{D_{Ram}}$ Ram drag $\frac{\dot{M}_s V_\infty}{qS}$

V_∞ Free stream velocity

Assuming the K_1 and K_2 terms from Reference (7) will hold for both augmenter and jet flap, the definition of ram drag, and utilizing an aspect ratio which accounts for the endplating of the augmenter end wall, it is possible to solve for the quantity $r\phi C_\mu$ or in the case of the jet flap rC_μ.

Figure 66 shows the drag coefficient as a function of C_μ for the TAW with the induced drag, profile drag, and ram drag removed. The $r\phi C_\mu$ variation indicates almost that thrust recovery (r) is nearly one for this particular configuration; $r\phi C_\mu$ for a $\phi = 1.4$ is approximately 1.4 C_μ. A similar comparison of the jet flap configurations is shown in Figure 67 for the two nose lengths. The results show rC_μ to be 0.9 C_μ to 0.95 C_μ. This is slightly higher than shown in Reference (7) where about 0.2 loss is taken for nozzle efficiency and scrubbing drag on the flap nose, however. The 0.9 value for r is not unrealistic. An r approaching 1.0 can be expected for the TAW at these angles since the ϕ term accounts for nozzle efficiency, scrubbing, drag, etc.

The data obtained during this investigation have shown that in the solution of the jet flap equations for an augmenter of this type the static value of augmentation ratio and the full ram drag due to the entrained secondary mass flow should be used. It is possible that other augmenter configurations, in particular those which rotate the inlet into the flow, may show increased augmentation with forward speed similar to that experienced by a jet engine.

Pitching Moment Characteristics

Reference (7) provides a suggested method of handling the pitching moment of jet flap configuration. Continuing the lift breakdown as a function of flap deflection, chord, and lift, a term of dC_M/dC_L (ac) as a function of C_f/C_w and C_μ has been developed. This variation is presented in Figure 68.

Utilizing this value for placement of the circulation lift and the thrust arm gives:

$$C_m = (cg - ac)C_{L_\Gamma} + \frac{a_T}{\bar{c}} C_\mu + \frac{Z_{cg}}{\bar{c}} C_{D_0} \qquad \text{(Eq.8)}$$

where

C_{L_Γ} is the lift due to circulation

$C_{L_\Gamma} = C_L - \phi C_\mu \sin(\theta + \alpha)$ Augmenter

$= C_L - C_\mu \sin(\theta + \alpha)$ Jet Flap

cg = distance from nose to cg (+ aft) $\sim \frac{\ell_{cg}}{\bar{c}}$

Z_{cg} = Drag arm

a = Thrust arm (+ ahead of cg)

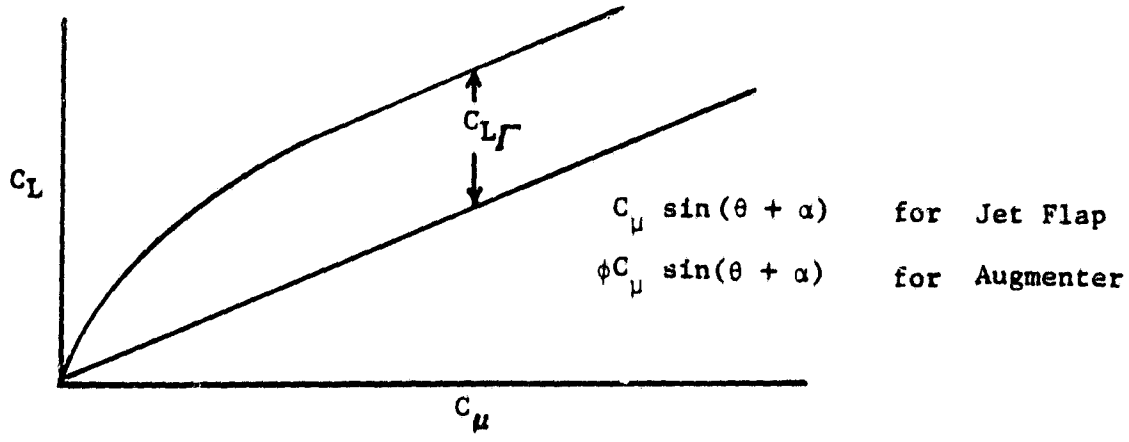

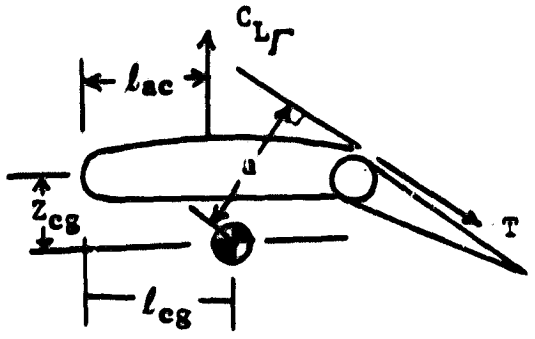

$$ac = \frac{\ell_{ac}}{c}$$

The agreement between the calculated C_m and the test data for the jet flap configuration is shown in Figure 69.

Computation of the pitching moment coefficients of the TAW has to consider the other variables which contribute to the pitching moment. Based on the data taken during this study, it appears the major other contributor is ram drag. The equation can be modified then to:

$$C_m = (cg - ac)C_{L_\Gamma} + \frac{Z_{cg}}{c} C_{D_0} \qquad \text{(Eq. 9)}$$

$$+ \left(\frac{aT}{c}\right) \phi C_\mu + \frac{\ell_r}{c} C_{D_R}$$

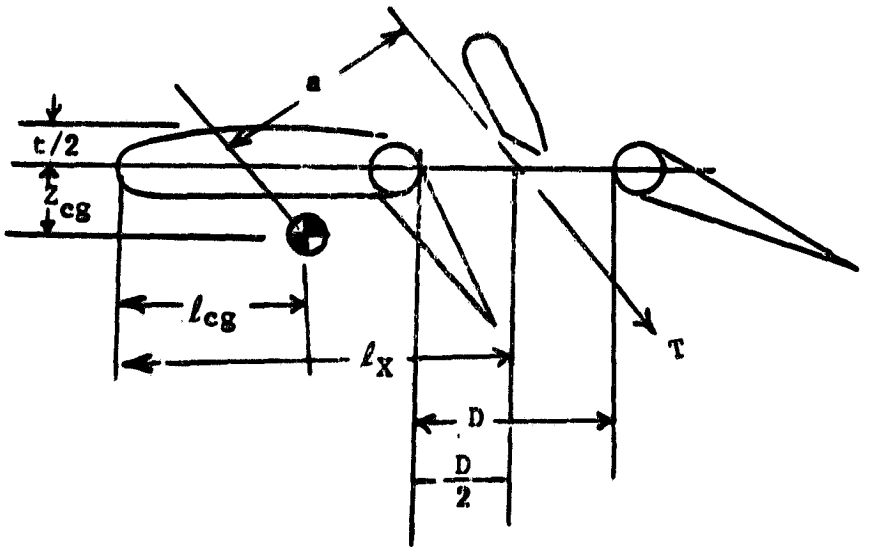

$$ac = \frac{\ell x}{2} \Big/ \bar{c}$$

$$\ell_r = \frac{D}{2} \cdot \phi C_\mu + Z_{cg} + \frac{t}{2}$$

Based on the pressure data, it appears that the circulation lift acts forward on the wing, at about 50% of the distance between the nose and the center of the augmenter throat.

The ram drag pitching moment arm is, as discussed earlier, a function of C_μ. At a $\phi C_\mu = 1$ the force acts at 1/2 a throat diameter above the augmenter inlet; at a $\phi C_\mu = 2$ the force acts at 1 throat diameter above the inlet, etc. Utilizing the above moment arms, a comparison of the calculated values for several configurations tested are shown in Figures 70 to 76. Here, again, as in the lift and drag correlations, the agreement is poorer at conditions where separation is apparent due to reduced entrainment.

CONFIGURATION PERFORMANCE

The augmenter performance can be seen in Figure 77. One possible sequence of angle of attack, thrust angle, and diffuser angle to accomplish an acceleration is presented. Starting at 60 knots with the Augmenter 1 configuration at a thrust angle of 40 degrees, the acceleration and transition are shown. Final transition to wingborne flight would be initiated at a lift coefficient of 1.3, a thrust angle of 30 degrees, a diffuser angle of 0 degree and with an acceleration of .075 at 117 knots.

This represents only one possible sequence and utilizes the data obtained during this investigation. It should be possible to delay transition to deflections of less than $\theta = 30$ degrees, and this would increase the acceleration at the higher speeds. The thrust to weight ratio was established by estimating an augmentation ratio at 90 degrees. The augmentation ratio at 90 degrees for the determination of primary blowing coefficients was obtained by

$$\phi_\theta = (\phi_{90} - 1)\sin\theta + 1 \qquad \text{(Eq. 10)}$$

CONCLUSIONS

The study of a VTOL thrusting ejector (TAW) in low speed flight has demonstrated an aerodynamic relationship between the jet flap and the thrust augmenter wing. Specific points of interest are:

1. Component breakdown of the loads and pressure distribution analysis have shown the majority of the induced lift of the augmenter to be concentrated on the wing nose section.

2. Forward speed has little effect on either the augmentation ratio or on the entrainment of this particular class of augmenters. Performance data are functions of the product of momentum coefficient and augmentation ratios (ϕC_μ) provided separation is not present on the wing.

3. Thrust recovery of the augmenter at the deflections investigated is 1.0. Thrust recovery of the jet flap is .9 to .95 at 40 degrees. Jet flap thrust recovery is probably reduced because of scrubbing losses.

4. Jet flap theory can be used to predict TAW aerodynamic characteristics with these assumptions:

   a. The correlating chord length of the TAW is the aft surface chord

   b. Replacing the blowing coefficient term C_μ with the product ϕC_μ

   c. Thrust recovery approaches 1.0 at $\delta_F = 40$ degrees for the TAW and about 0.9 for the jet flap due to the surface scrubbing loss of the jet flap.

   d. Ram drag must be included in drag and pitching moment equations

   e. Ram drag moment arm for computing pitching moment is a function of blowing coefficient.

5. Downwash angles of 20 to 30 degrees are shown behind the TAW at thrust angles of 40 degrees.

RECOMMENDATIONS

Since several of the augmenter wing combinations of interest for airplane configurations utilize tandem augmenters, either spanwise in the case of the XFV-12A or chordwise as in the case of some NASA fighter studies, it is recommended that additional forward speed studies be undertaken to investigate the particular characteristics of tandem augmenters.

REFERENCES

(1) Alperin, M., Wu, J. J., "Recent Development of a Jet Diffuser Ejector", AIAA Paper No. 80-0231, Jan. 1980.

(2) Whittley, D. C., "Large-Scale Model Tests of a New Technology V/STOL Concept", AIAA Paper No. 80-0233, Jan. 1980.

(3) Aoyagi, K., Aiken, T. N., "Wind Tunnel Investigation of a Large Scale VTOL Aircraft Model with Wing Root and Wing Thrust Augmenters", NASA TM 78589, Sept. 1979.

(4) Stewart, V. R., White, E. R., Palmer, W. E., "Aerodynamic Analysis of an Integrated V/STOL Thrust Augmenter Lift System Concept", Proceedings of Navy Jet V/STOL Workshop, pages 664 to 701, July 1975.

(5) Mark, L., DeHart, J. H., "High Speed Aerodynamic Design of an Innovative V/STOL Canard-Wing Configuration", AIAA Paper 76-910, Sept. 1976.

(6) Maskell, E. C., Spence, D. A., "A Theory of the Jet Flap in Three Dimensions", Proceedings of the Royal Aircraft Society, Vol. 251, pp. 407-425, 1959.

(7) McCormick, B. W., Jr., "Aerodynamics of V/STOL Flight", Academic Press, pp. 194-211, 1967.

(8) Heyson, H. H., "Linearized Theory of Wind Tunnel Jet Boundary Corrections and Ground Effect for VTOL-STOL Aircraft", NASA TR R-124 1962.

(9) Heyson, H. H., "Nomographic Solution of the Momentum Equation for VTOL-STOL Aircraft", NASA TN D-814, April 1961.

(10) Heyson, H. H., "Rapid Estimation of Wind Tunnel Corrections with Application to Wind Tunnel and Model Design", NASA TN D-6416, Sept. 1971.

(11) Heyson, H. H., "Use of Superposition in Digital Computers to Obtain Wind Tunnel Interference Factors for Arbitrary Configurations with Particular Reference to V/STOL Models", NASA TR R-302, Feb. 1969.

(12) Young, A. D., "The Induced Drag of Flapped Elliptic Wings with Cut-out and with Flaps that Extend the Local Chord", Royal Aircraft Establishment, R&M 2544, Feb. 1942.

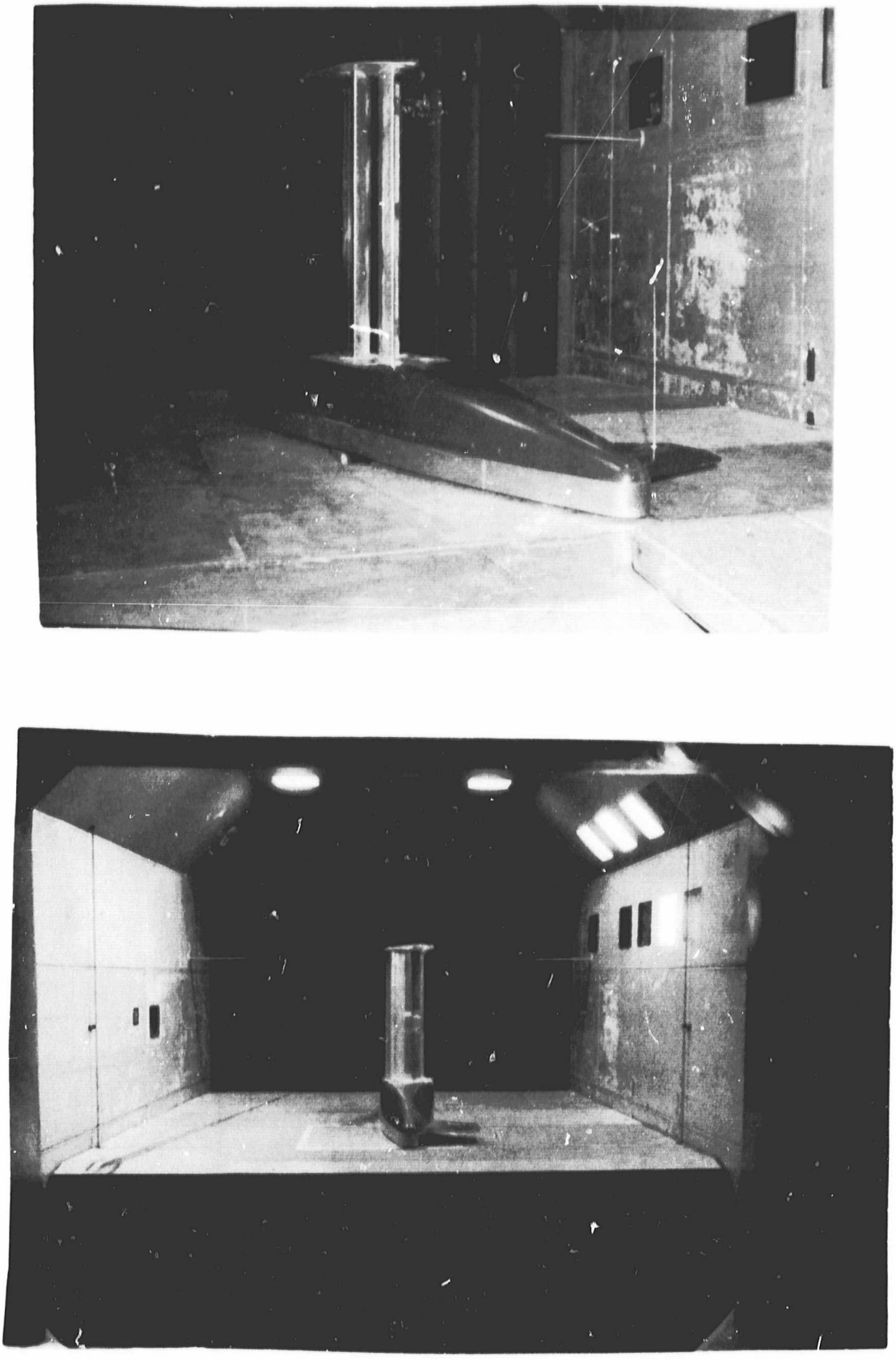

Figure 1 Model Picture

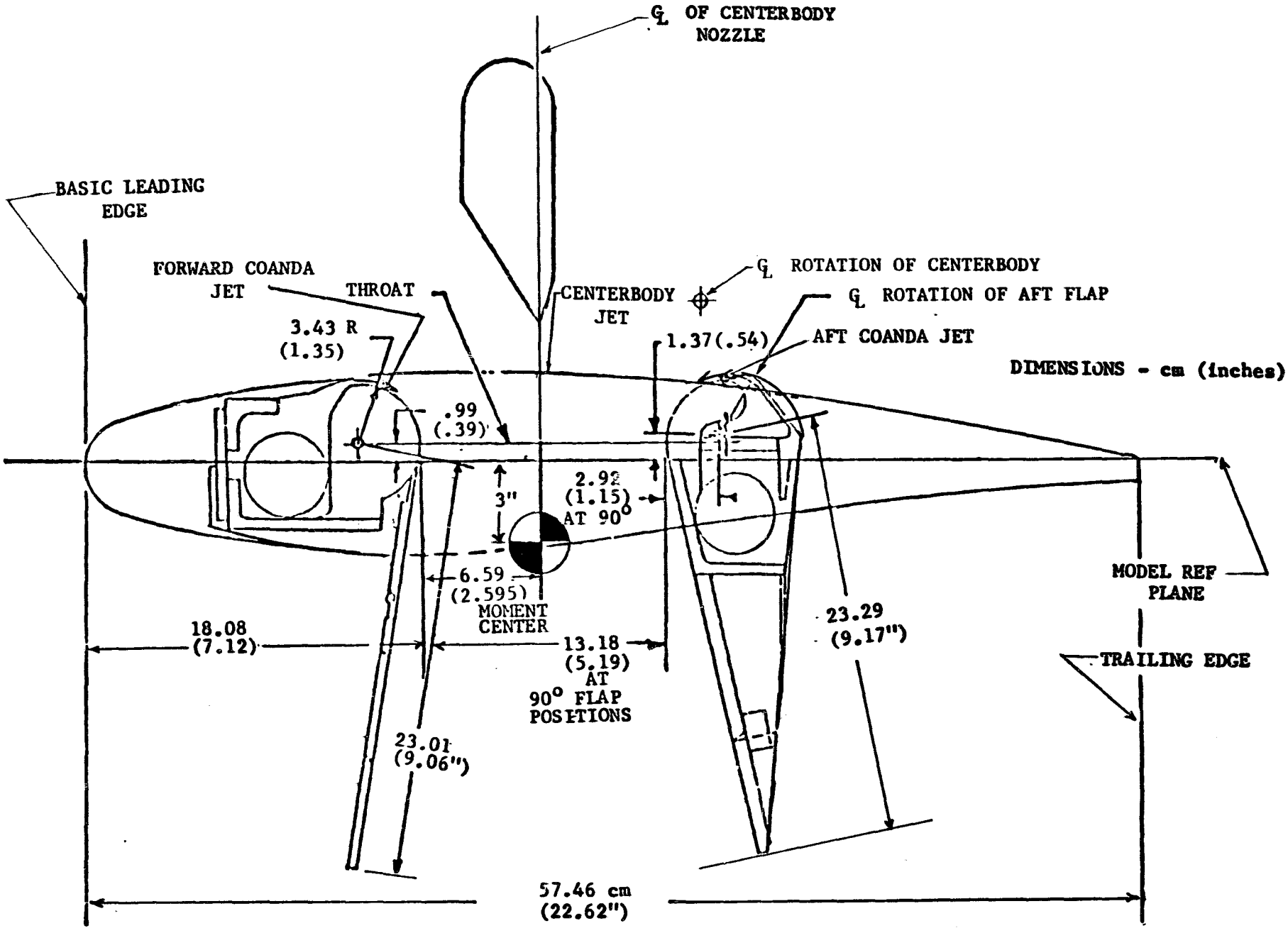

Figure 2 Model Wing Configuration Augmenter 1

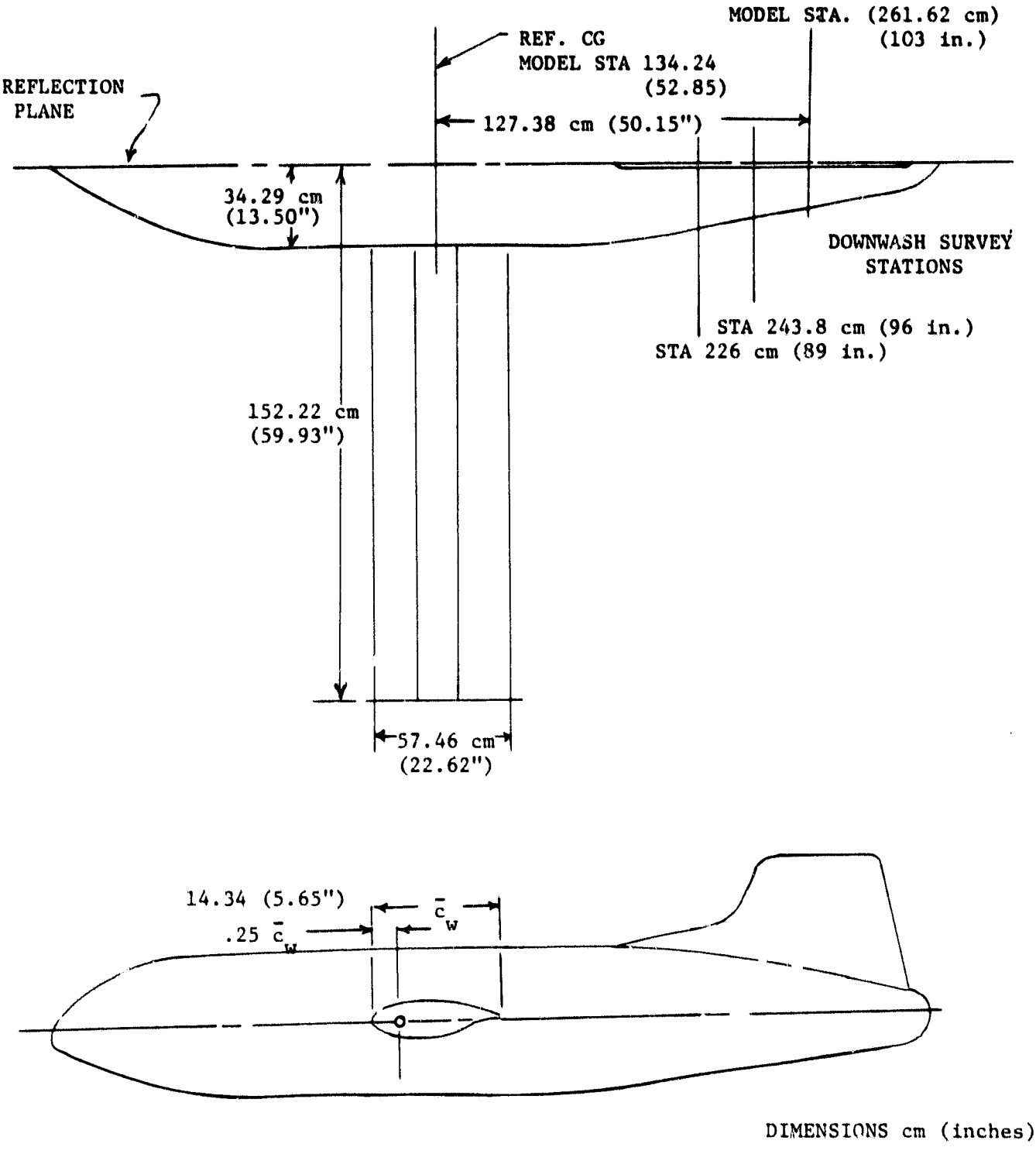

(a) Dimensional

Figure 3 Model Configuration Sketch

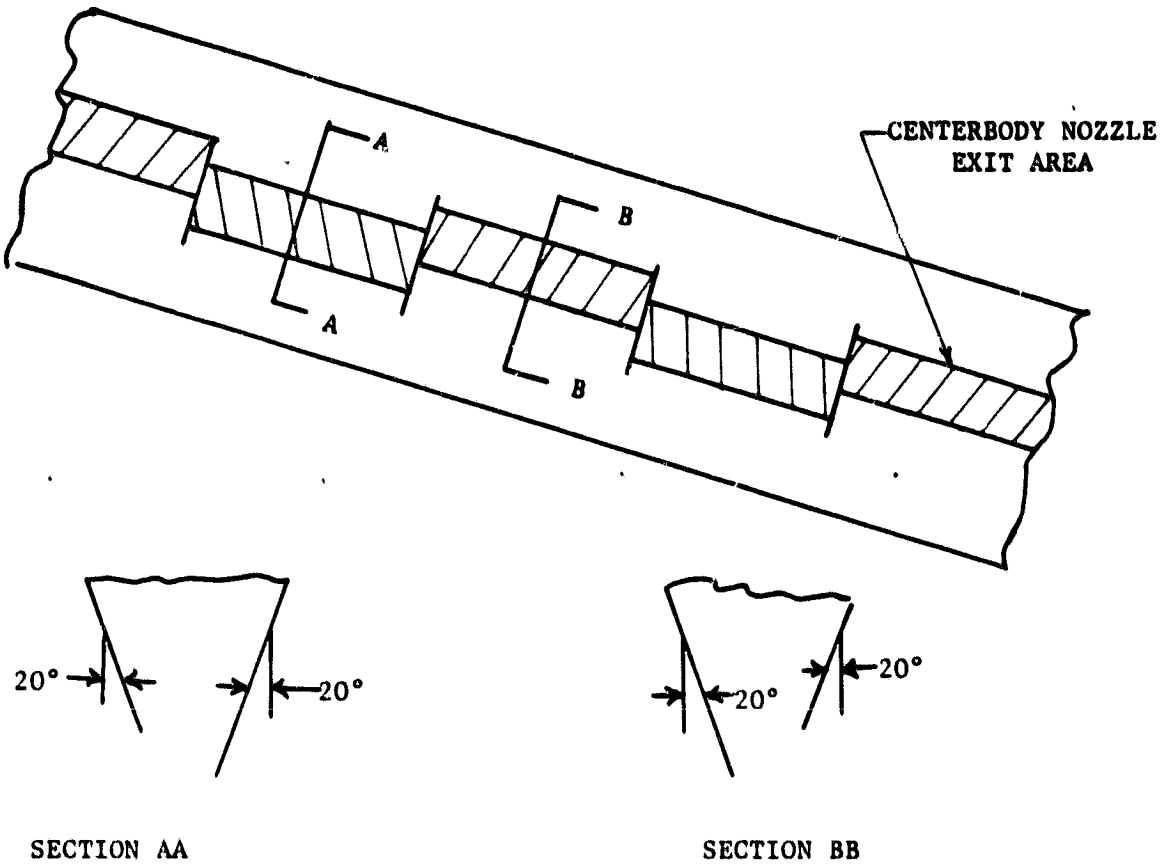

(b) Hypermixing Centerbody Nozzle

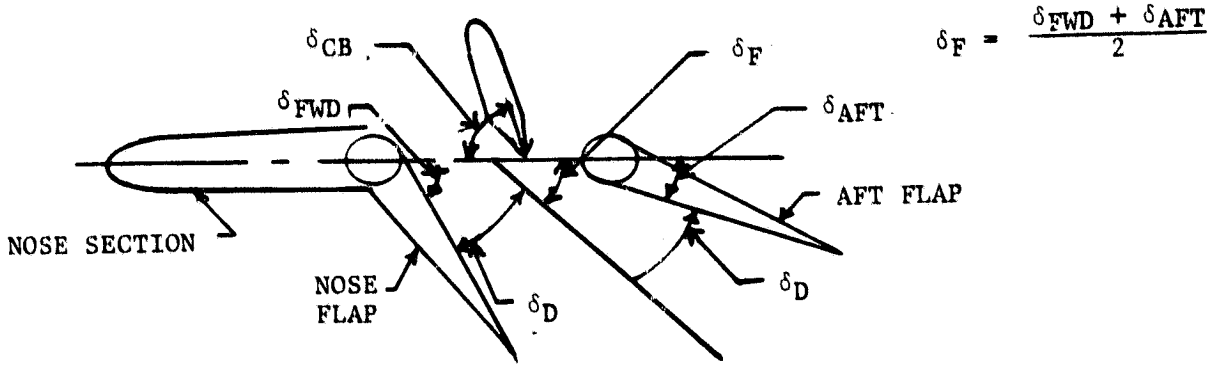

(c) Augmenter Nomenclature

Figure 3 (Concluded)

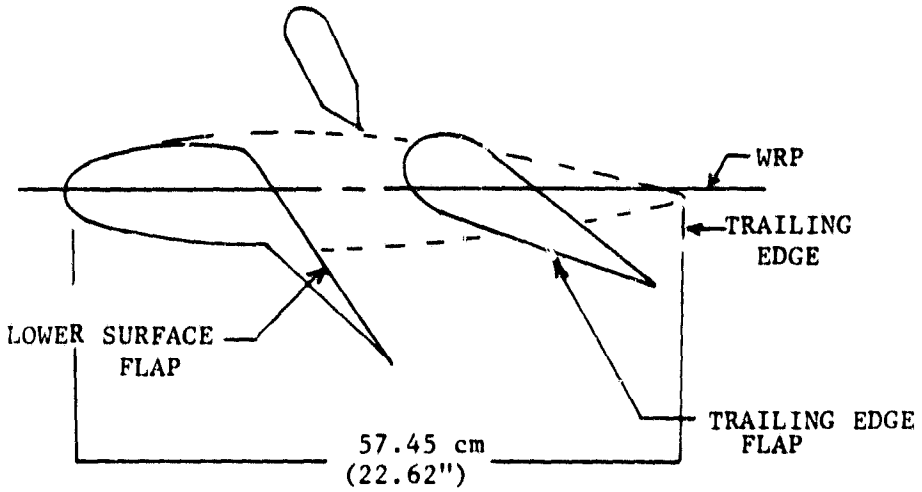

AUGMENTER 1

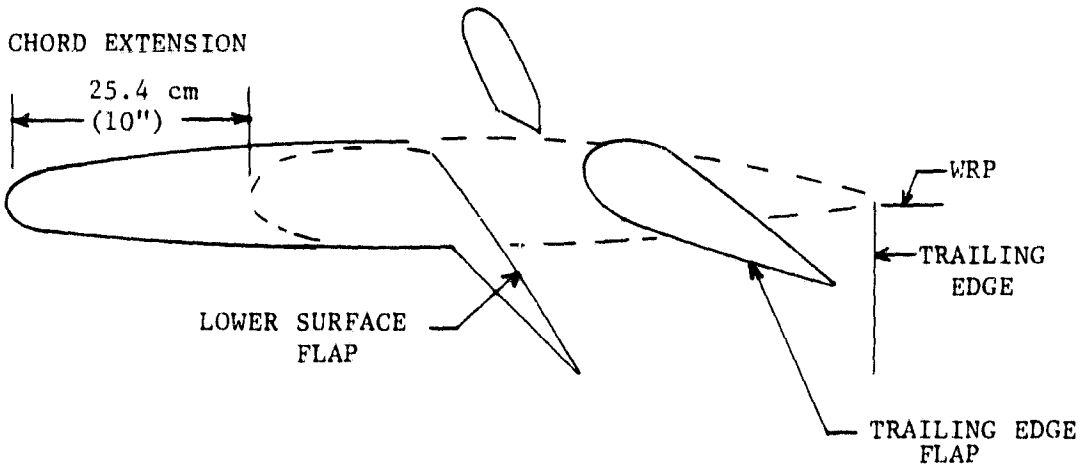

AUGMENTER 2

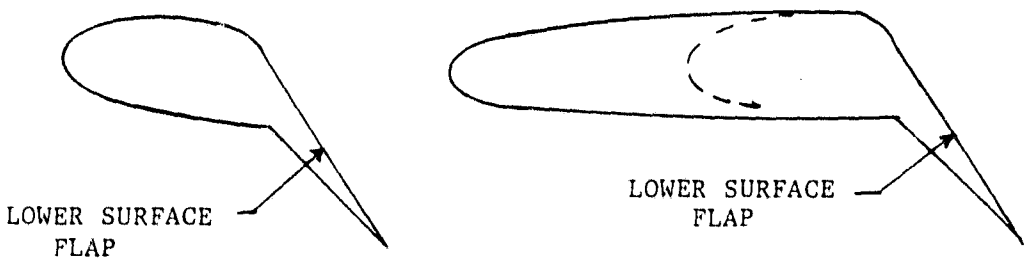

JET FLAP 1

JET FLAP 2

Figure 4 Wing Cross Section

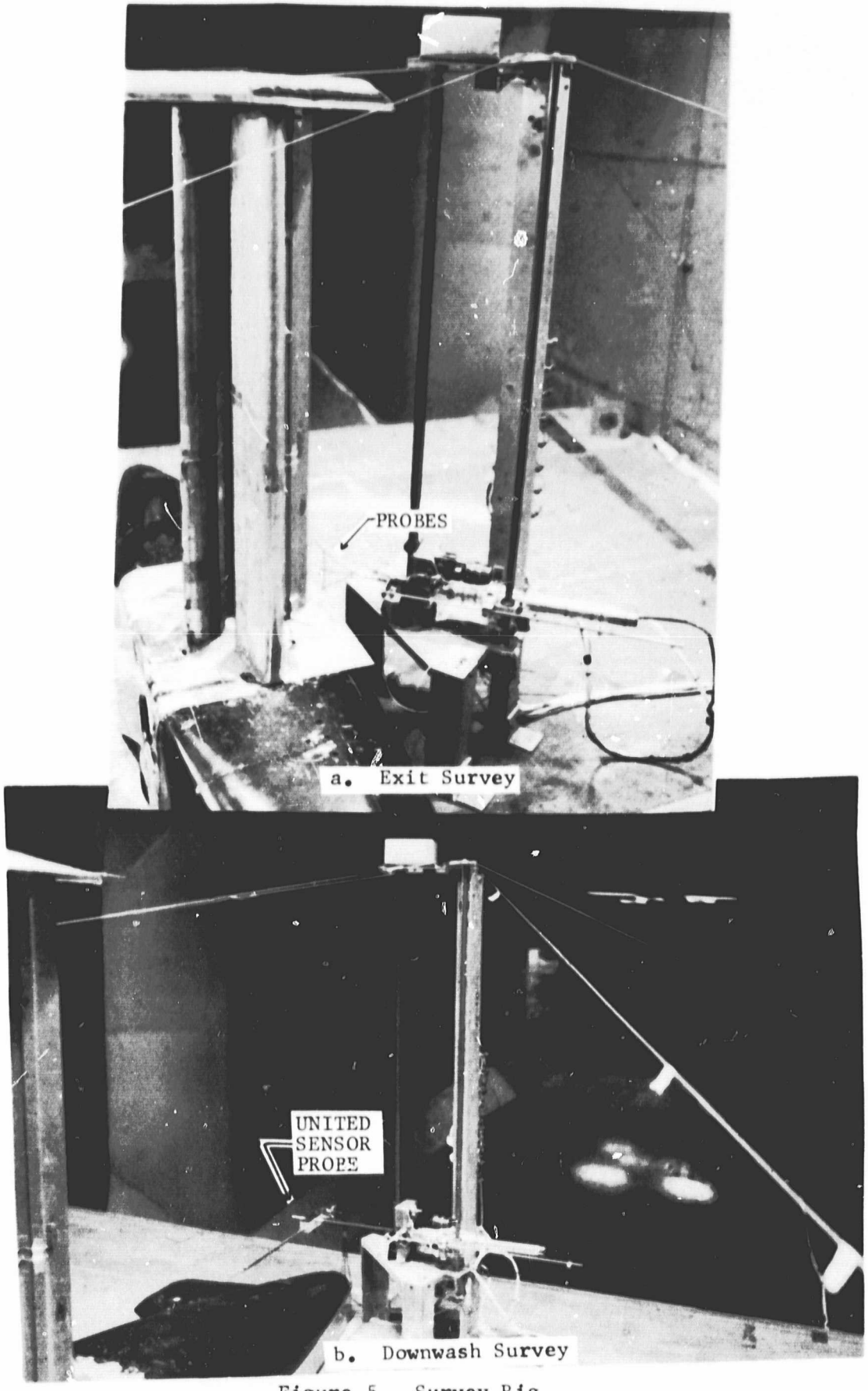

Figure 5 Survey Rig

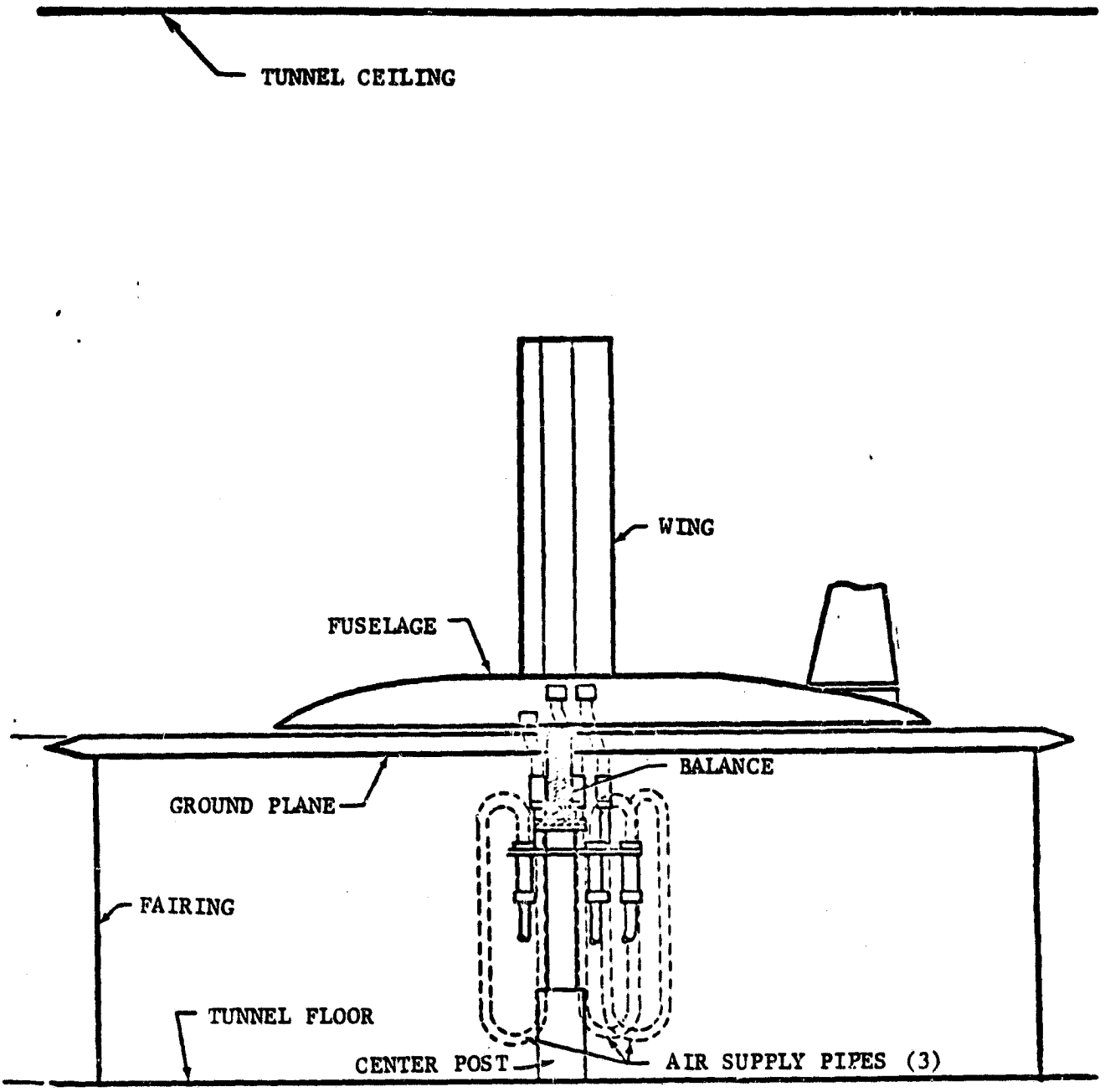

Figure 6 Model Installation in NACAL

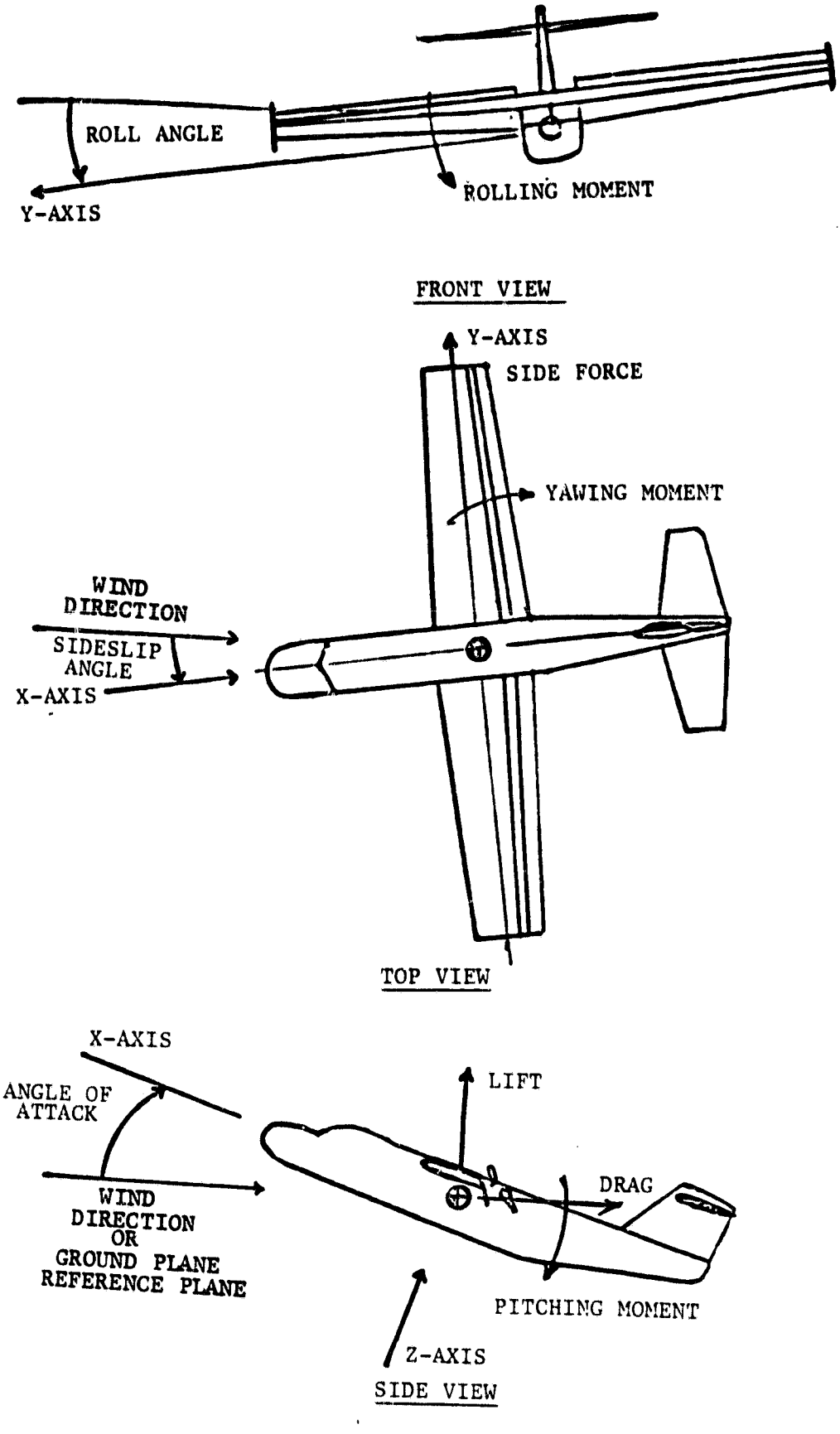

Figure 7. Model Axis System

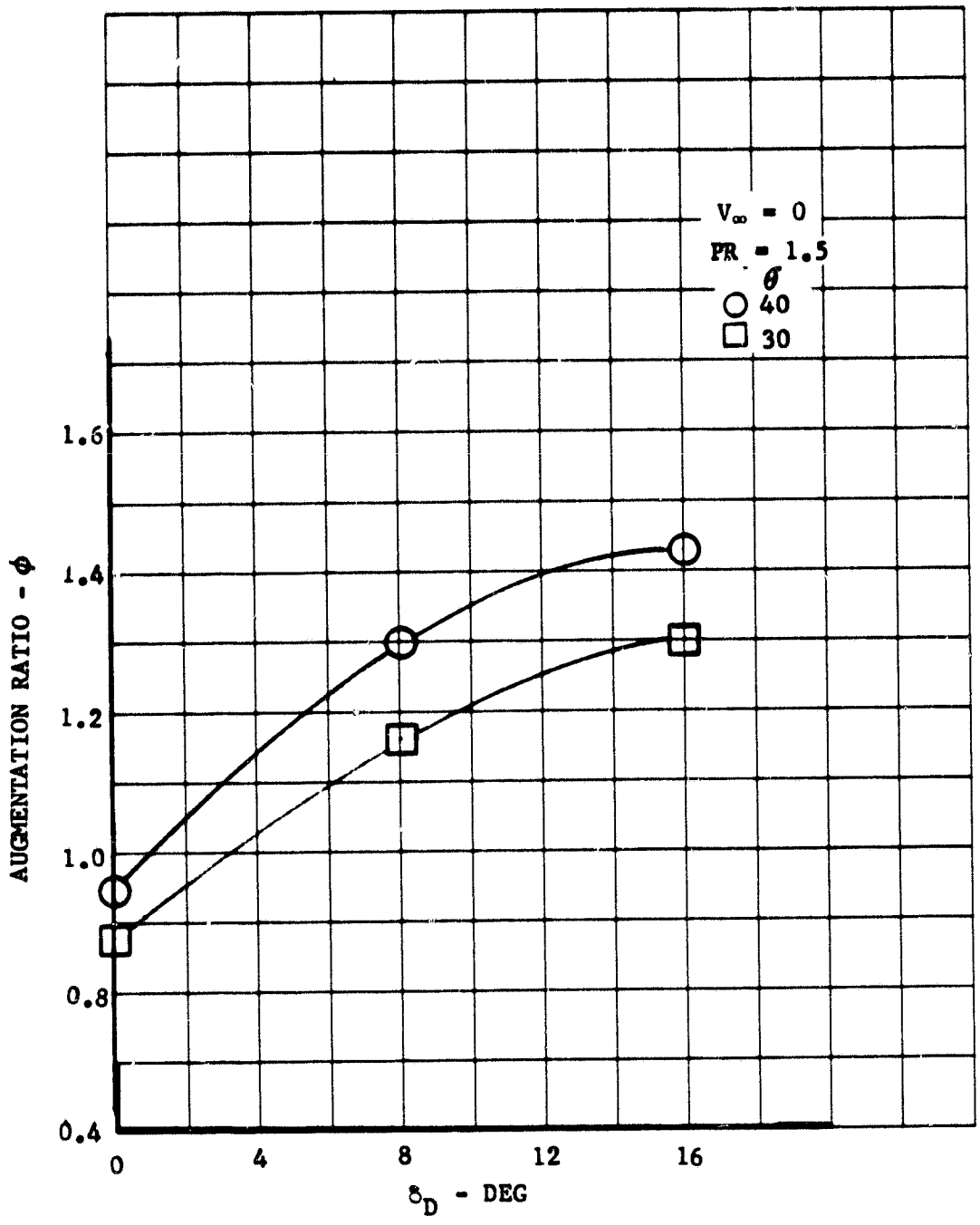

Figure 8 Variation of Augmentation Ratio with Diffuser Angle

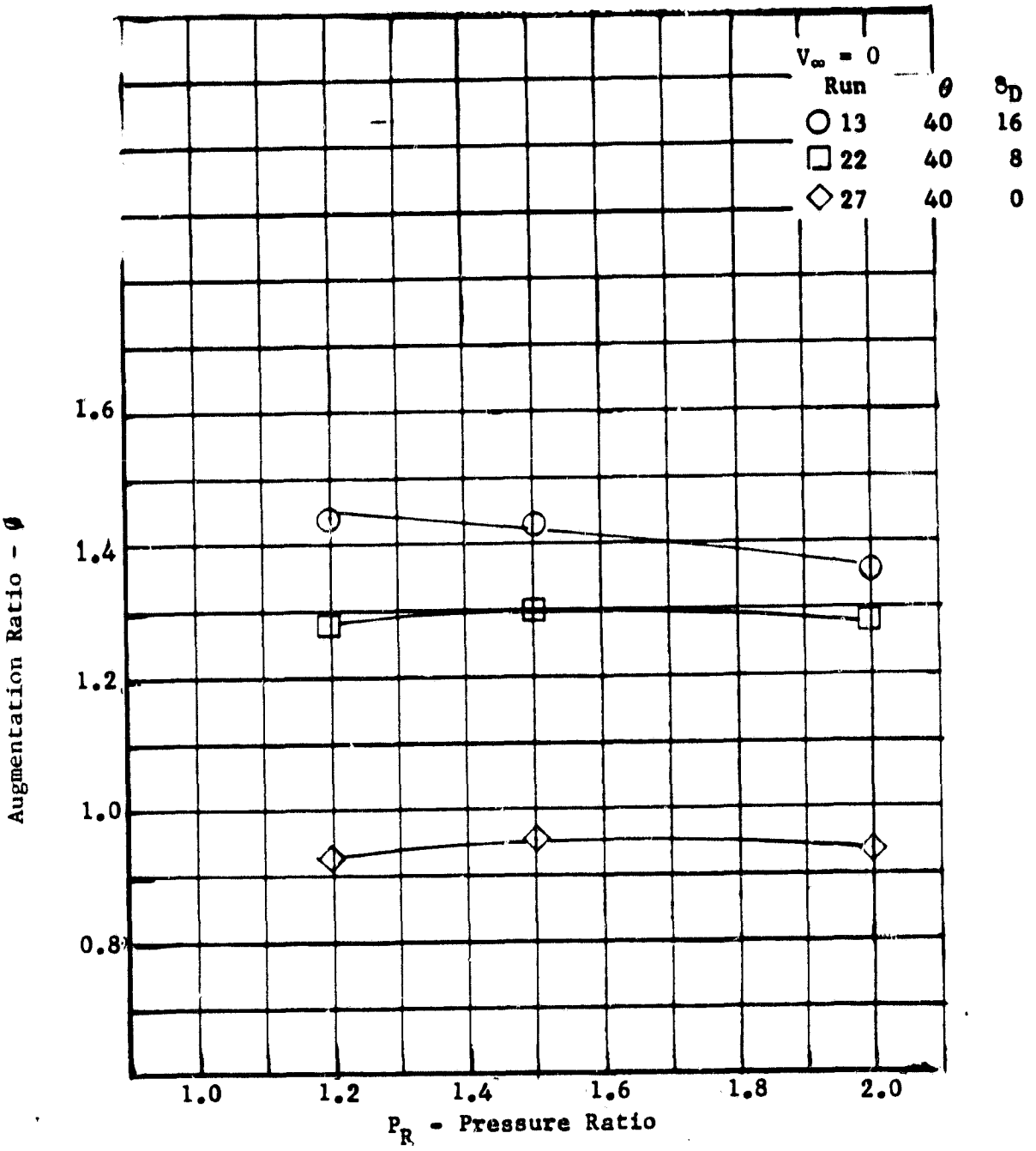

Figure 9 Variation of Augmentation Ratio with Pressure Ratio, $\theta = 40^o$

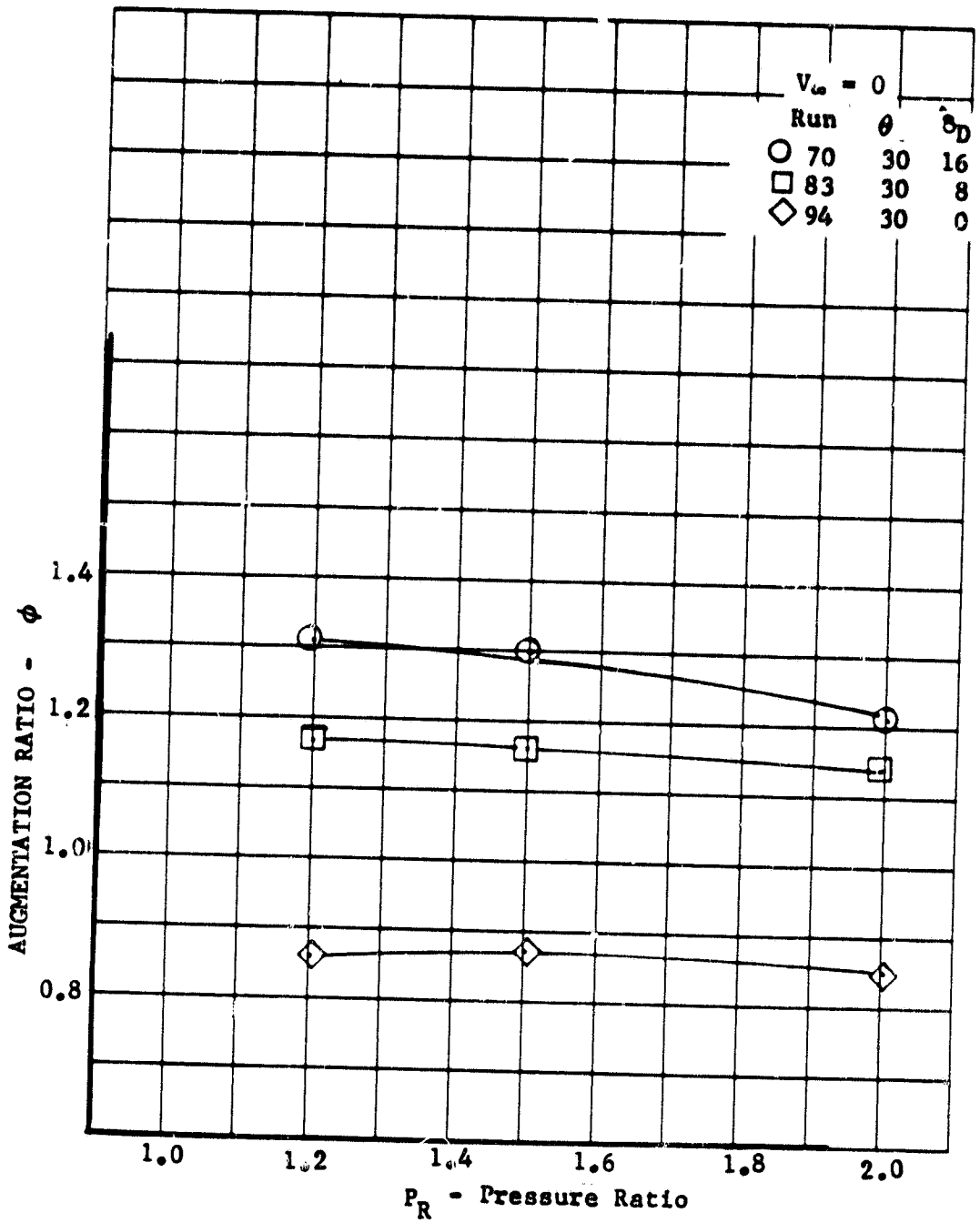

Figure 10 Variation of Augmentation Ratio with Pressure Ratio, $\theta = 30^\circ$

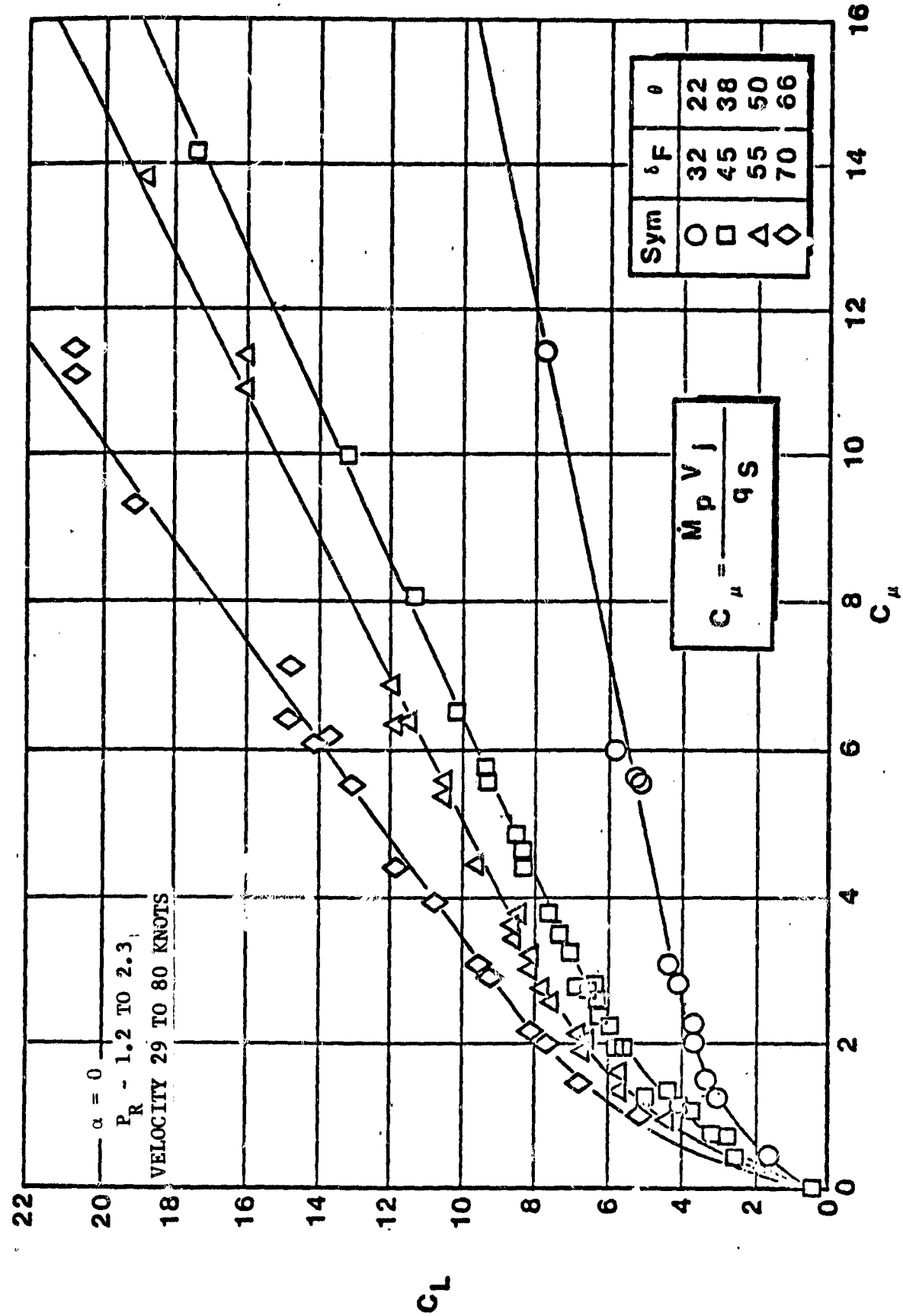

Figure 11 Variation of Lift Coefficient with Momentum Coefficient

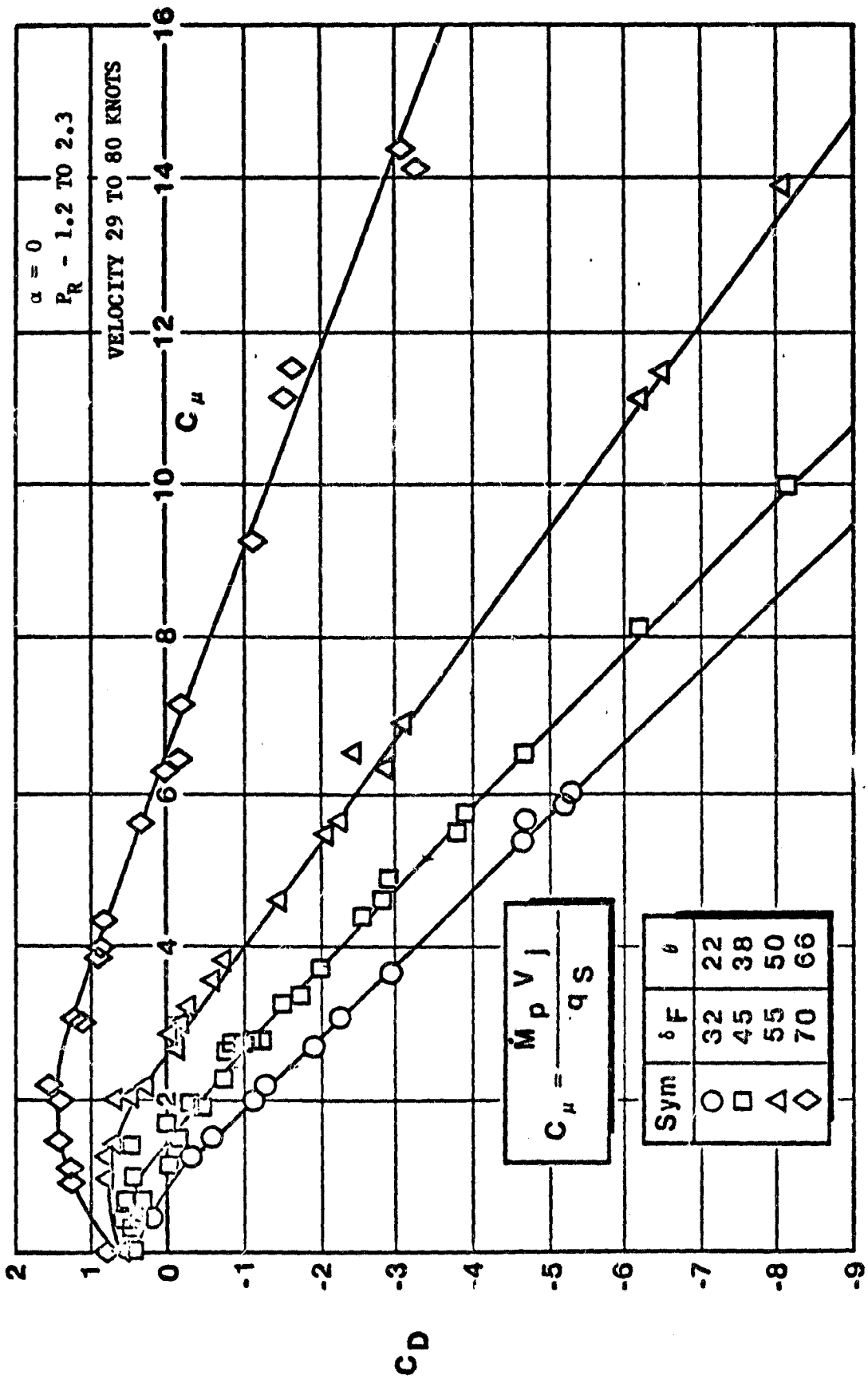

Figure 12 Variation of Drag Coefficient with Momentum Coefficient

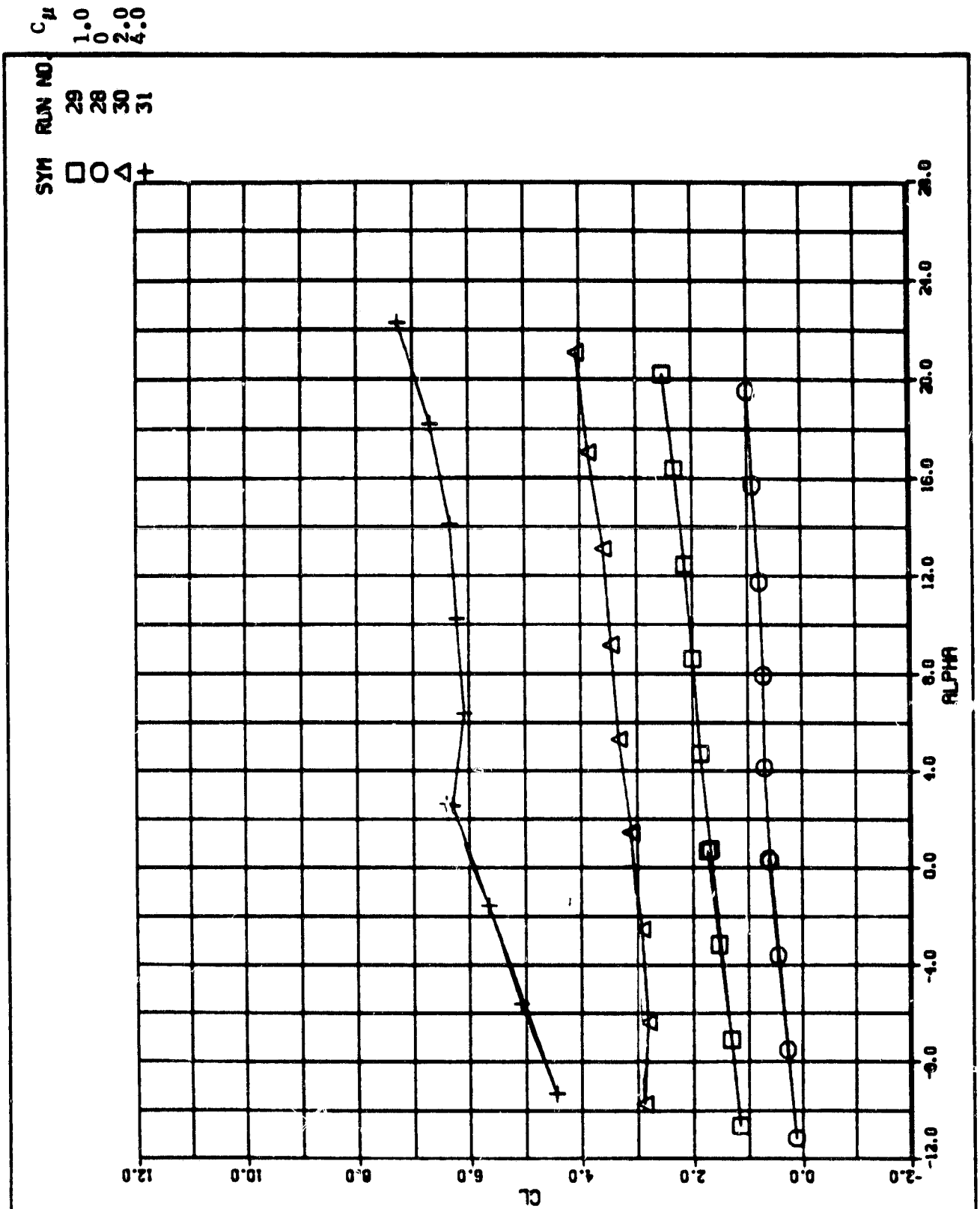

a. Lift vs α

Figure 13 Basic Aerodynamic Characteristics, Thrust Augmenter 1; $\theta = 40^\circ$, $\delta_D = 0^\circ$

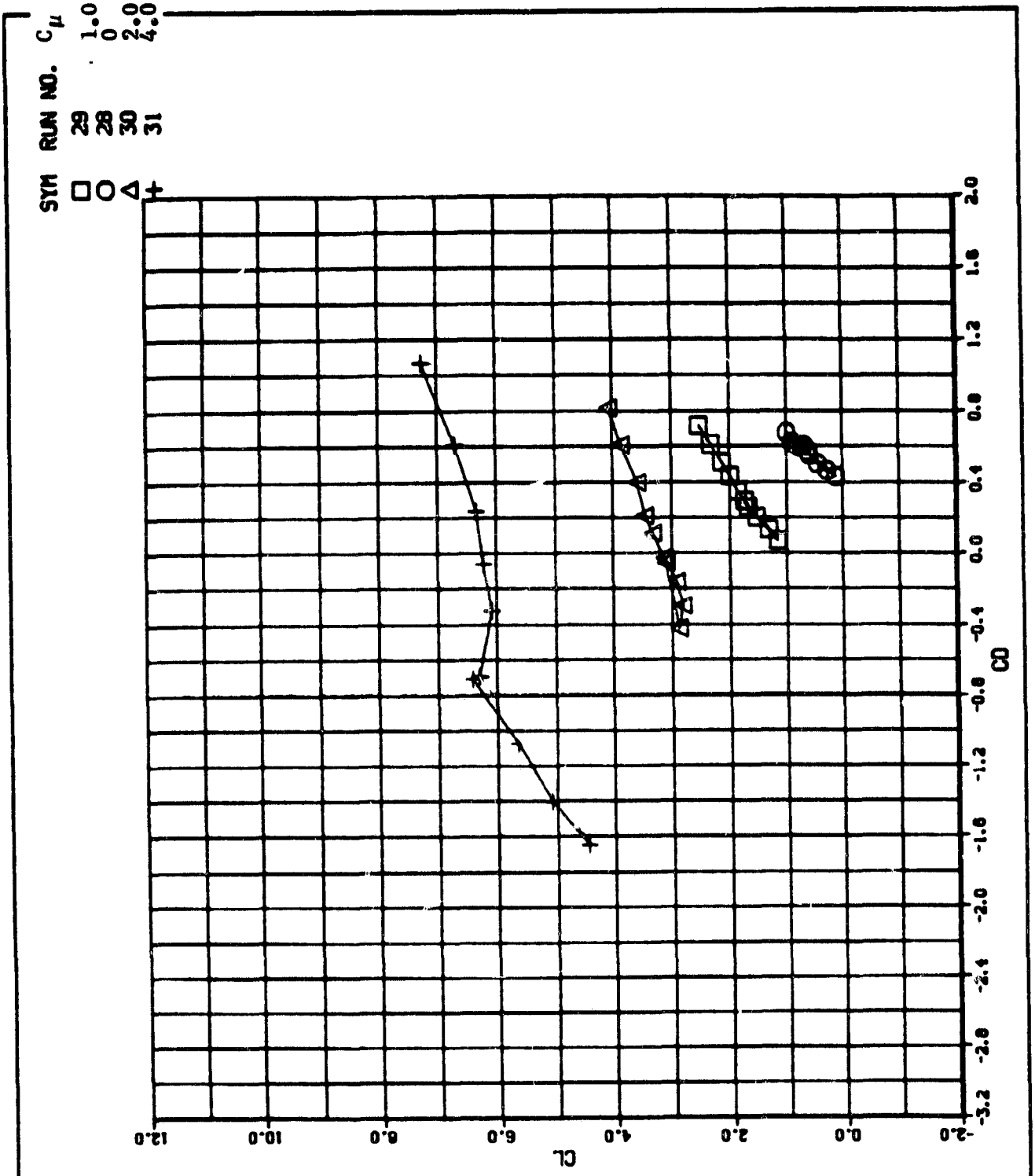

b. Lift vs Drag

Figure 13. Continued

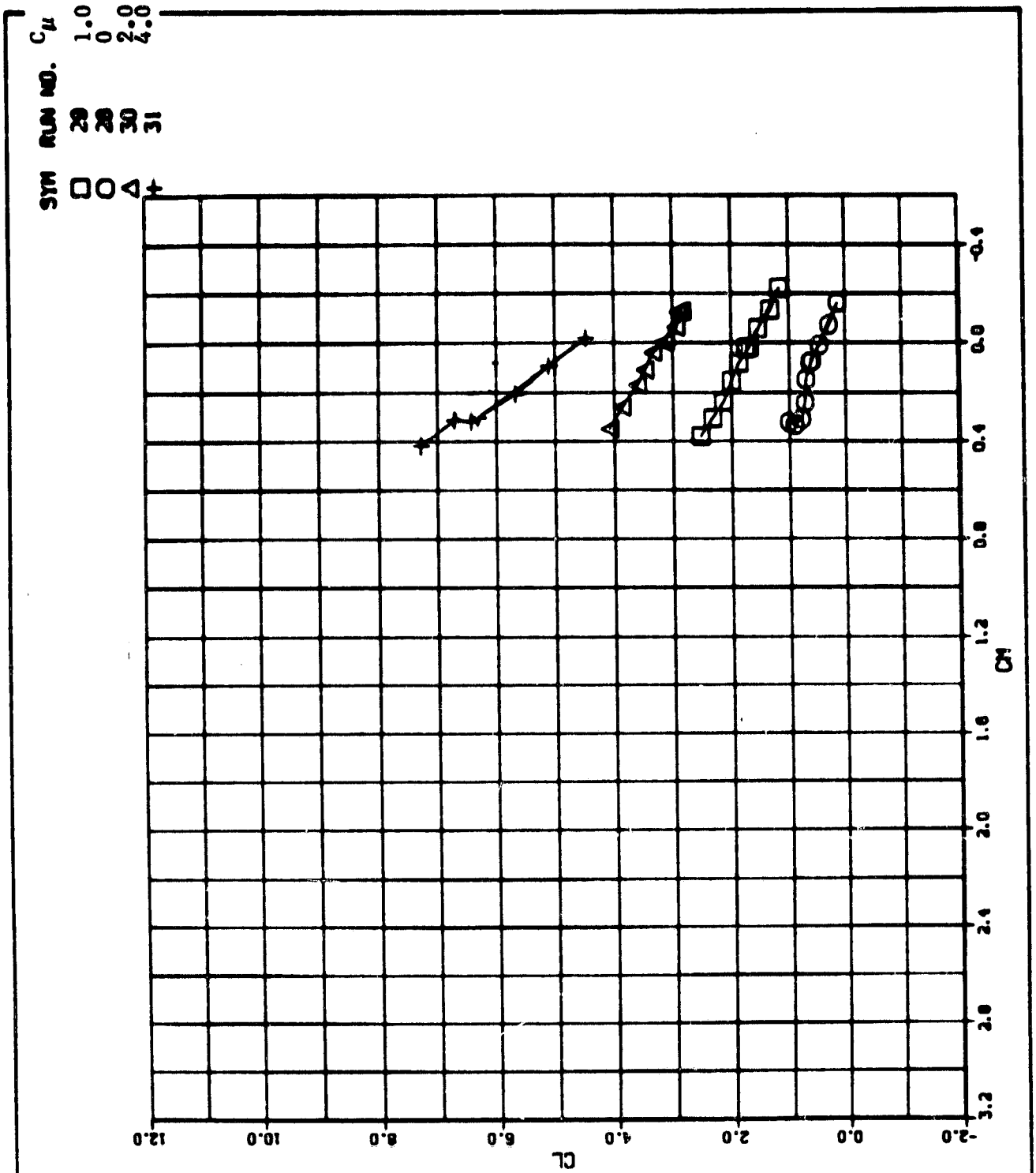

c. Lift vs Pitching Moment

Figure 13. Continued

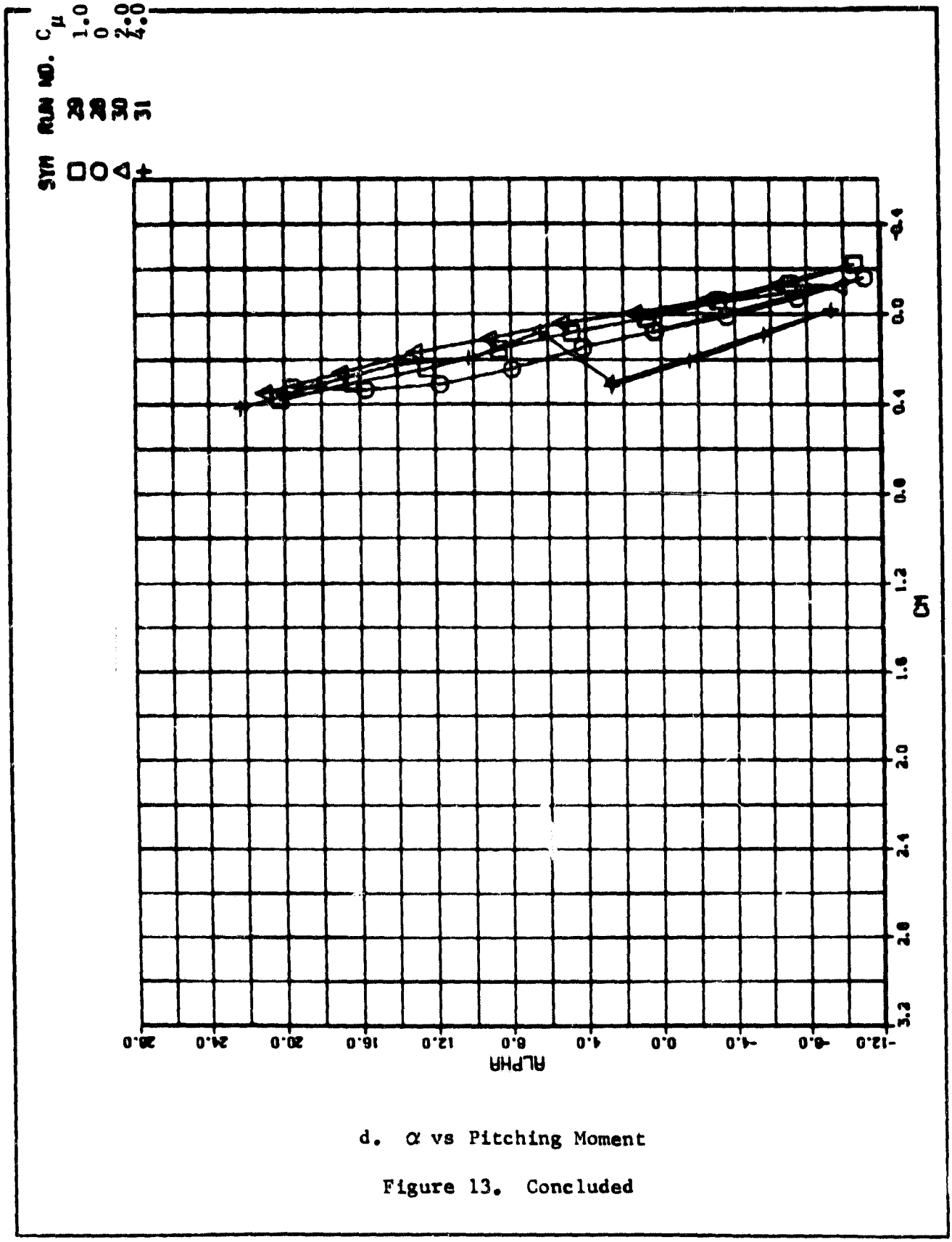

d. α vs Pitching Moment

Figure 13. Concluded

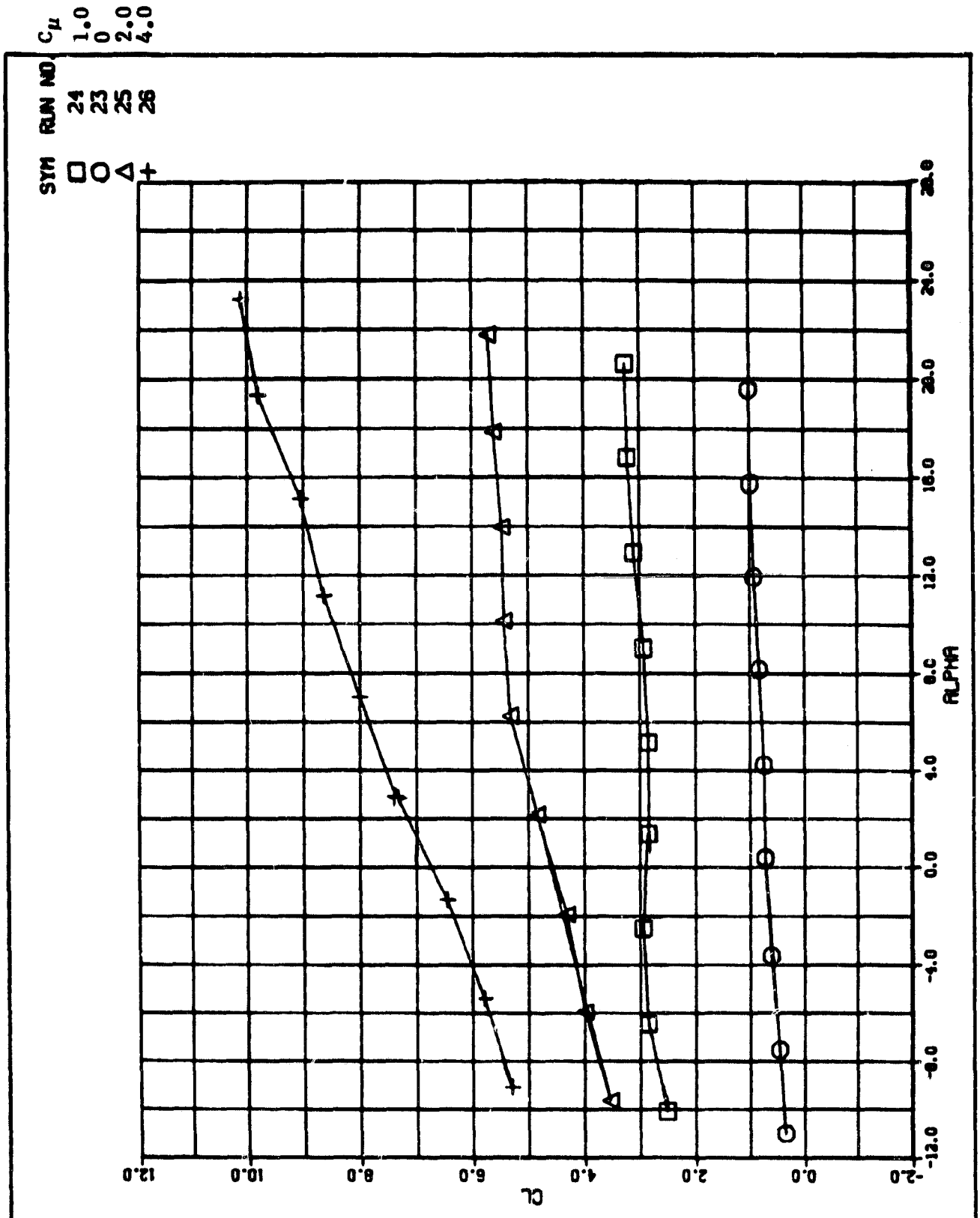

a. Lift vs α

Figure 14 Basic Aerodynamic Characteristics, Thrust Augmenter 1; $\theta = 40^{\circ}$, $\delta_D = 8^{\circ}$

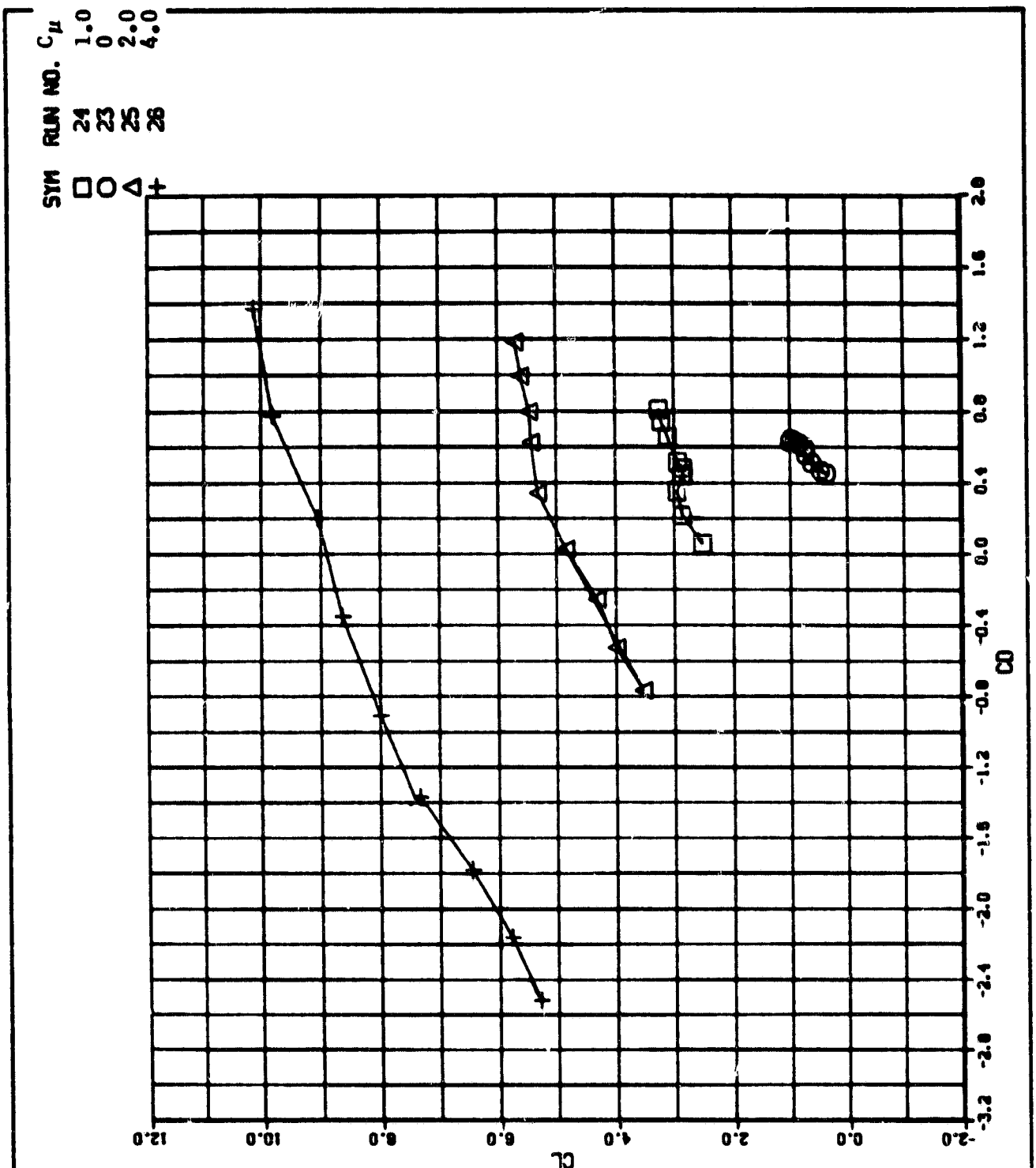

b. Lift vs Drag

Figure 14. Continued

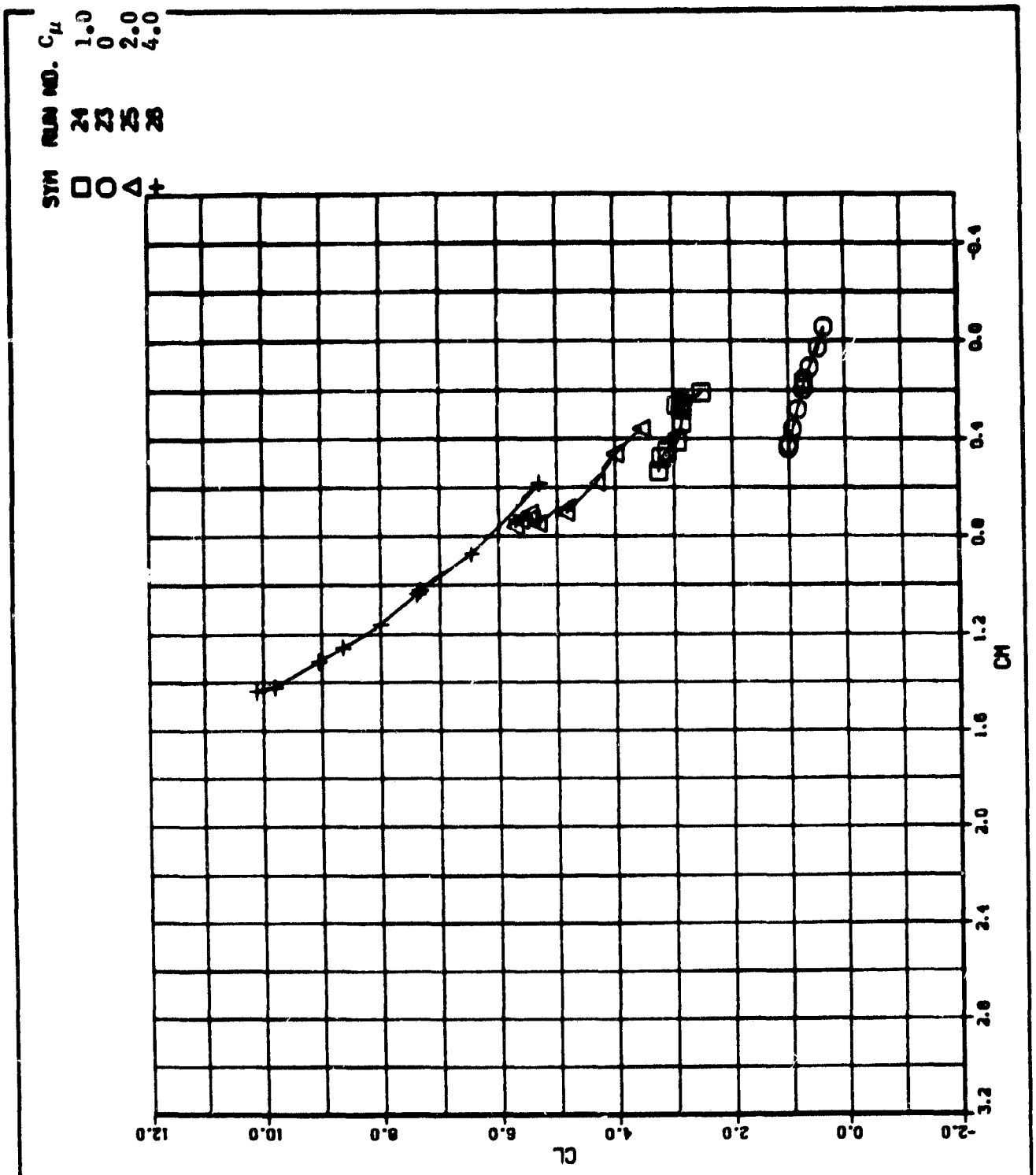

c. Lift vs Pitching Moment

Figure 14. Continued

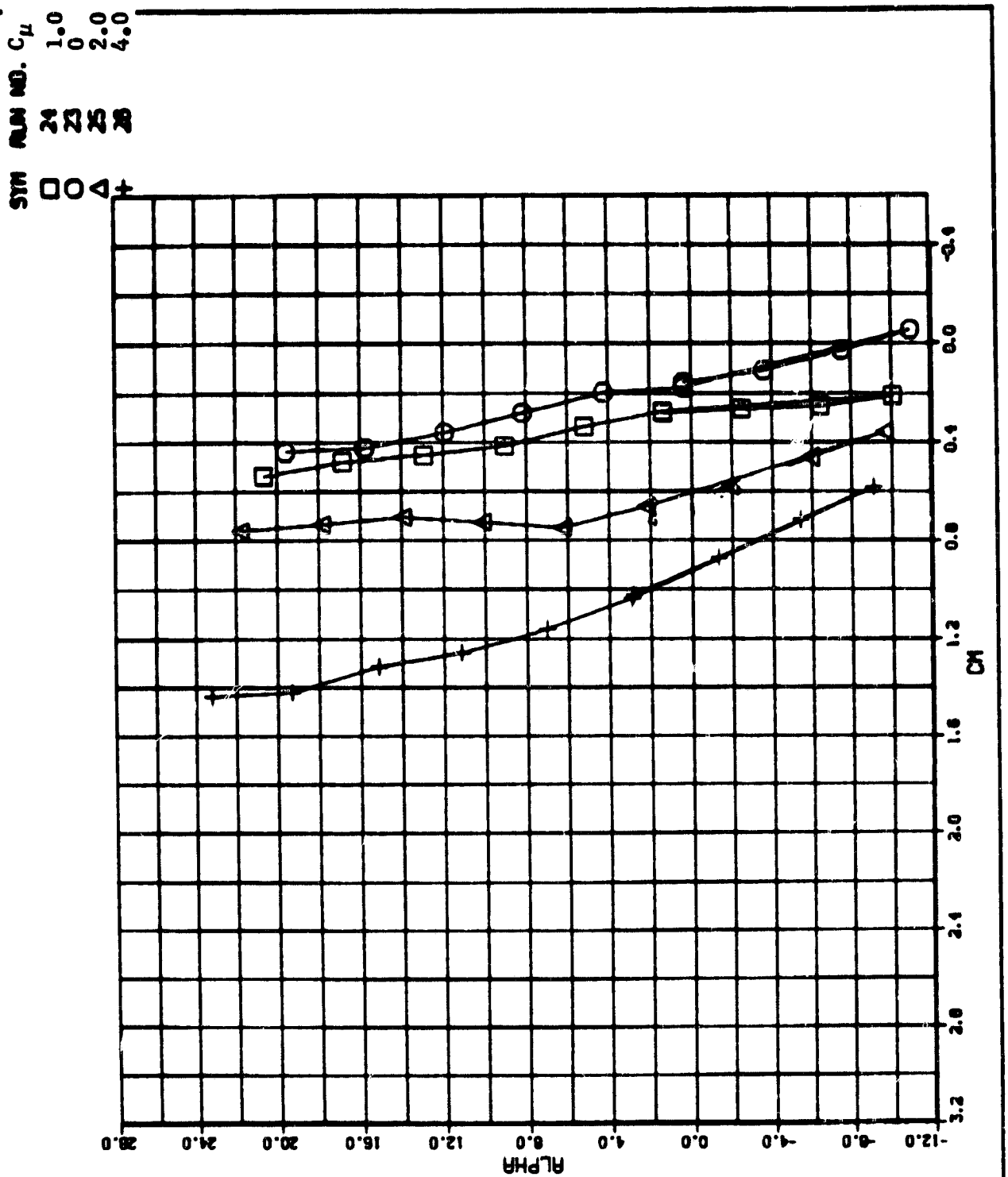

d. α vs Pitching Moment

Figure 14. Concluded

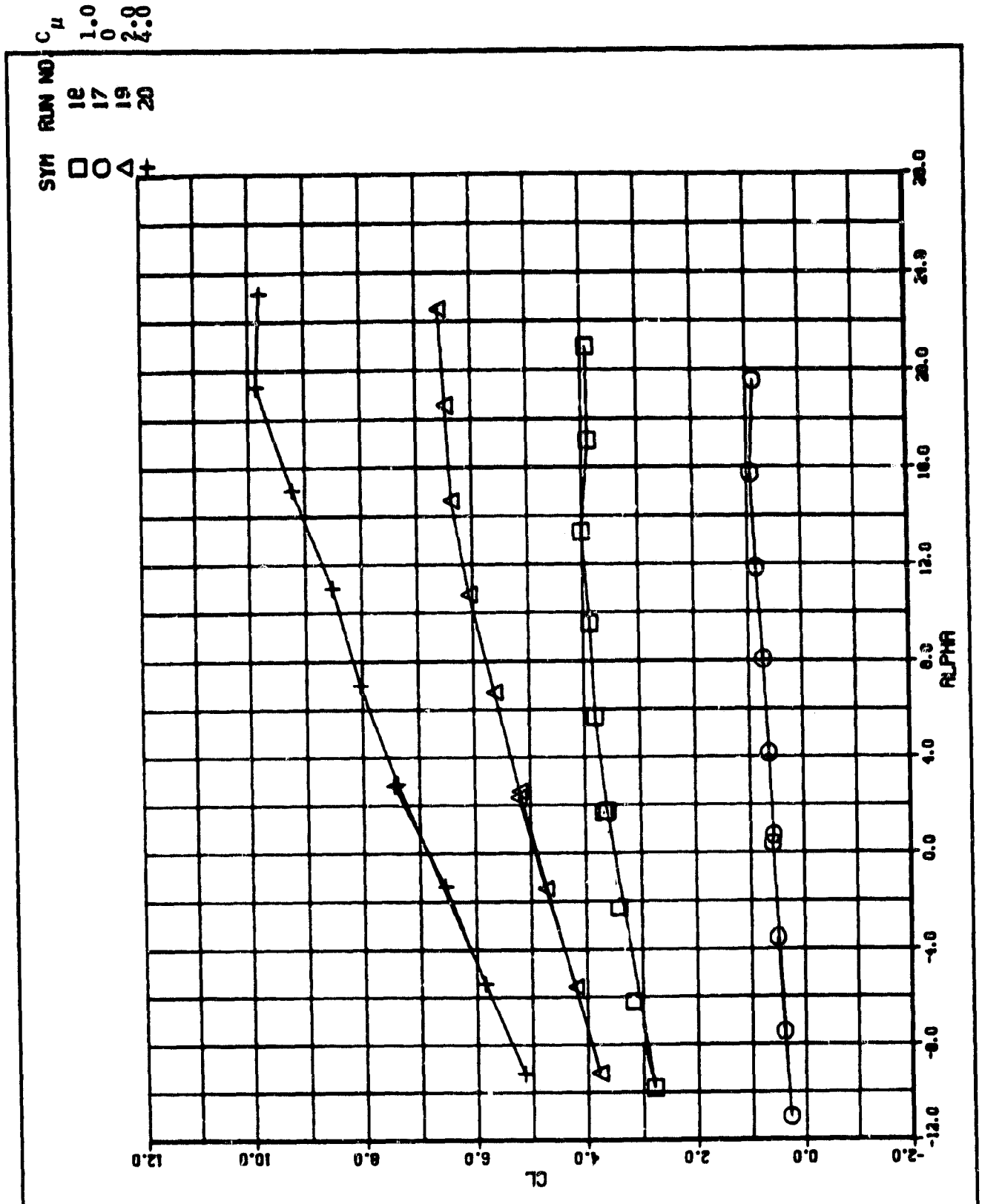

a. Lift vs α

Figure 15. Basic Aerodynamic Characteristics, Thrust Augmenter 1; $\theta = 40^{\circ}$, $\delta_D = 16^{\circ}$

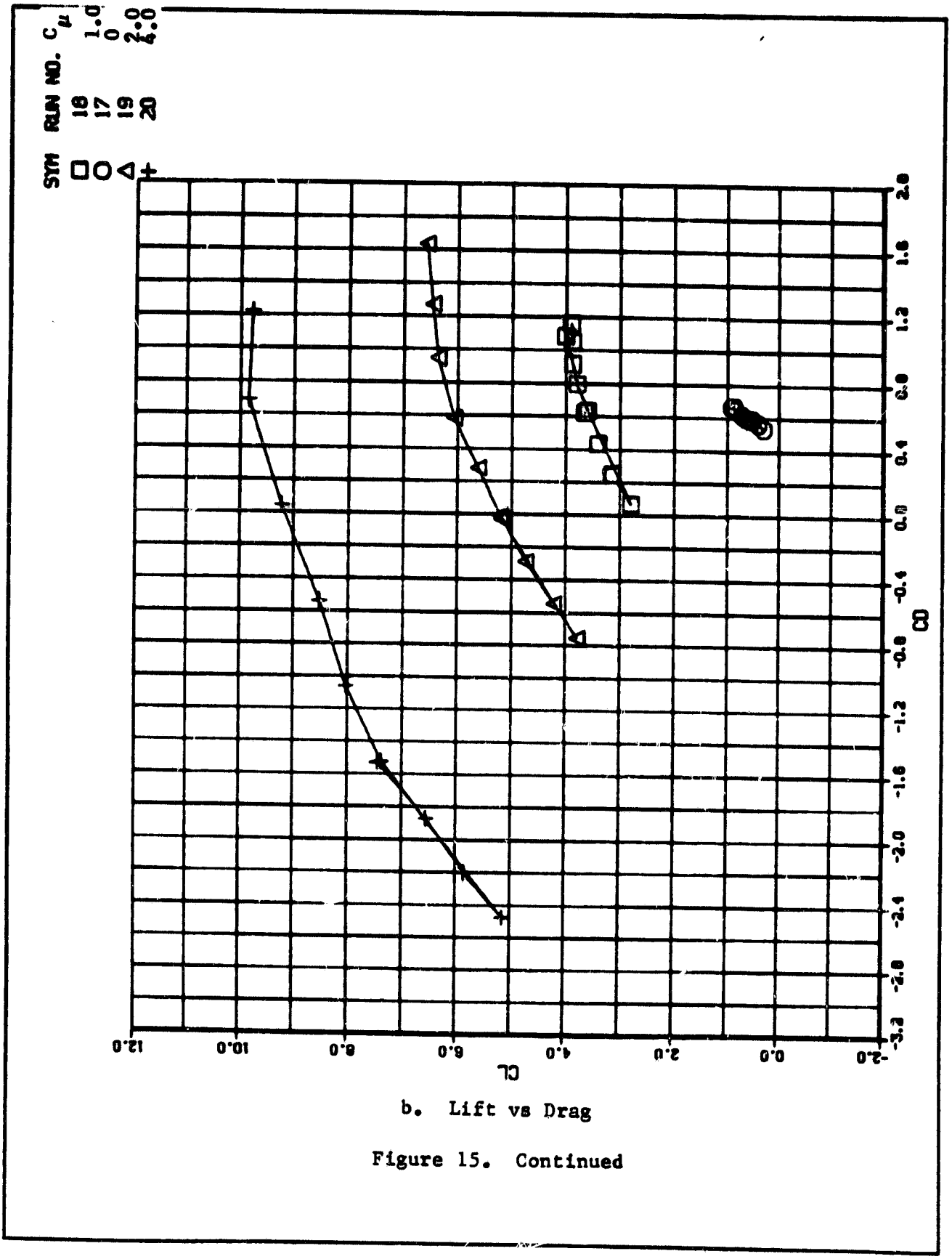

b. Lift vs Drag

Figure 15. Continued

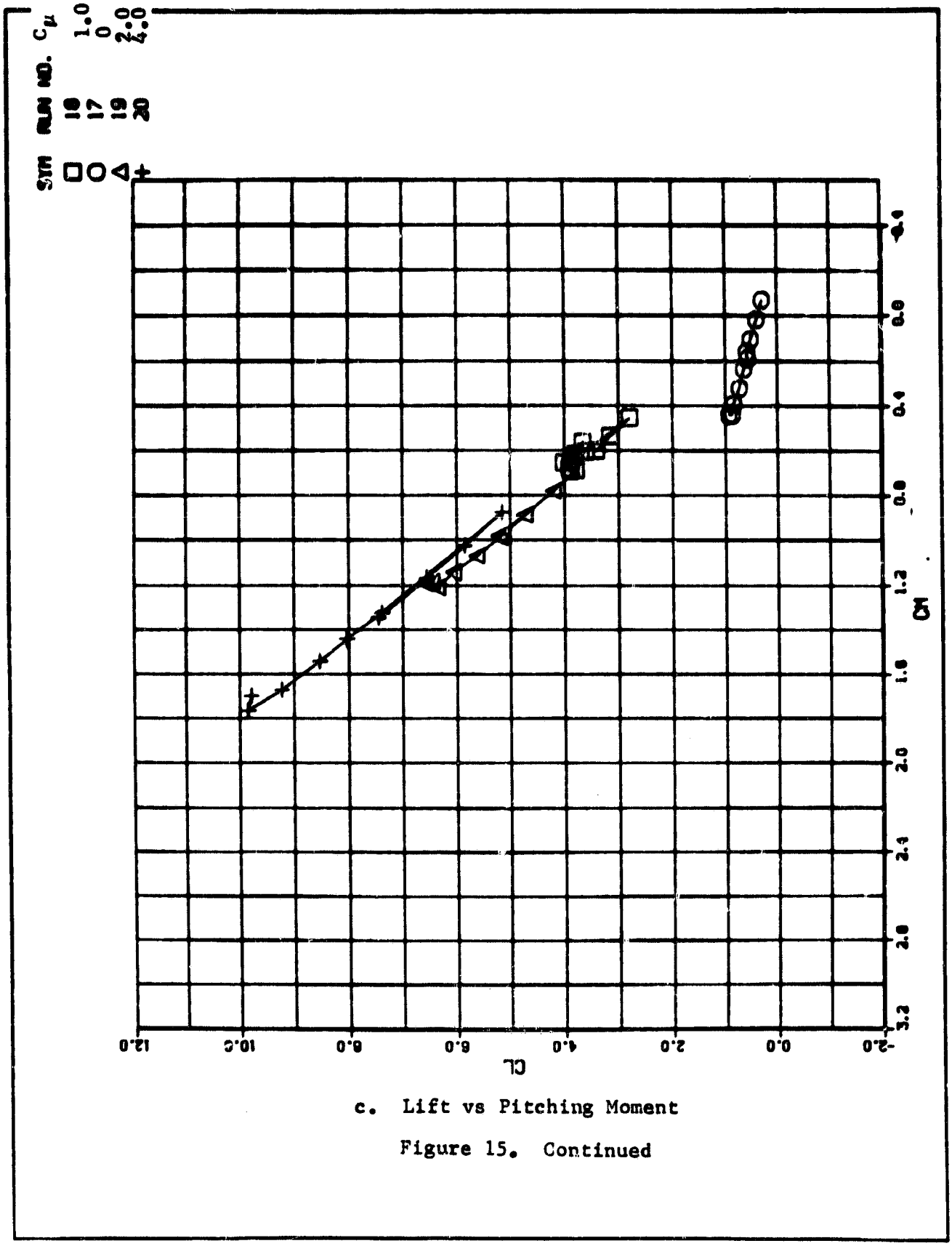

c. Lift vs Pitching Moment

Figure 15. Continued

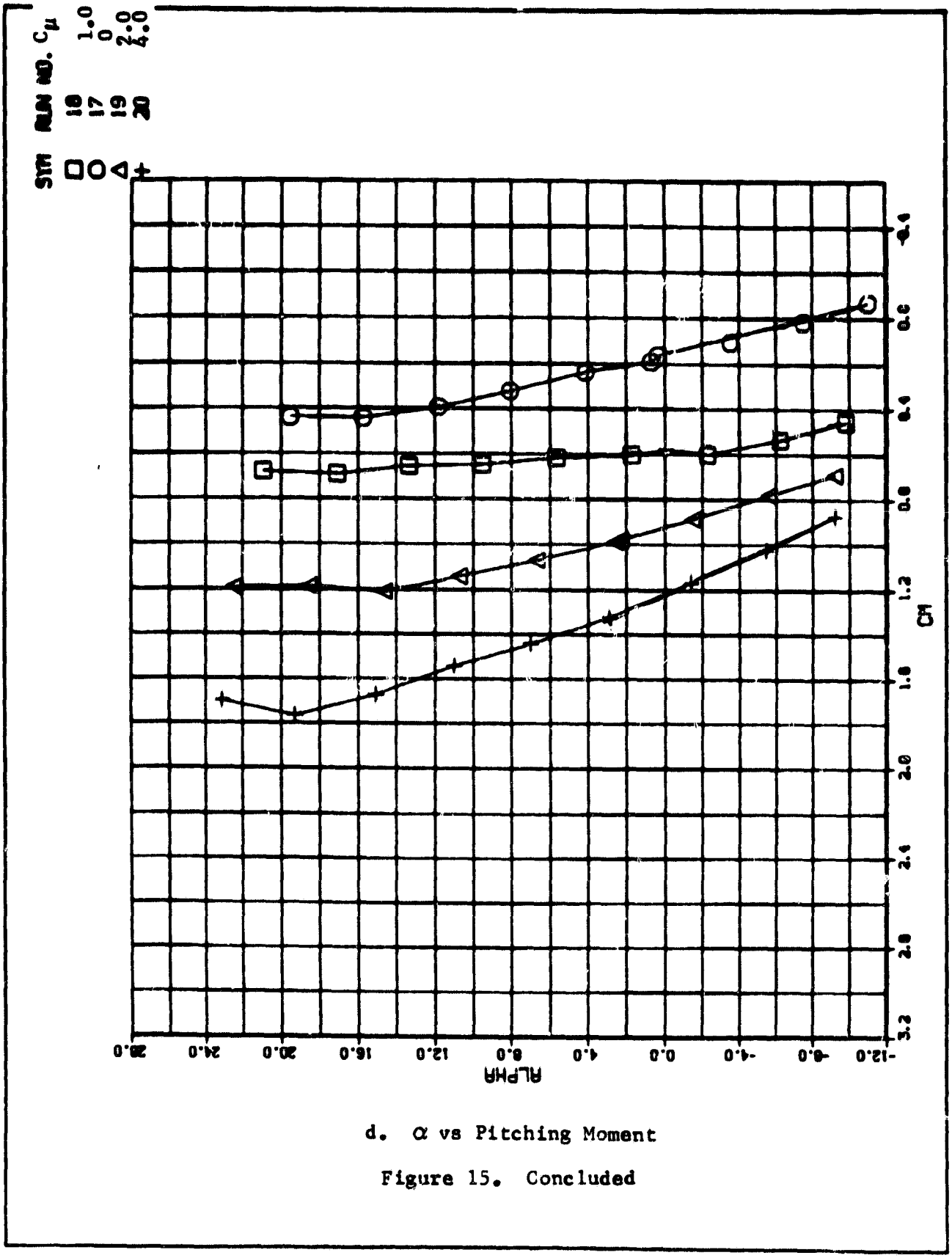

d. α vs Pitching Moment

Figure 15. Concluded

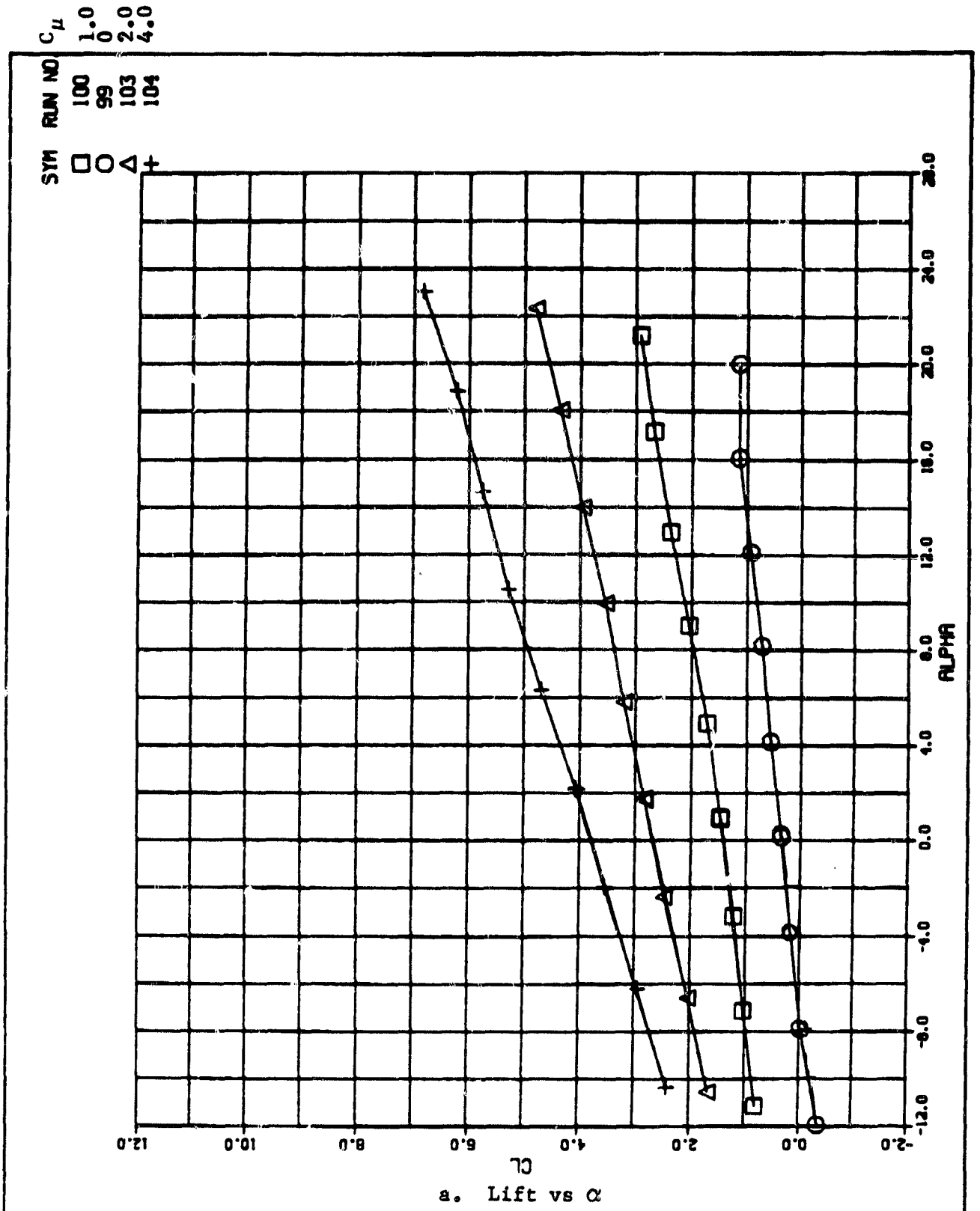

a. Lift vs α

Figure 16. Basic Aerodynamic Characteristics, Thrust Augmenter 1; $\theta = 30^{\circ}$, $\delta_D = 0^{\circ}$

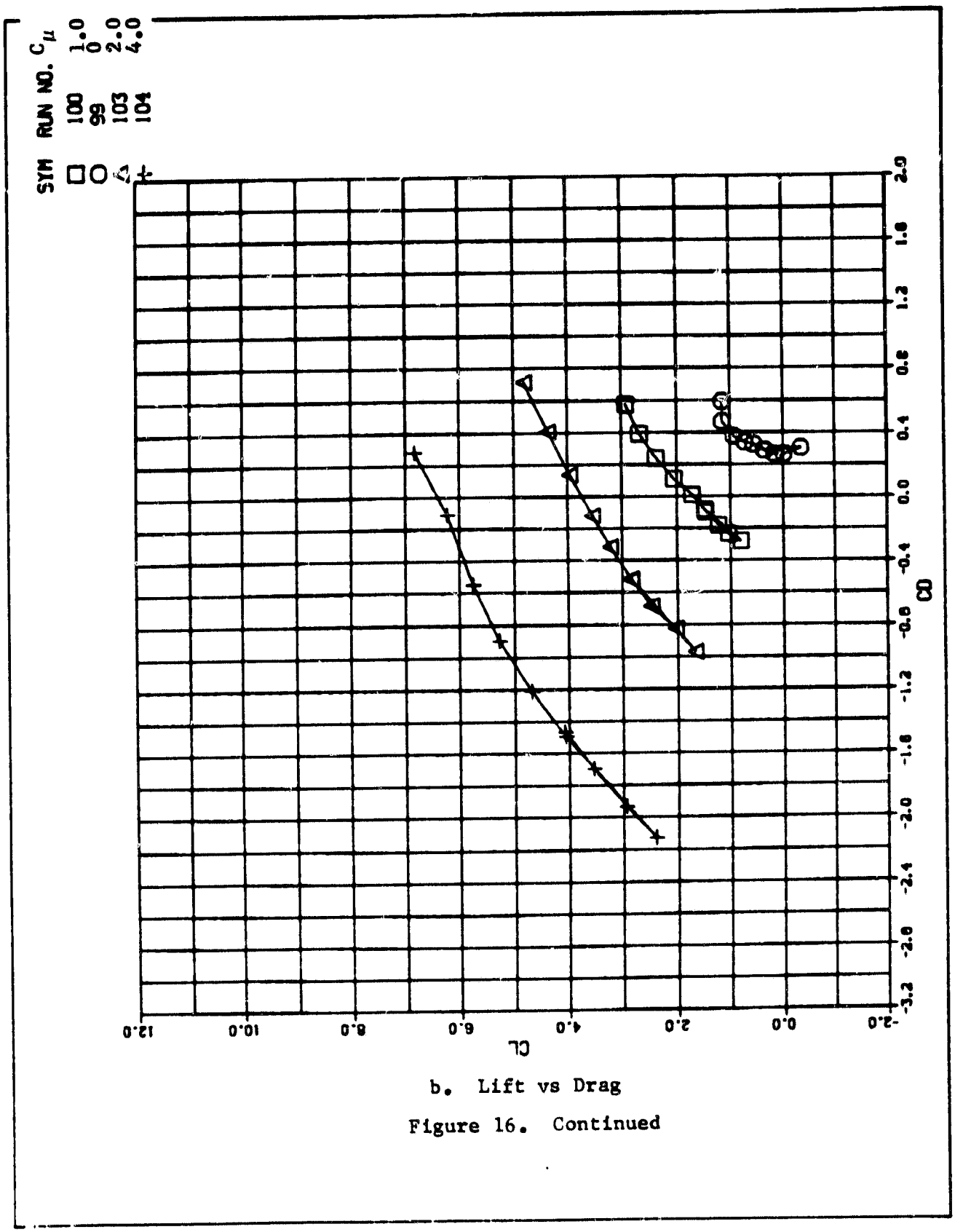

b. Lift vs Drag

Figure 16. Continued

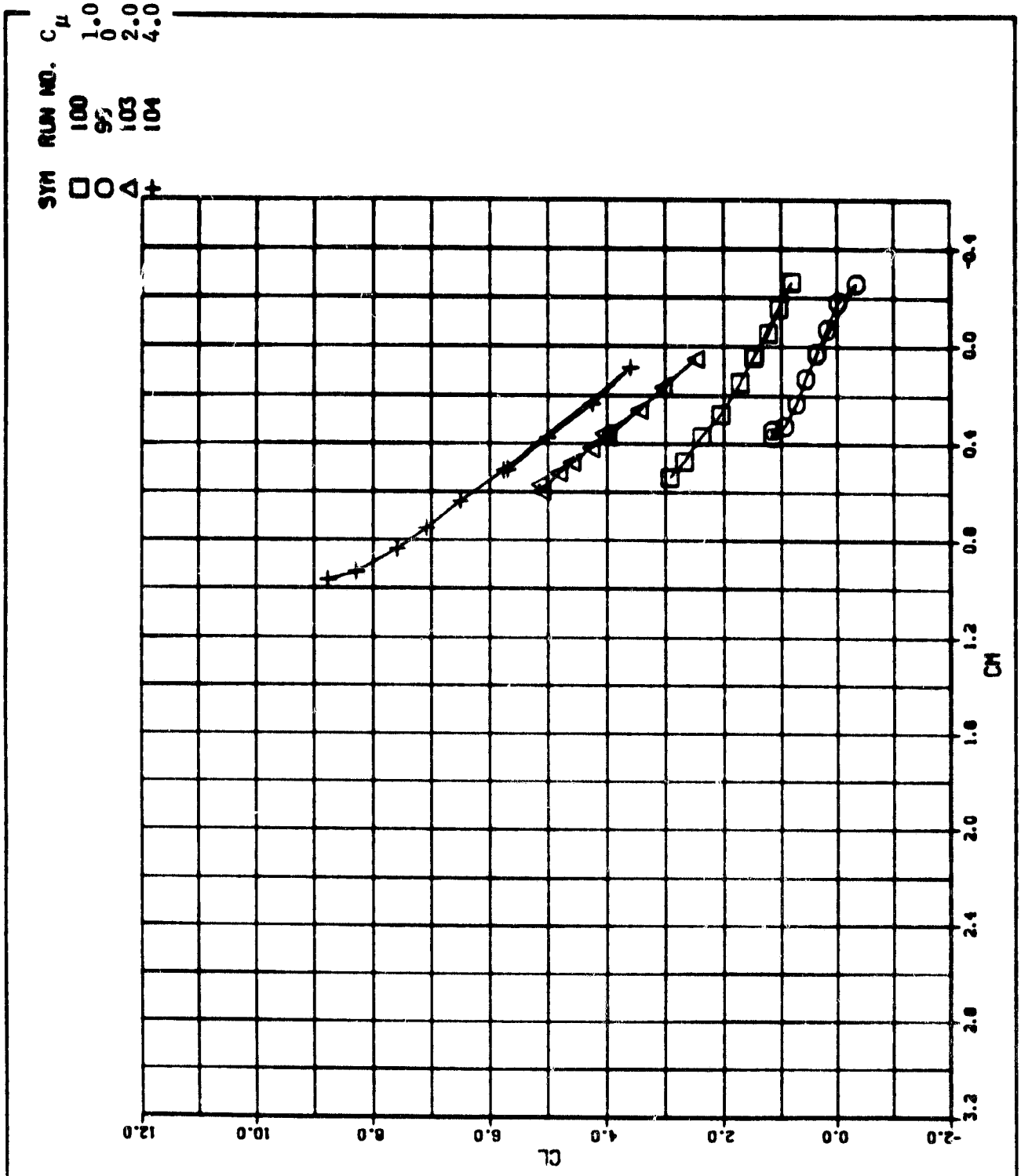

c. Lift vs Pitching Moment

Figure 16. Continued

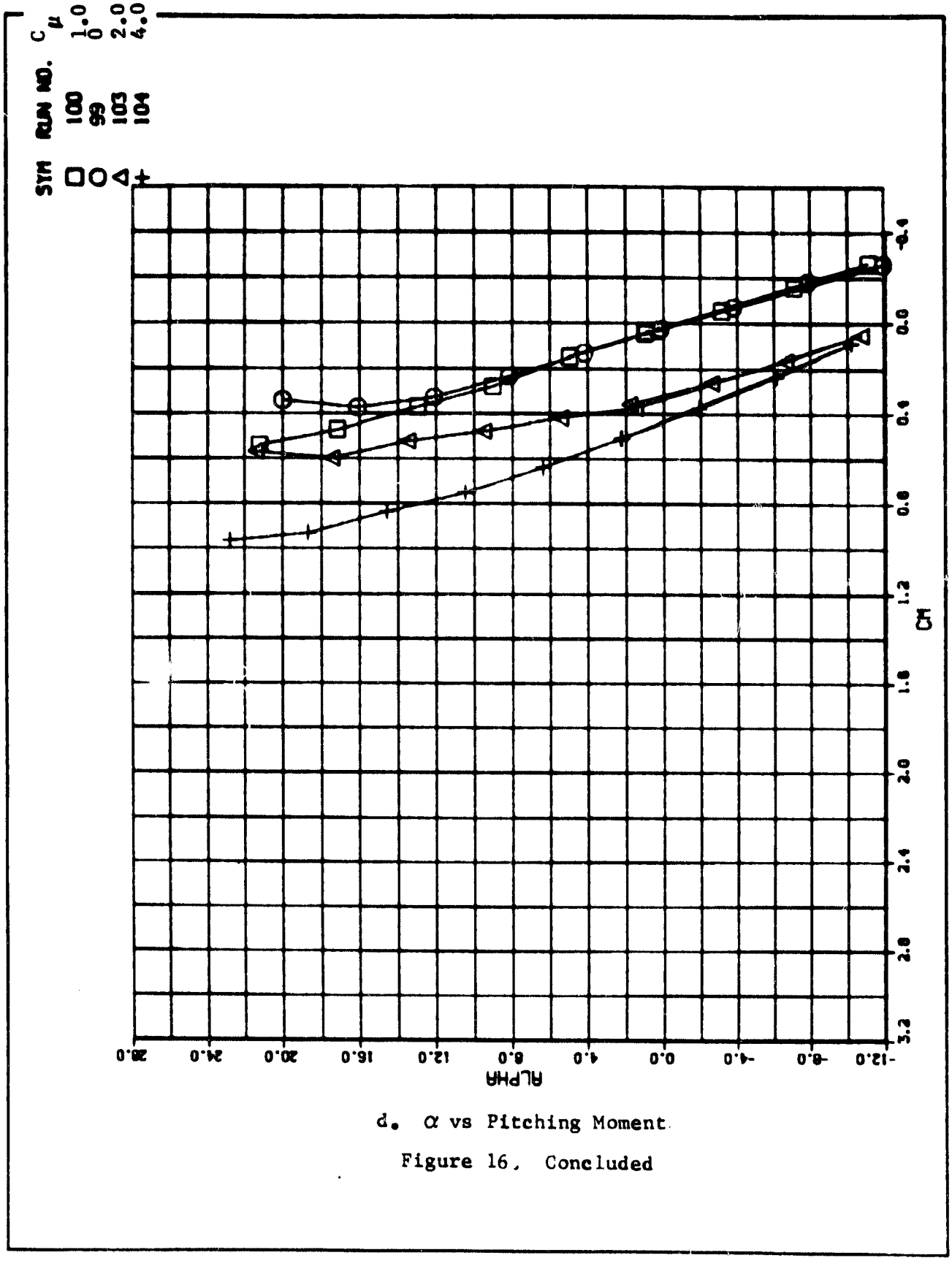

d. α vs Pitching Moment

Figure 16. Concluded

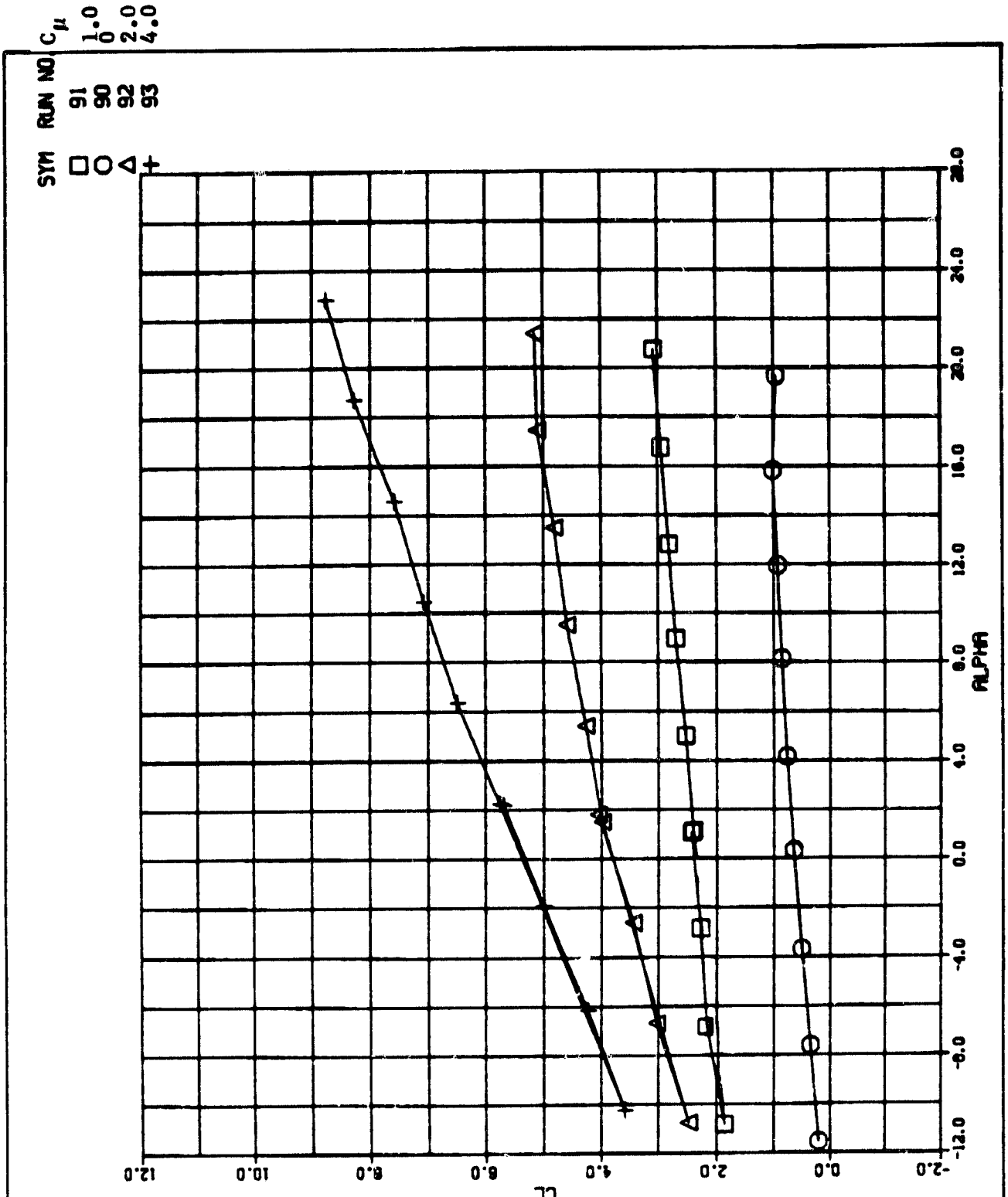

a. Lift vs α

Figure 17. Basic Aerodynamic Characteristics, Thrust Augmenter 1; $\theta = 30^\circ$, $\delta_D = 8^\circ$

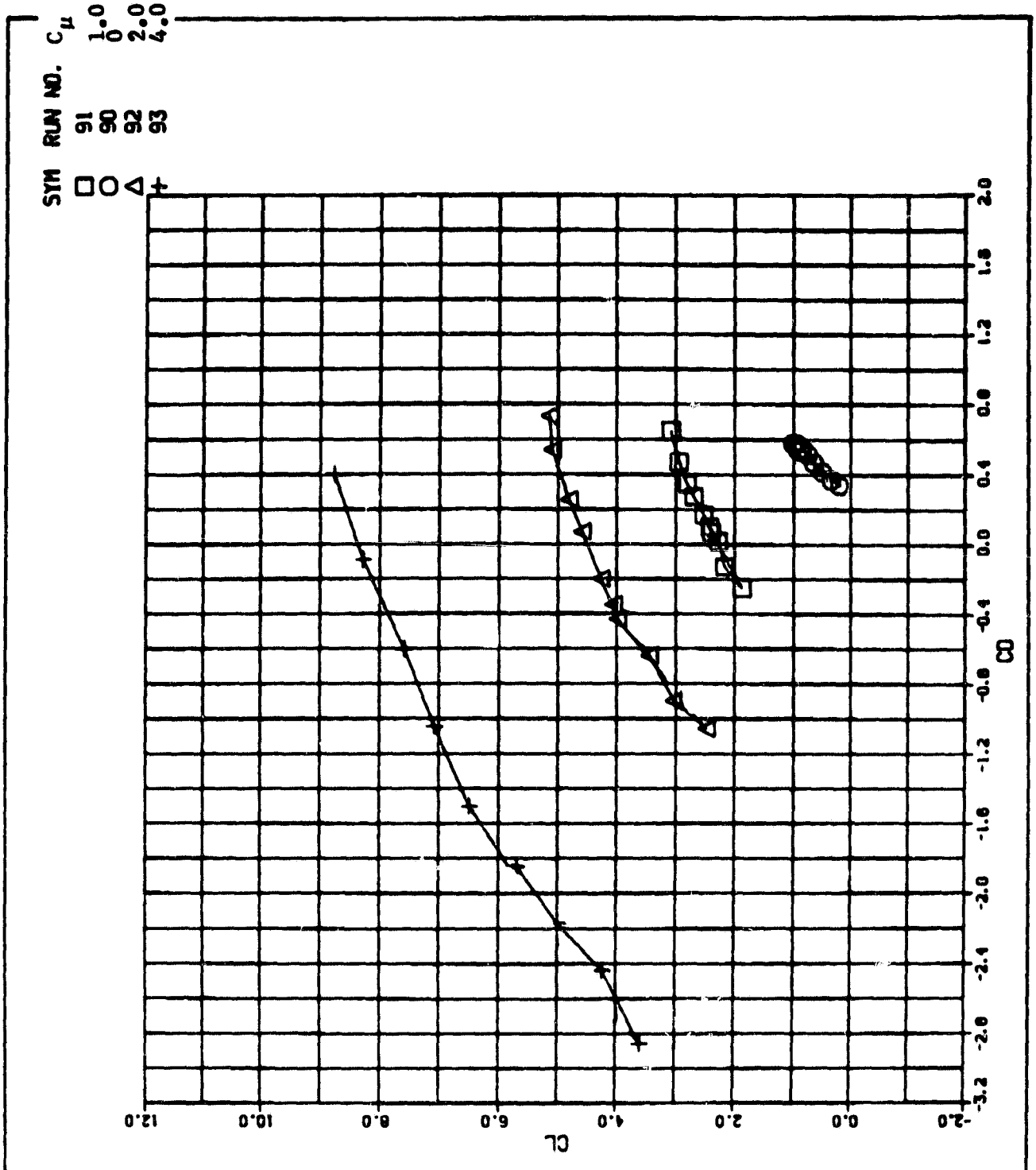

b. Lift vs Drag

Figure 17. Continued

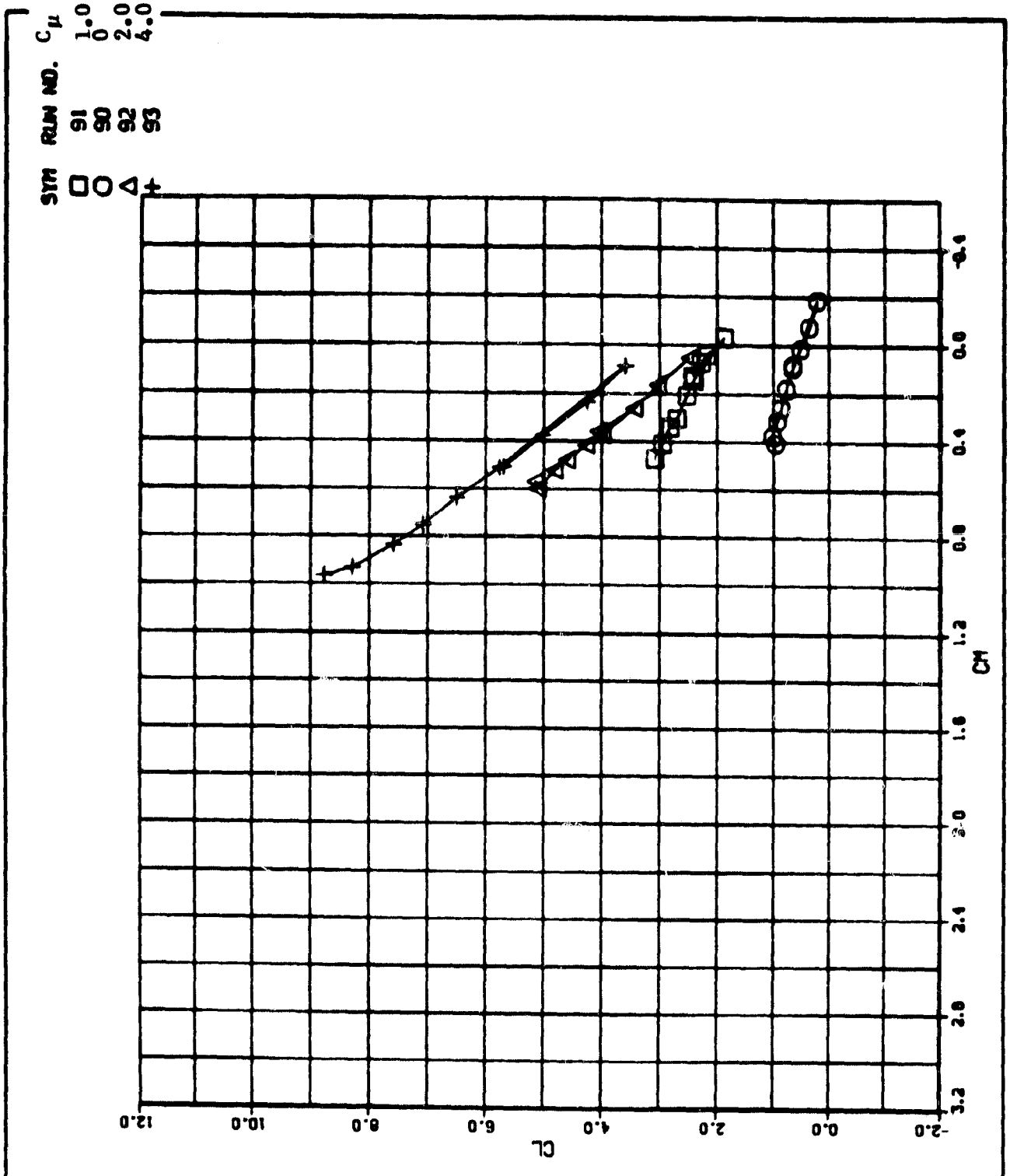

c. Lift vs Pitching Moment

Figure 17. Continued

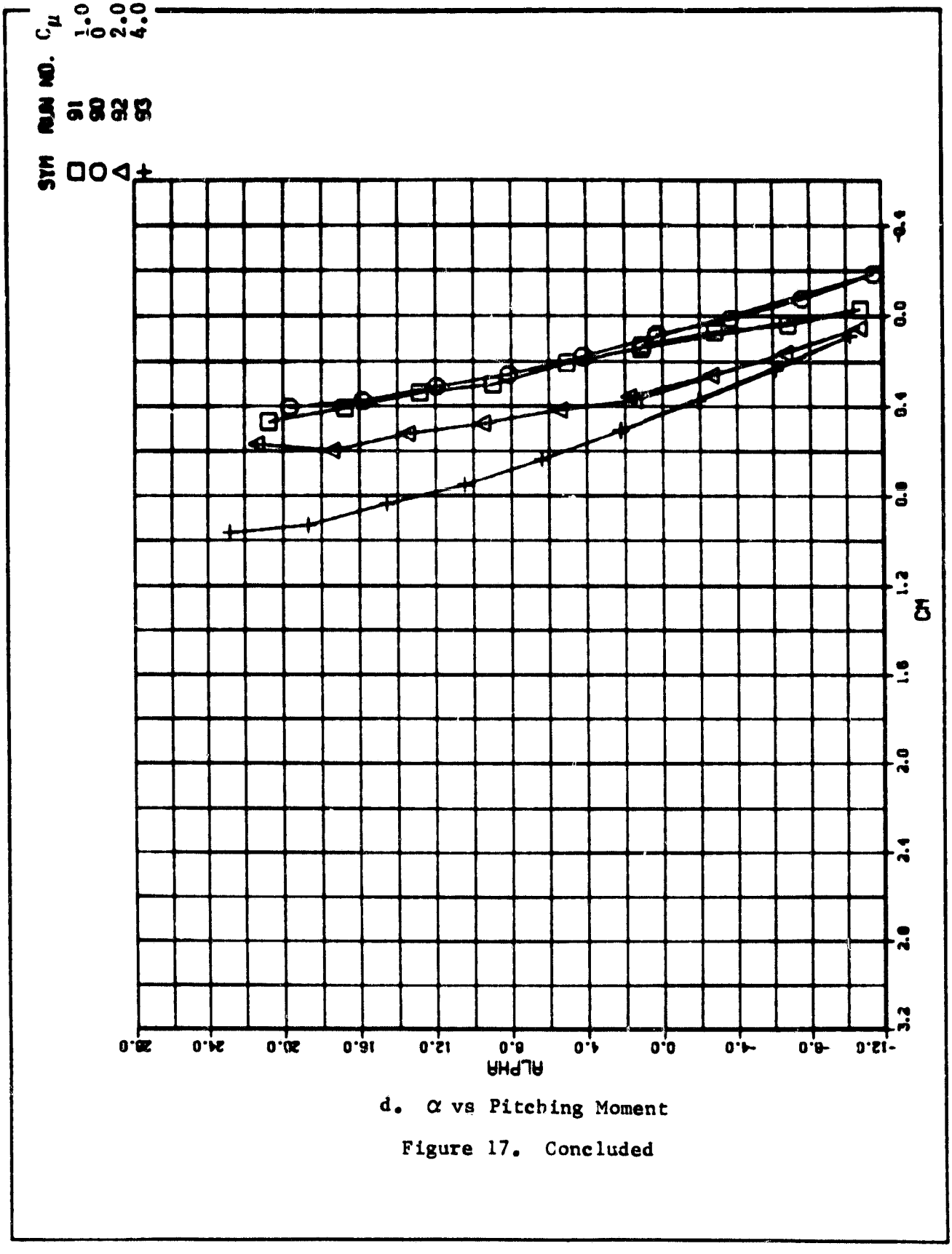

d. α vs Pitching Moment

Figure 17. Concluded

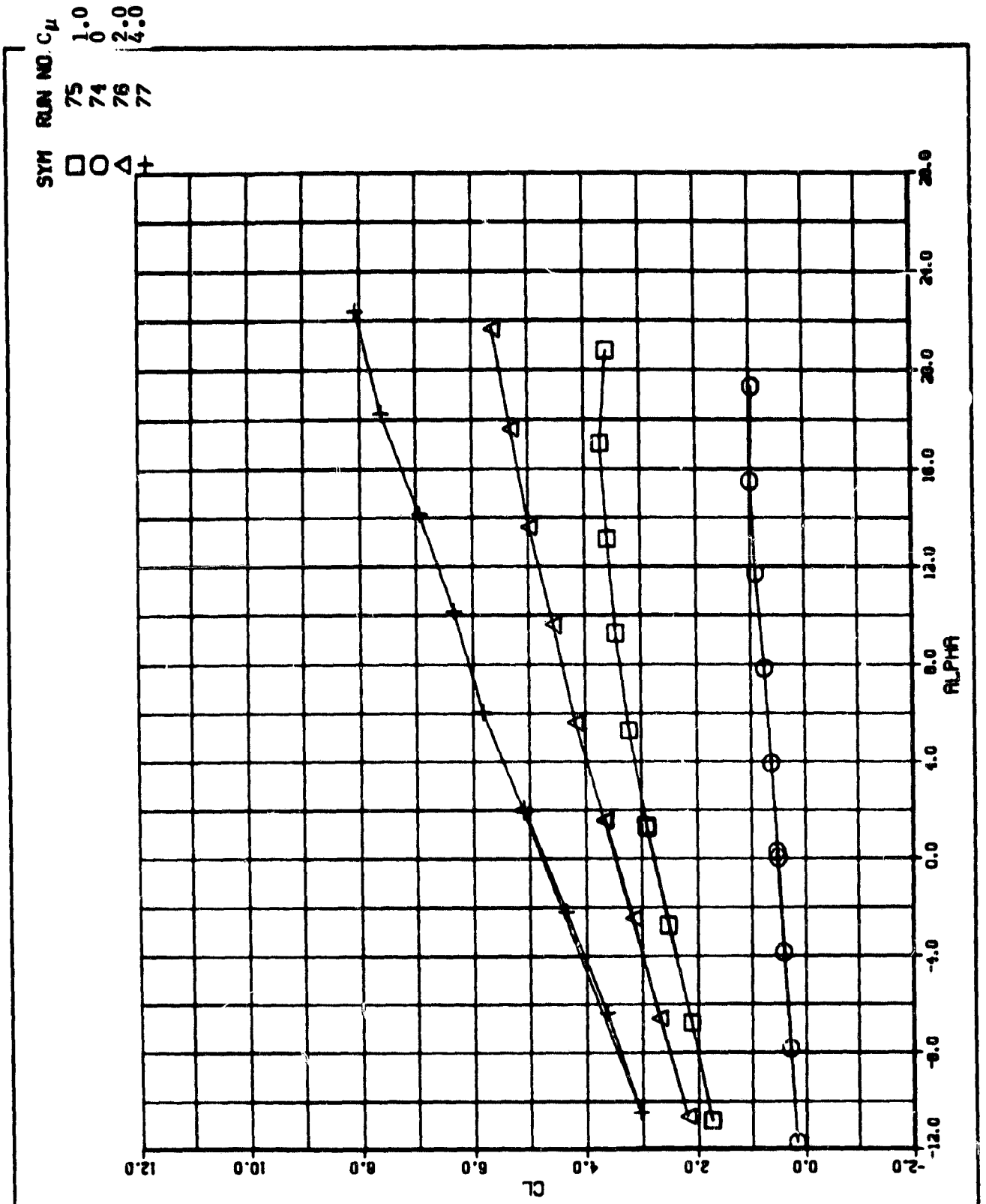

a. Lift vs α

Figure 18. Basic Aerodynamic Characteristics, Thrust Augmenter 1; $\theta = 30^\circ$, $\delta_D = 16^\circ$

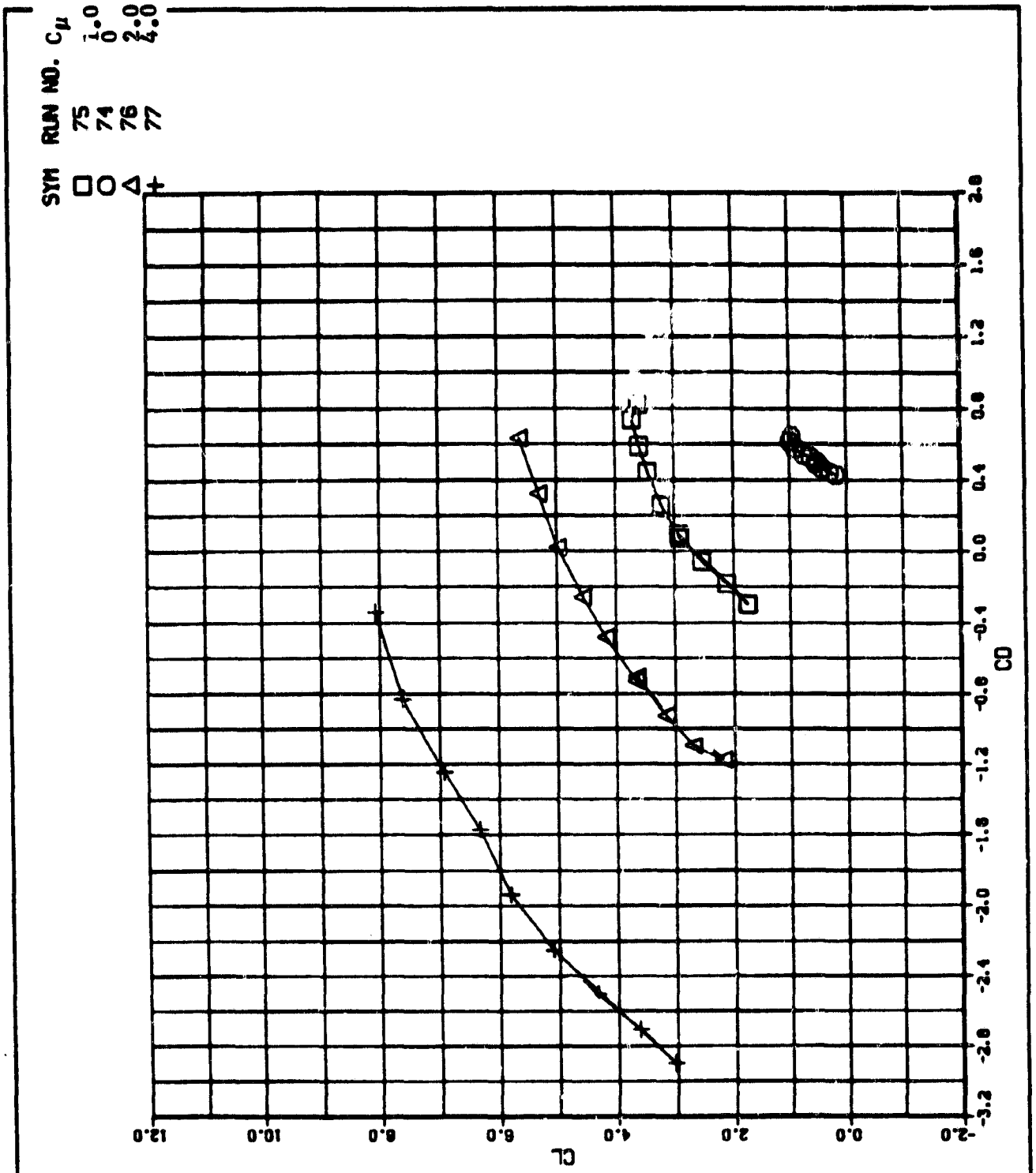

b. Lift vs Drag

Figure 18. Continued

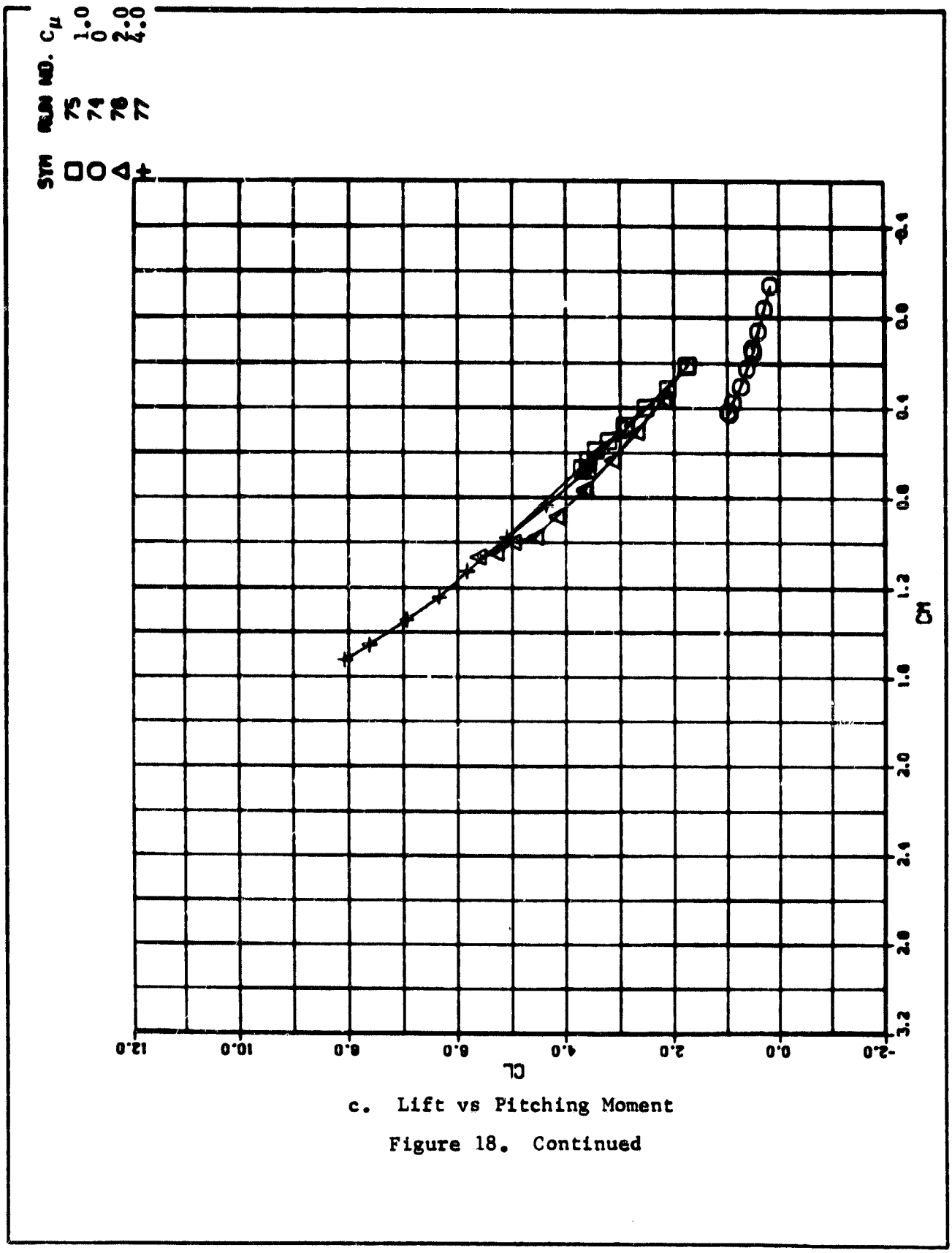

c. Lift vs Pitching Moment

Figure 18. Continued

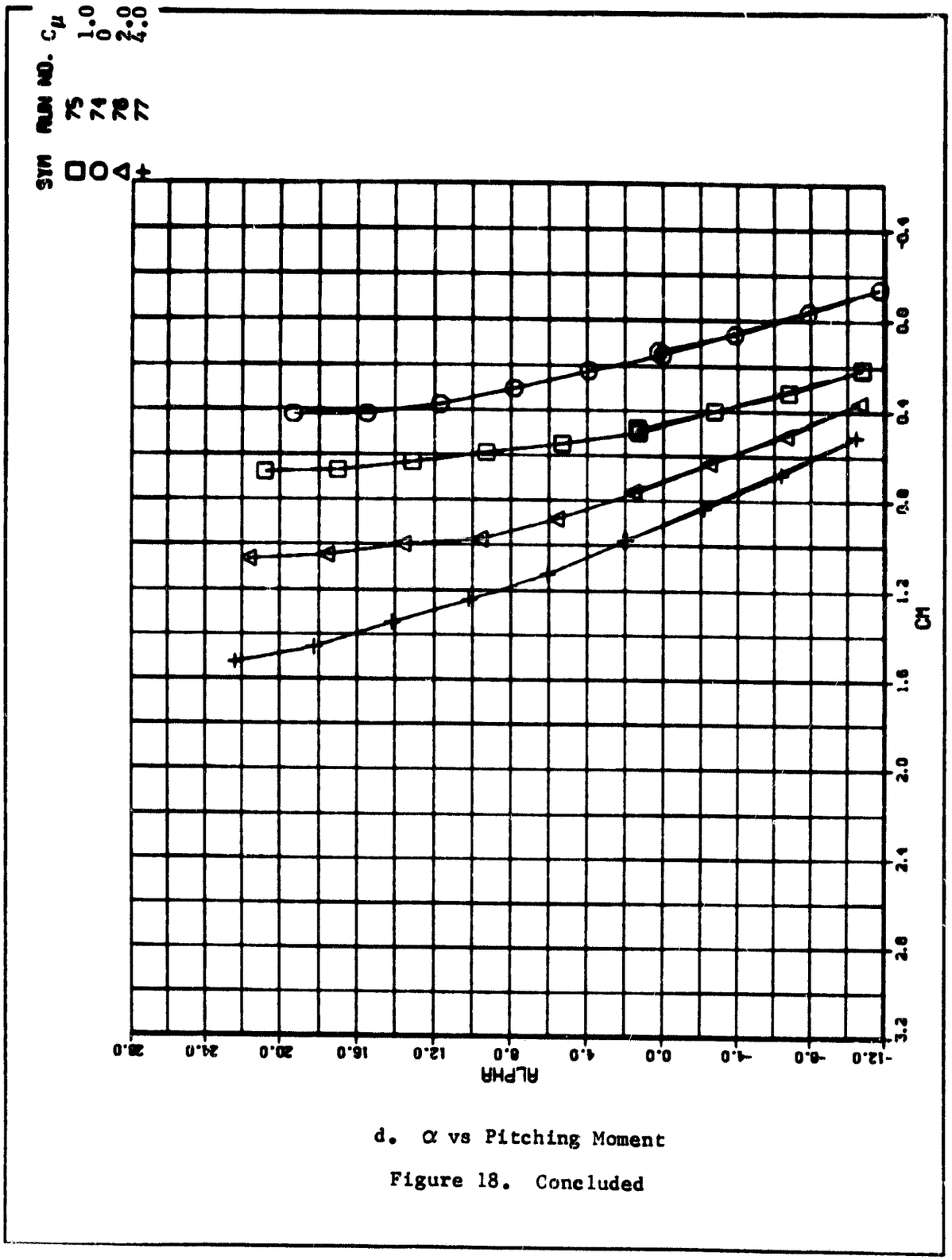

d. α vs Pitching Moment

Figure 18. Concluded

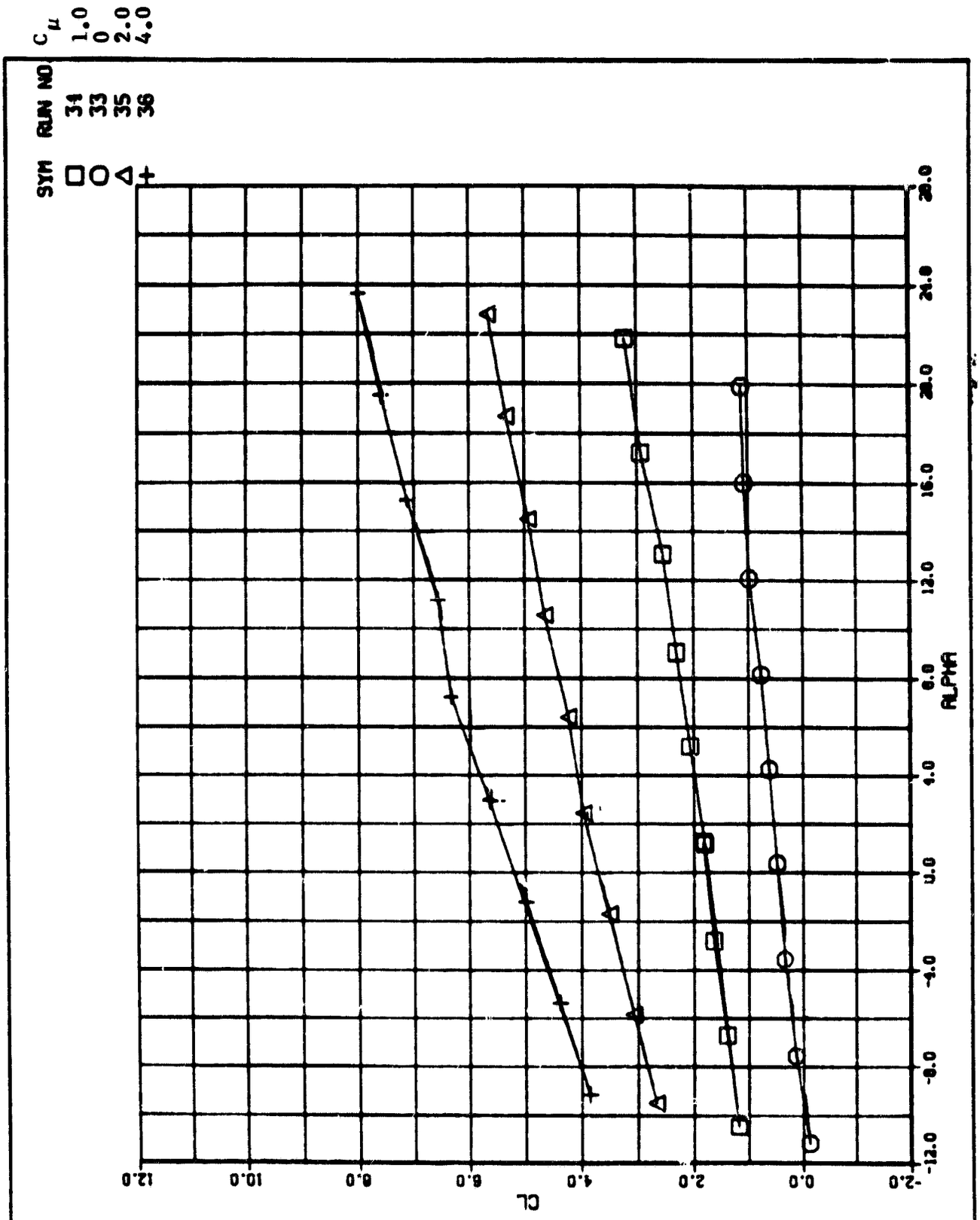

a. Lift vs α

Figure 19. Basic Aerodynamic Characteristics, Thrust Augmenter 2; $\phi = 40^\circ$, $\delta_D = 0^\circ$

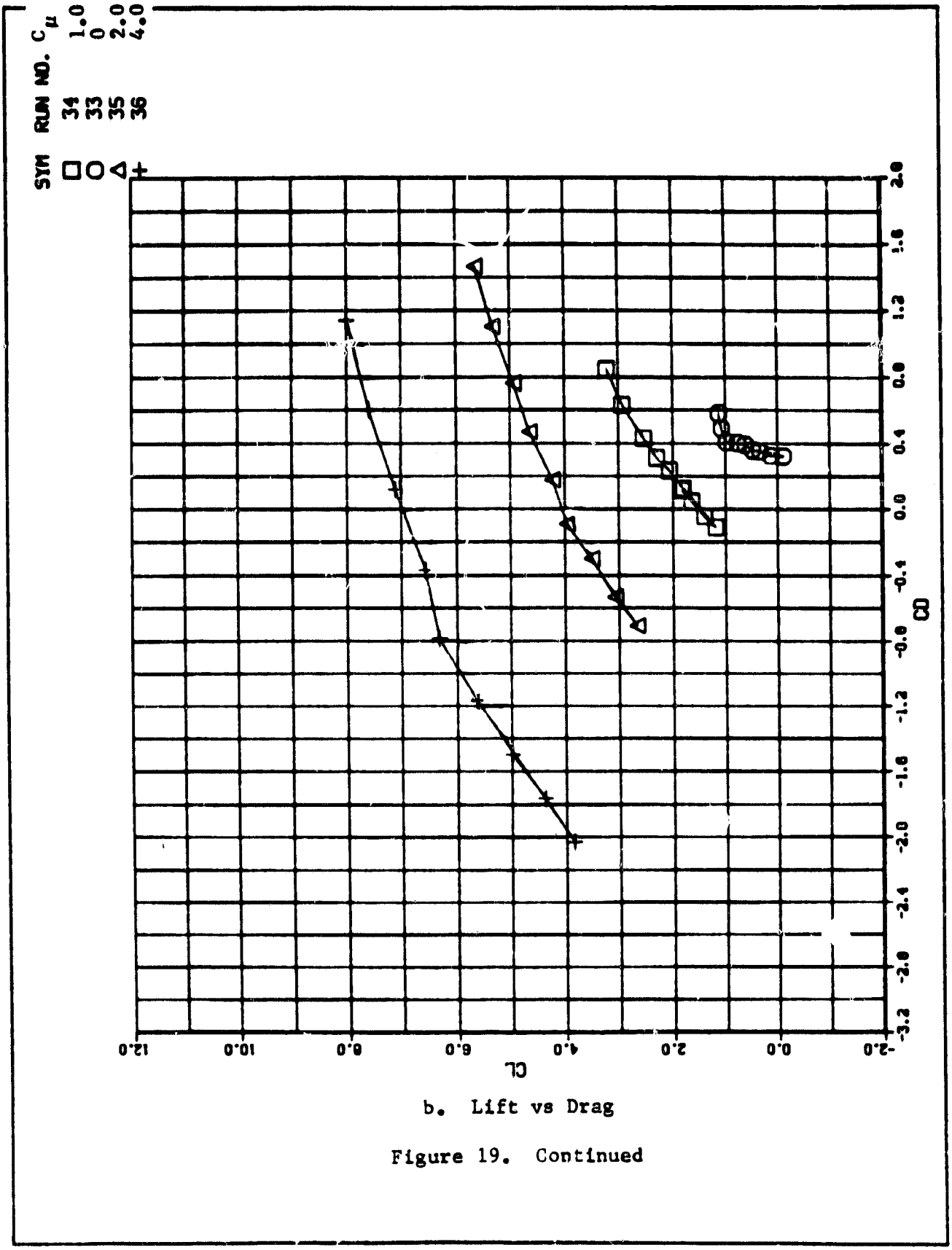

b. Lift vs Drag

Figure 19. Continued

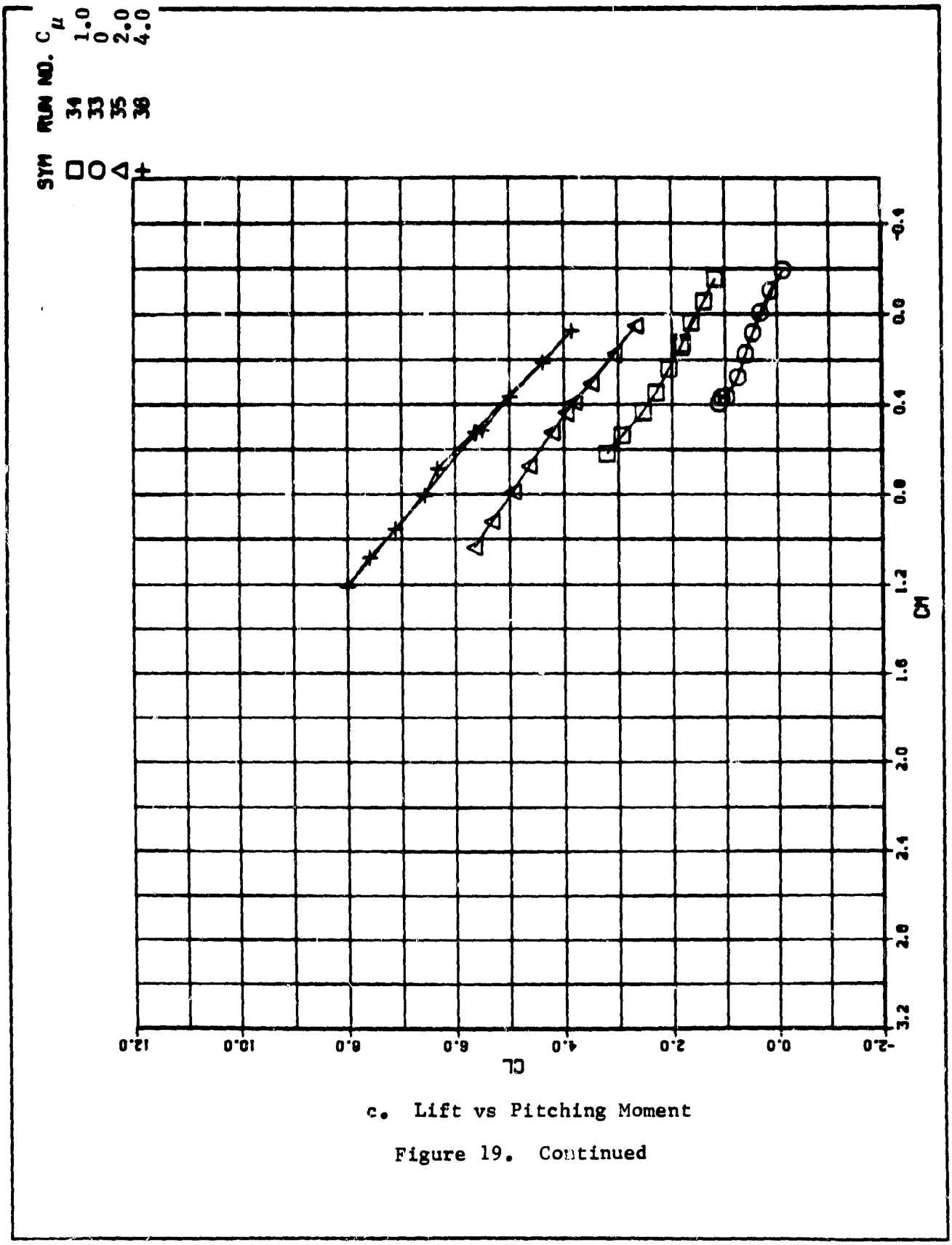

c. Lift vs Pitching Moment

Figure 19. Continued

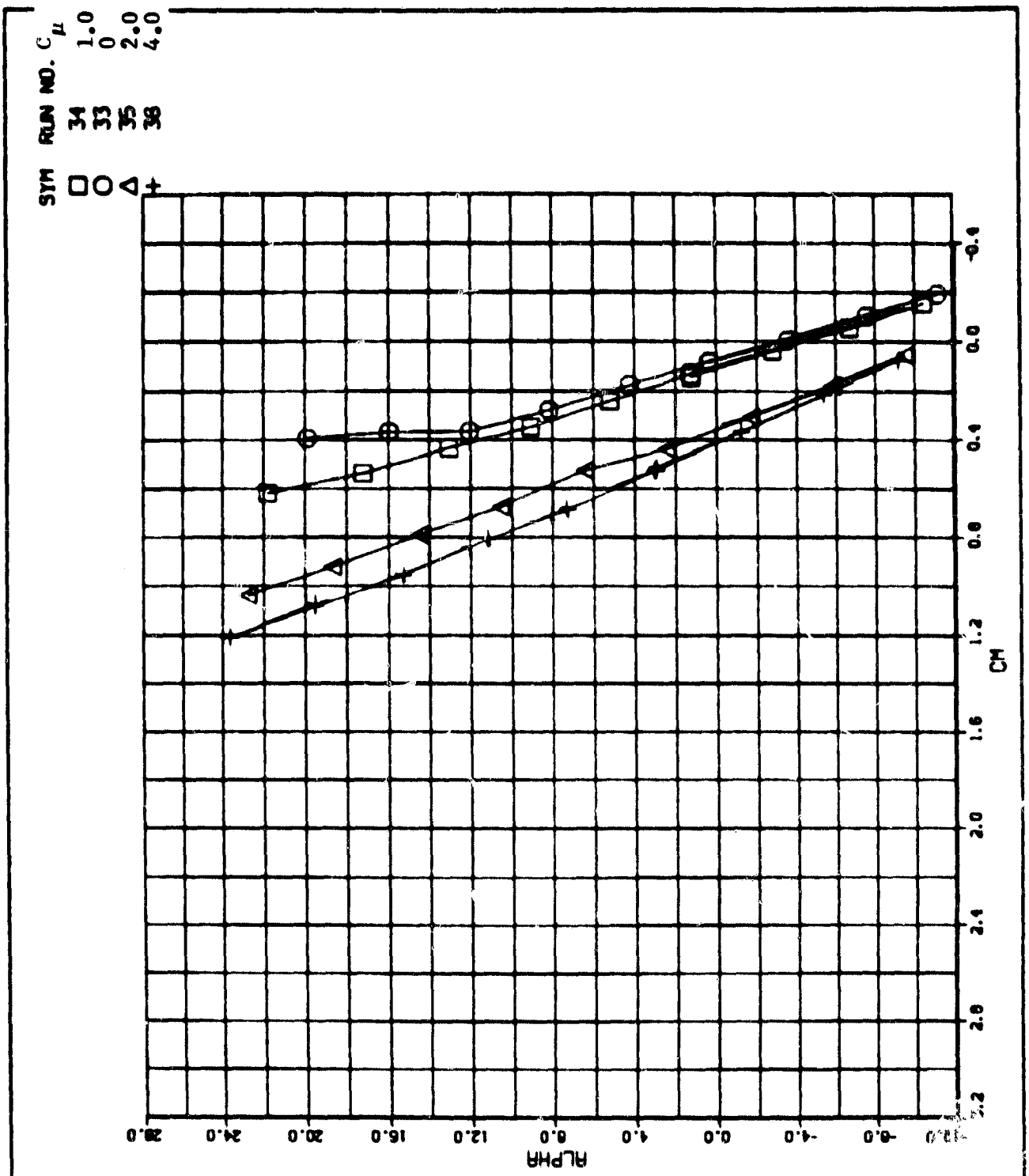

d. α vs Pitching Moment

Figure 19. Concluded

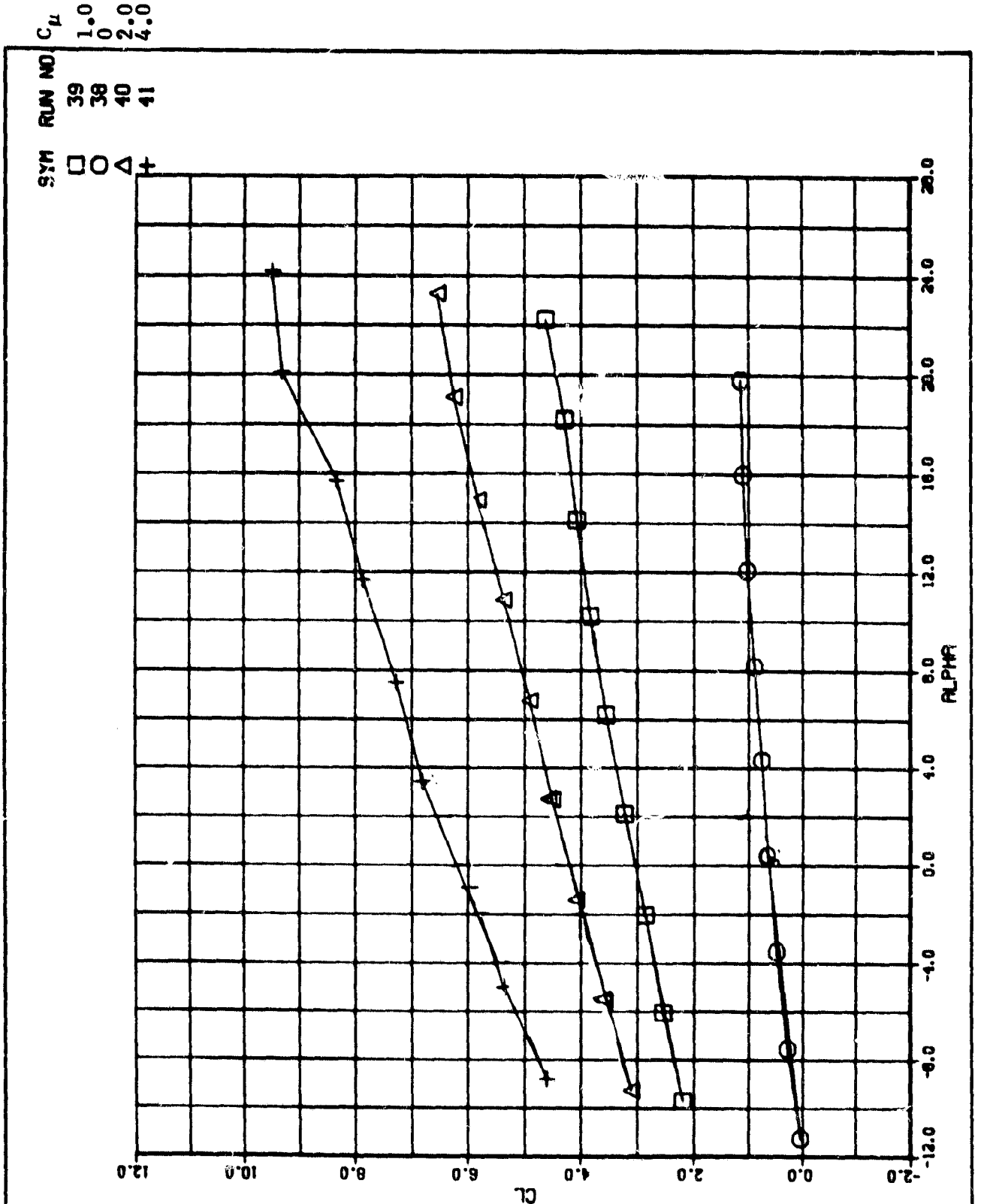

a. Lift vs α

Figure 20. Basic Aerodynamic Characteristics, Thrust Augmenter 2; $\phi = 40^\circ$, $\delta_D = 8^\circ$

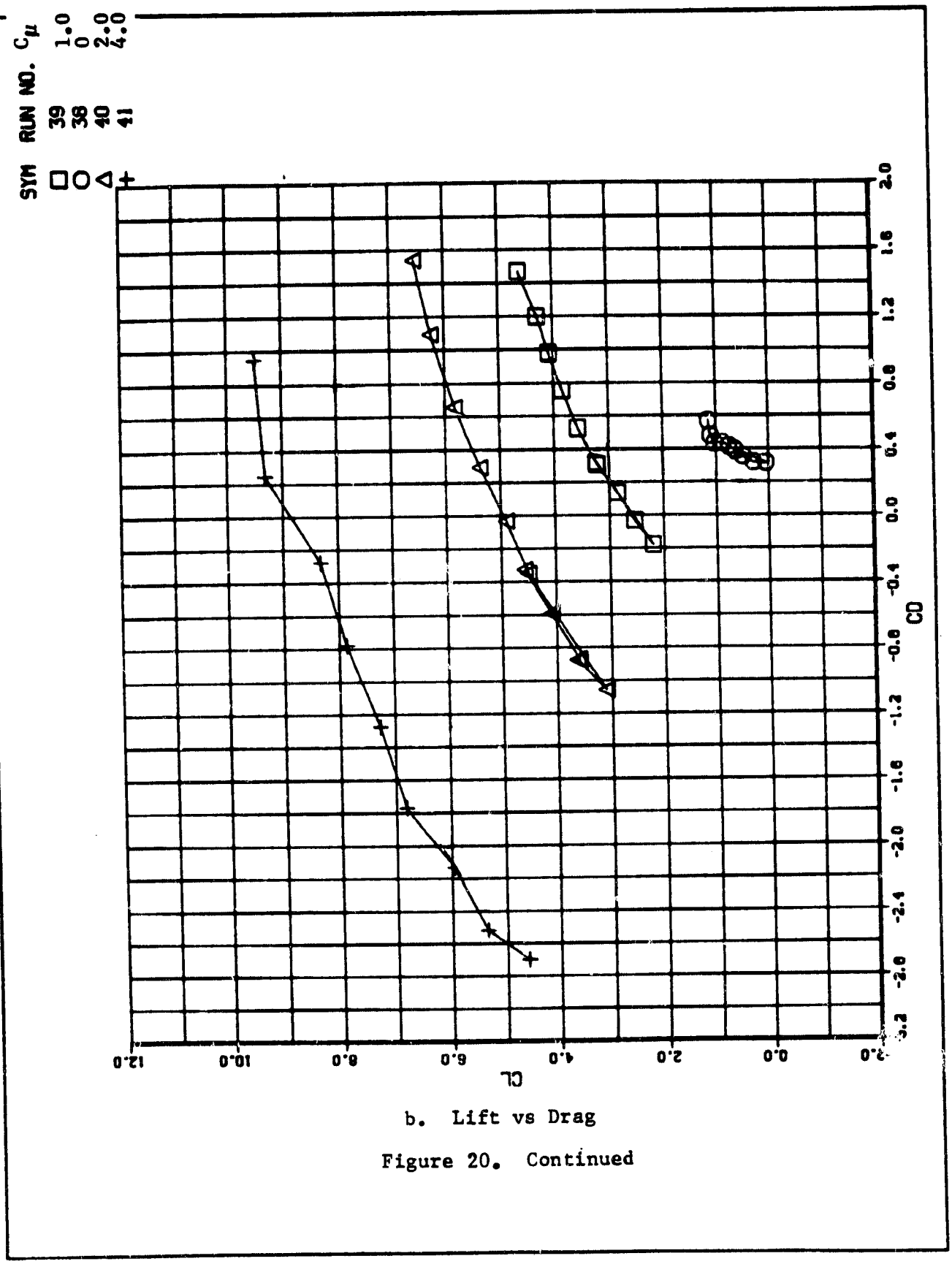

b. Lift vs Drag

Figure 20. Continued

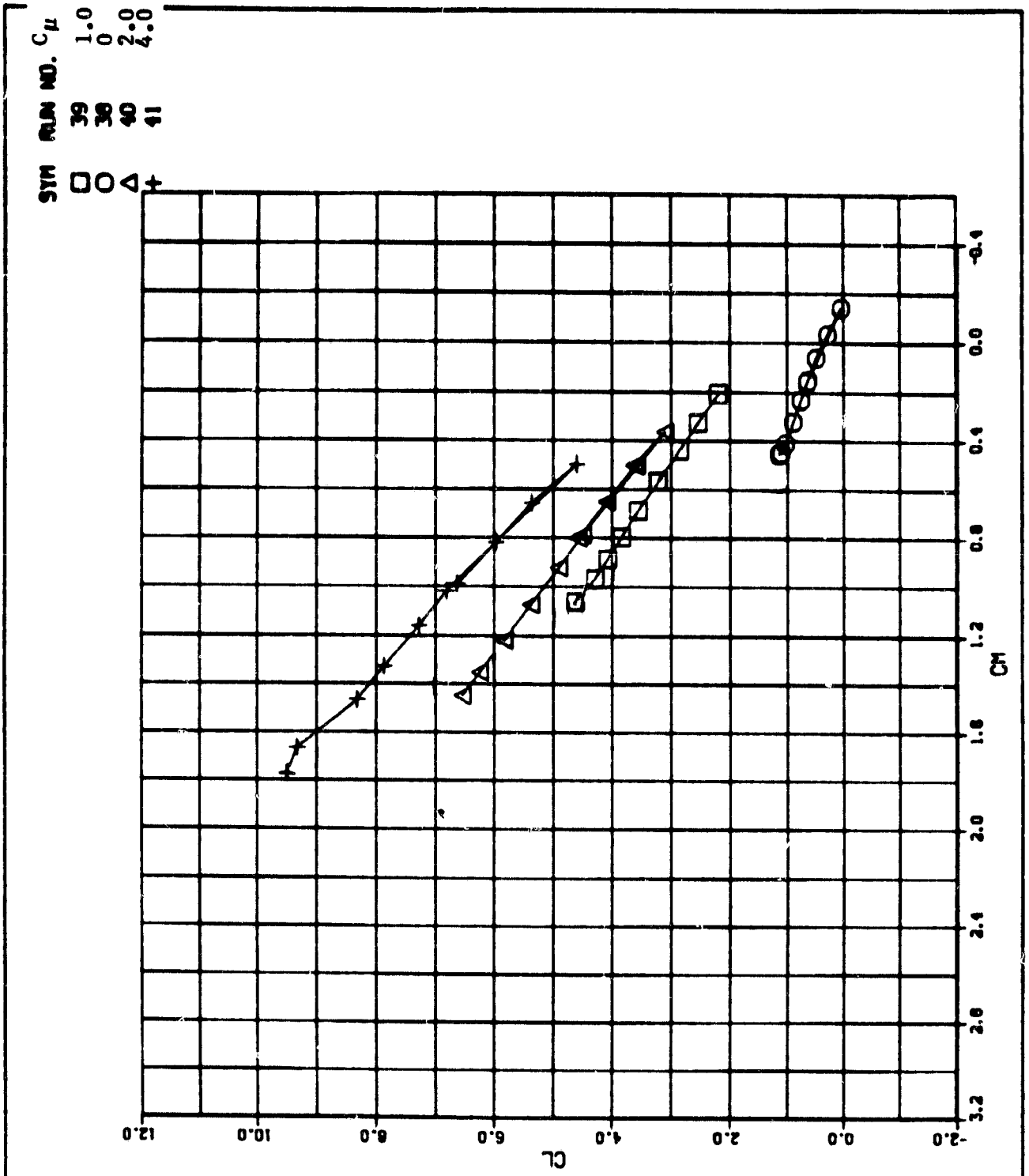

c. Lift vs Pitching Moment

Figure 20. Continued

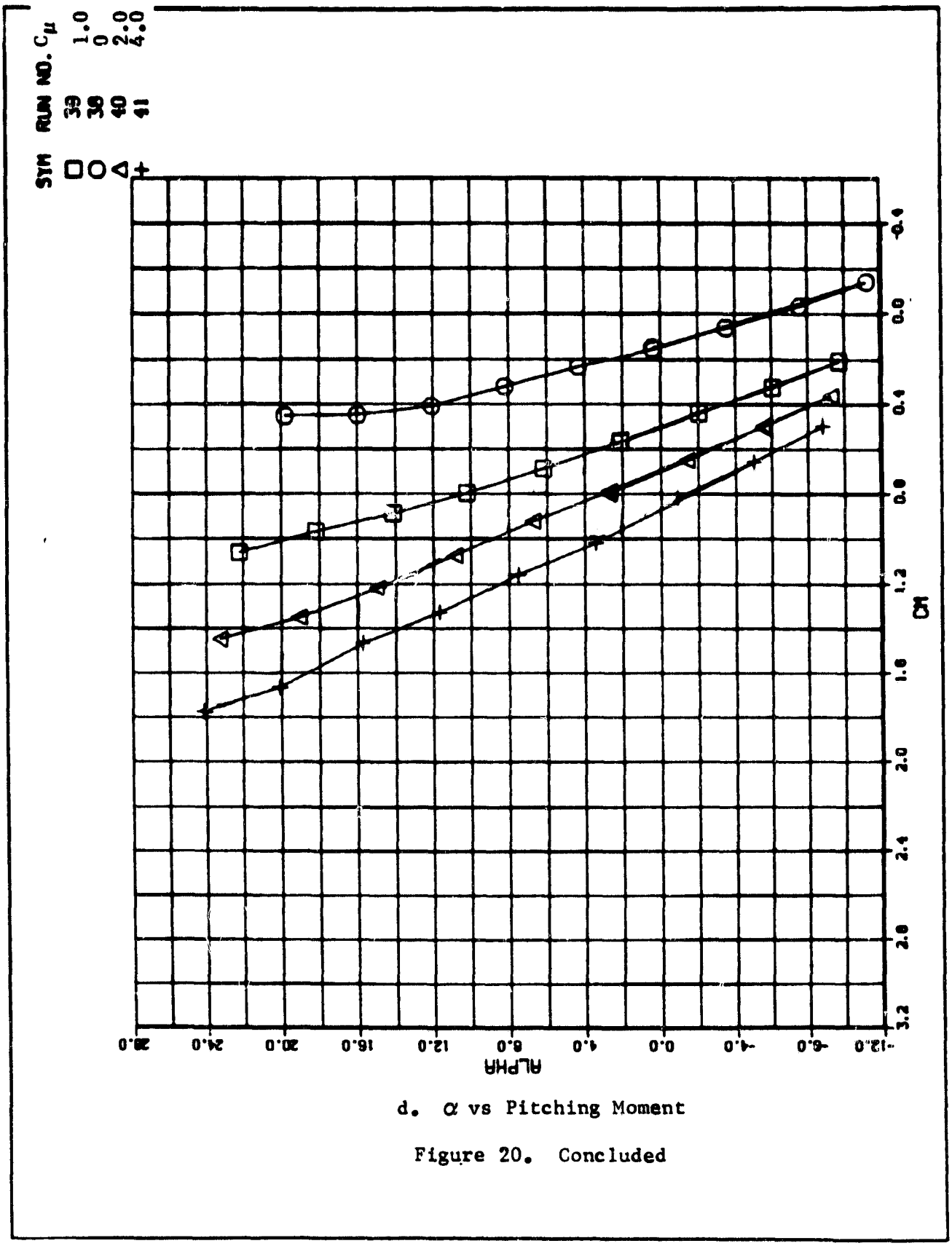

d. α vs Pitching Moment

Figure 20. Concluded

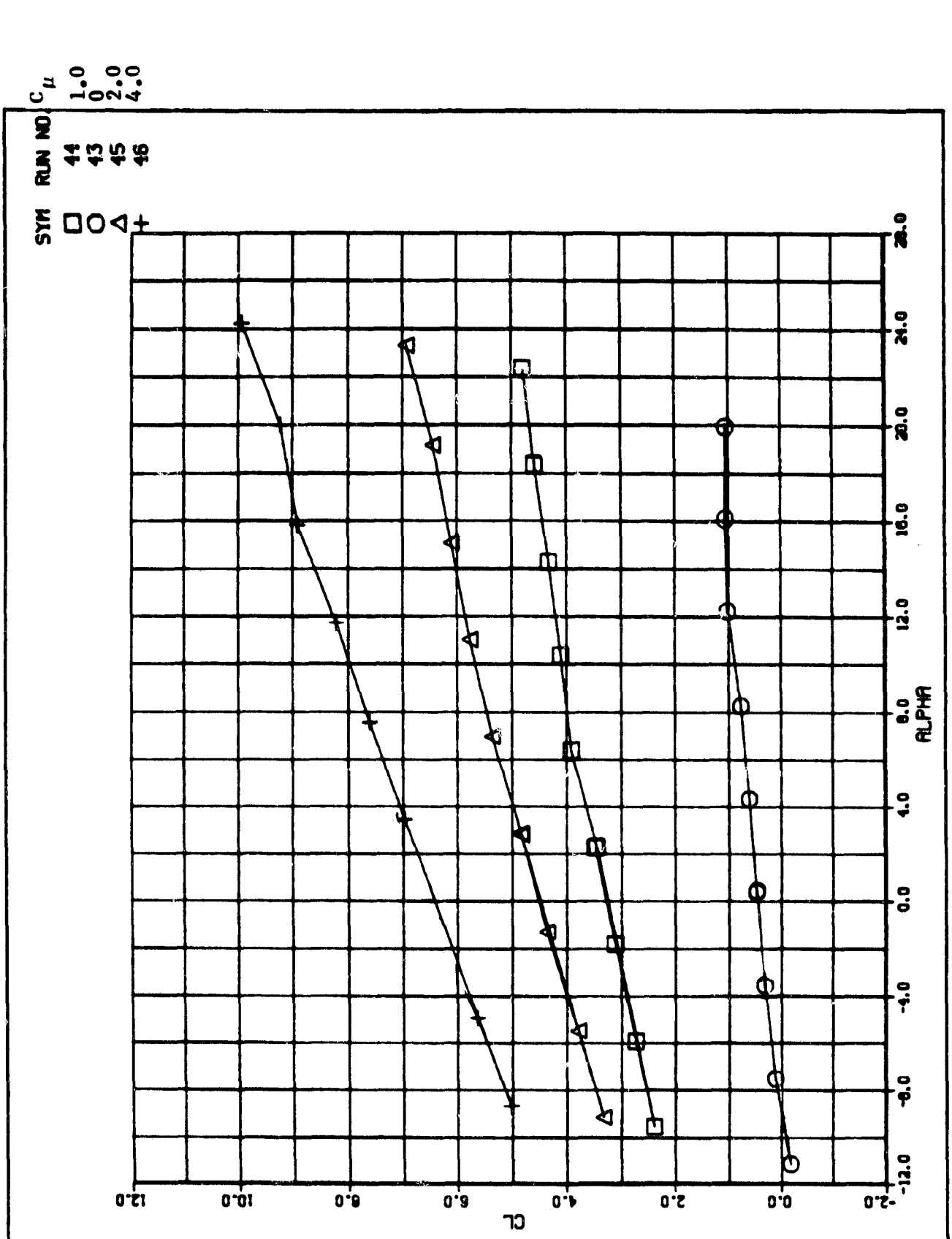

a. Lift vs α

Figure 21. Basic Aerodynamic Characteristics, Thrust Augmenter 2; $\phi = 40^{\circ}$, $\delta_D = 16^{\circ}$

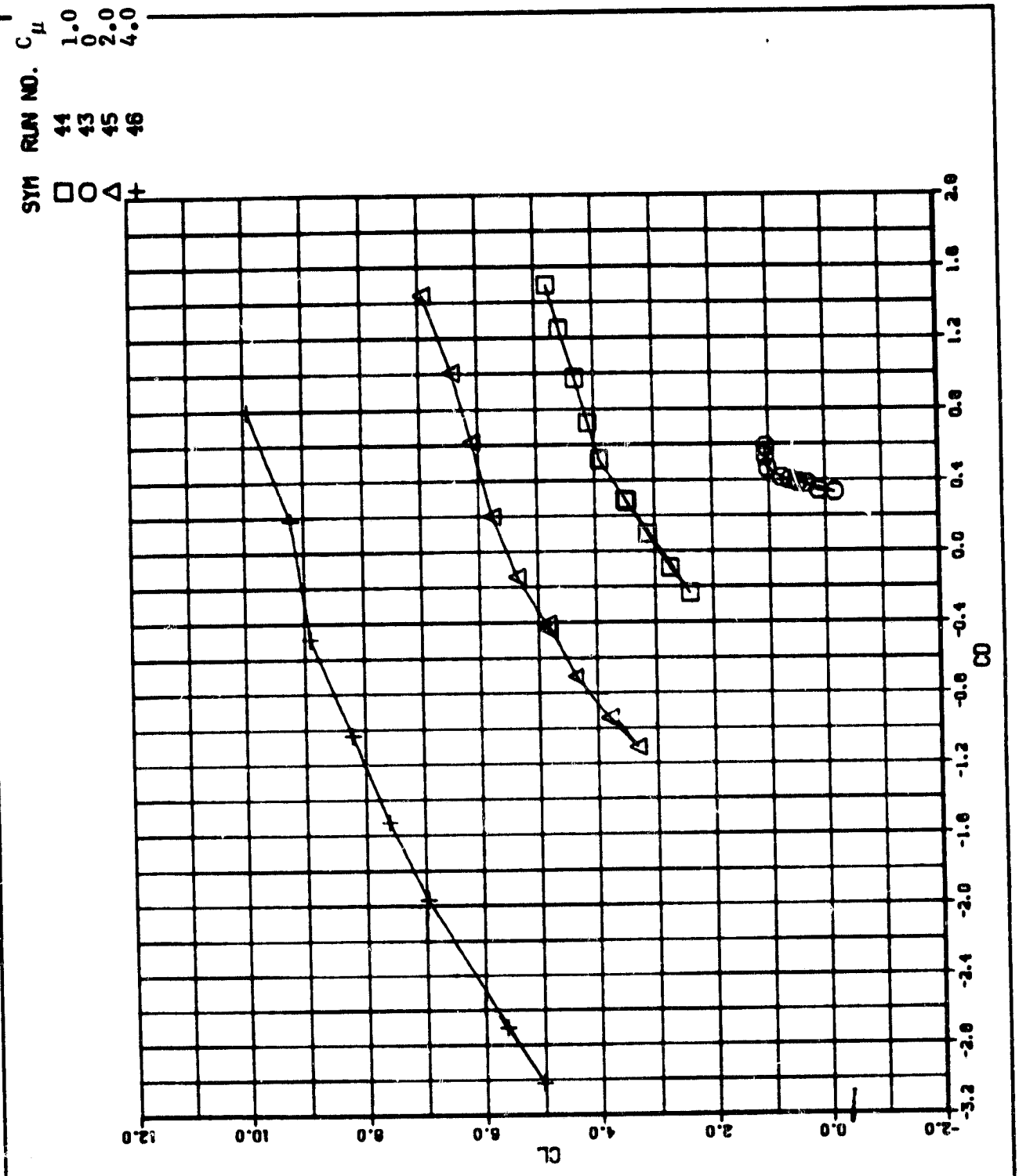

b. Lift vs Drag

Figure 21. Continued

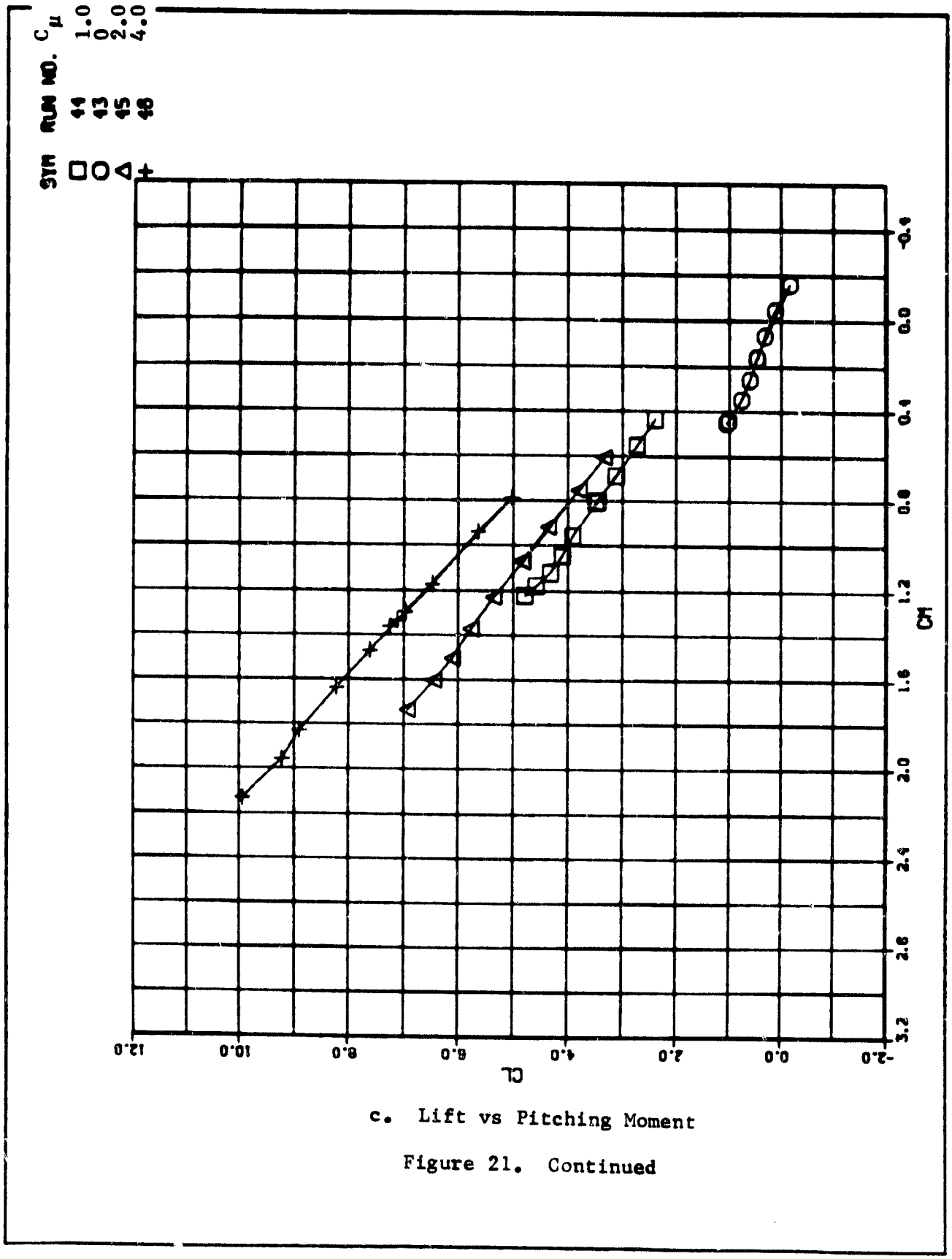

c. Lift vs Pitching Moment

Figure 21. Continued

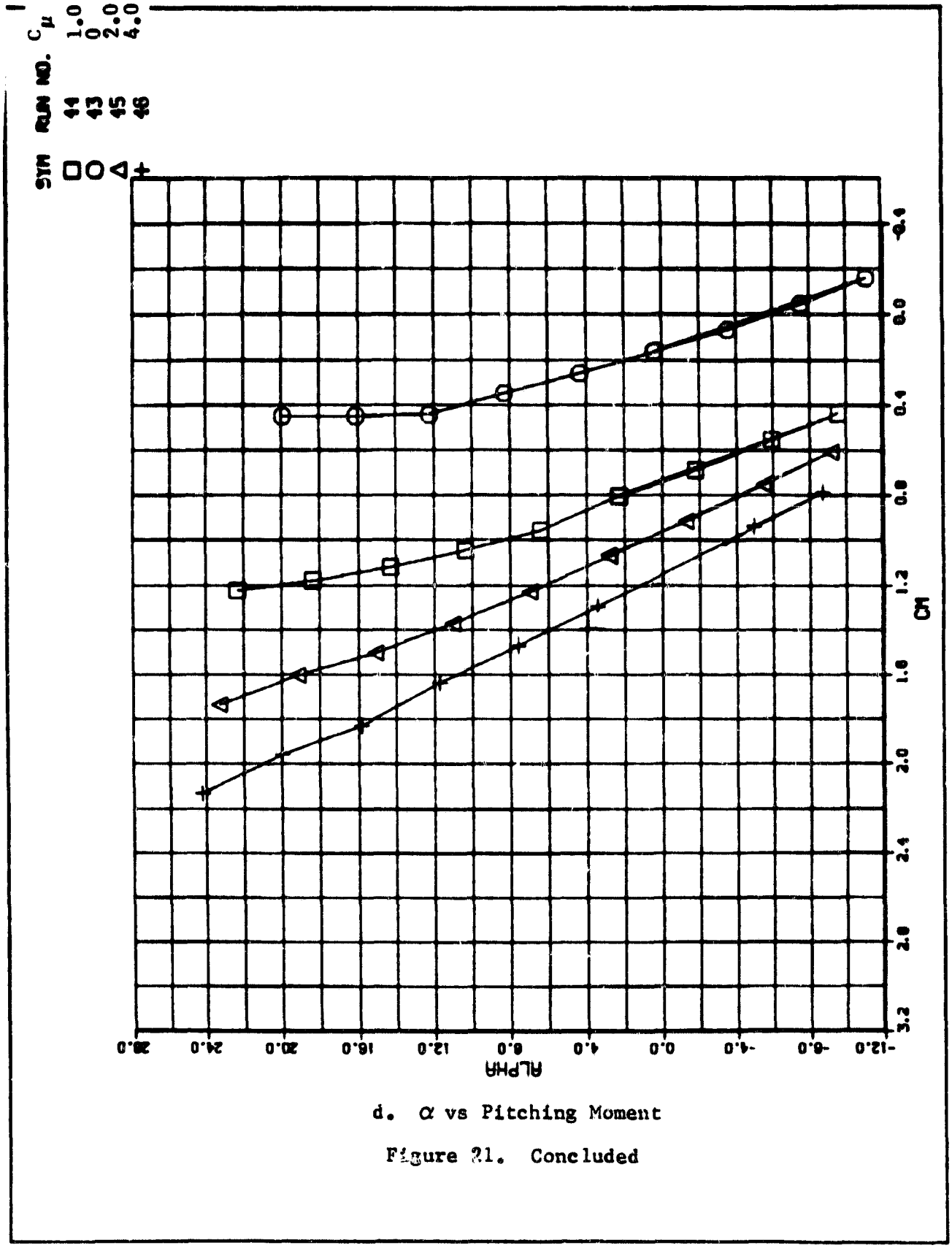

d. α vs Pitching Moment

Figure 21. Concluded

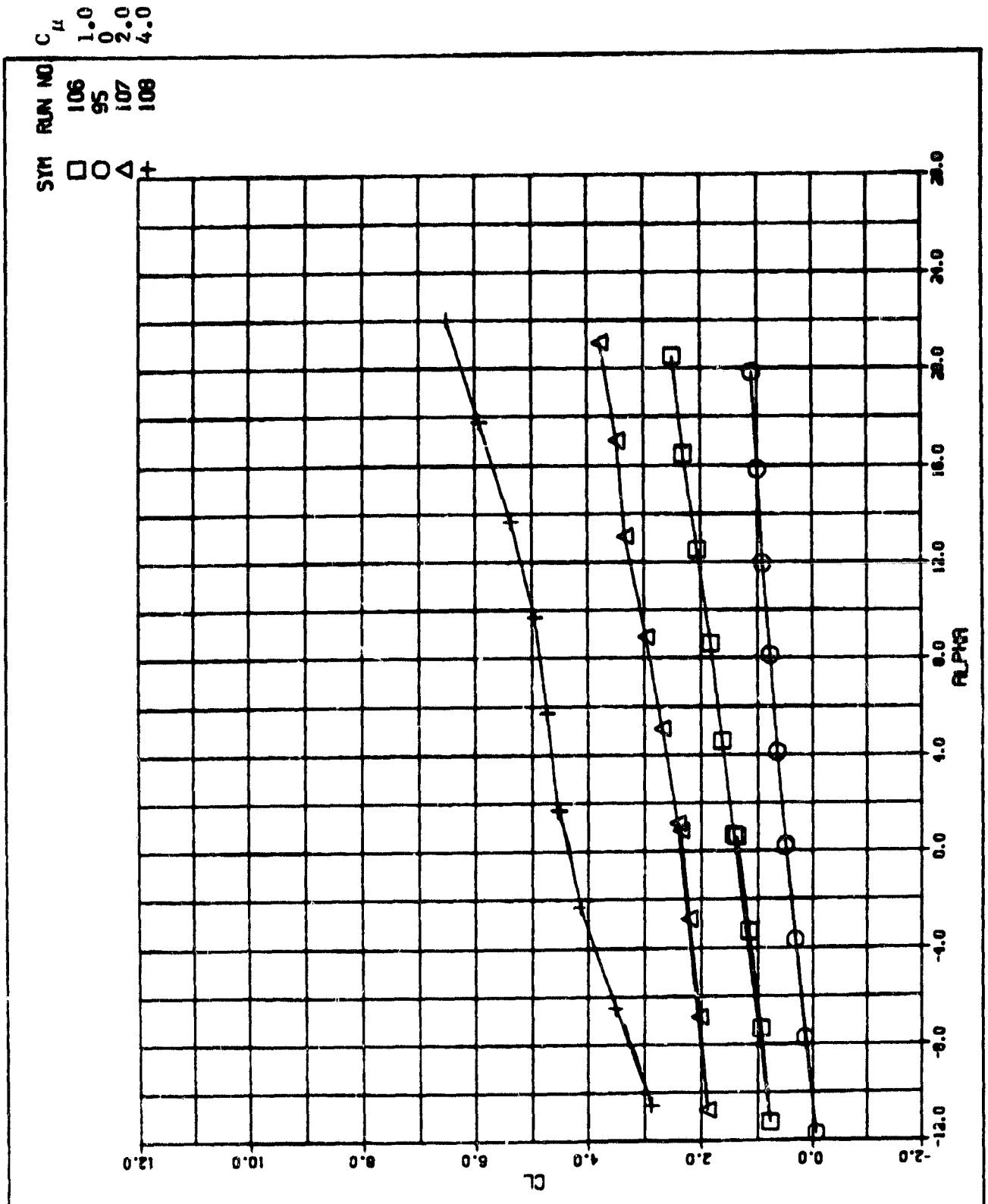

a. Lift vs α

Figure 22. Basic Aerodynamic Characteristics, Thrust Augmenter 2; $\Phi = 30^{o}$, $\delta_D = 0^{o}$

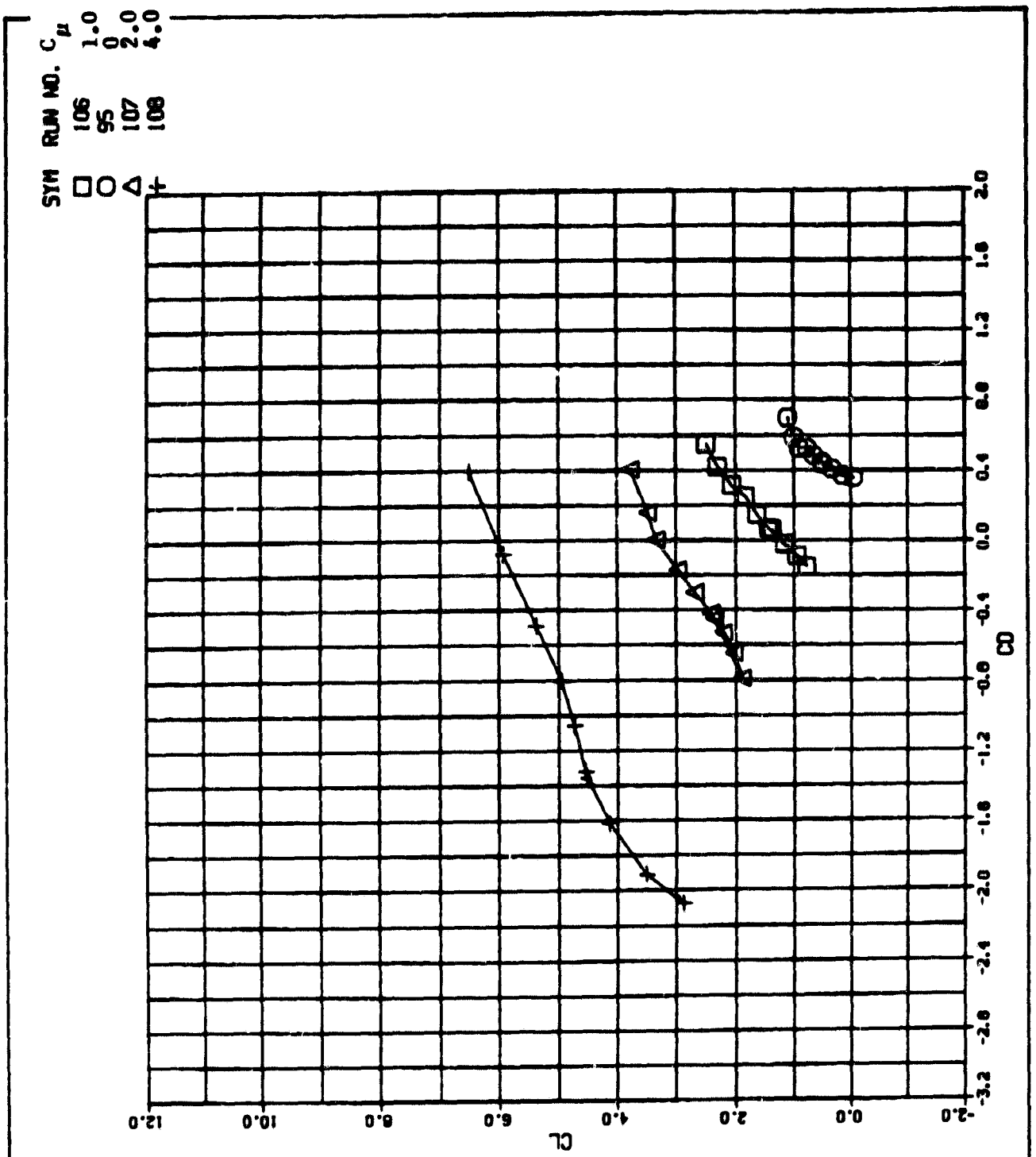

b. Lift vs Drag

Figure 22. Continued

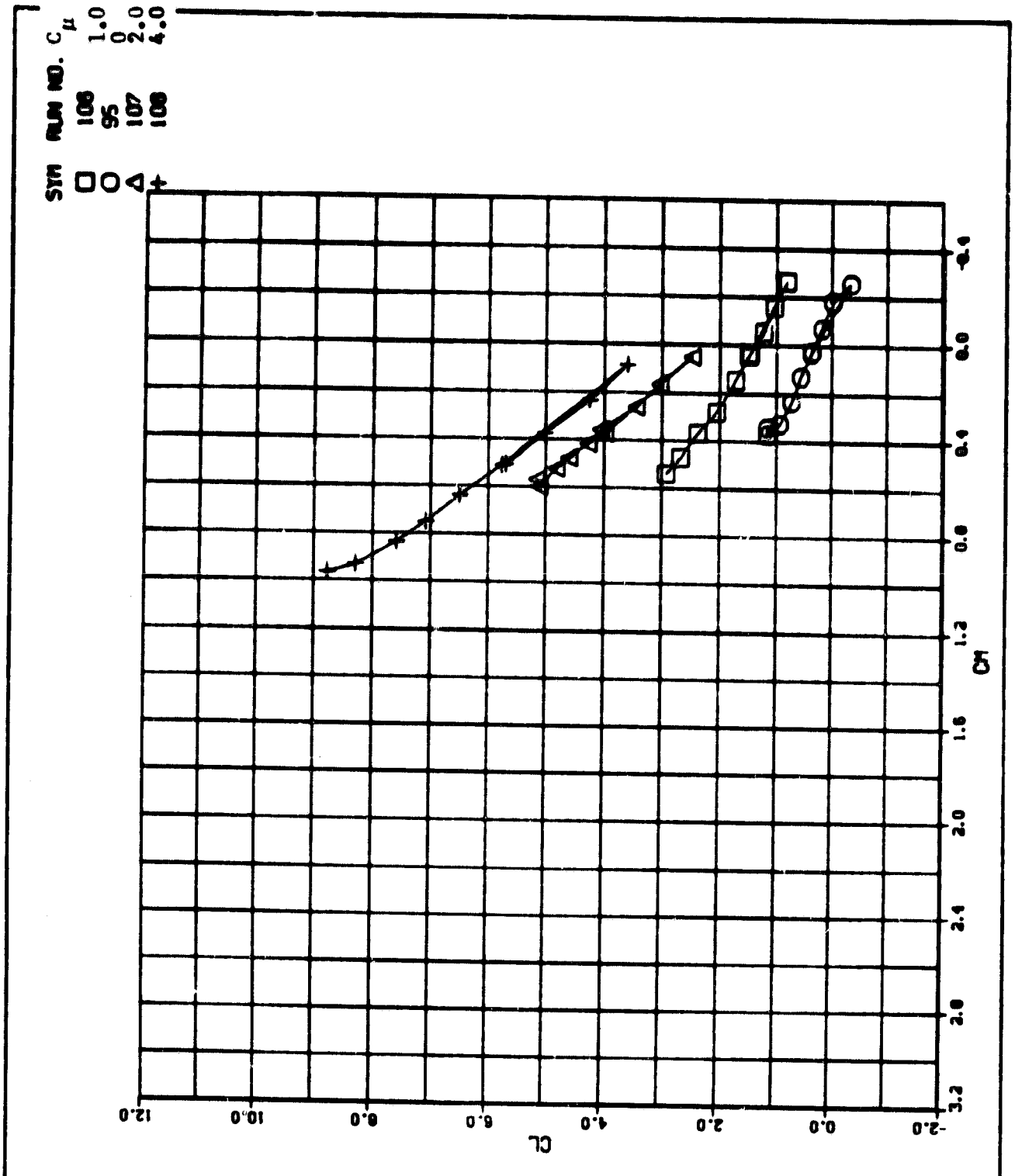

c. Lift vs Pitching Moment

Figure 22. Continued

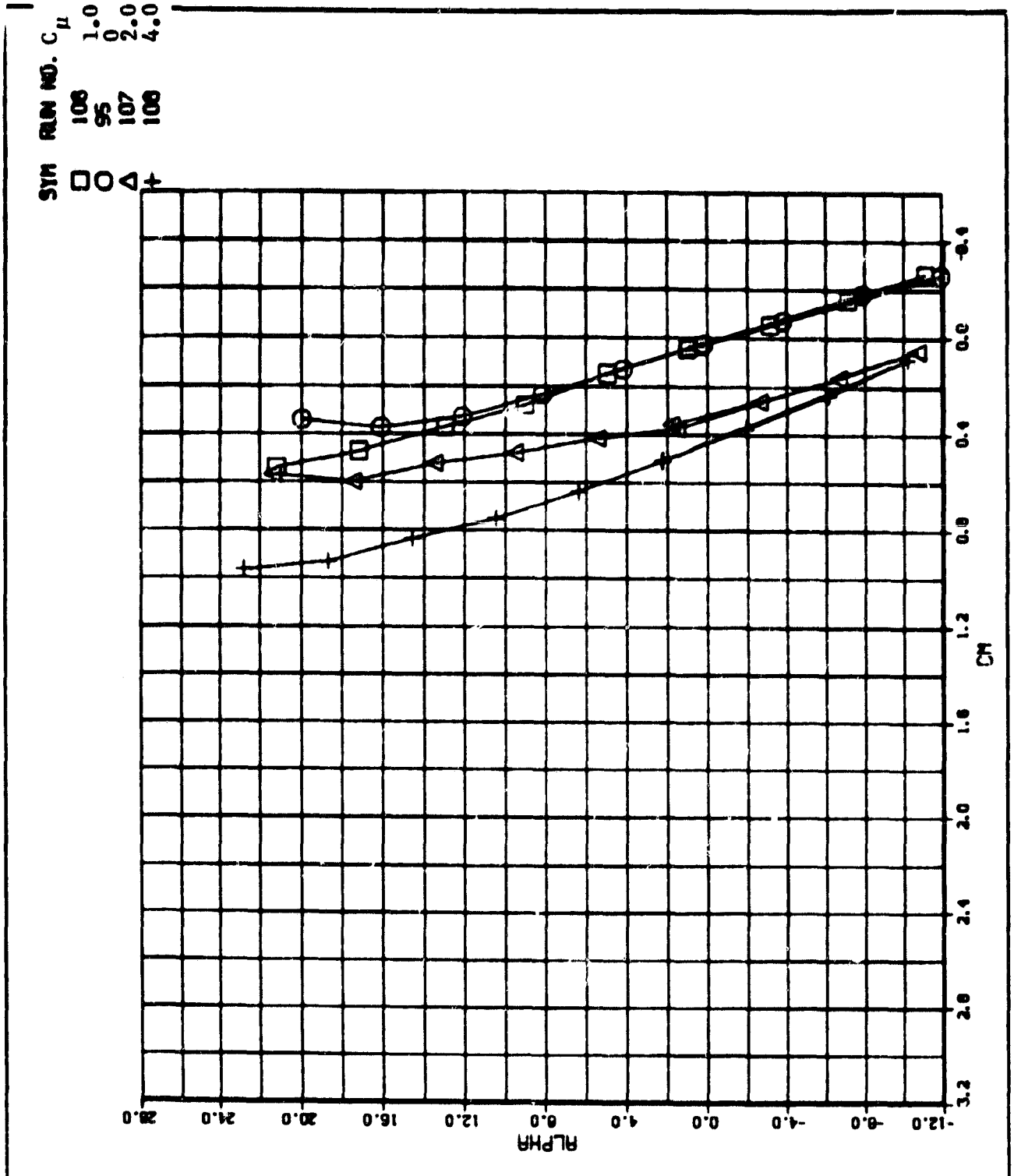

d. α vs Pitching Moment

Figure 22. Concluded

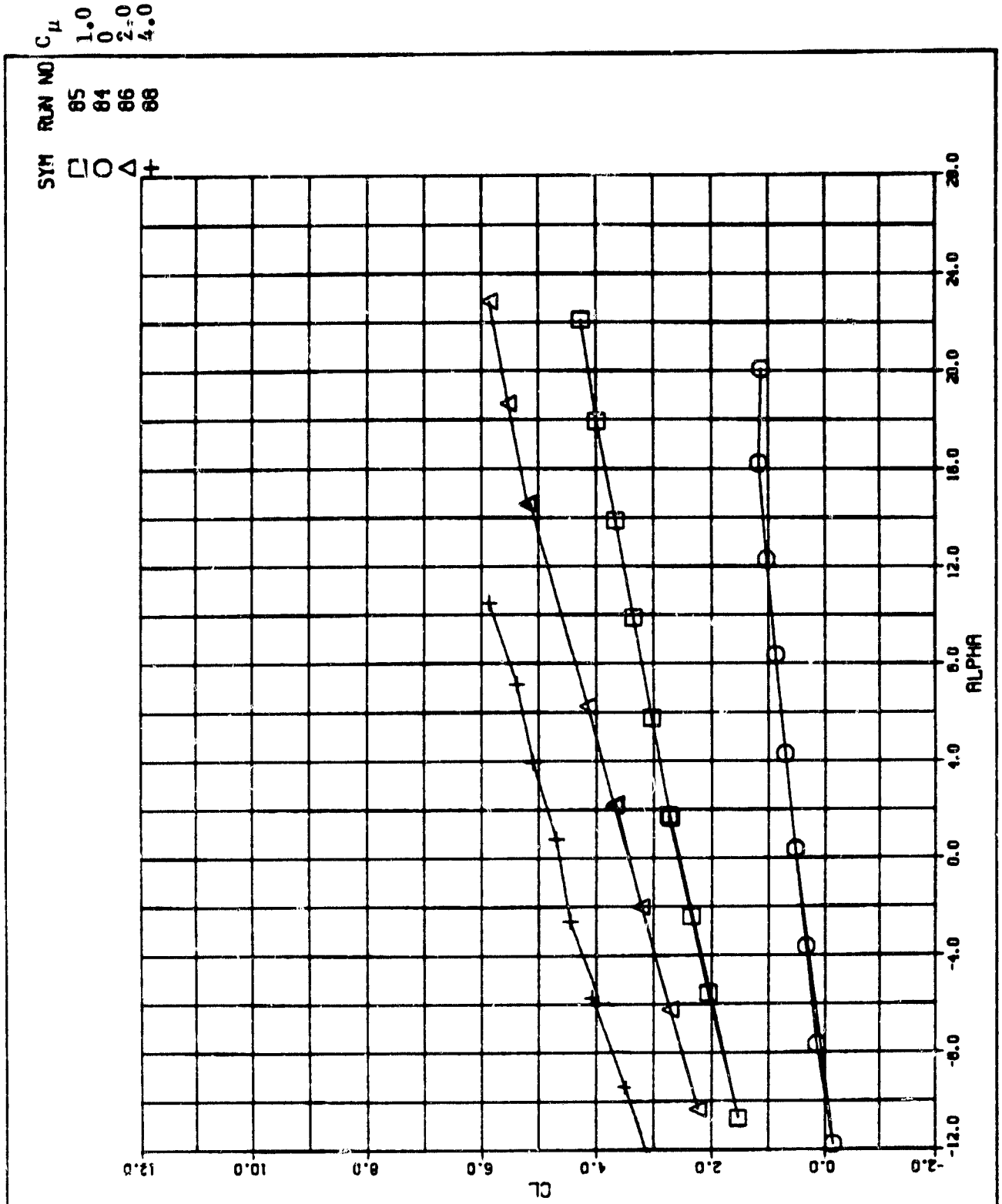

a. Lift vs α

Figure 23. Basic Aerodynamic Characteristics, Thrust Augmenter 2; $\phi = 30^\circ$, $\delta_D = 8^\circ$

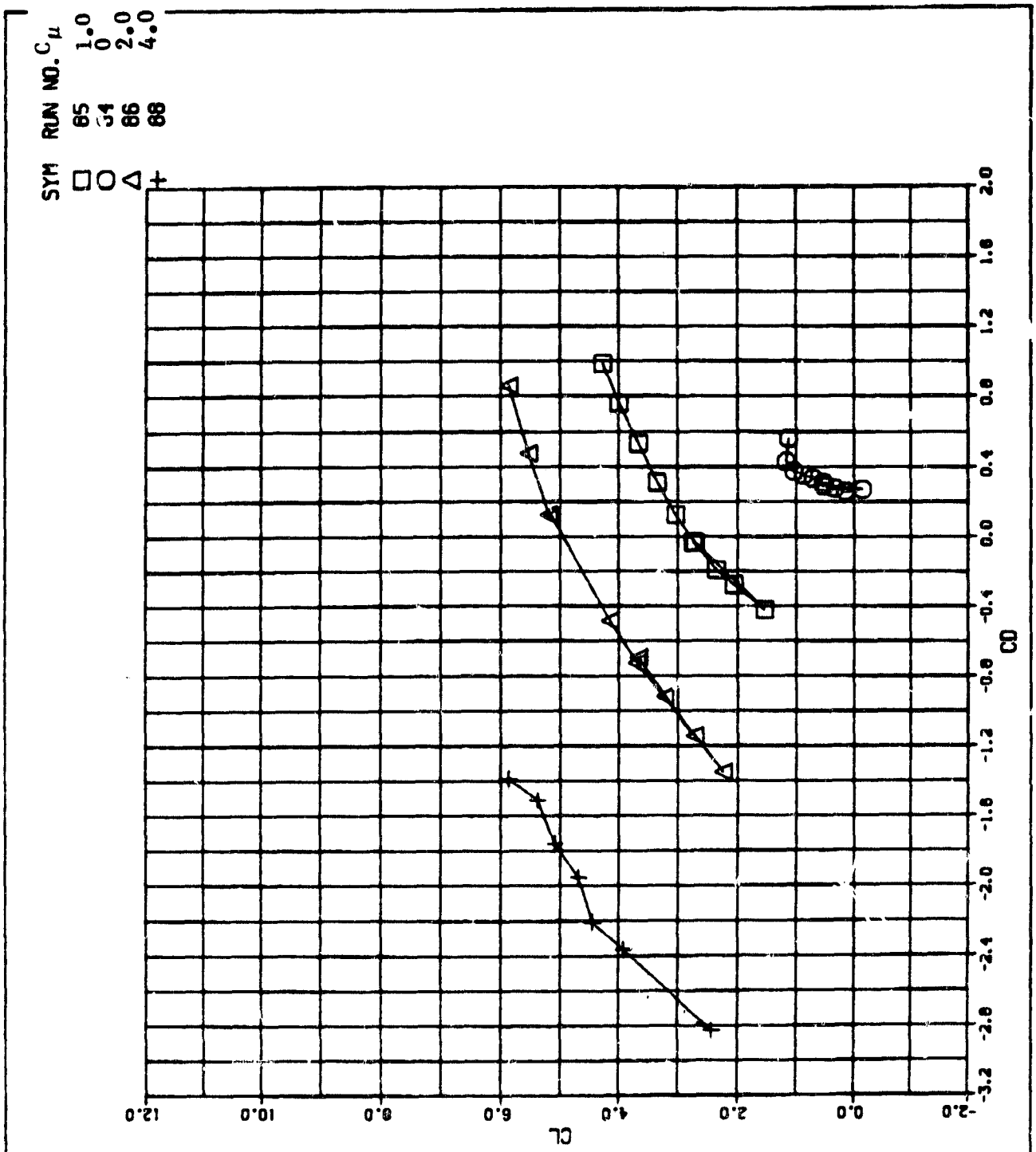

b. Lift vs Drag

Figure 23. Continued

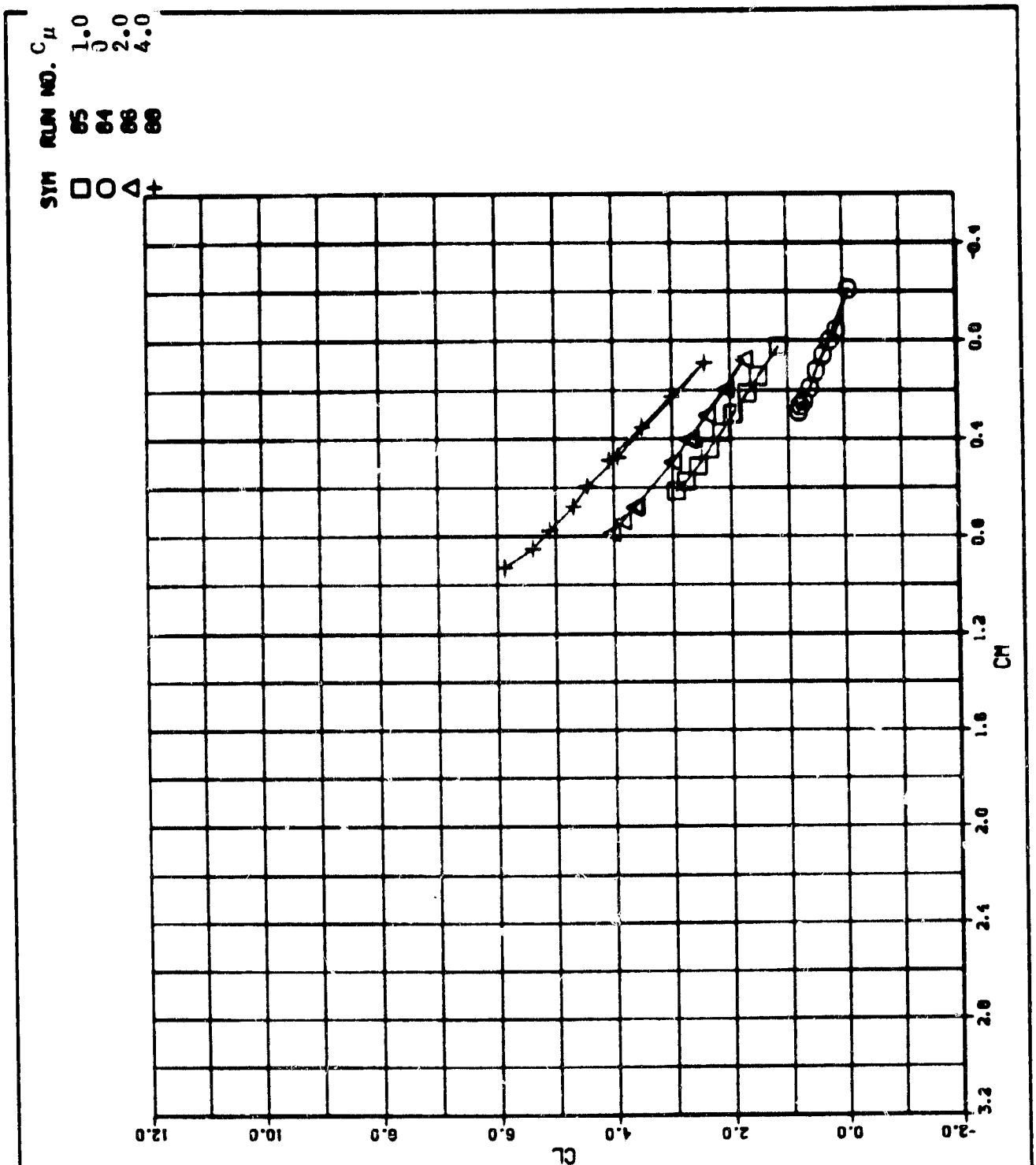

c. Lift vs Pitching Moment

Figure 23. Continued

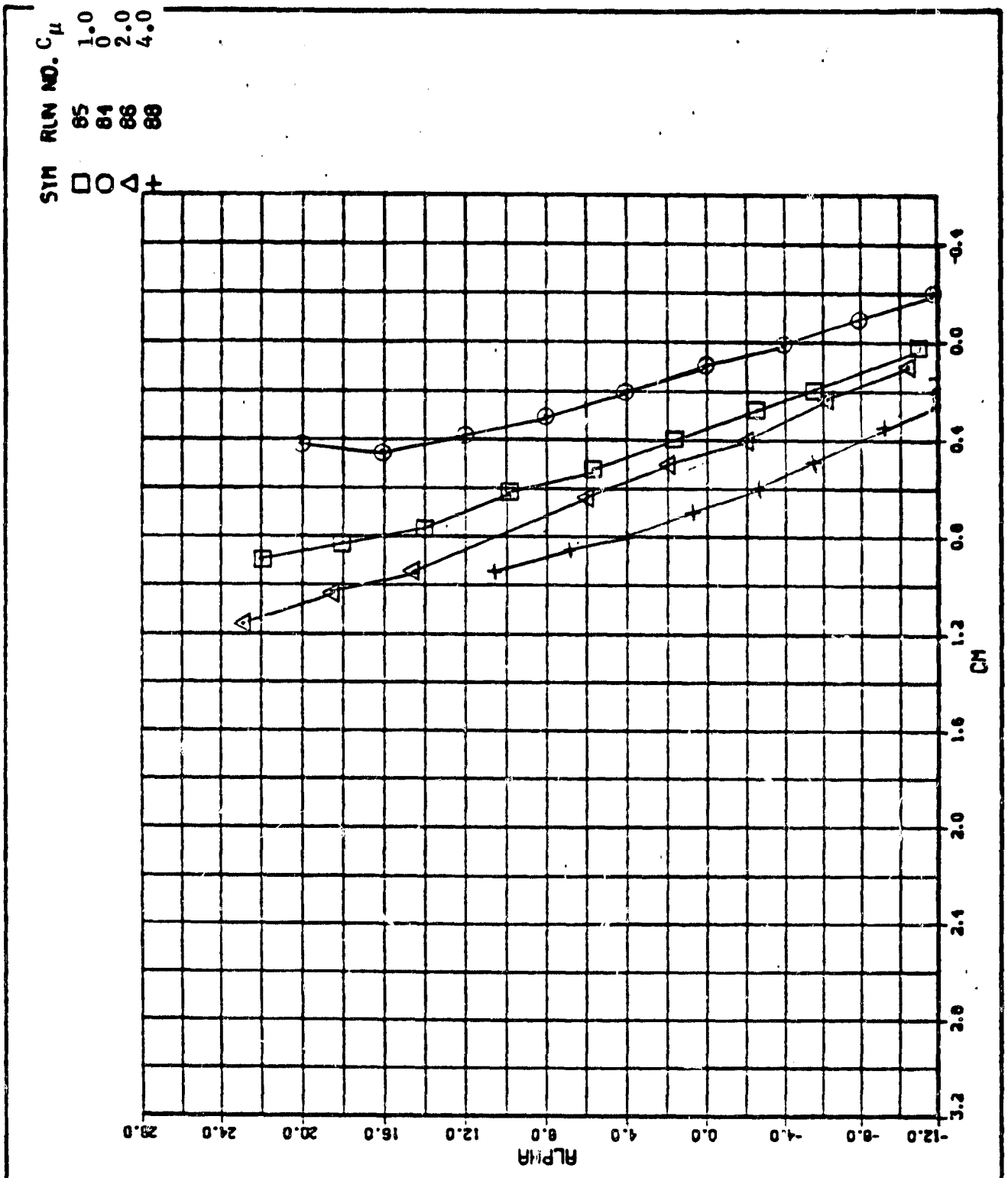

d. α vs Pitching Moment

Figure 23. Concluded

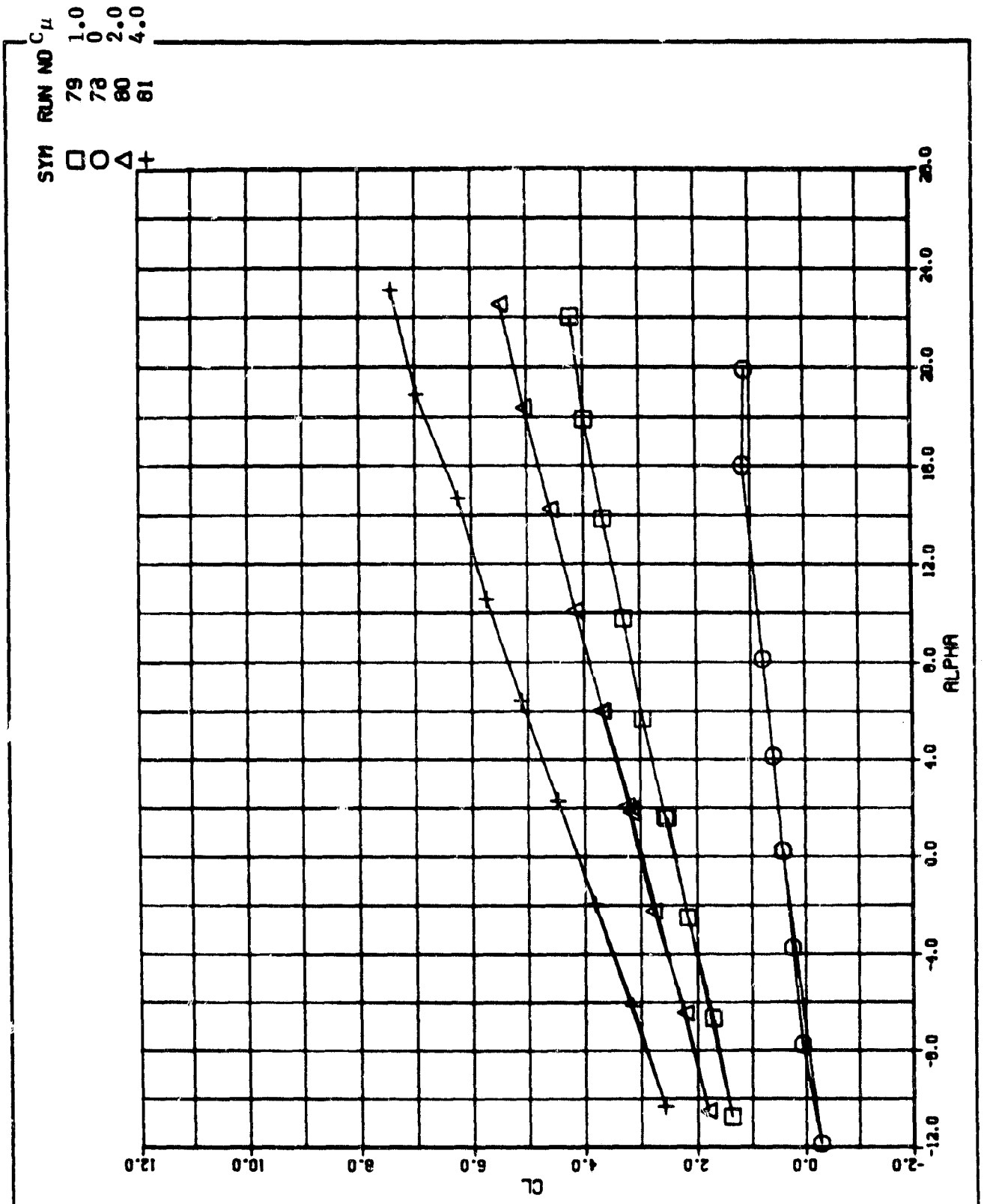

a. Lift vs α

Figure 24. Basic Aerodynamic Characteristics, Thrust Augmenter 2; $\phi = 30^{\circ}$, $\delta_D = 16^{\circ}$

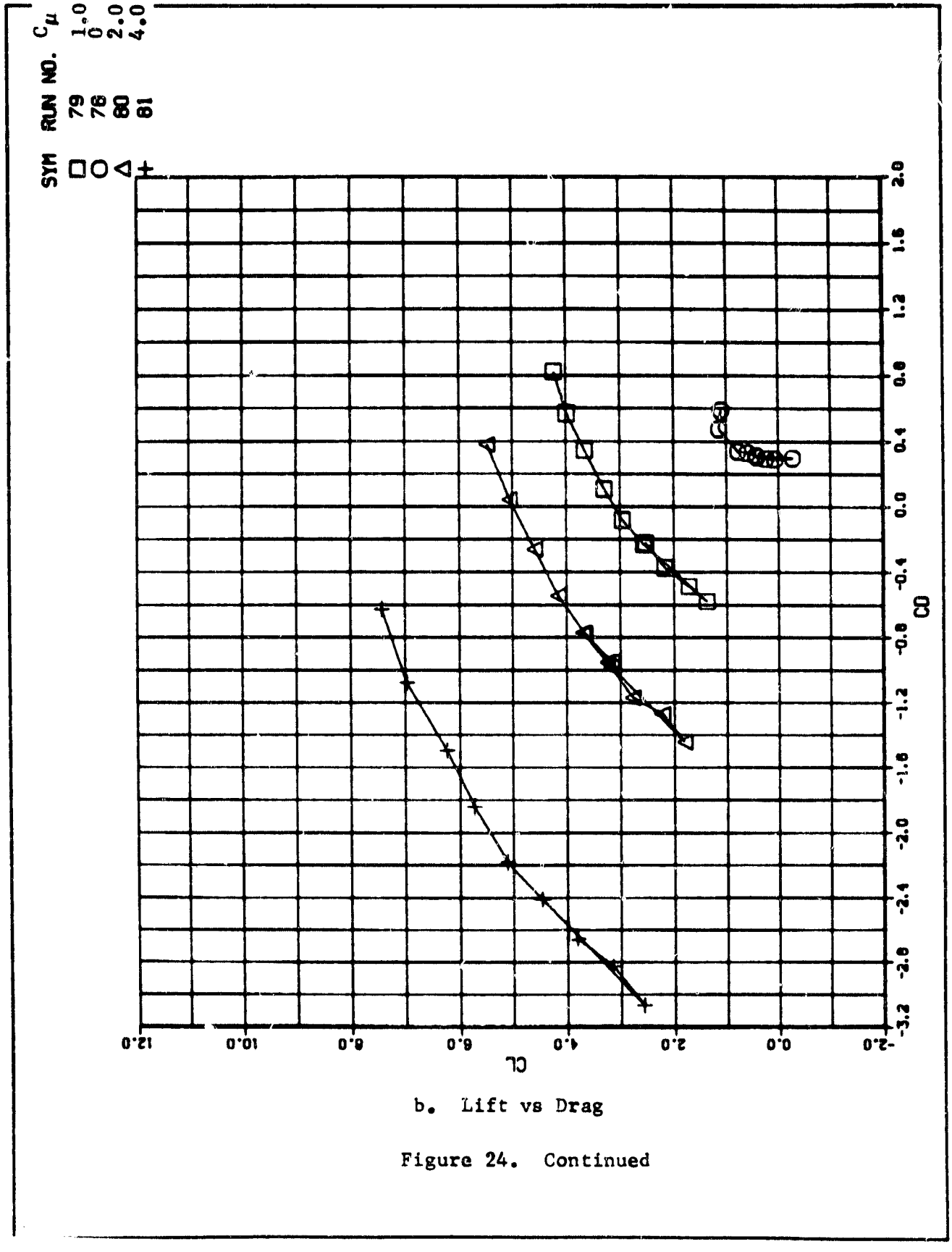

b. Lift vs Drag

Figure 24. Continued

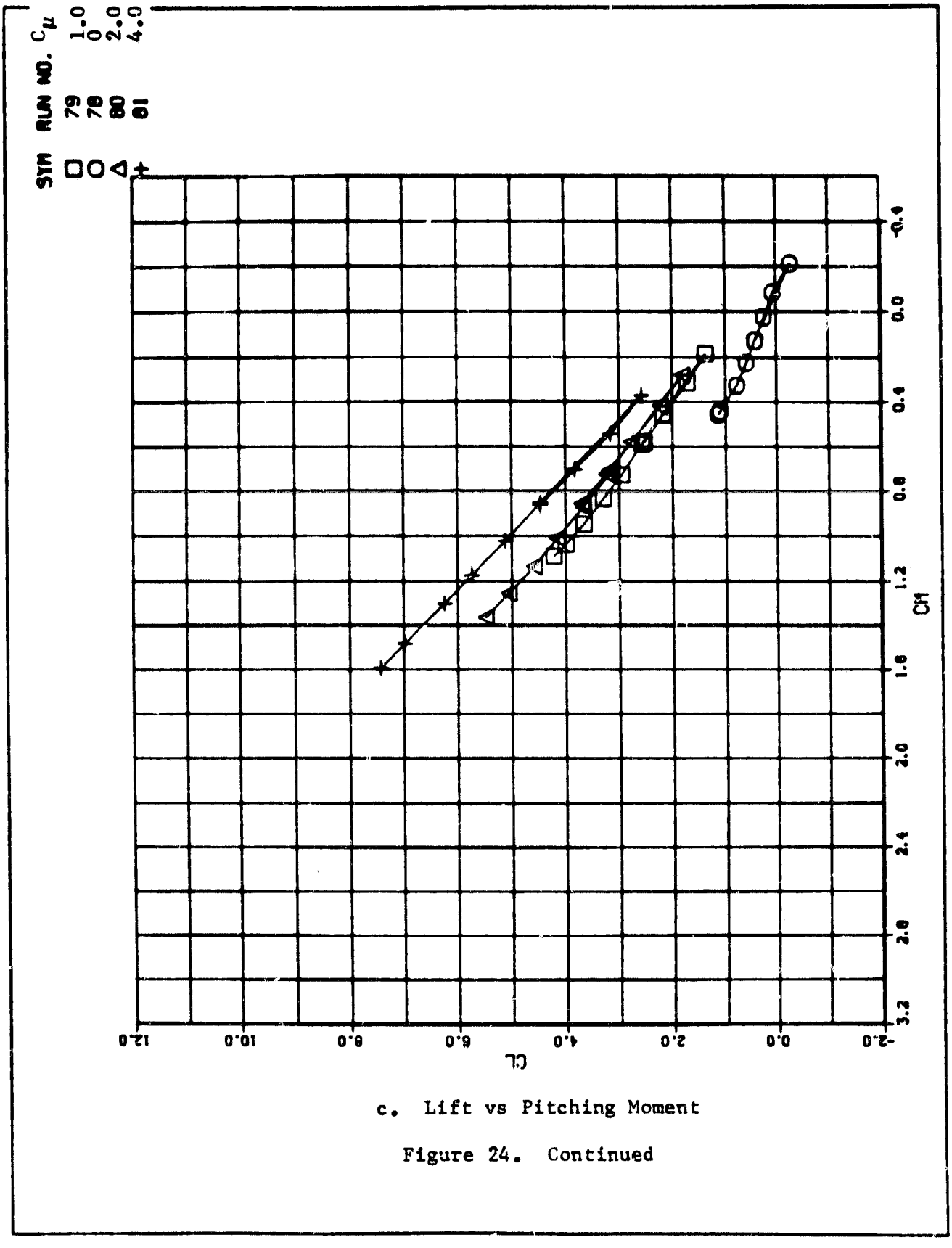

c. Lift vs Pitching Moment

Figure 24. Continued

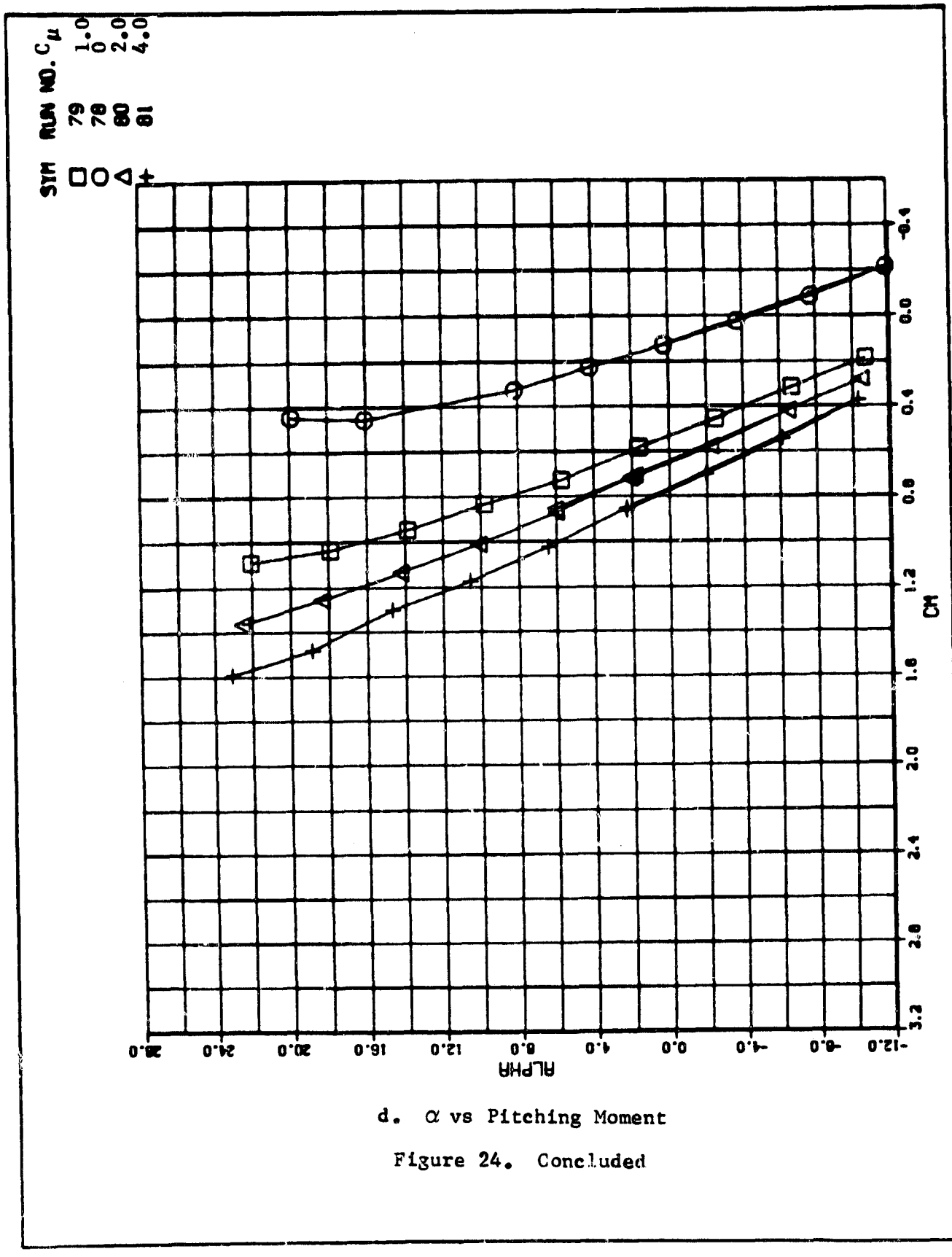

d. α vs Pitching Moment

Figure 24. Concluded

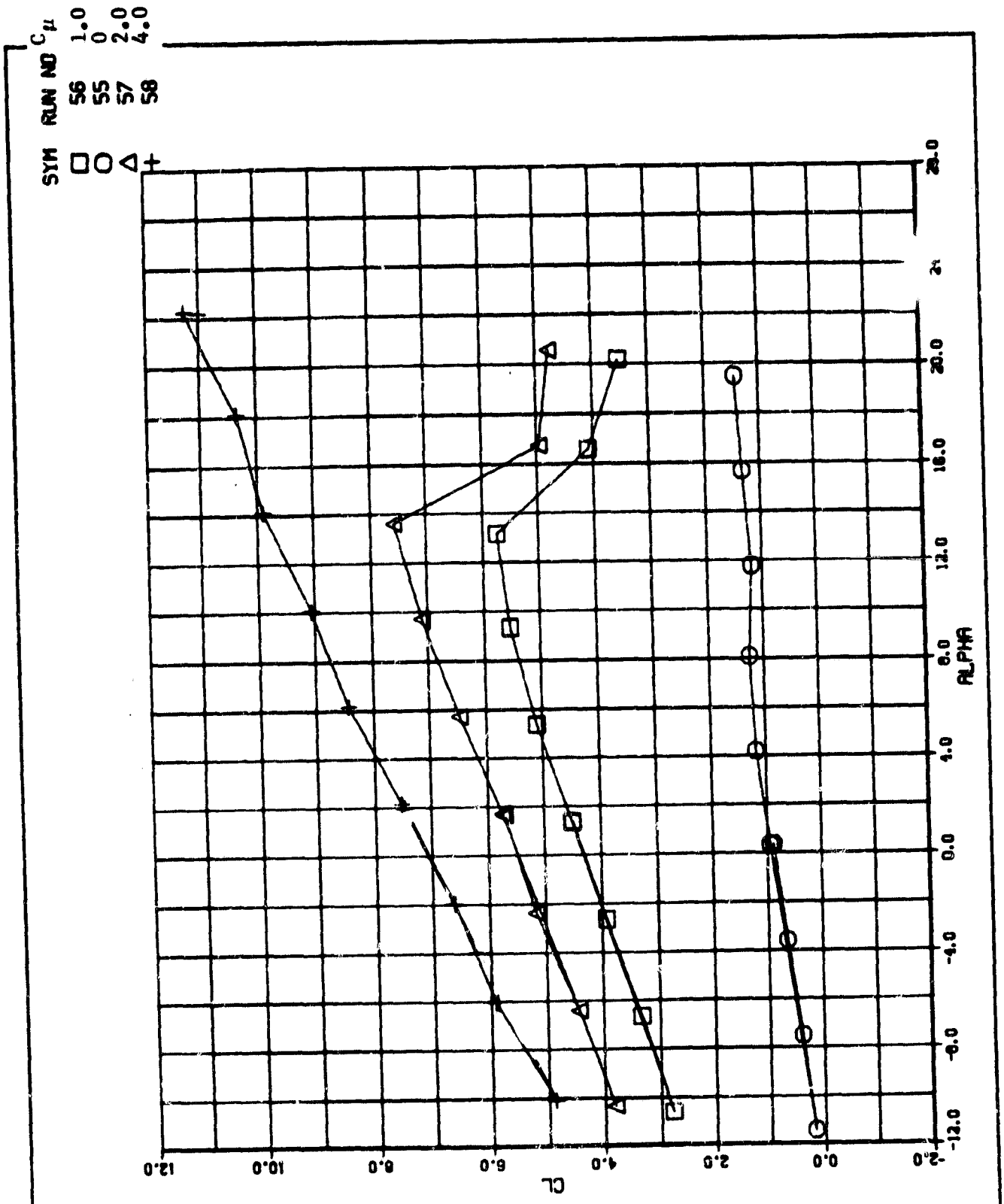

a. Lift vs α

Figure 25. Basic Aerodynamic Characteristics, Jet Flap 1; $\theta = 40^{\circ}$

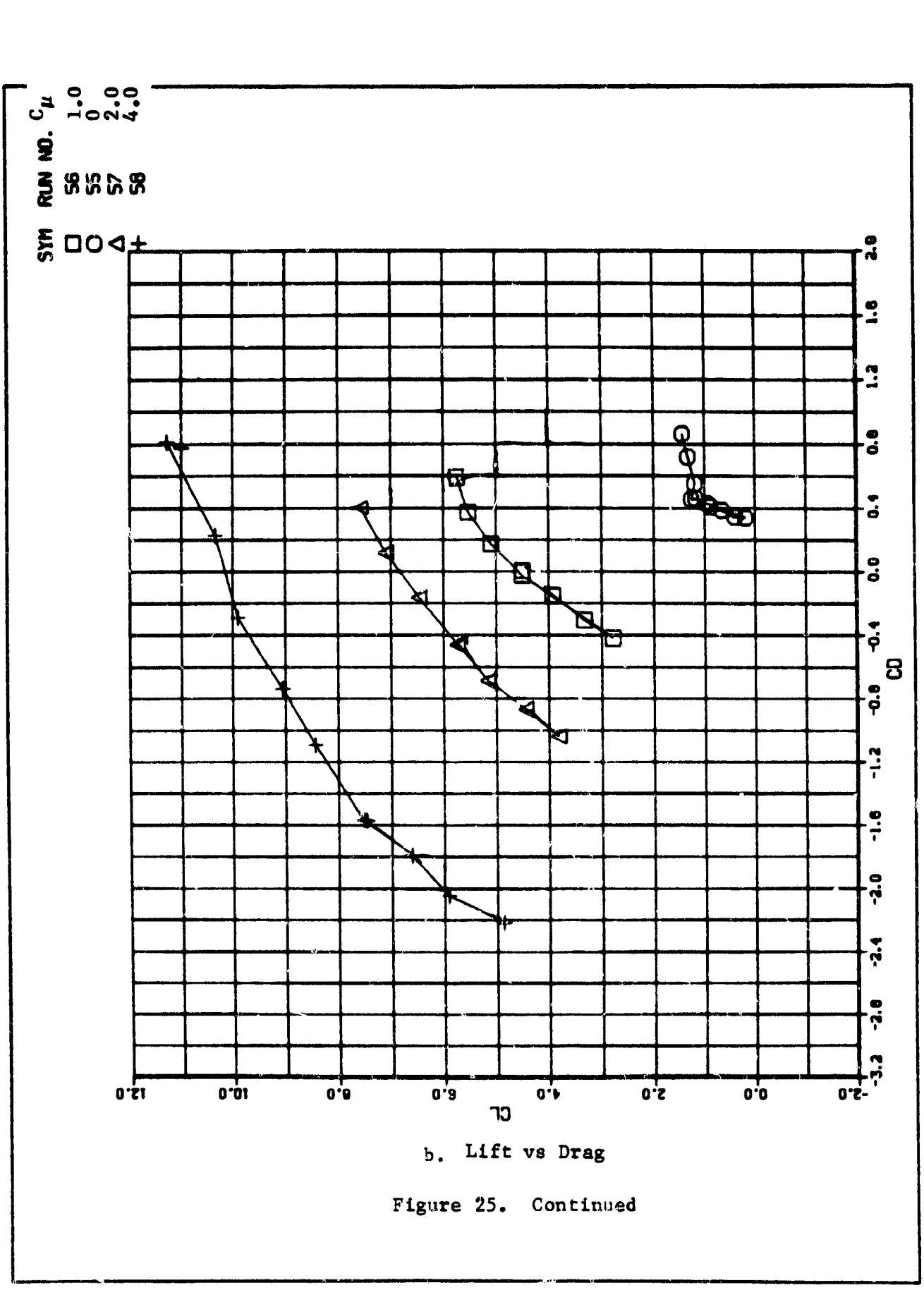

b. Lift vs Drag

Figure 25. Continued

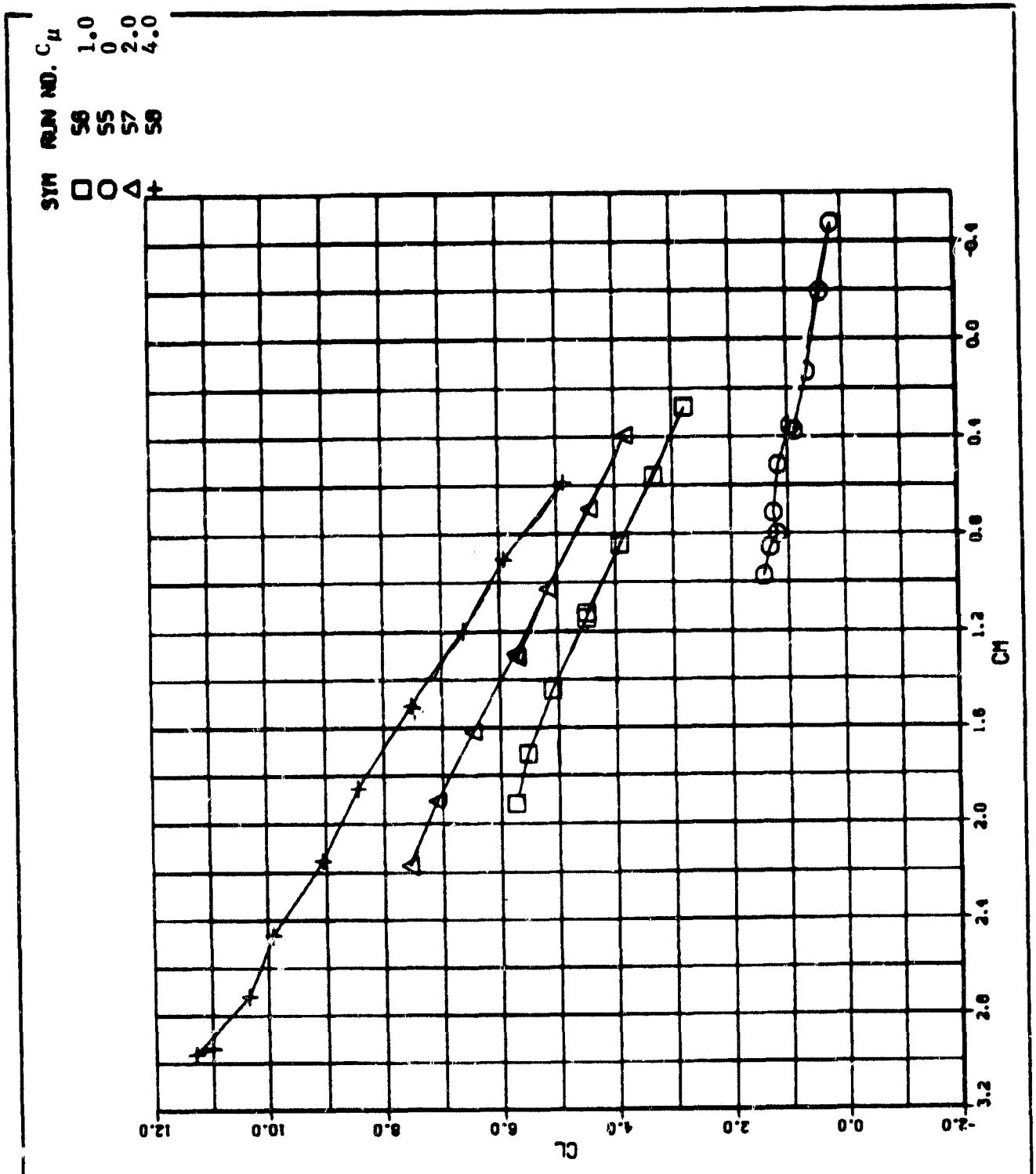

c. Lift vs Pitching Moment

Figure 25. Continued

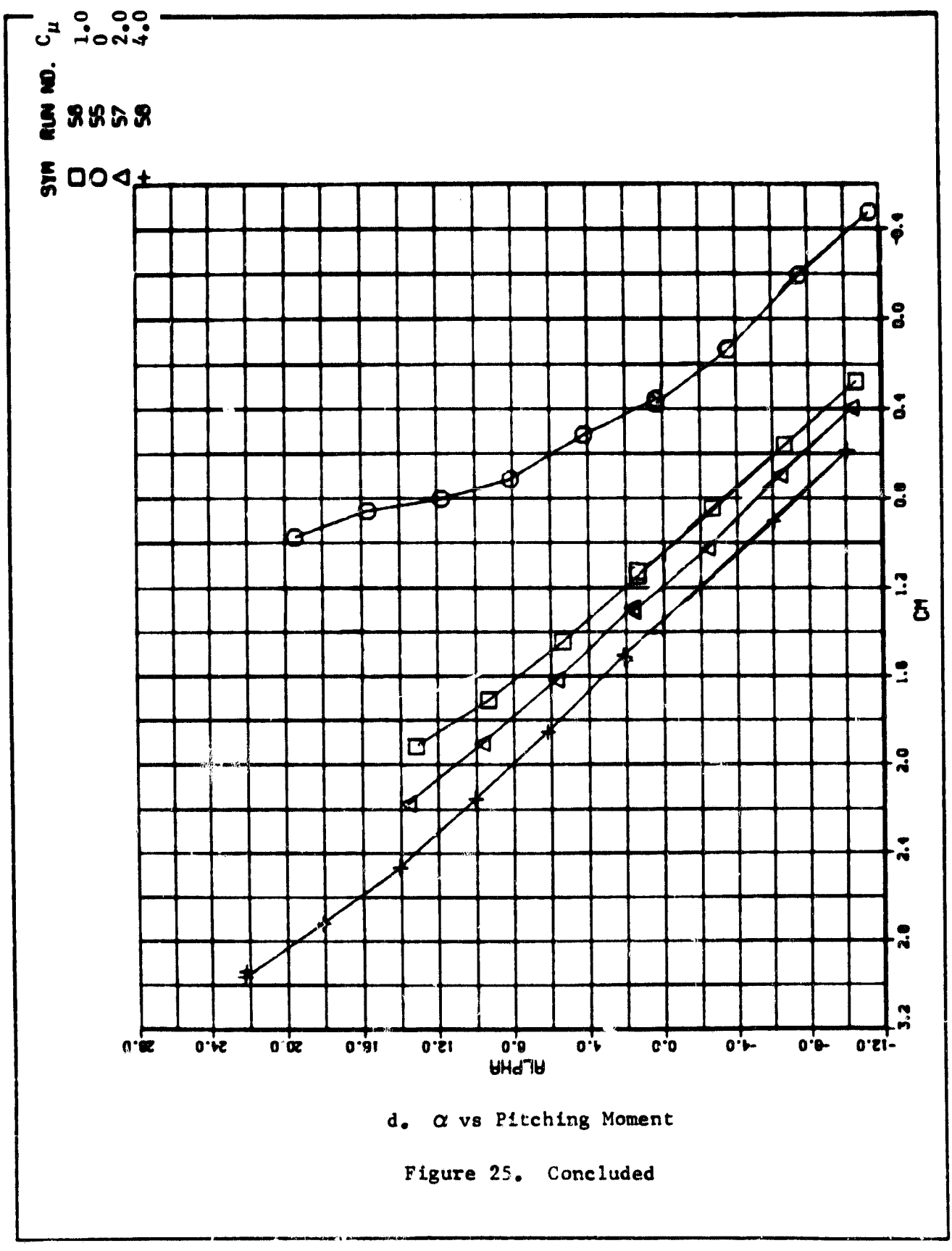

d. α vs Pitching Moment

Figure 25. Concluded

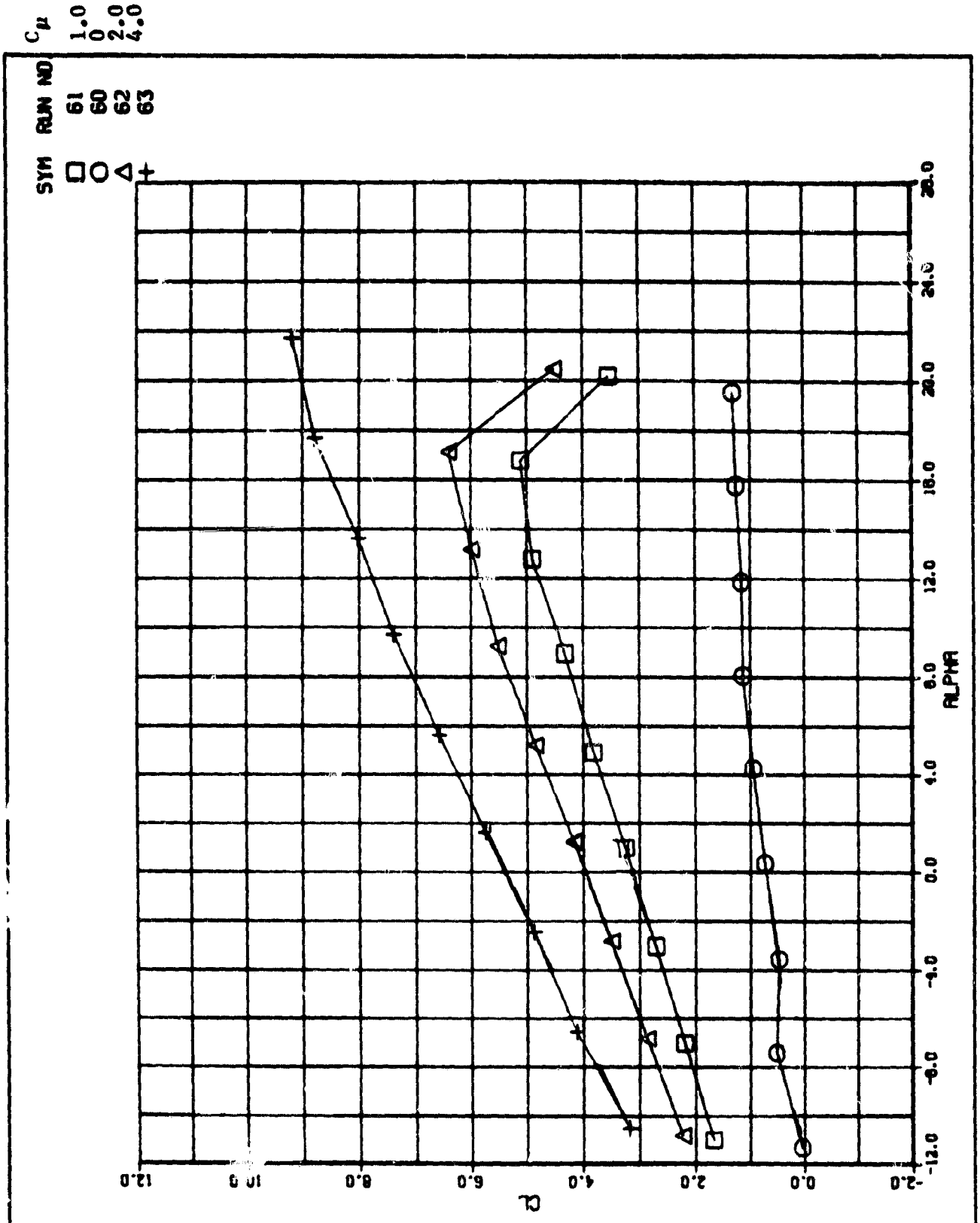

a. Lift vs α

Figure 26. Basic Aerodynamic Characteristics, Jet Flap 1, $\theta = 30^{\circ}$

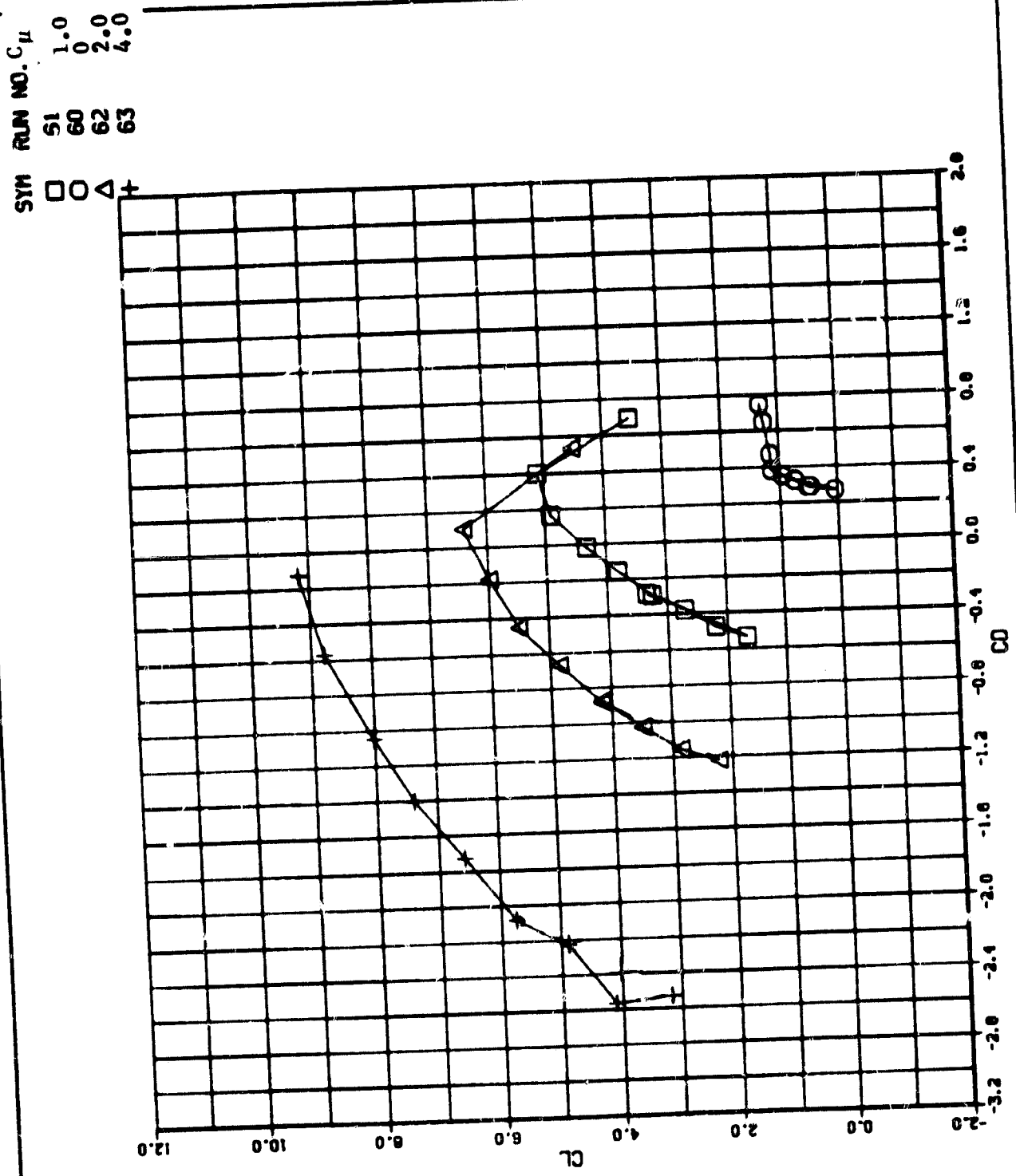

b. Lift vs Drag

Figure 26. Continued

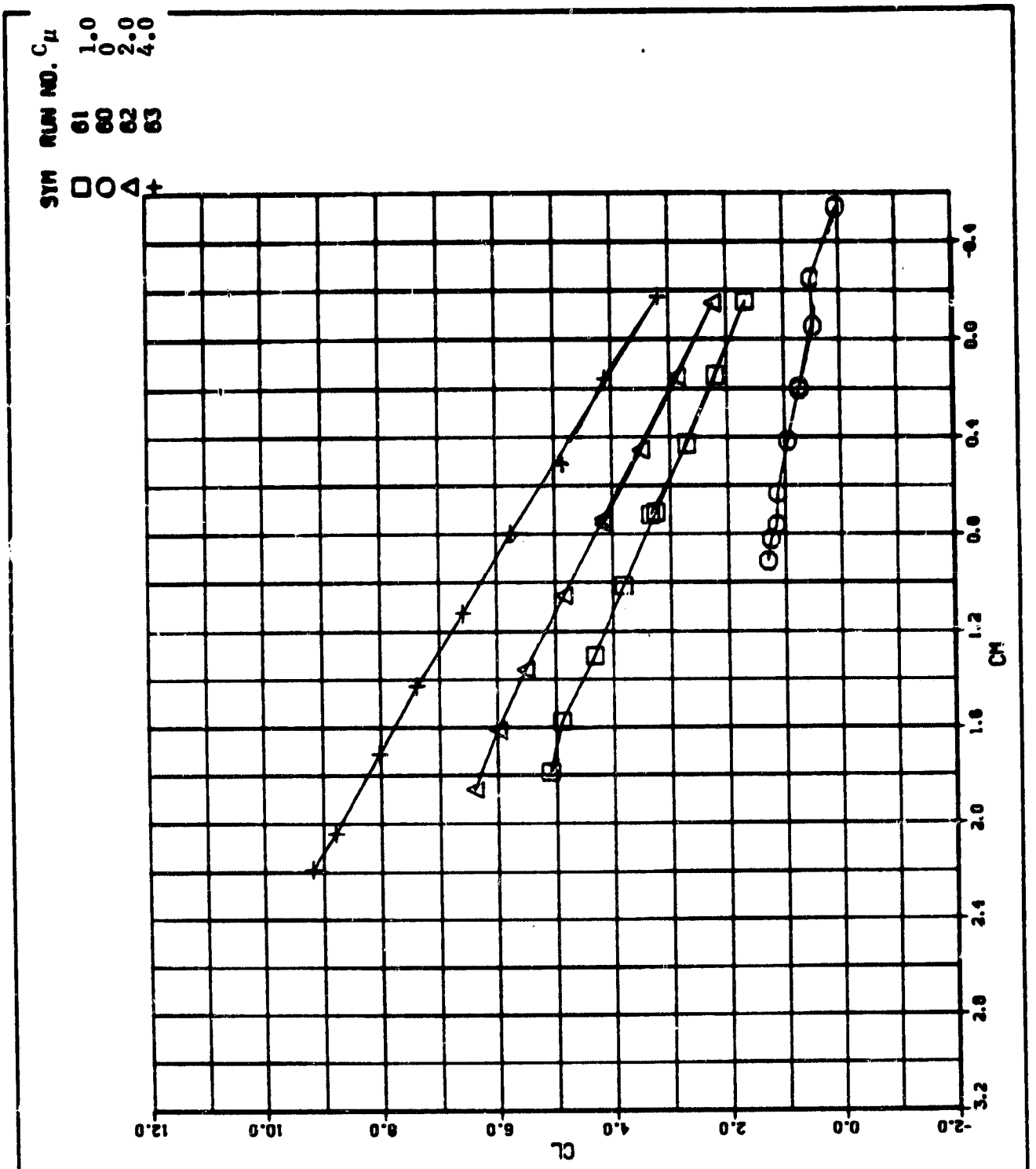

c. Lift vs Pitching Moment

Figure 26. Continued

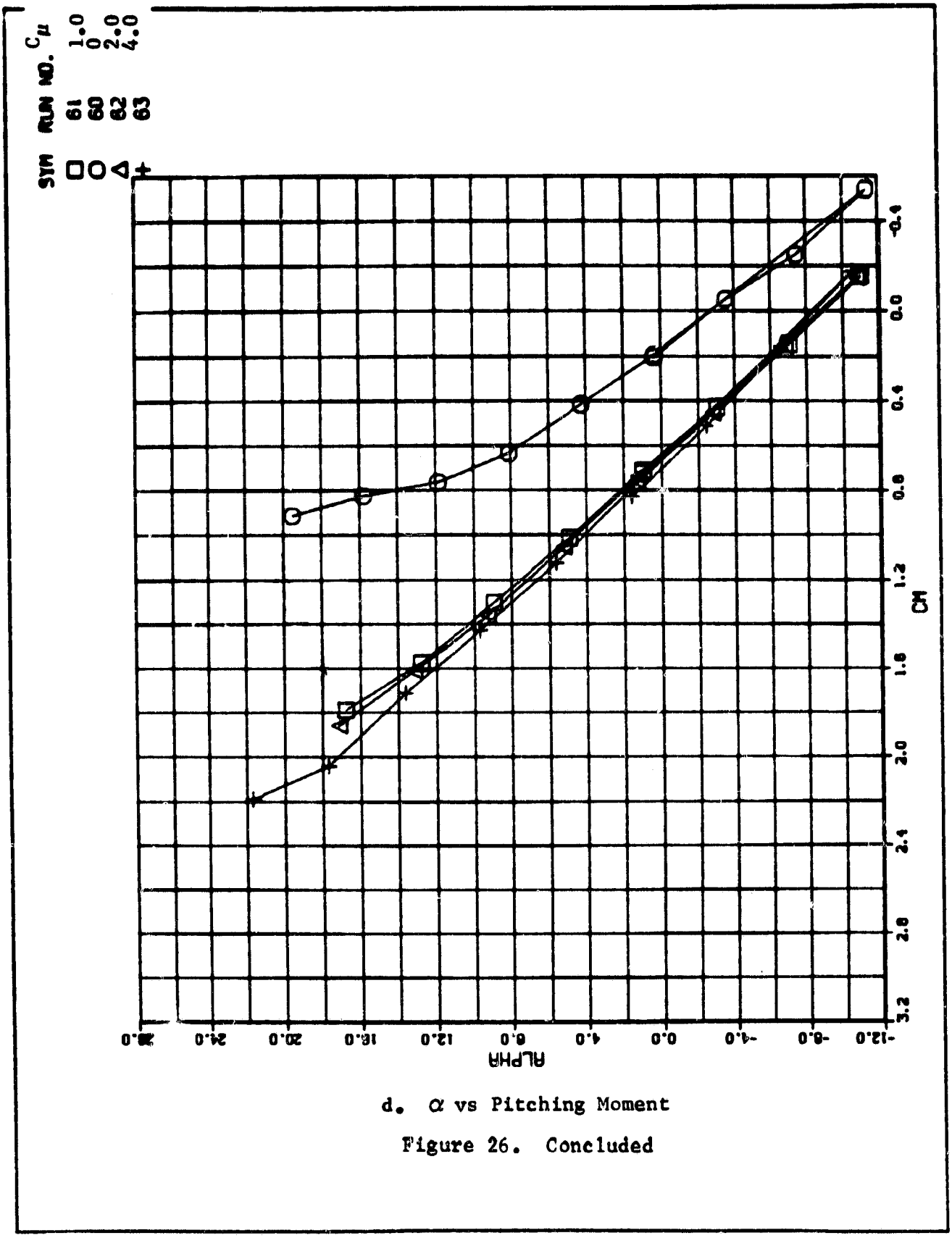

d. α vs Pitching Moment

Figure 26. Concluded

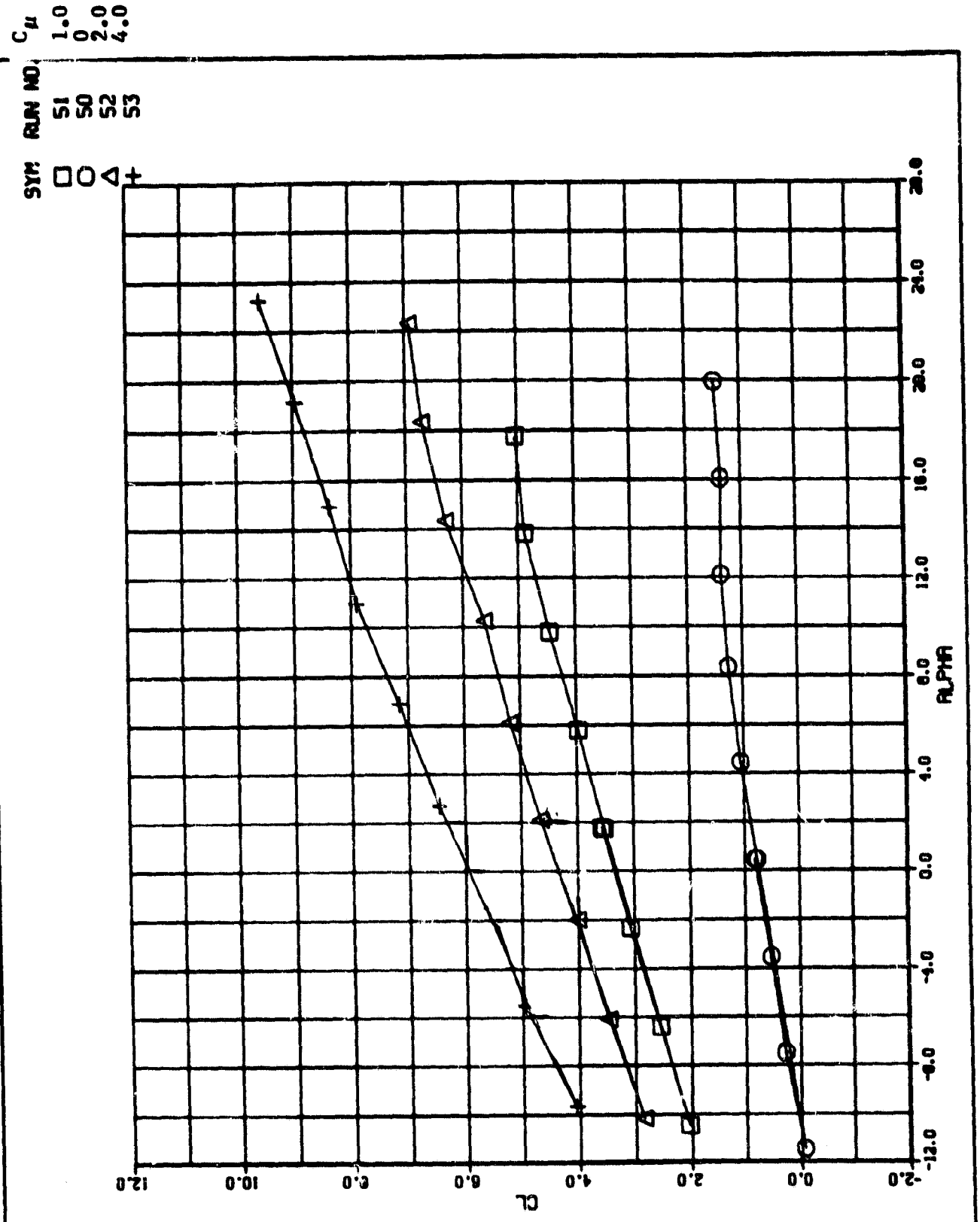

a. Lift vs α

Figure 27. Basic Aerodynamic Characteristics, Jet Flap 2; $\theta = 40^{\circ}$

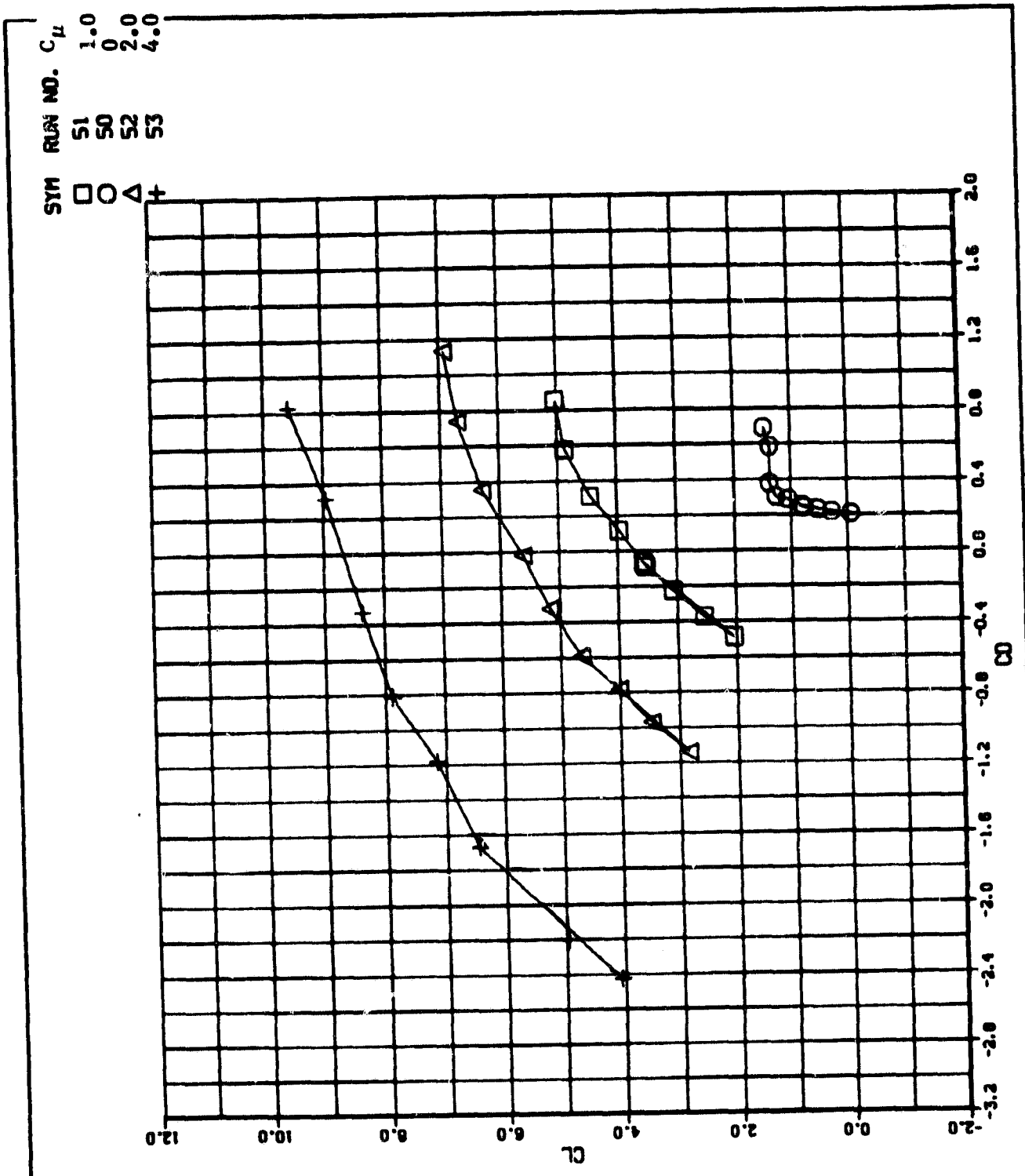

b. Lift vs Drag

Figure 27. Continued

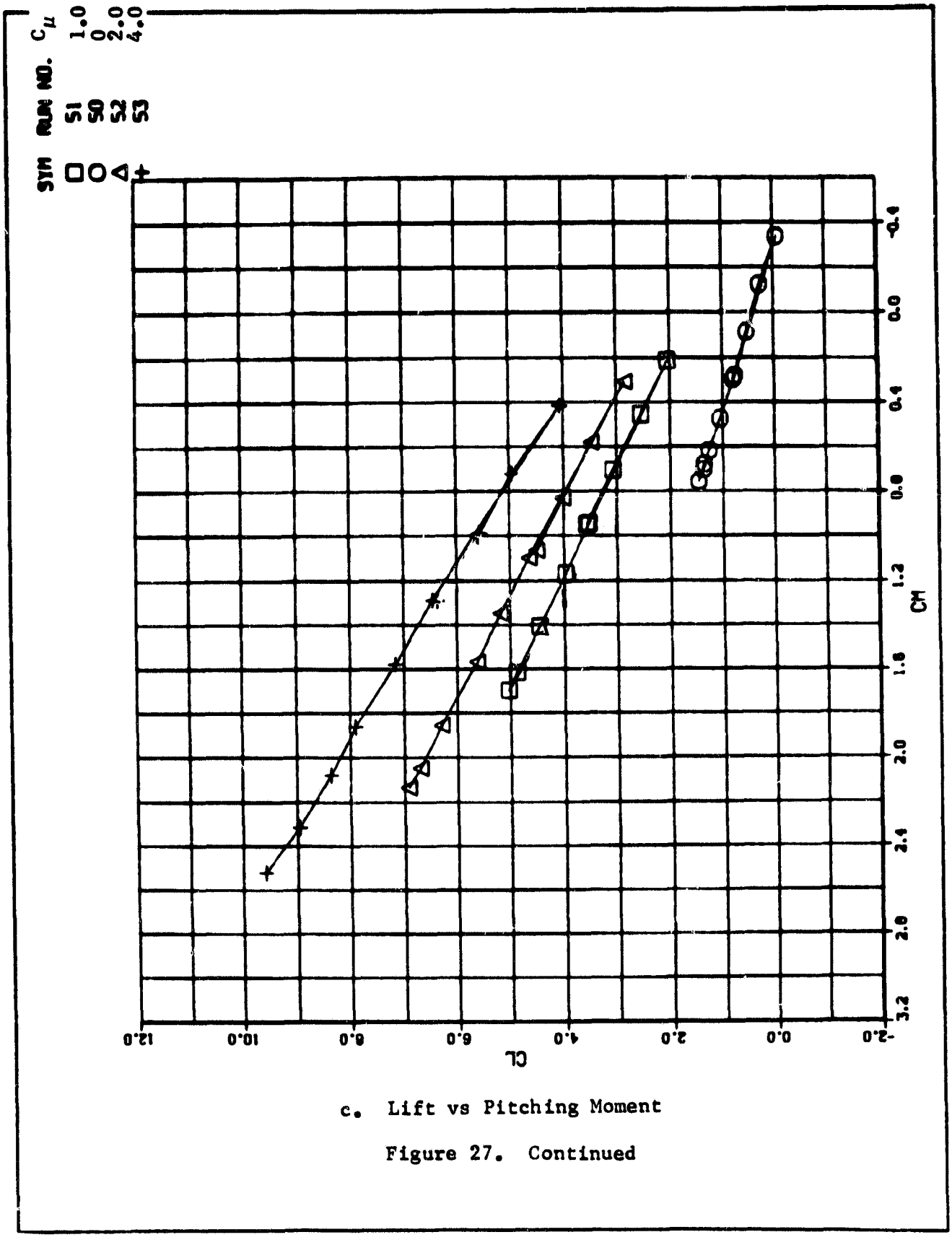

c. Lift vs Pitching Moment

Figure 27. Continued

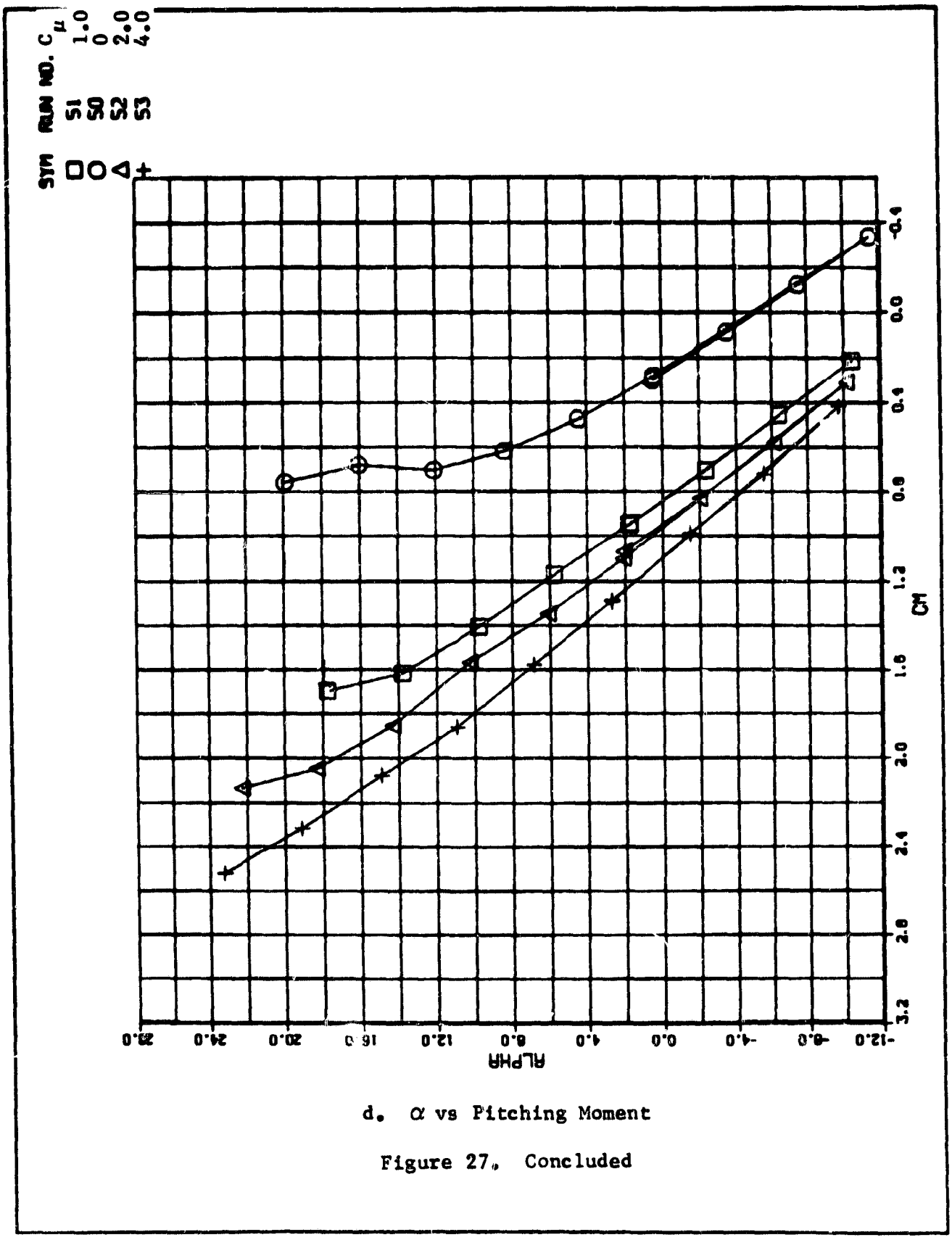

d. α vs Pitching Moment

Figure 27. Concluded

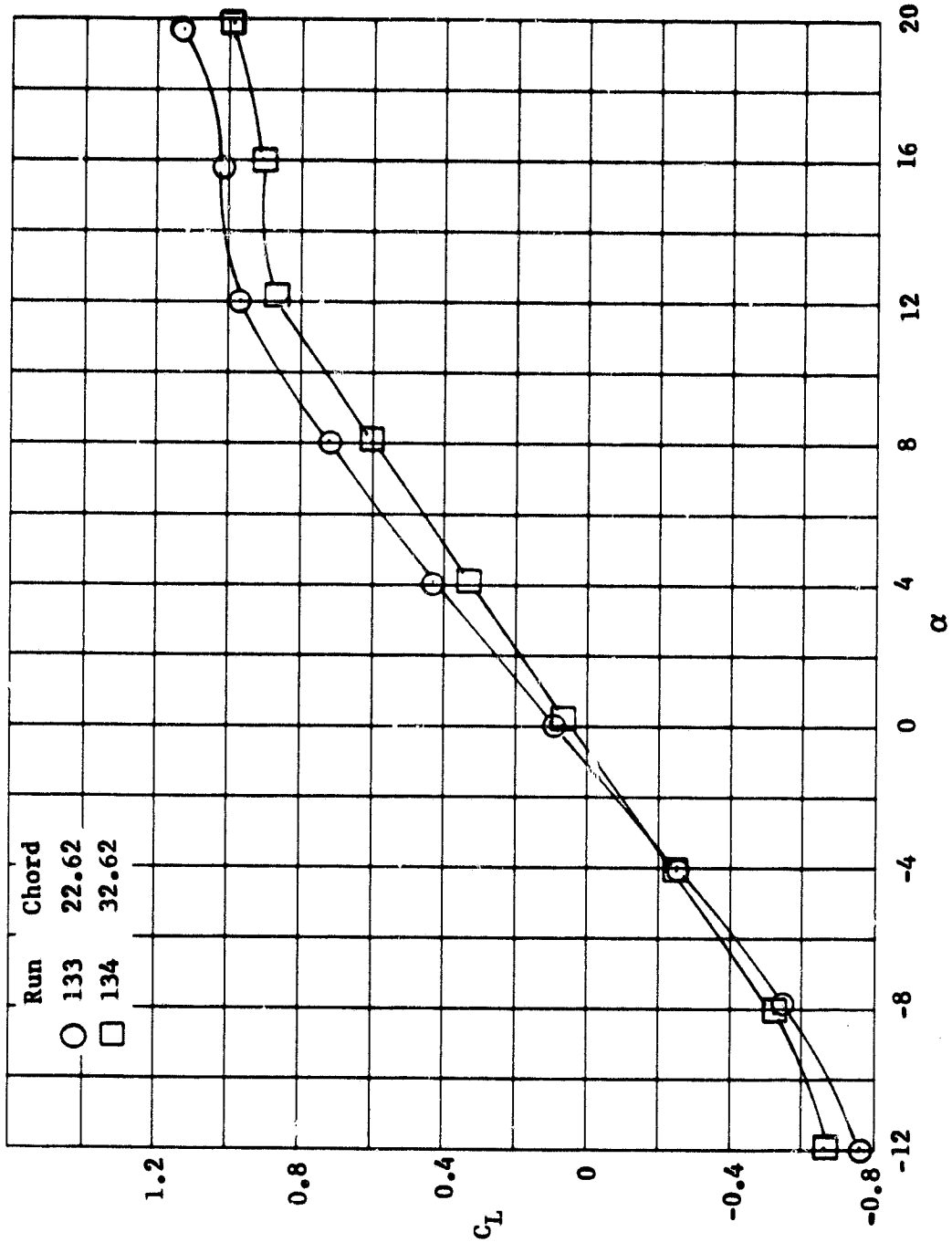

a. Lift vs α

Figure 28. Basic Aerodynamic Characteristics, Basic Wing; $\delta_F = 0^o$, $C_\mu = 0^o$

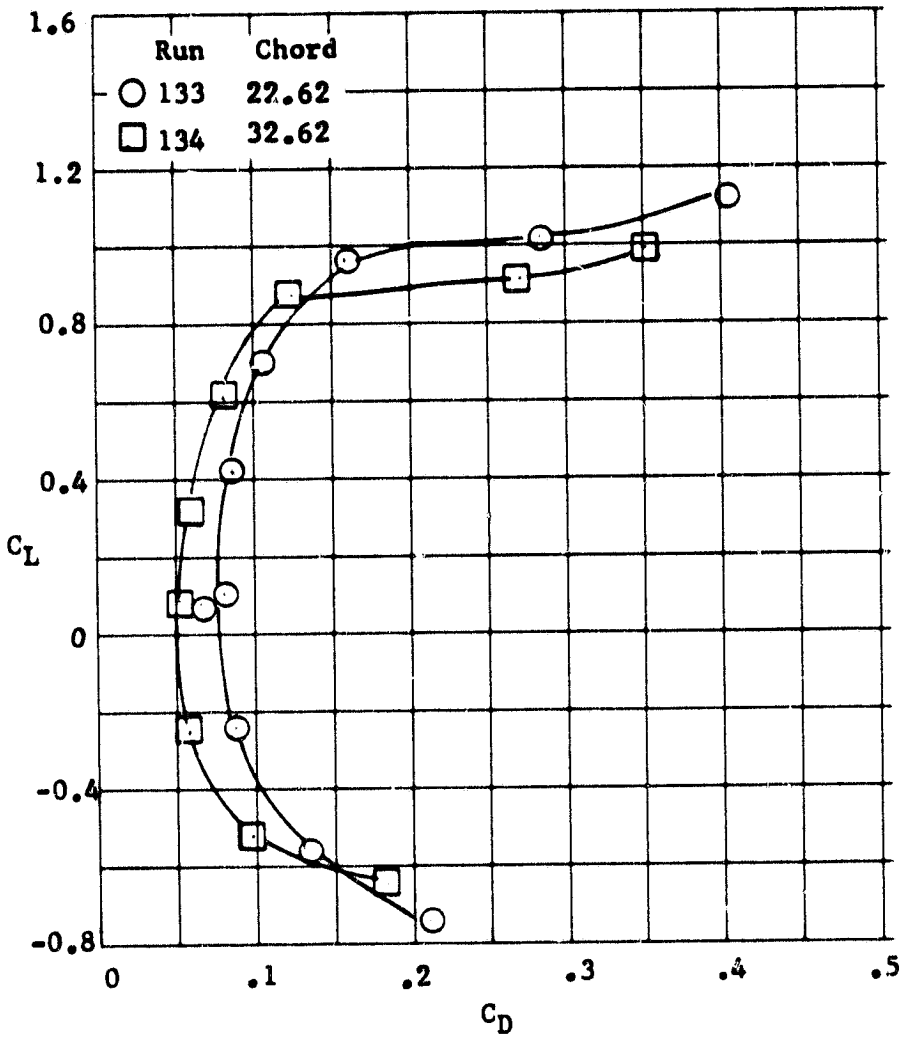

b. Lift vs Drag

Figure 28. Continued

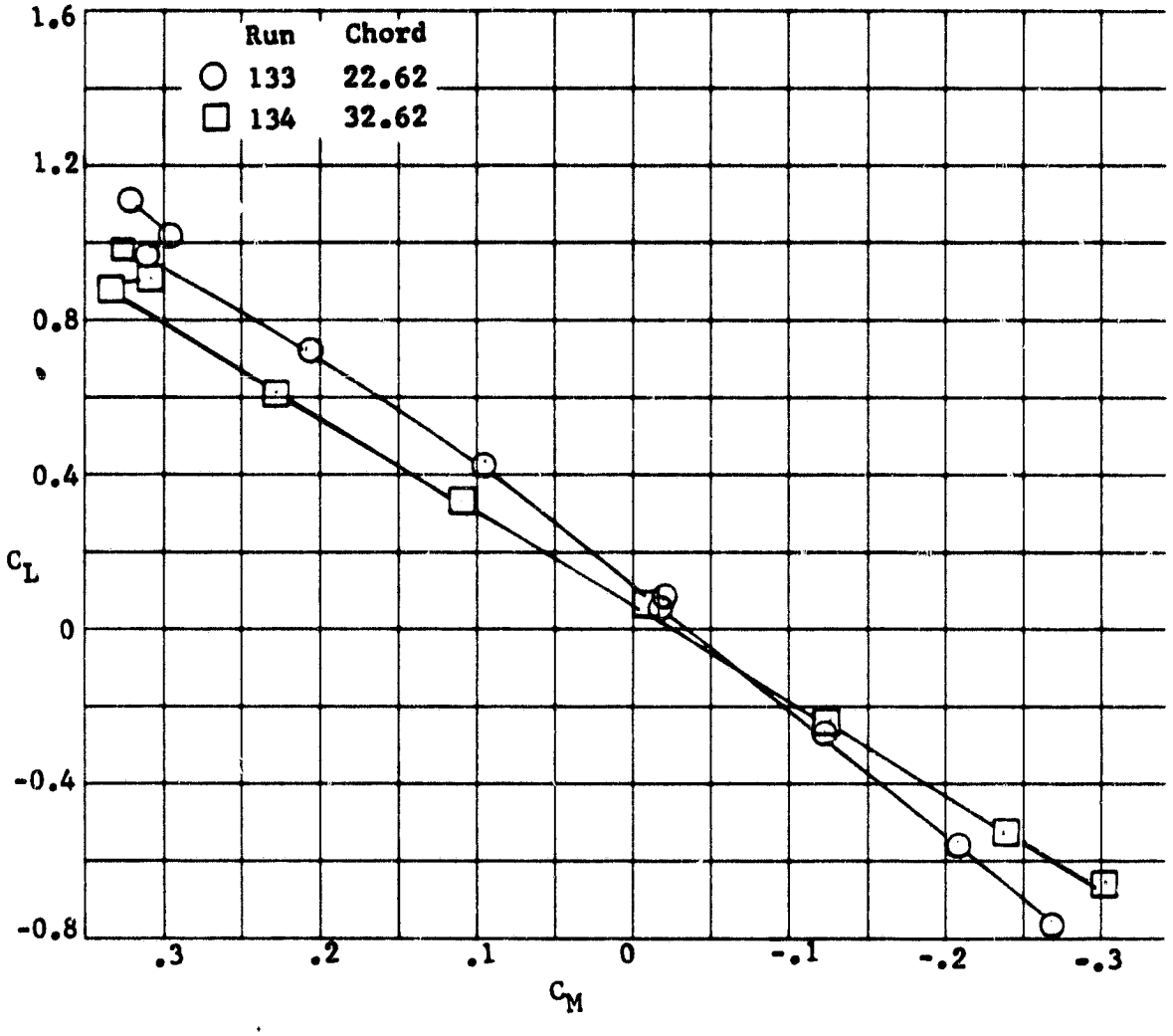

c. Lift vs Pitching Moment

Figure 28. Continued

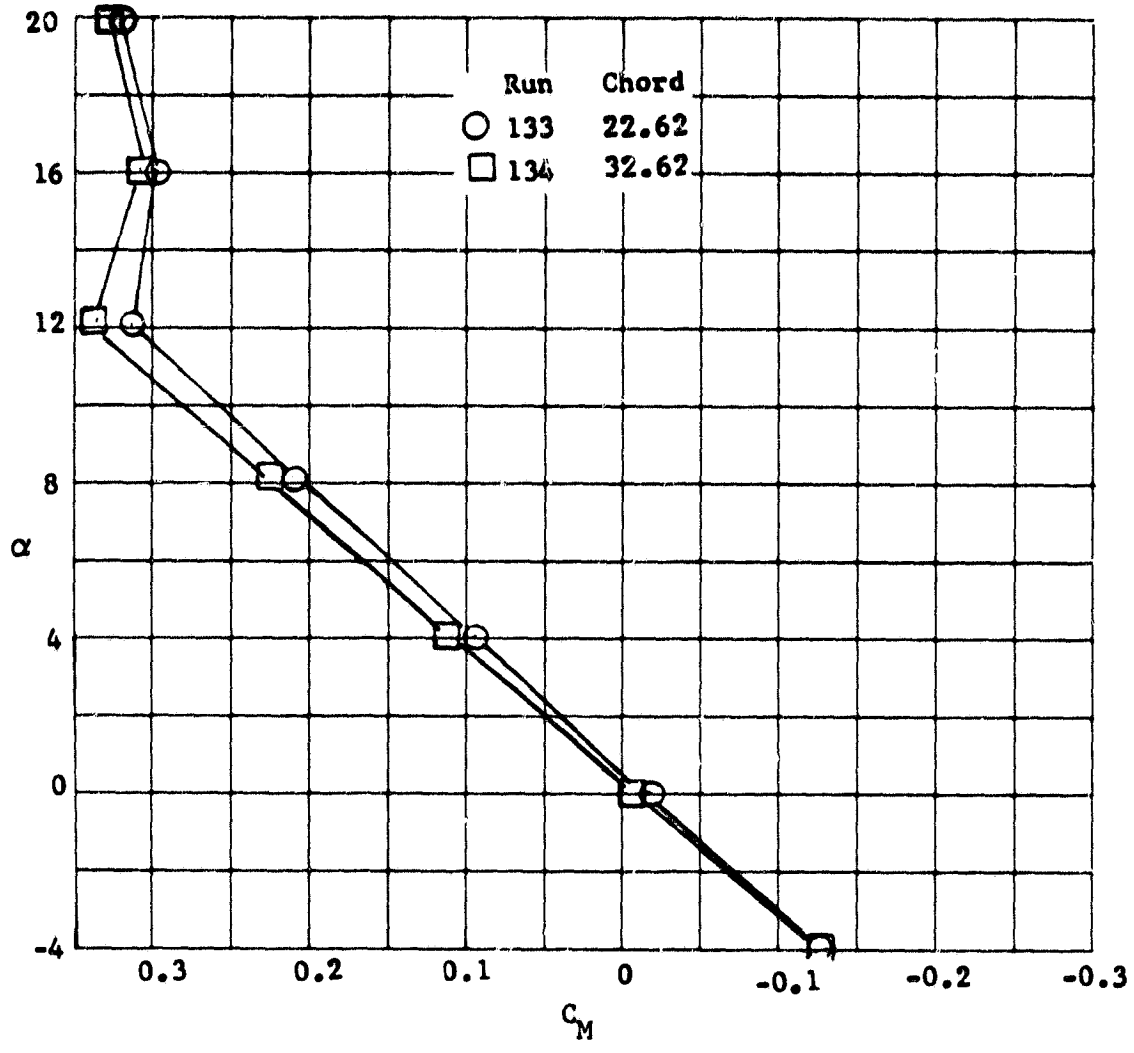

d. α vs Pitching Moment

Figure 28. Concluded

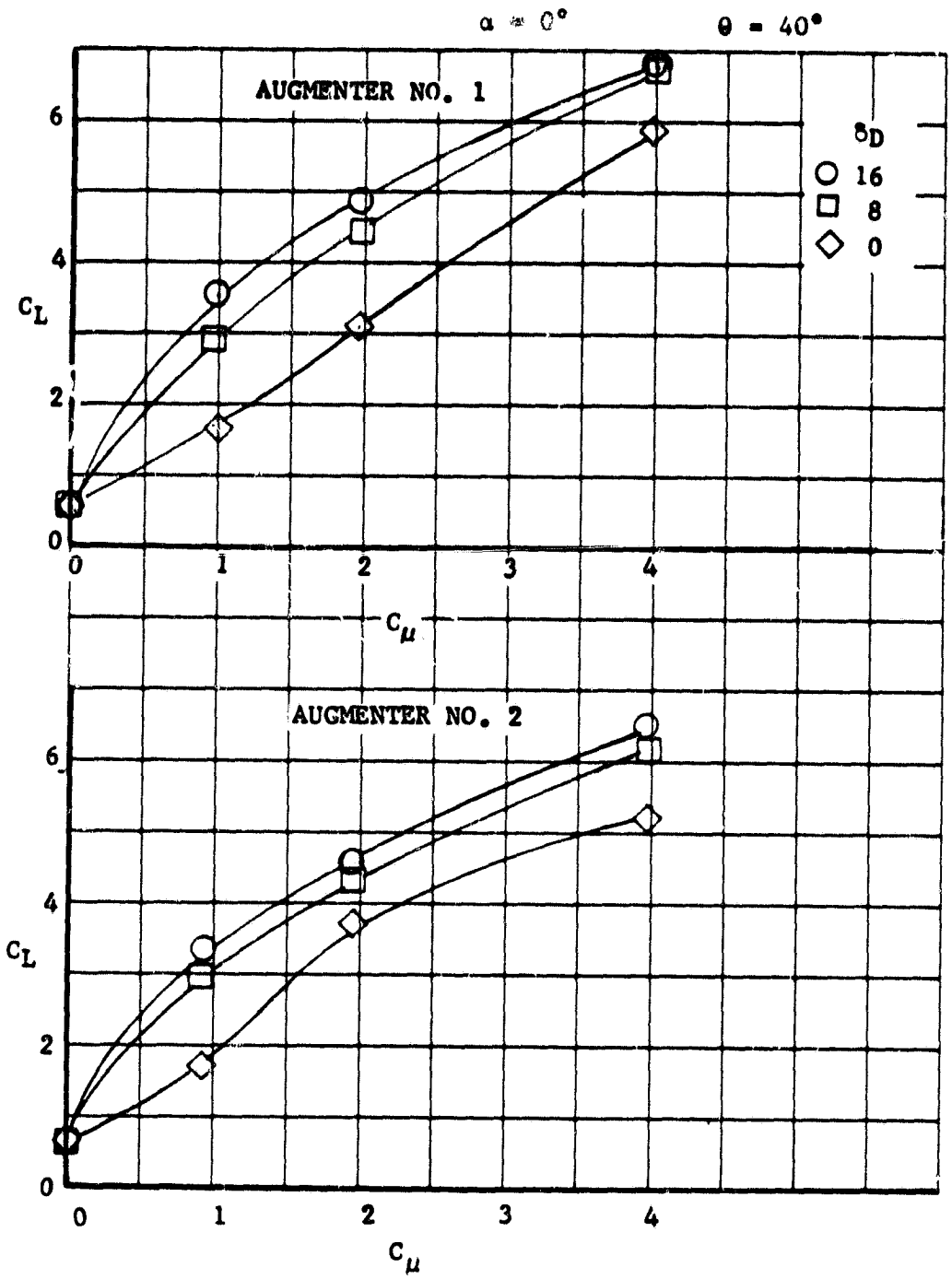

Figure 29. Variation of Lift Coefficient with Blowing Momentum Coefficient (C_μ)

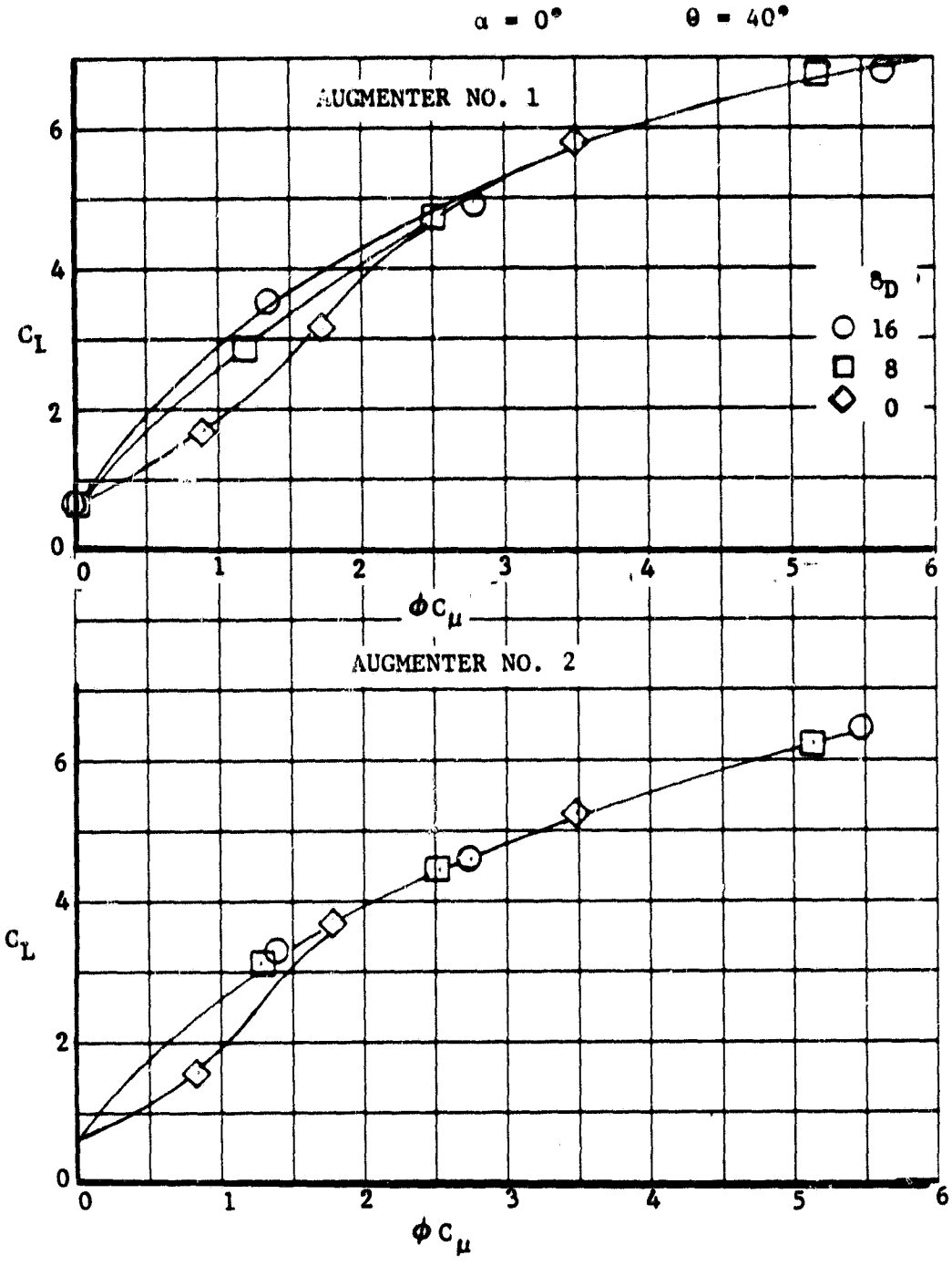

Figure 30. Variation of Lift with Augmented Blowing Momentum Coefficient (ϕC_μ)

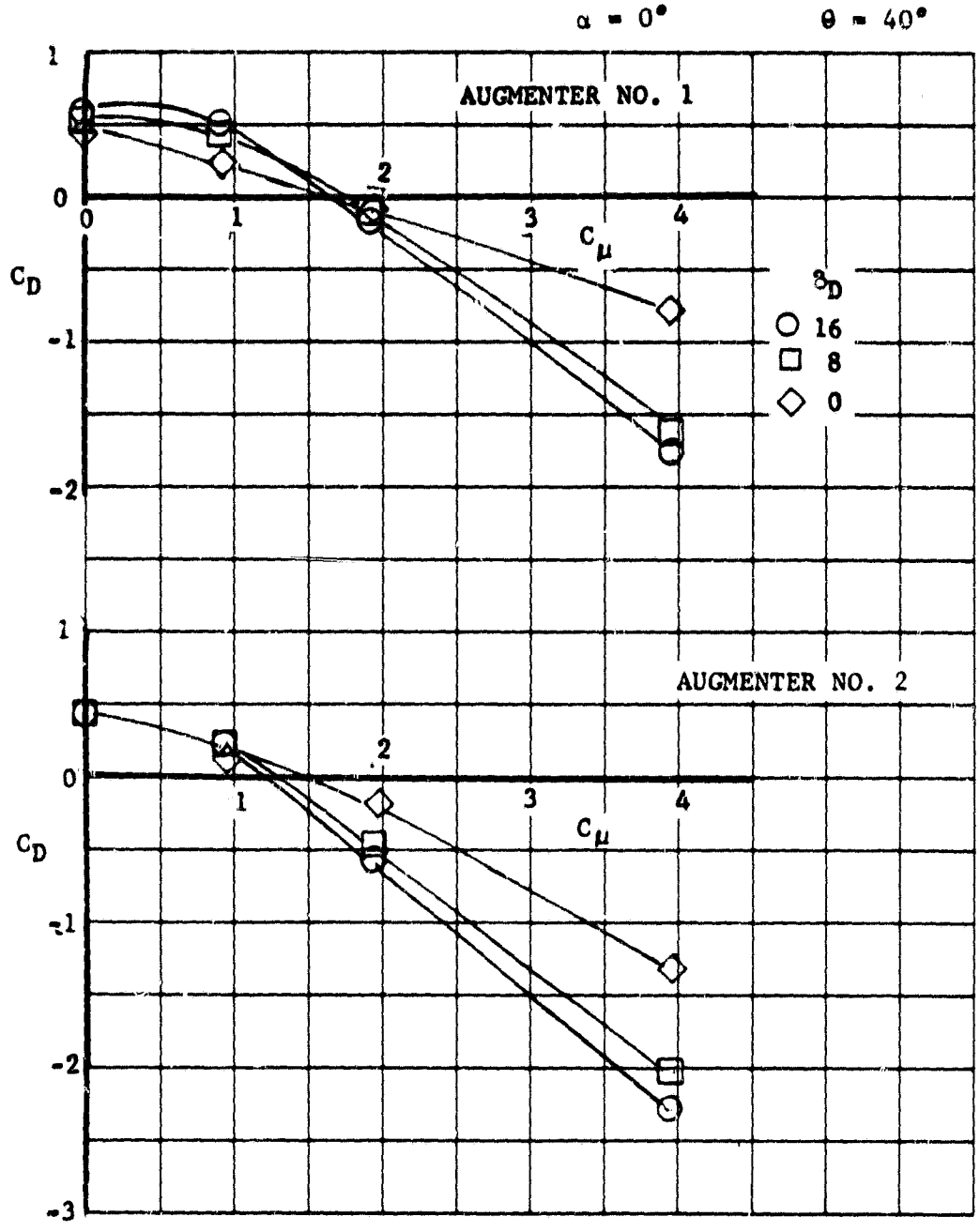

Figure 31. Variation of Drag Coefficient with Blowing Momentum Coefficient (C_μ)

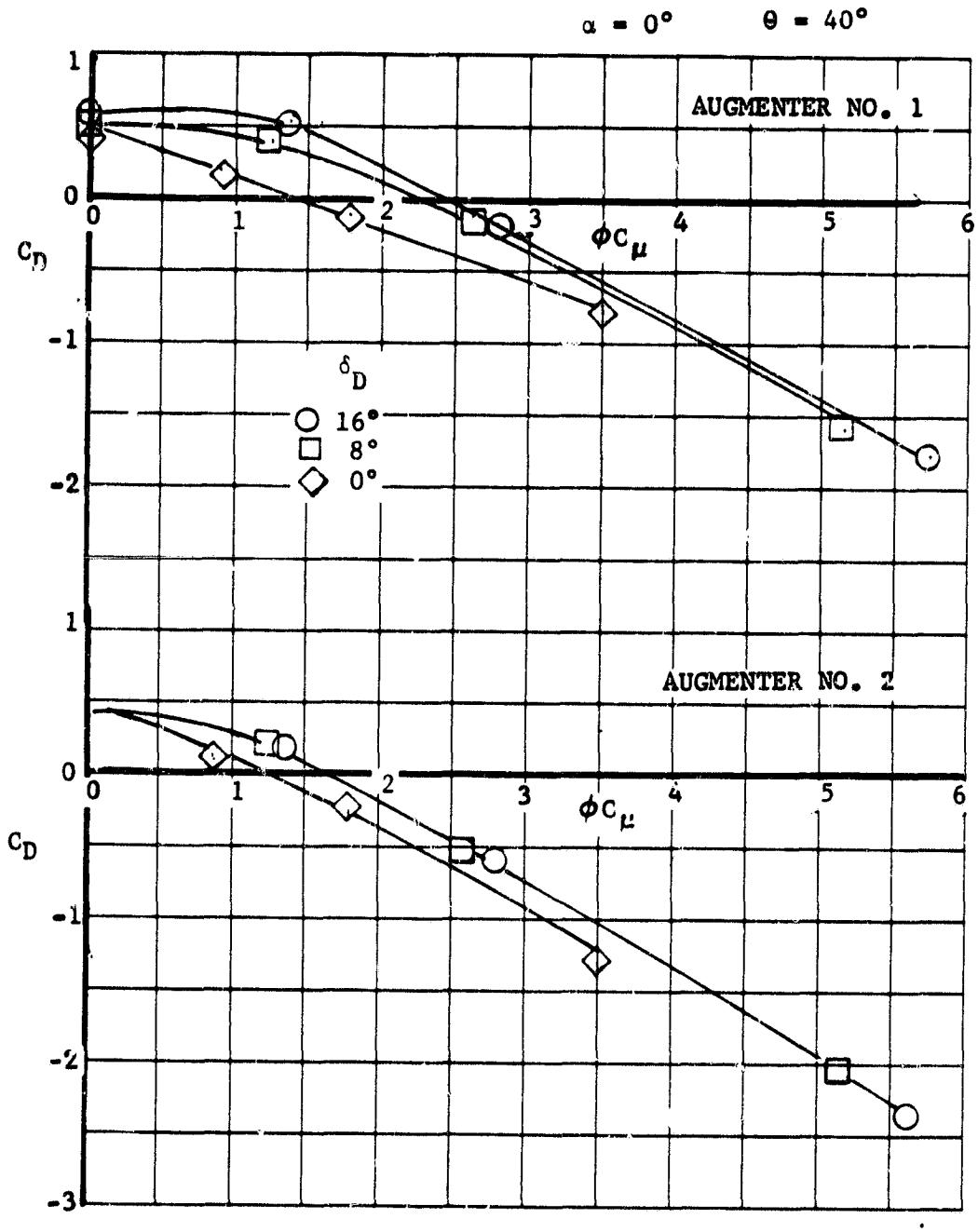

Figure 32. Variation of Drag Coefficient with Augmented Blowing Momentum Coefficient (ϕC_μ)

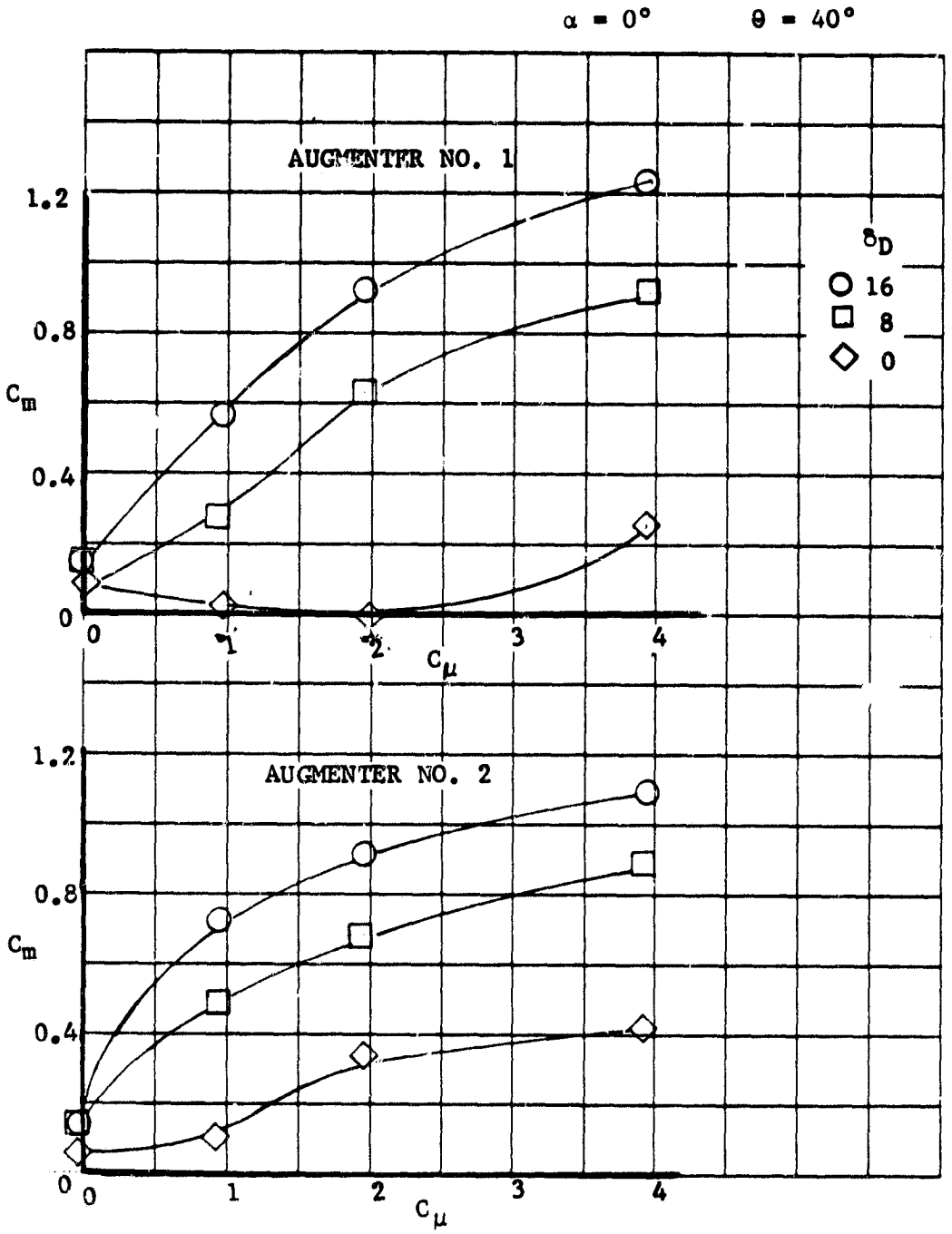

Figure 33. Variation of Pitching Moment Coefficient with Blowing Momentum Coefficient (C_μ)

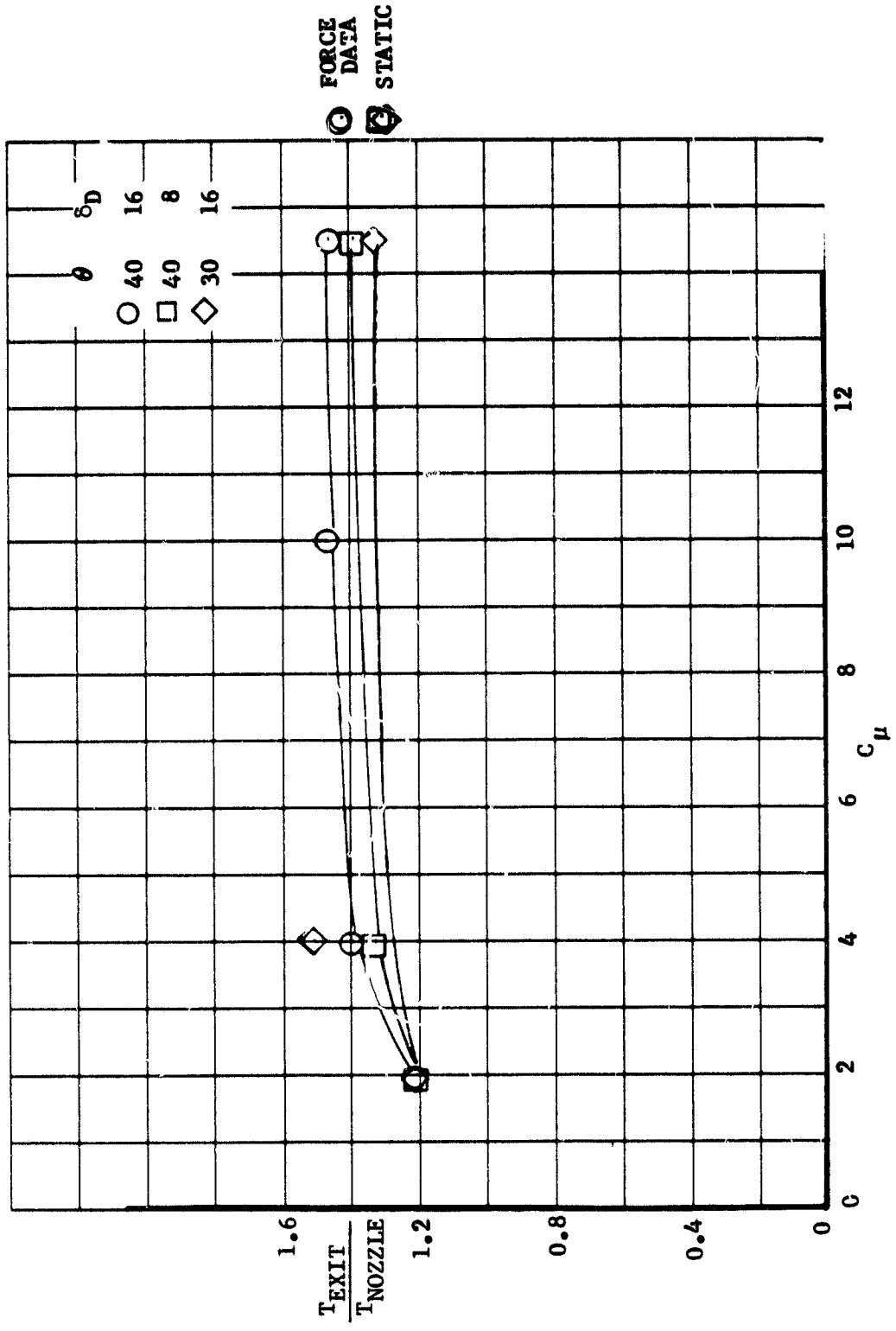

Figure 34. Variation of Exit Thrust with Blowing Momentum Coefficient

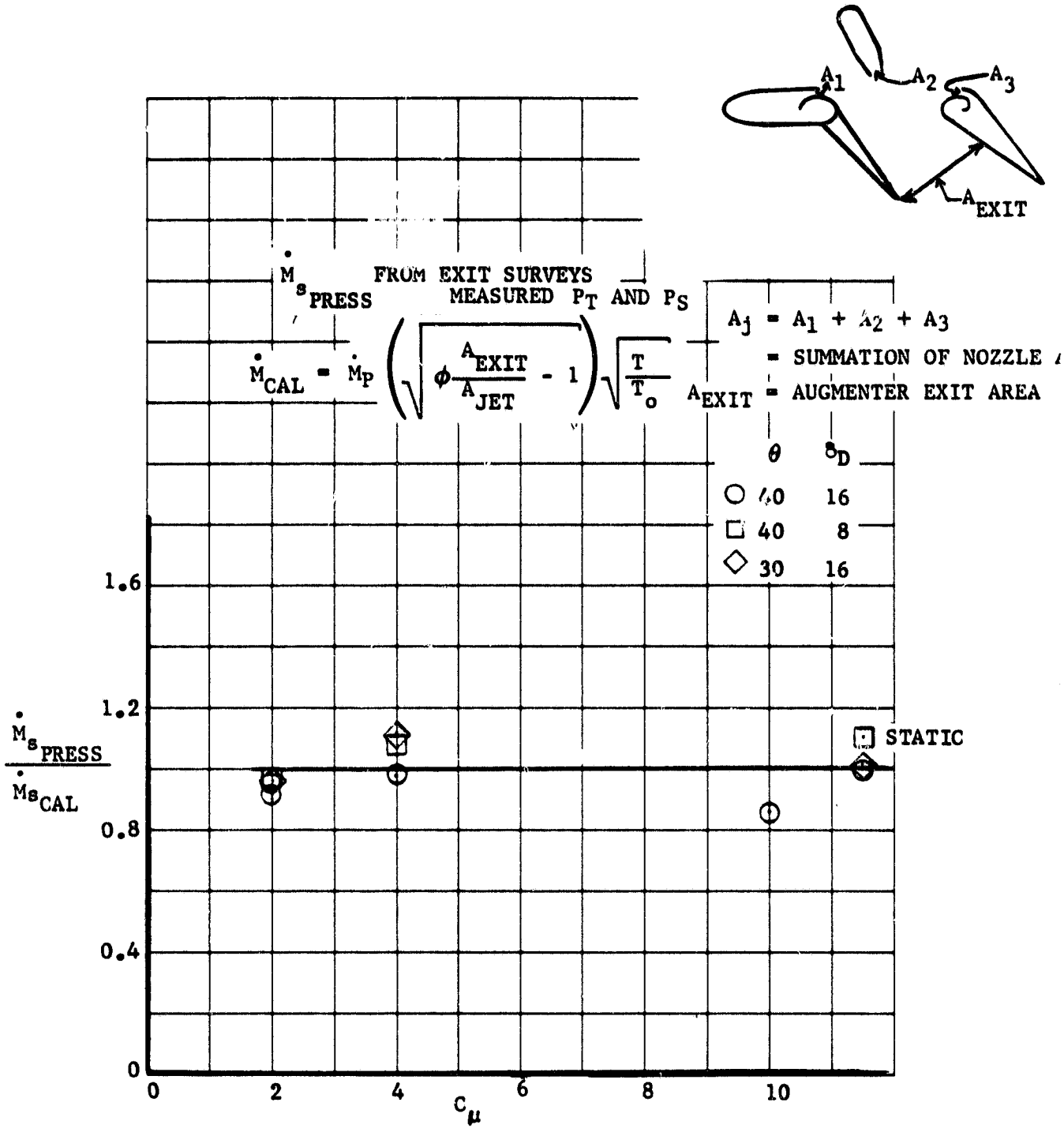

Figure 35. Variation of Secondary Mass Flow with Momentum Coefficient

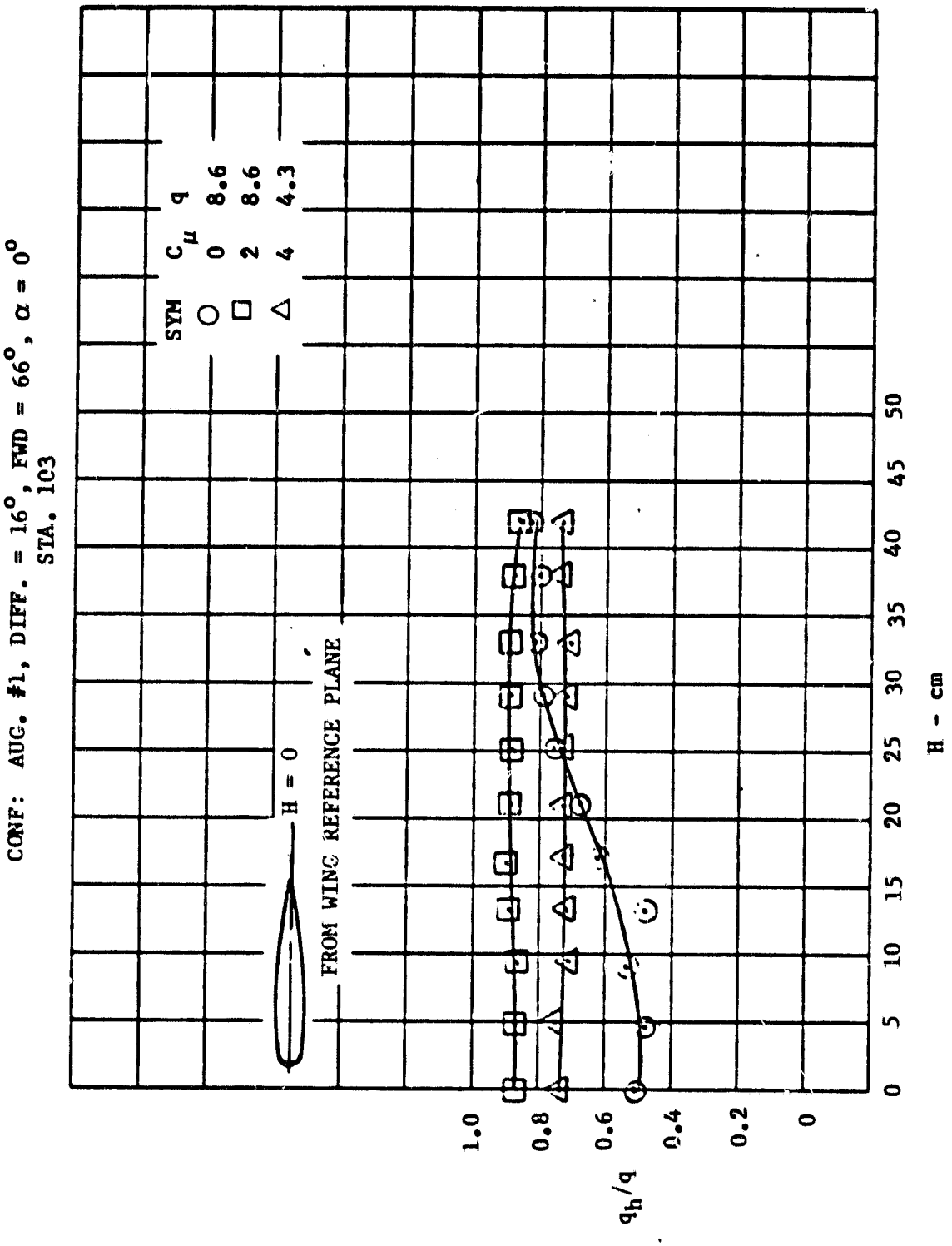

Figure 36. Variation of Dynamic Pressure Behind the Augmenter with Height

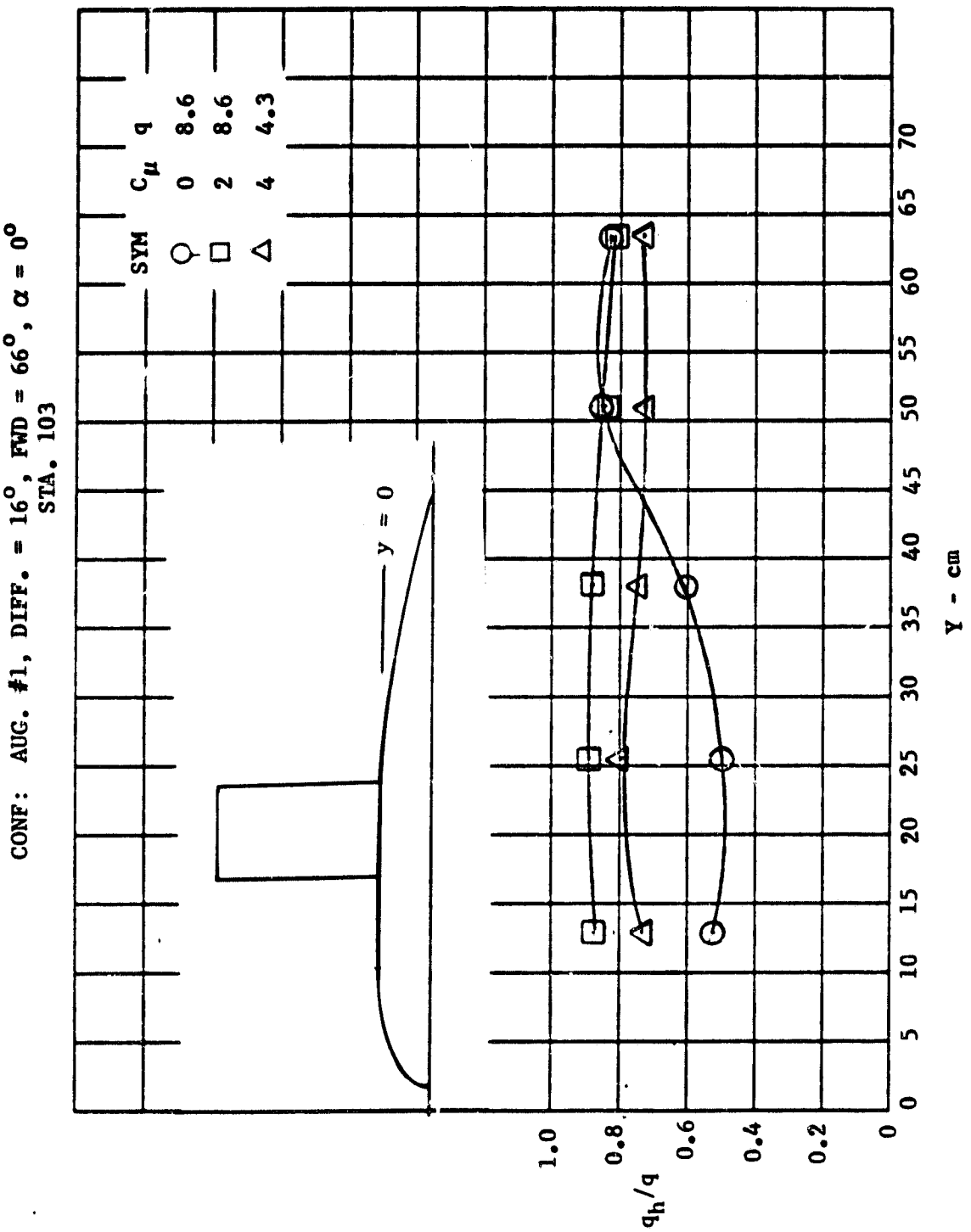

Figure 37. Variation of Dynamic Pressure Behind the Augmenter with Span

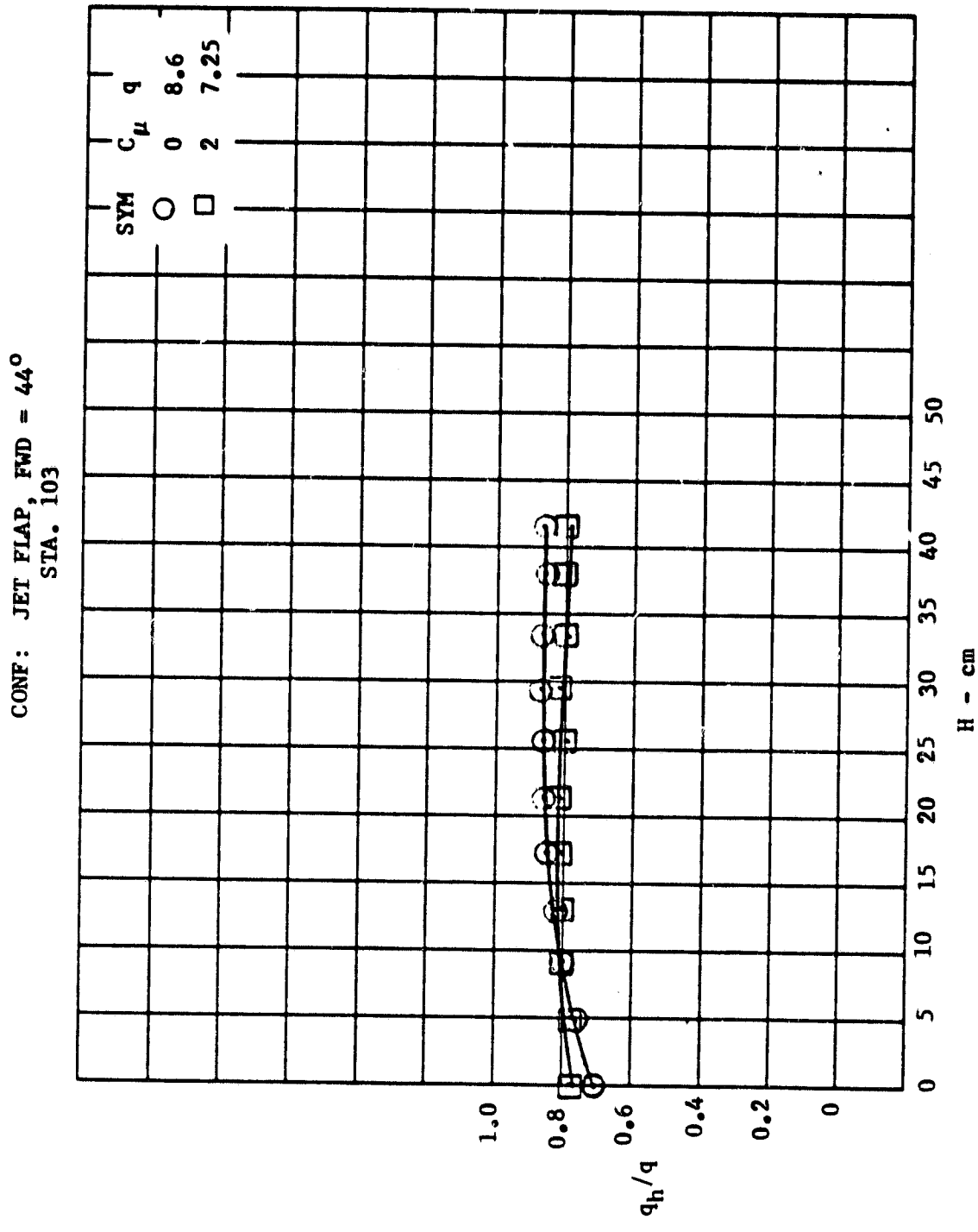

Figure 38. Variation of Dynamic Pressure Behind the Jet Flap with Height

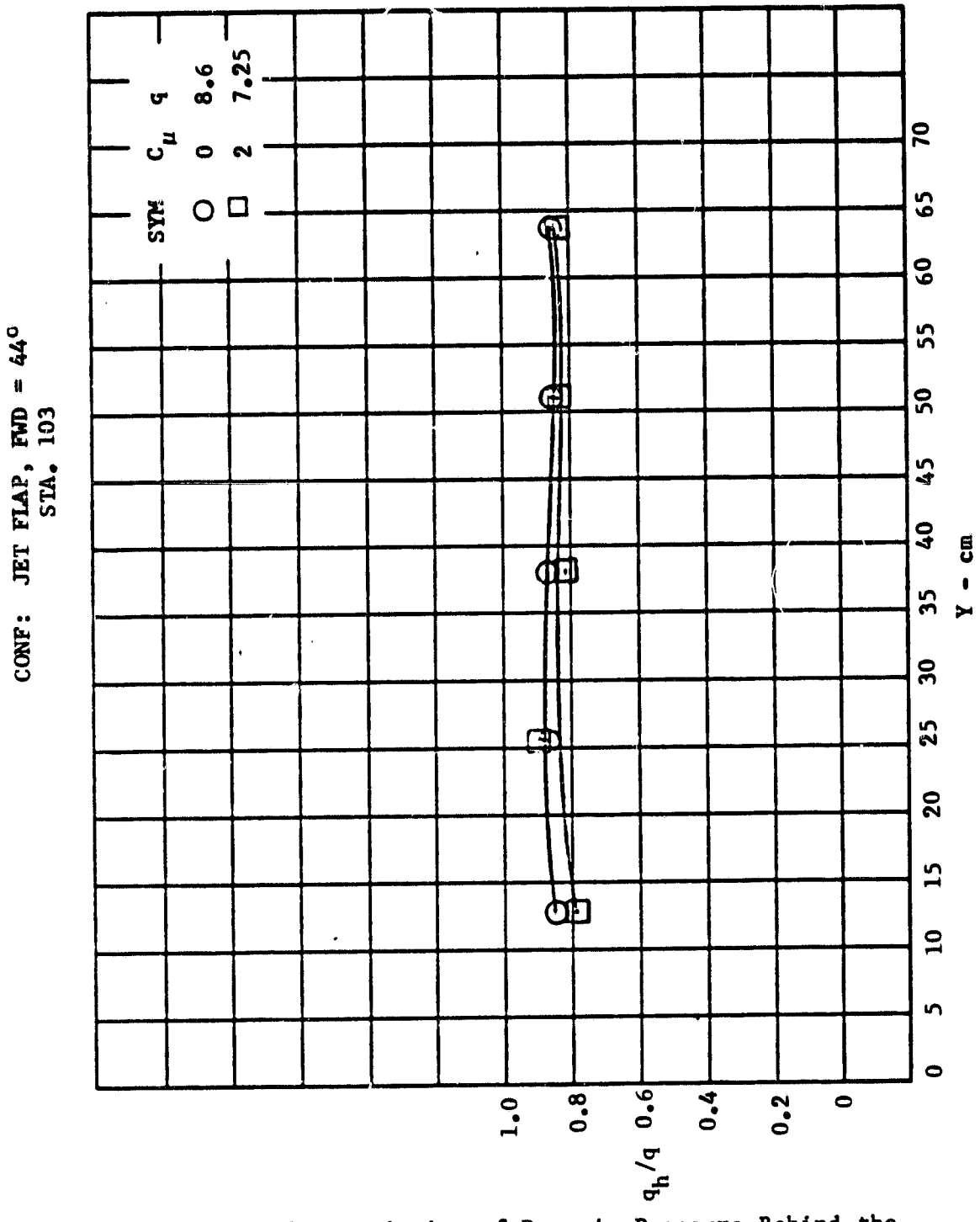

Figure 39. Variation of Dynamic Pressure Behind the Jet Flap with Span

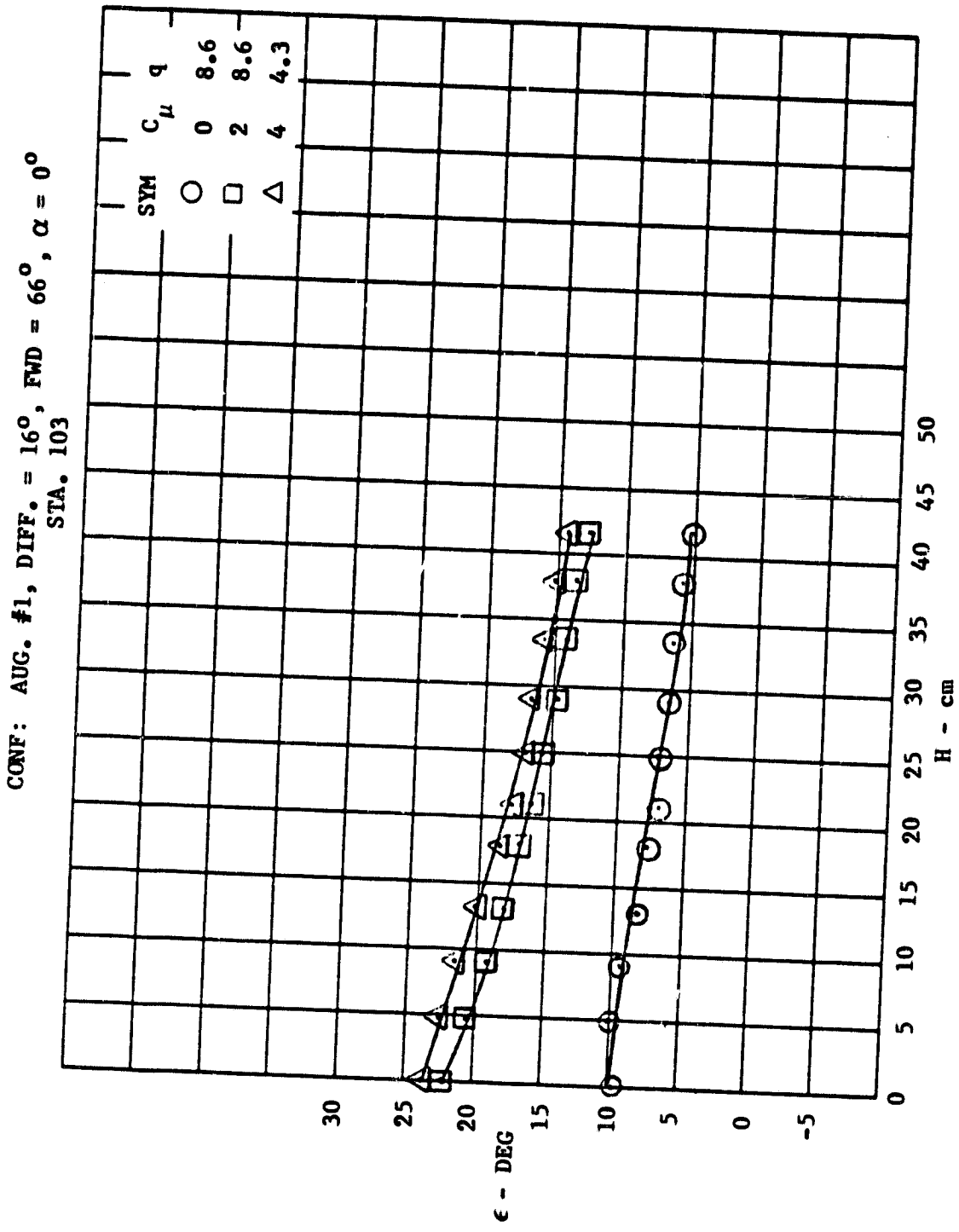

Figure 40. Variation of Downwash Angle Behind the Augmenter with Height

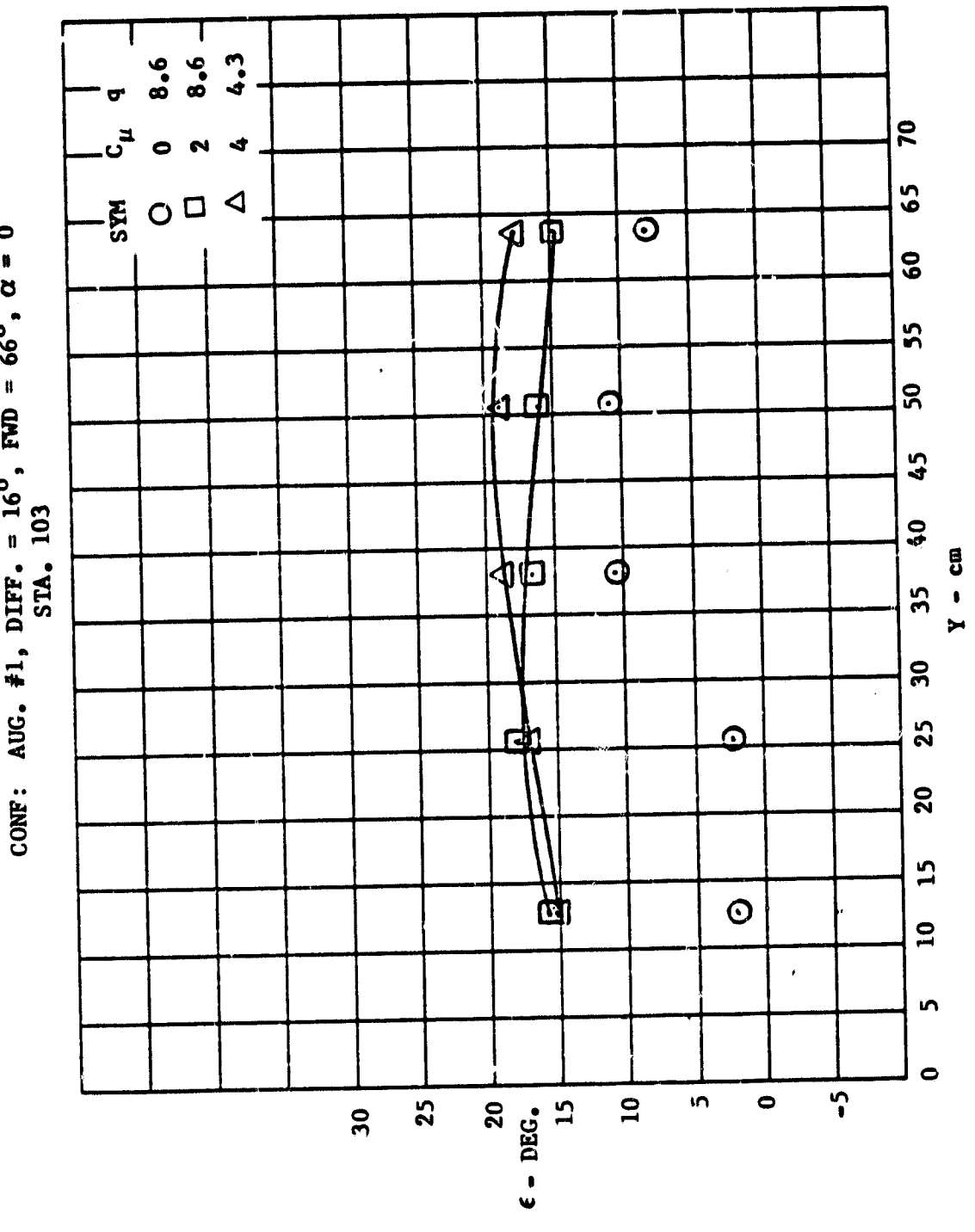

Figure 41. Variation of Downwash Angle Behind the Augmenter with Span

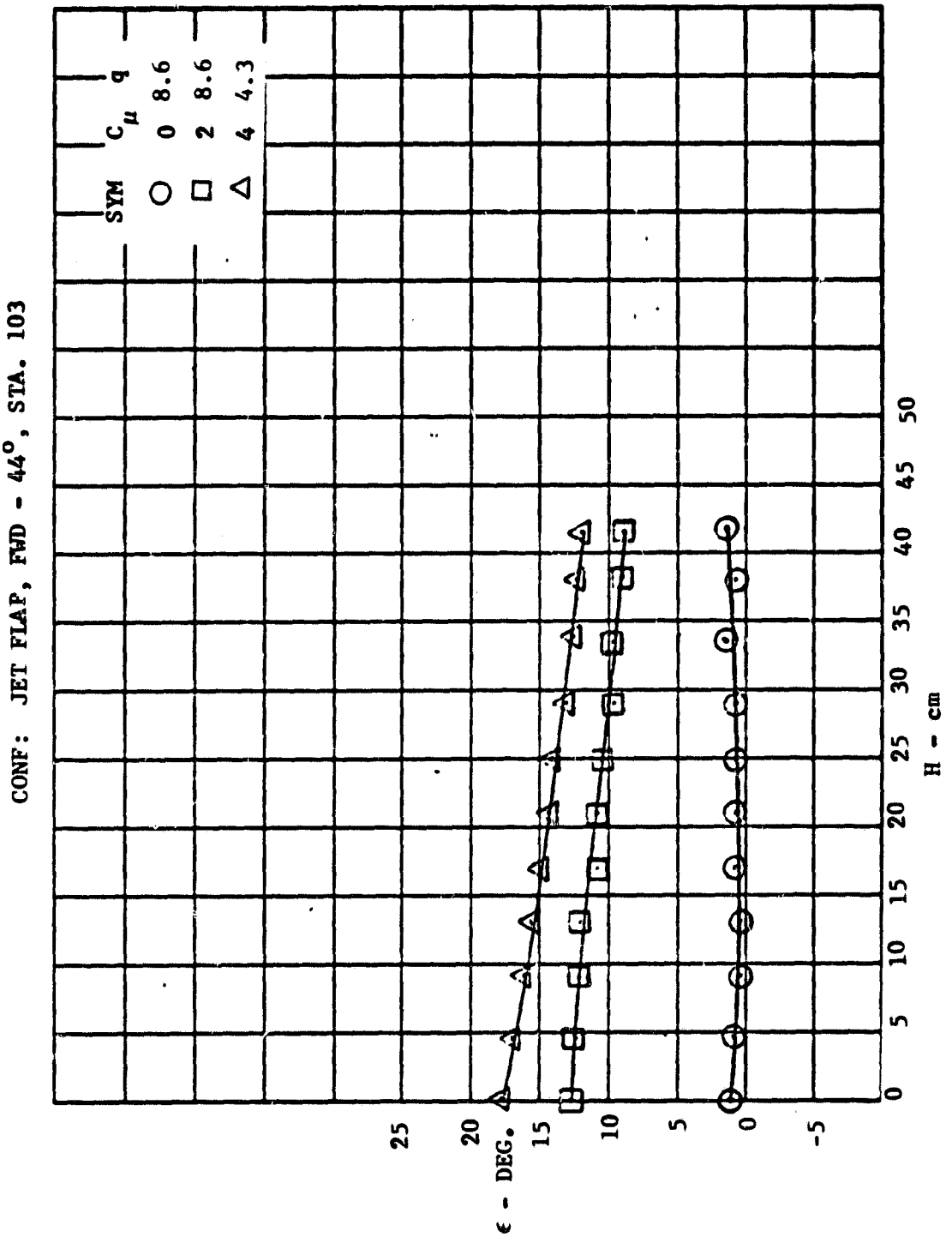

Figure 42. Variation of Downwash Angle Behind the Jet Flap with Height, Aft Location

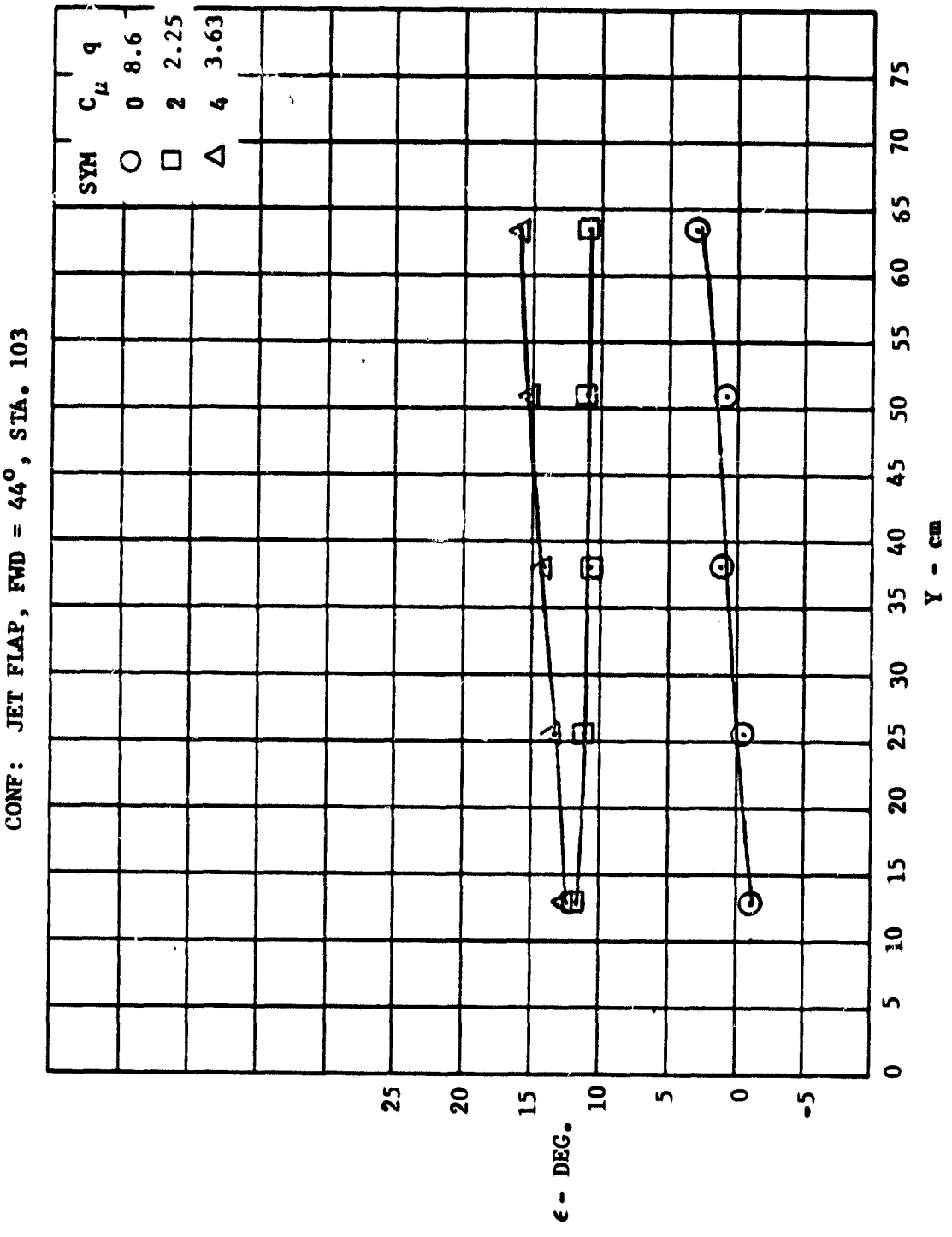

Figure 43. Variation of Downwash Angle Behind the Jet Flap with Span, Aft Location

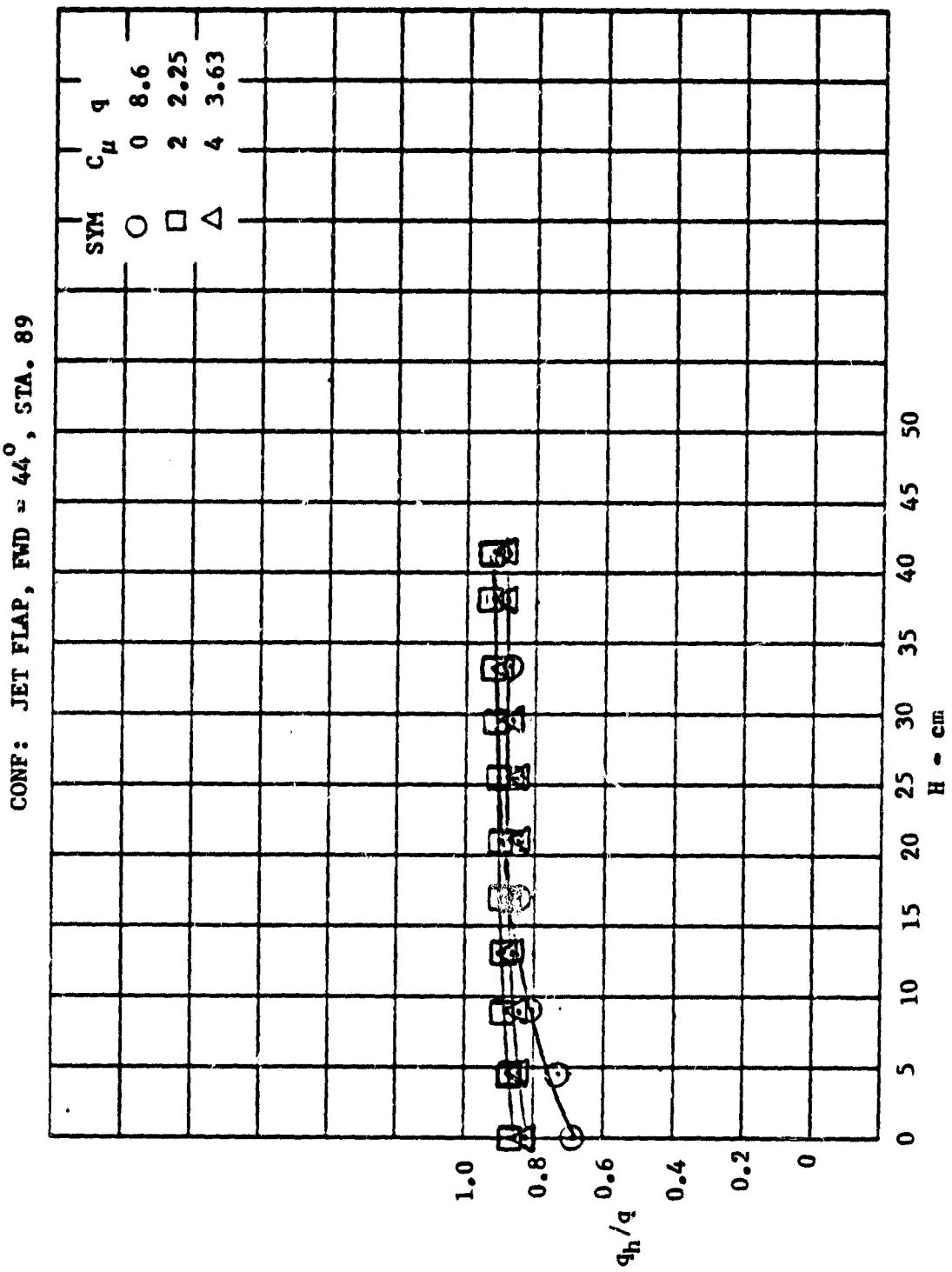

Figure 44. Variation of Downwash Angle Behind the Jet Flap with Height, Forward Location

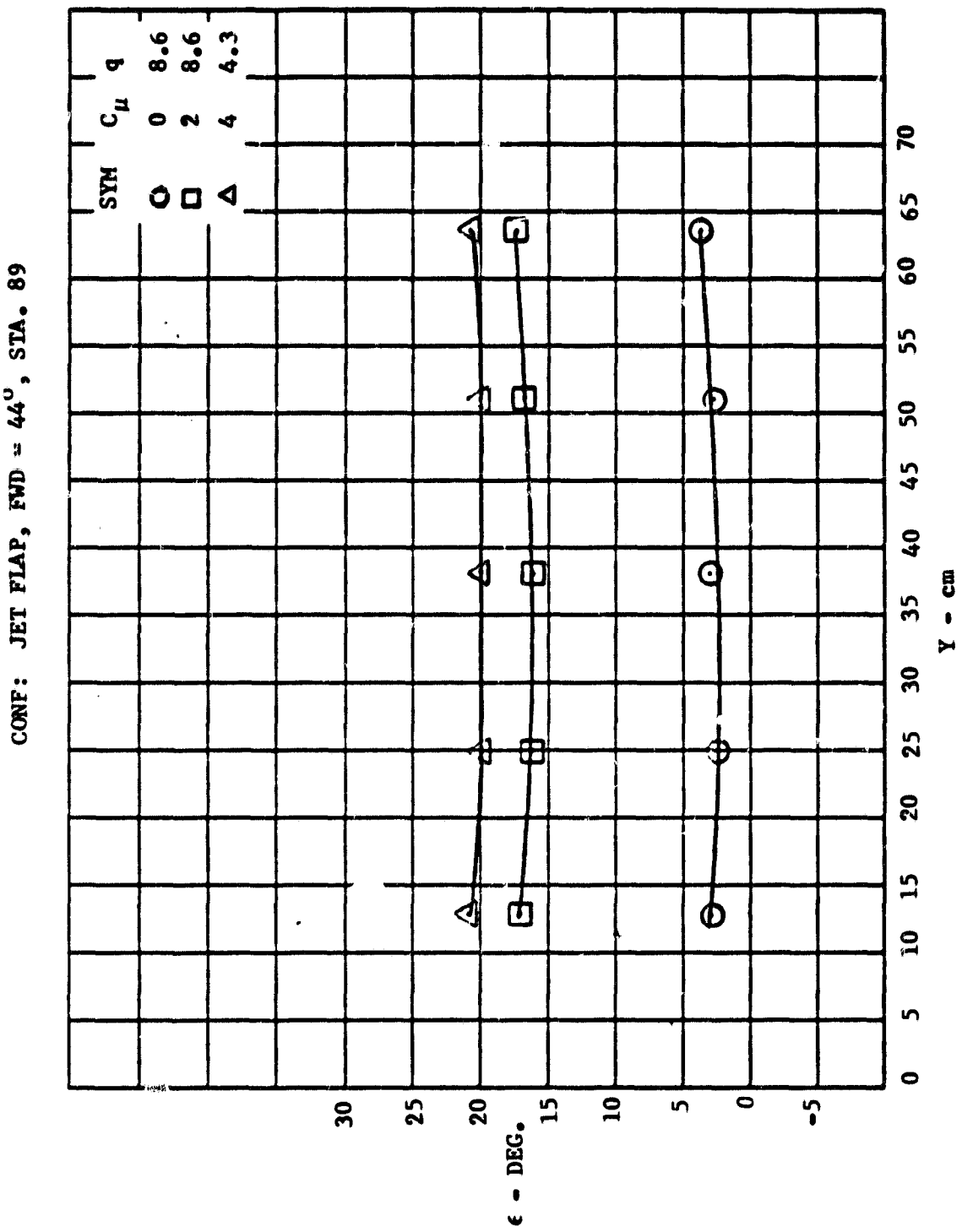

Figure 45. Variation of Downwash Angle Behind the Jet Flap with Span, Forward Location

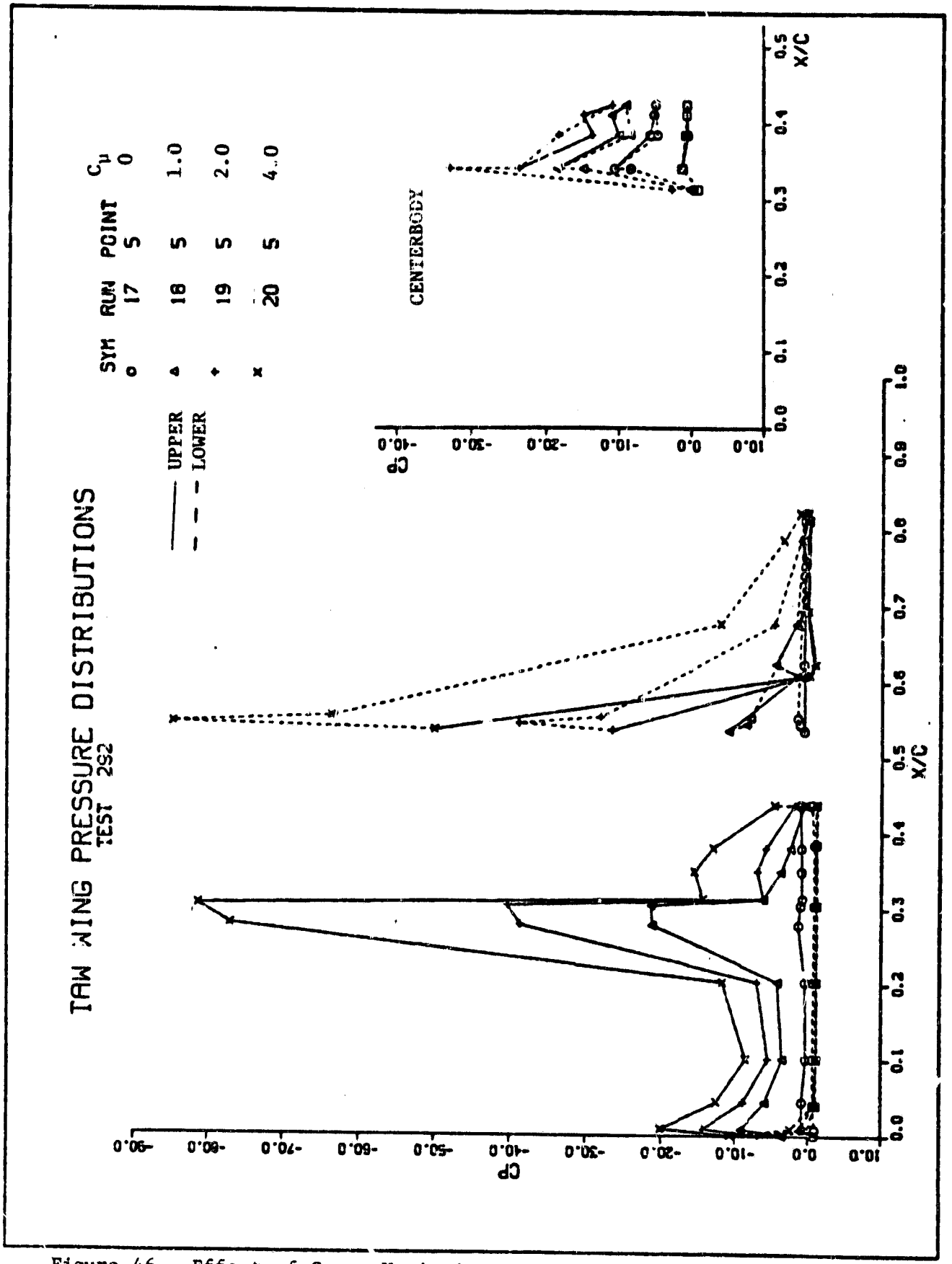

Figure 46. Effect of C_μ on Variation of Chordwise Surface Pressure Distribution, Augmenter 1, $\alpha = 0$

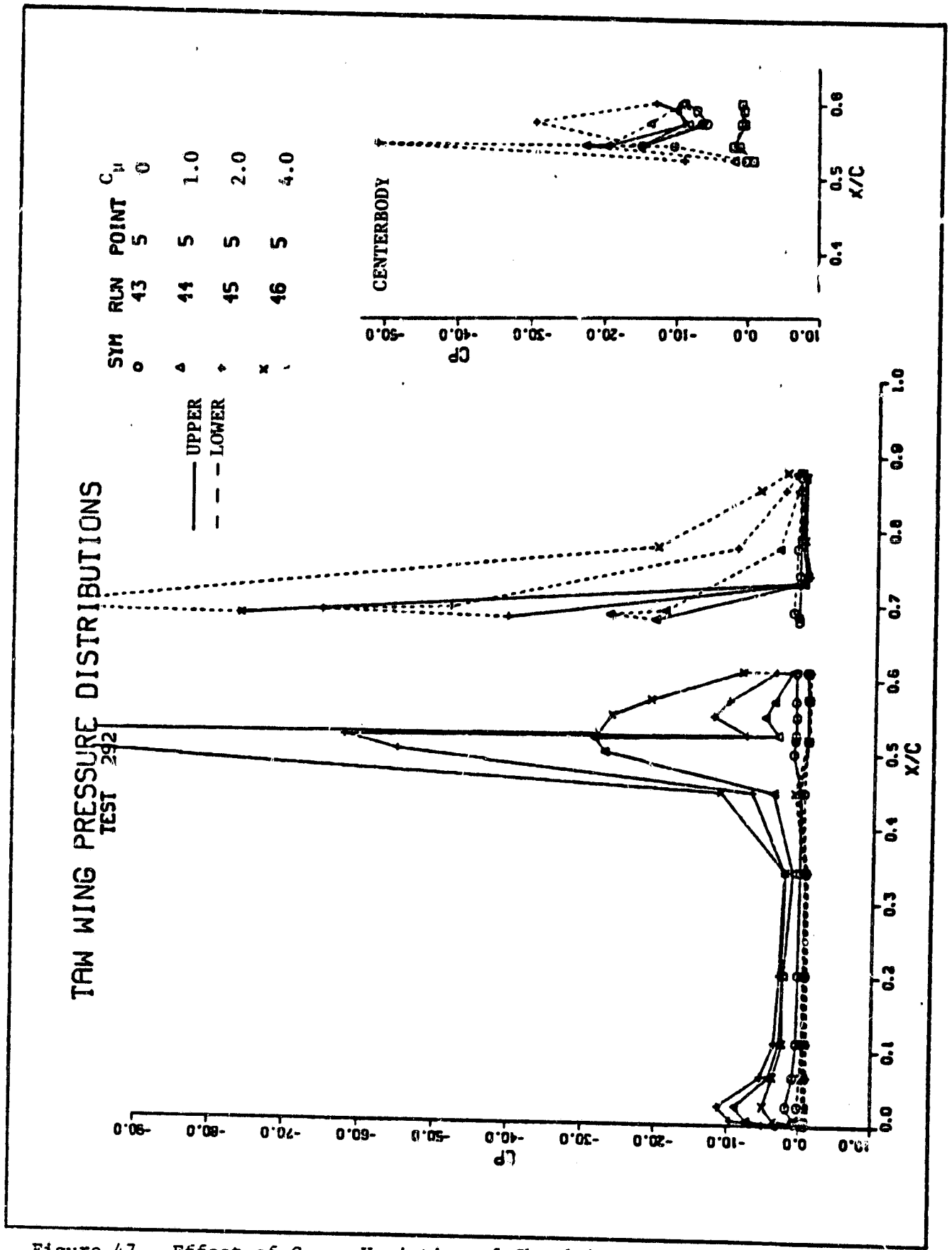

Figure 47. Effect of C_μ on Variation of Chordwise Surface Pressure Distribution, Augmenter 2, α = 0

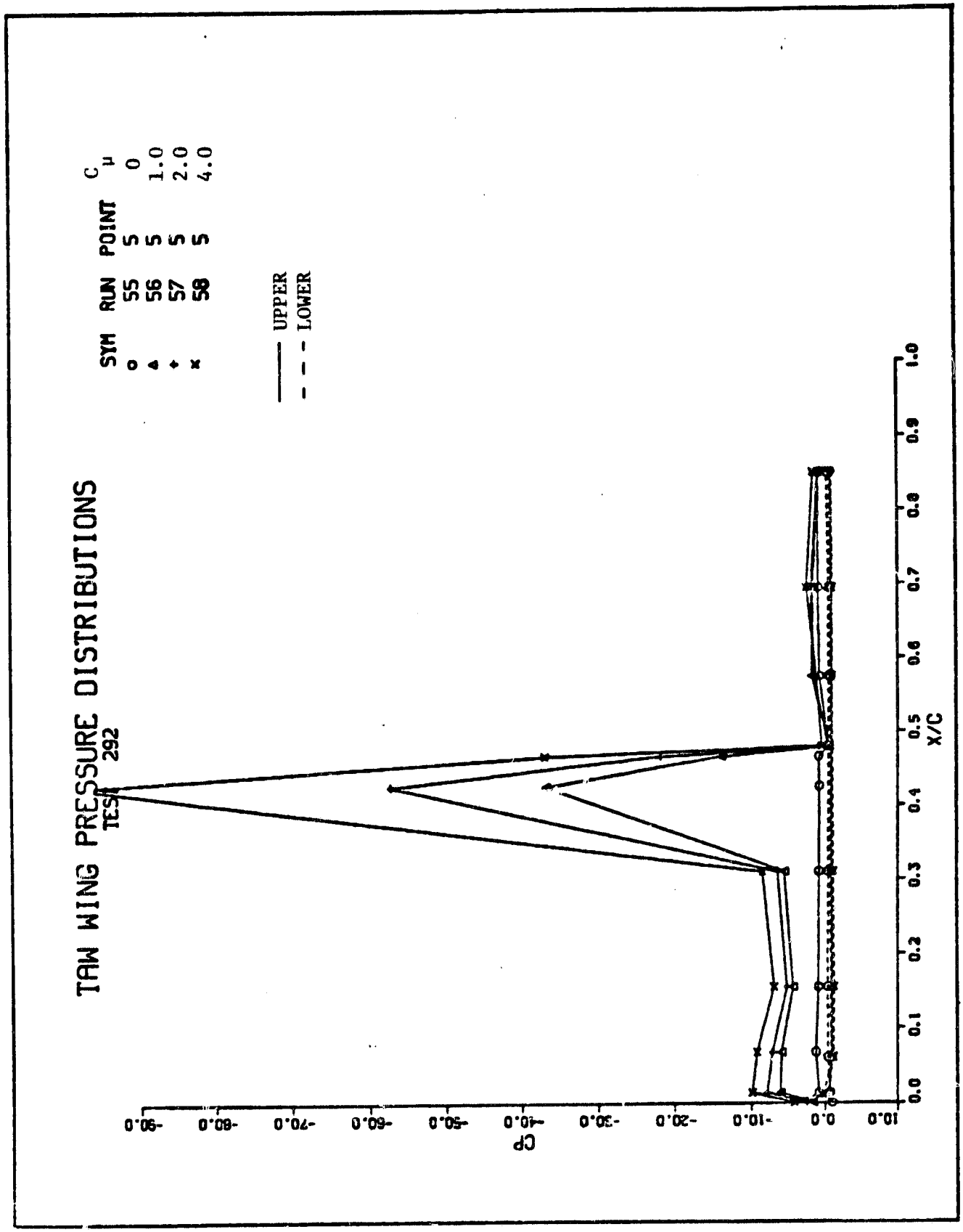

Figure 48 Effect of C_μ on Variation of Chordwise Surface Pressure Distribution, Jet Flap 1, $\alpha = 0$

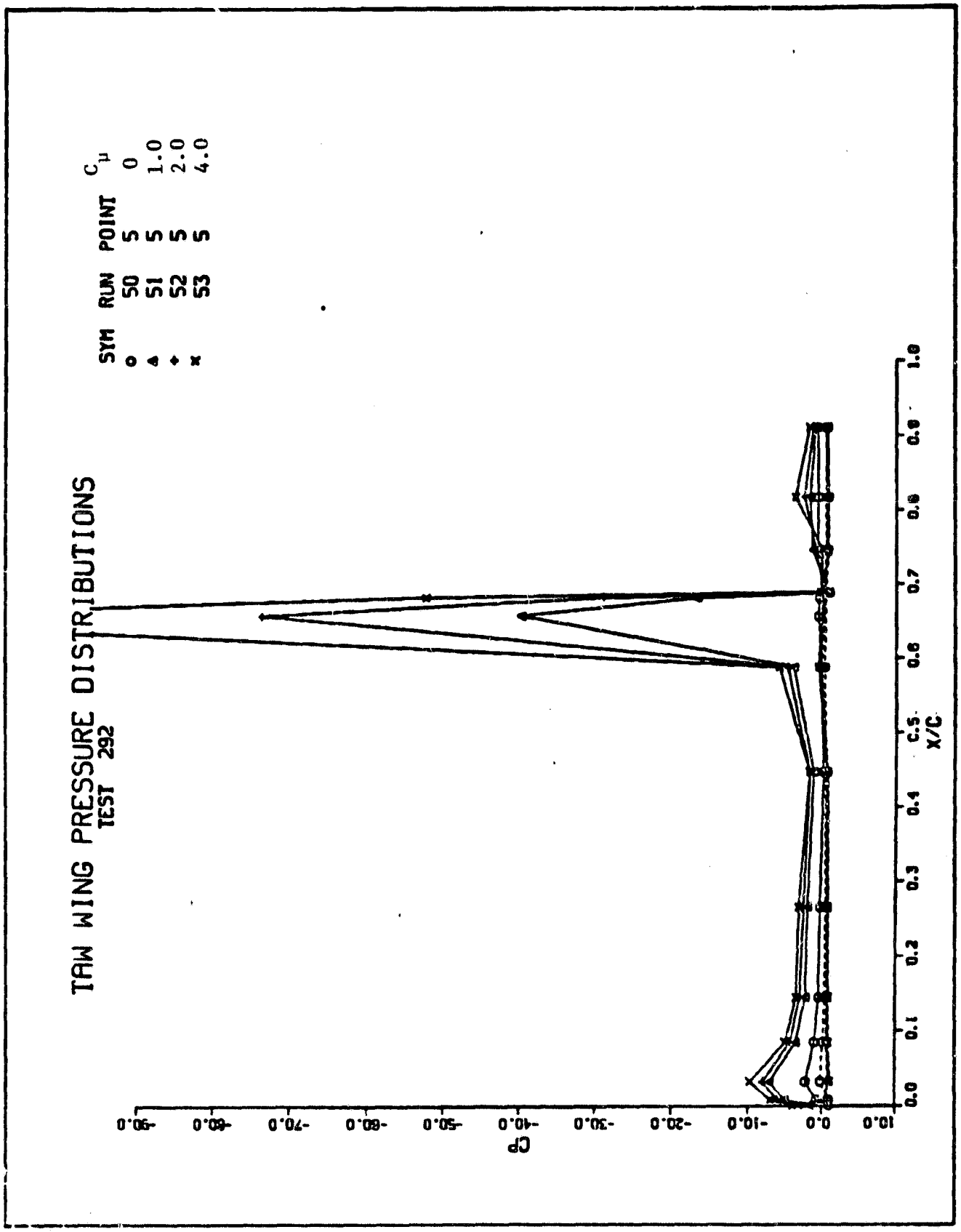

Figure 49 Effect of C_μ on Variation of Chordwise Surface Pressure Distribution, Jet Flap 2, $\alpha = 0$

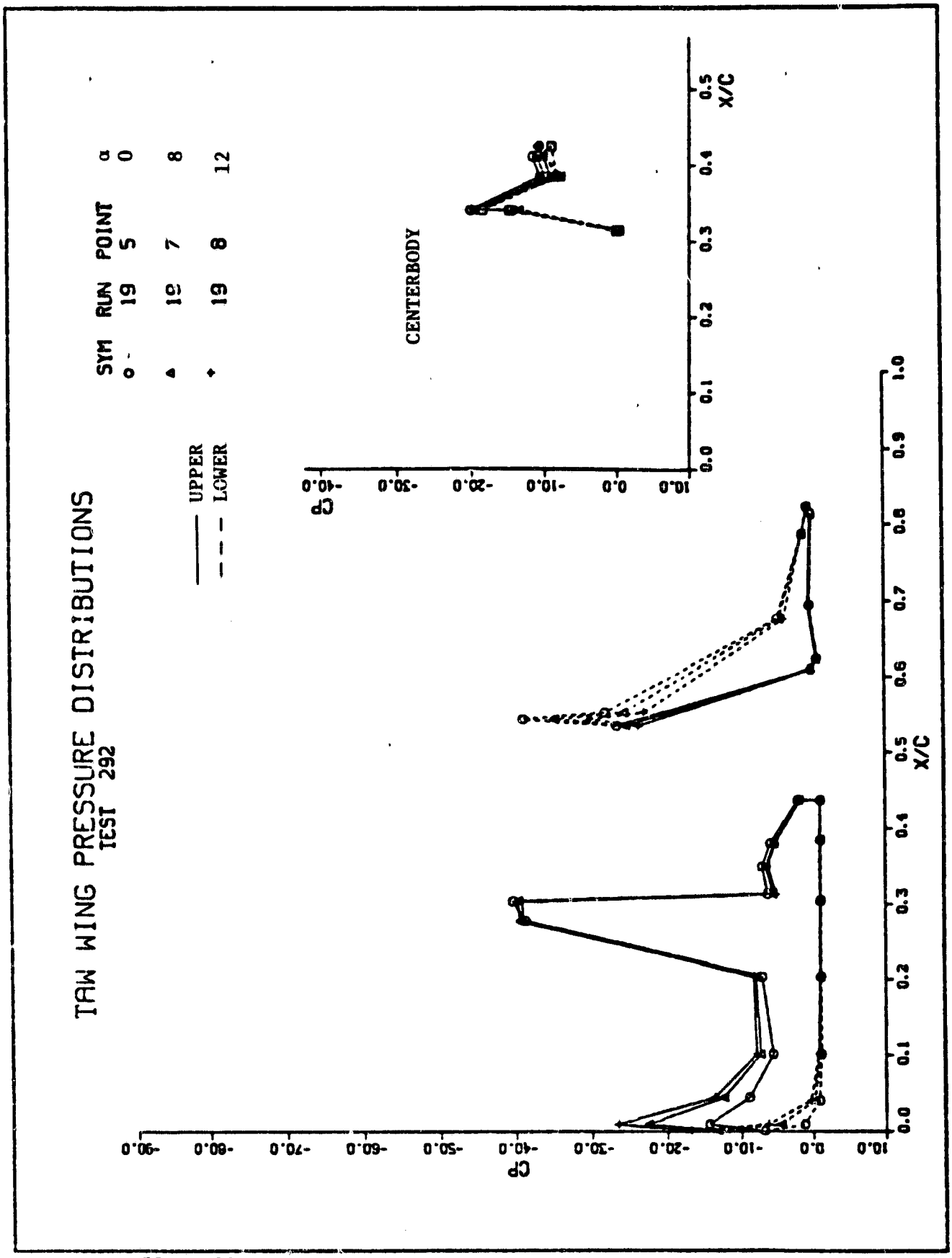

Figure 50. Effect of α on Variation of Chordwise Surface Pressure Distribution, Augmenter 1, C_μ = 2.0

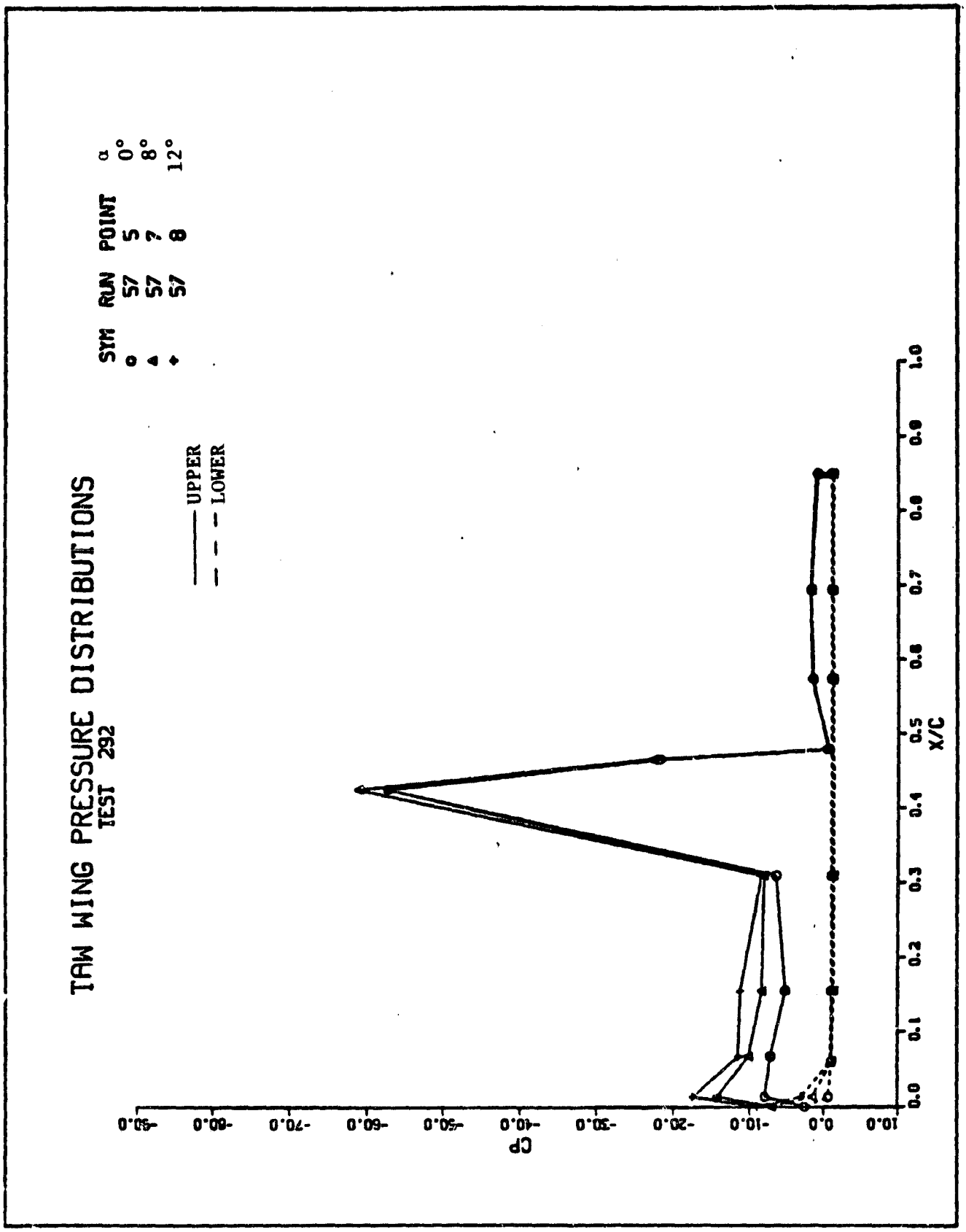

Figure 51 Effect of α on Variation of Chordwise Surface Pressure Distribution, Jet Flap 1, C_μ = 2.0

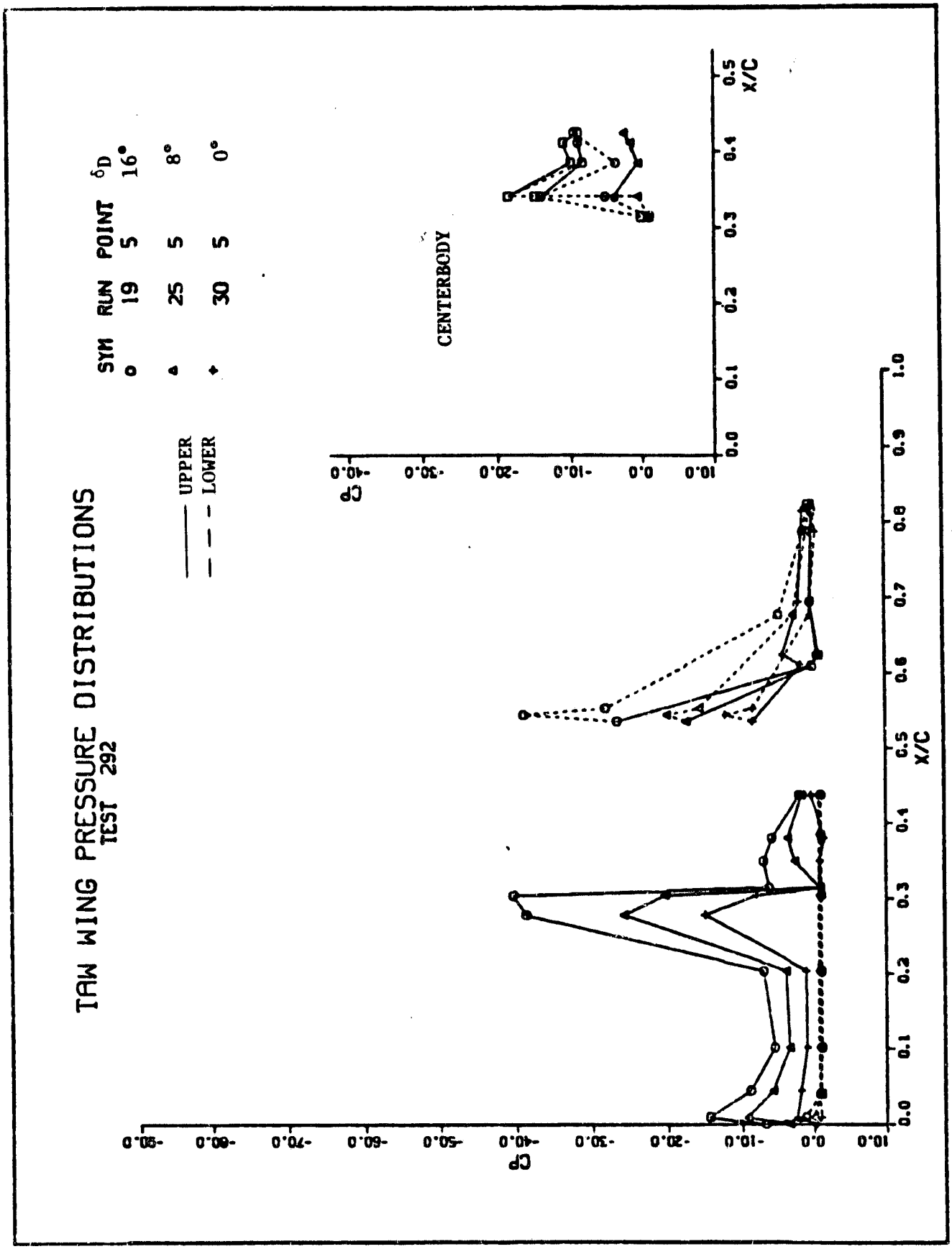

Figure 52 Effect of Diffuser Angle on Variation of Chordwise Surface Pressure Distribution, Augmenter 1, C_μ = 2.0, α = 0

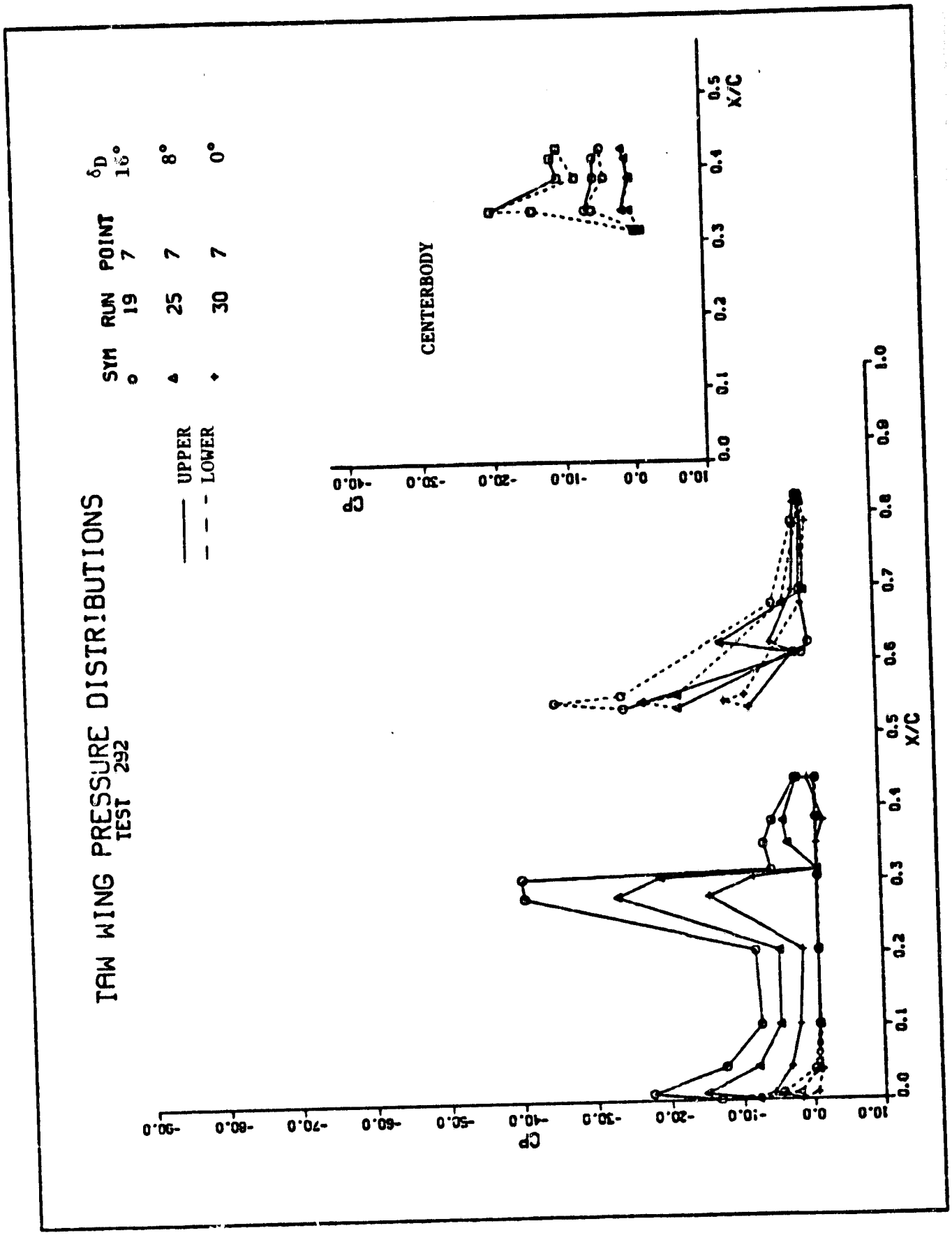

Figure 53 Effect of Diffuser Angle on Variation of Chordwise Surface Pressure Distribution, Augmenter 1, C_μ = 2.0, α = 8°

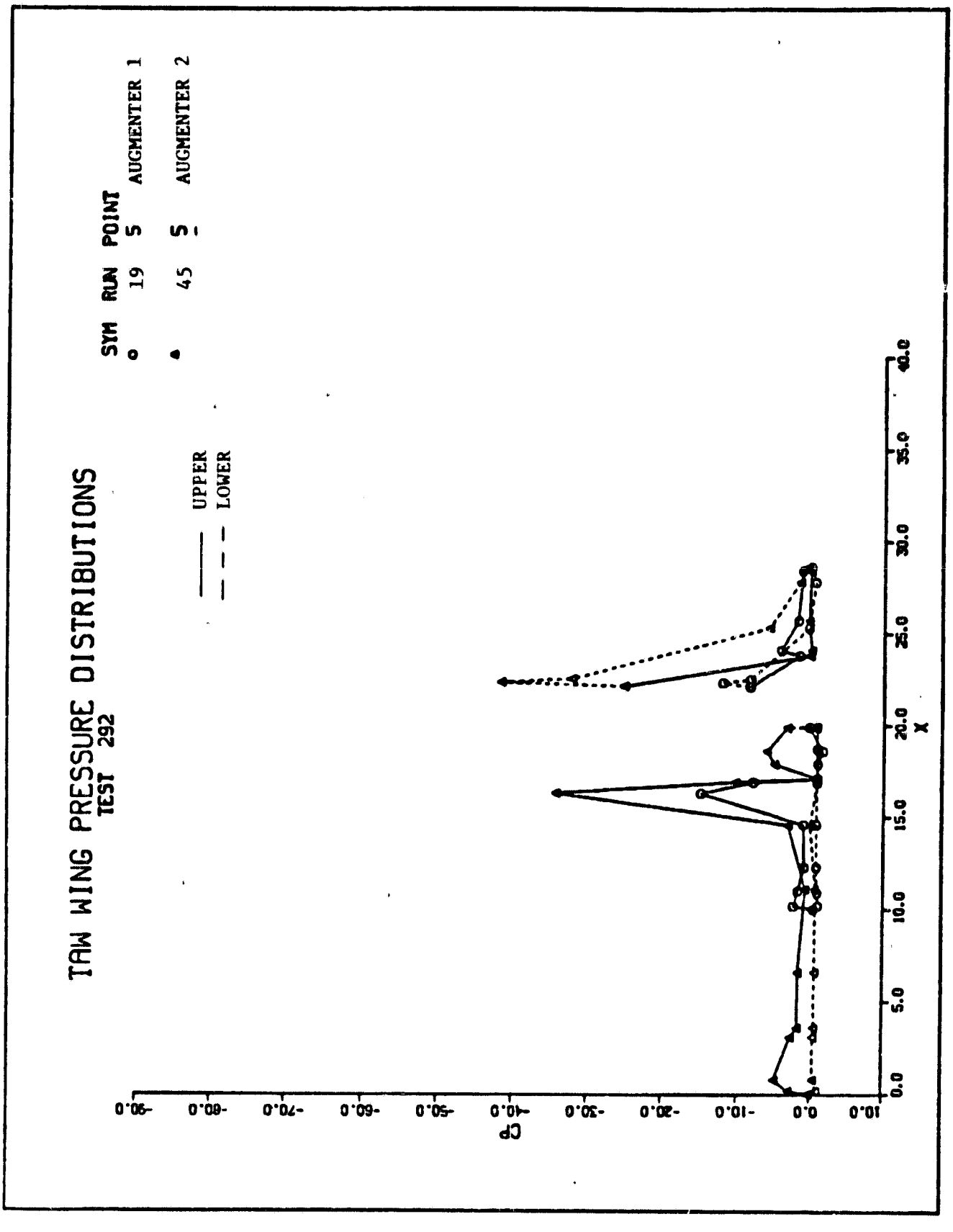

Figure 54 Effect of Nose Length on Augmenter Chordwise Surface Pressure Distributions, $\alpha = 0$, $C_\mu = 2.0, \delta_D = 16°$

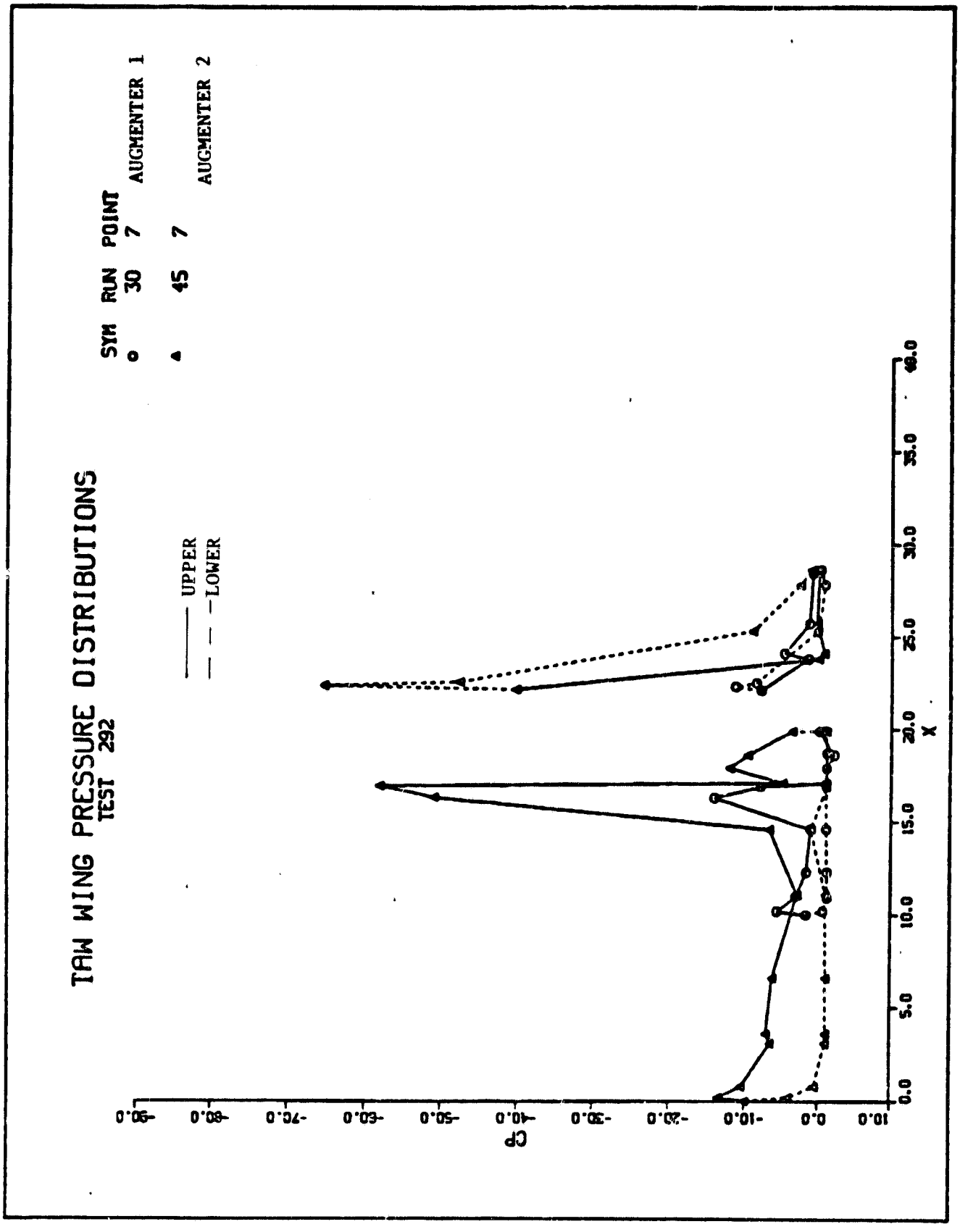

Figure 55 Effect of Nose Length on Augmenter Chordwise Surface Pressure Distributions, $\alpha = 8°$, $C_\mu = 2.0$, $\delta_D = 16°$

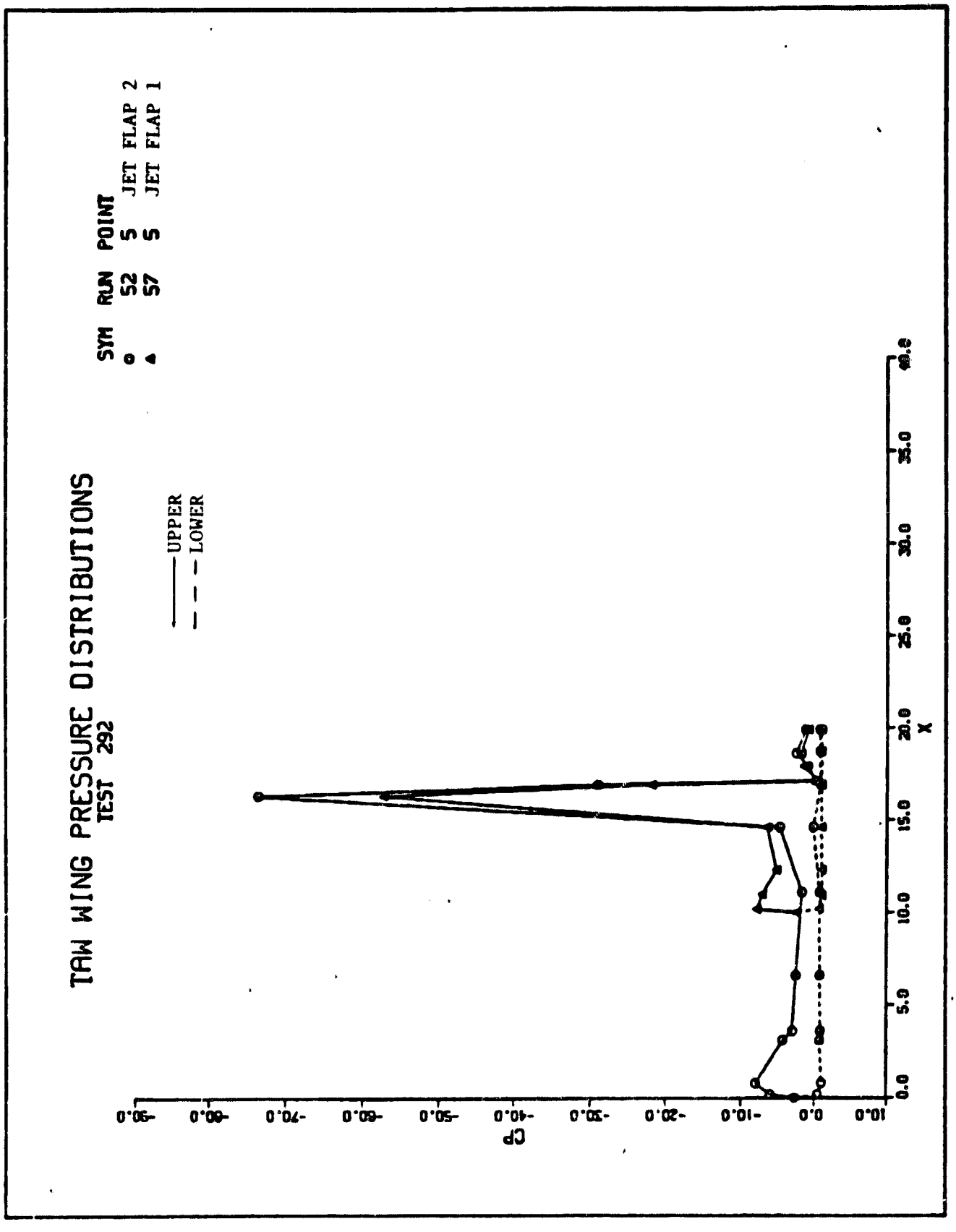

Figure 56 Effect of Nose Length on Jet Flap Chordwise Surface Pressure Distributions, $\alpha = 0$, $C_\mu = 2.0$

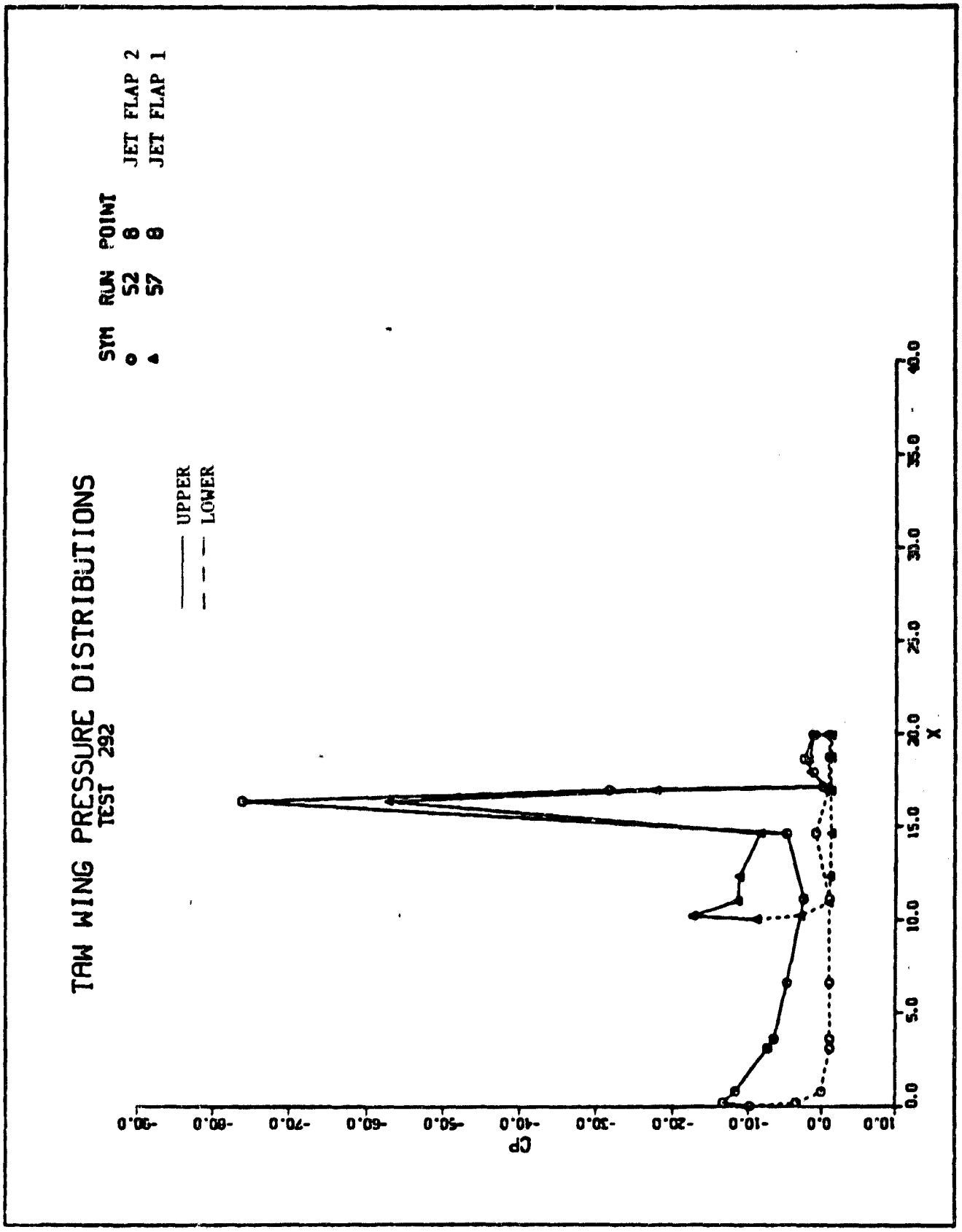

Figure 57 Effect of Nose Length on Jet Flap Chordwise Surface Pressure Distributions, $\alpha = 8°$, $C_\mu = 2.0$

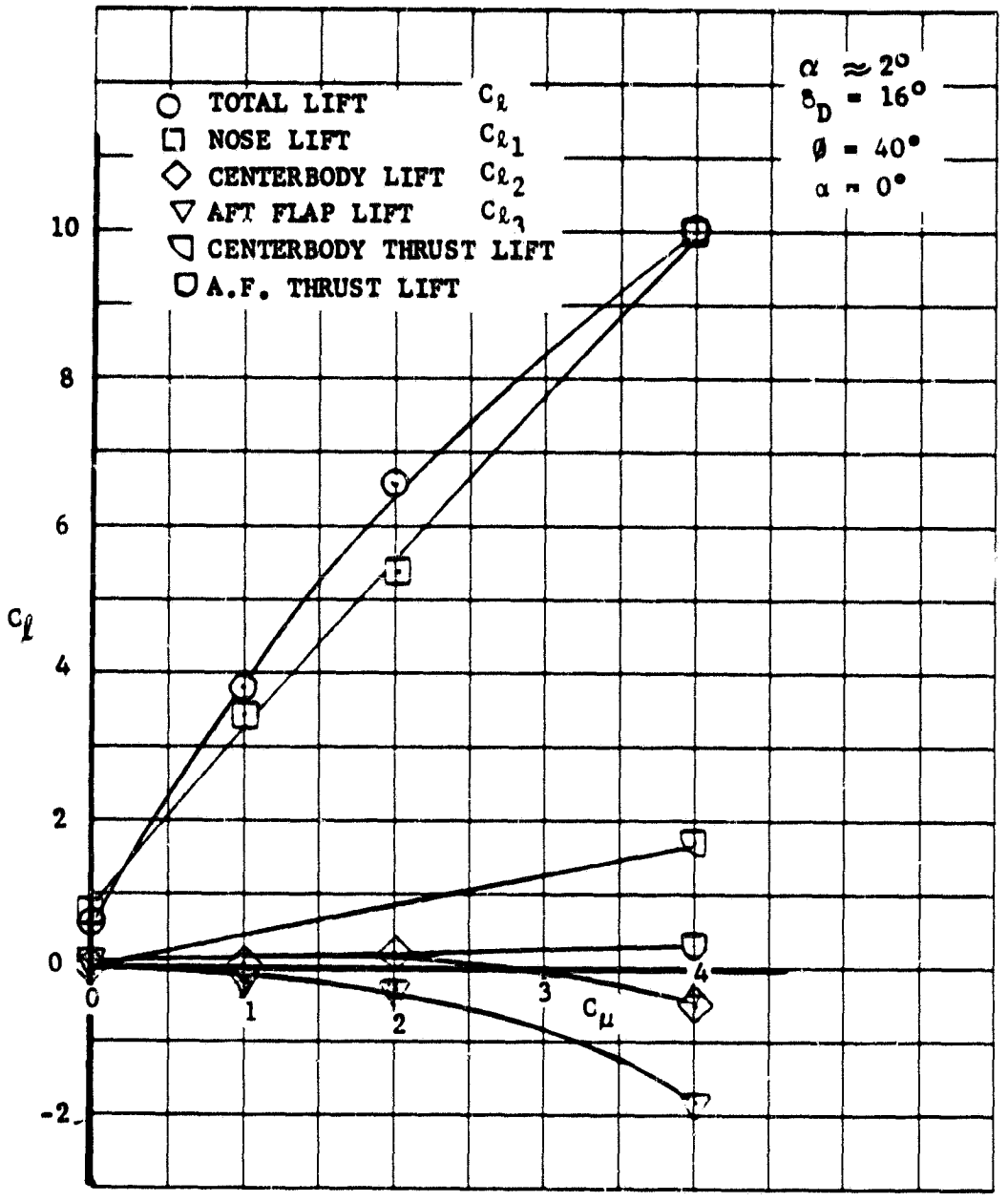

Figure 58 Lift Buildup for Each Wing Component, Augmenter Number 1

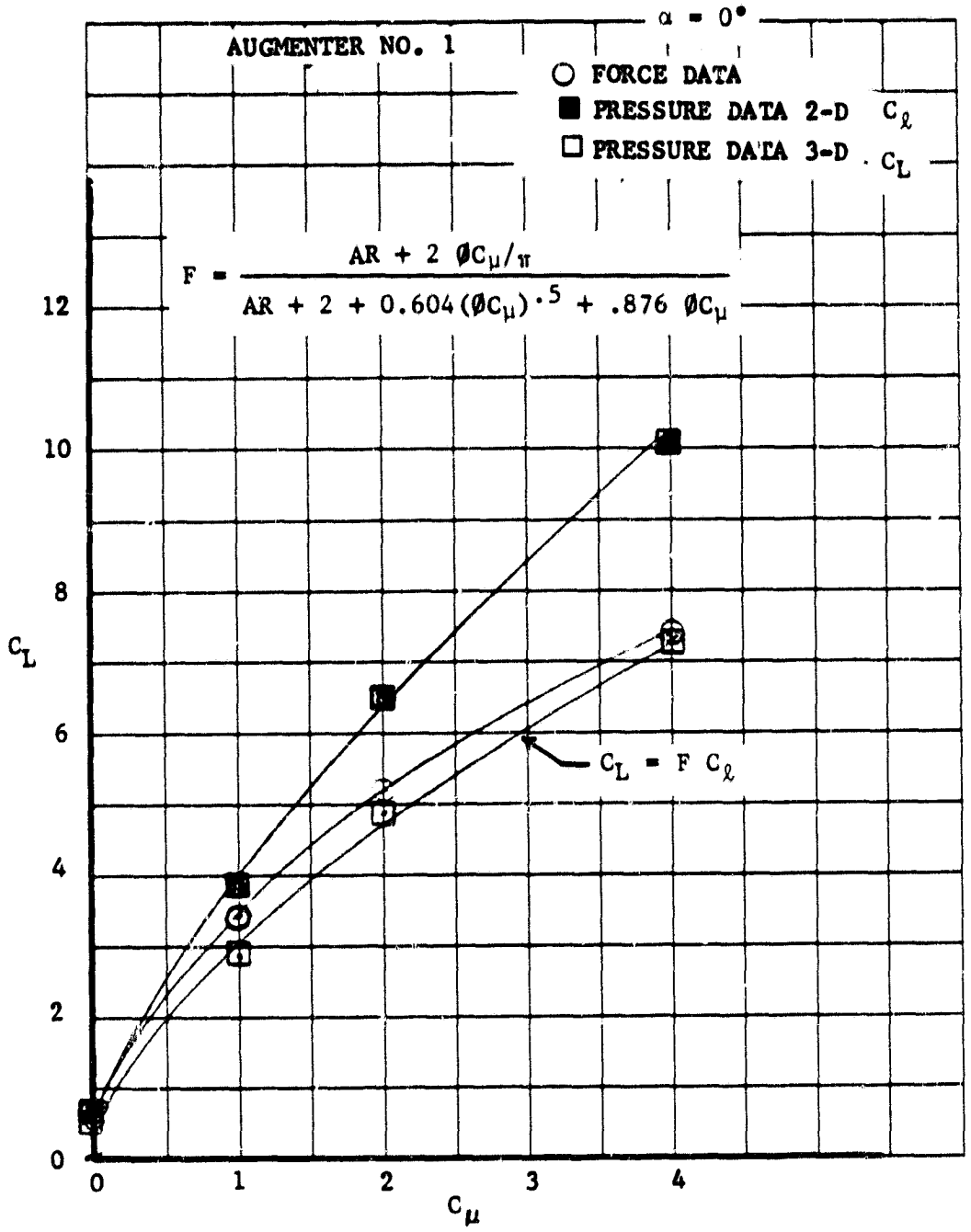

Figure 59 Comparison of Force and Pressure Measurements, Augmenter Number 1

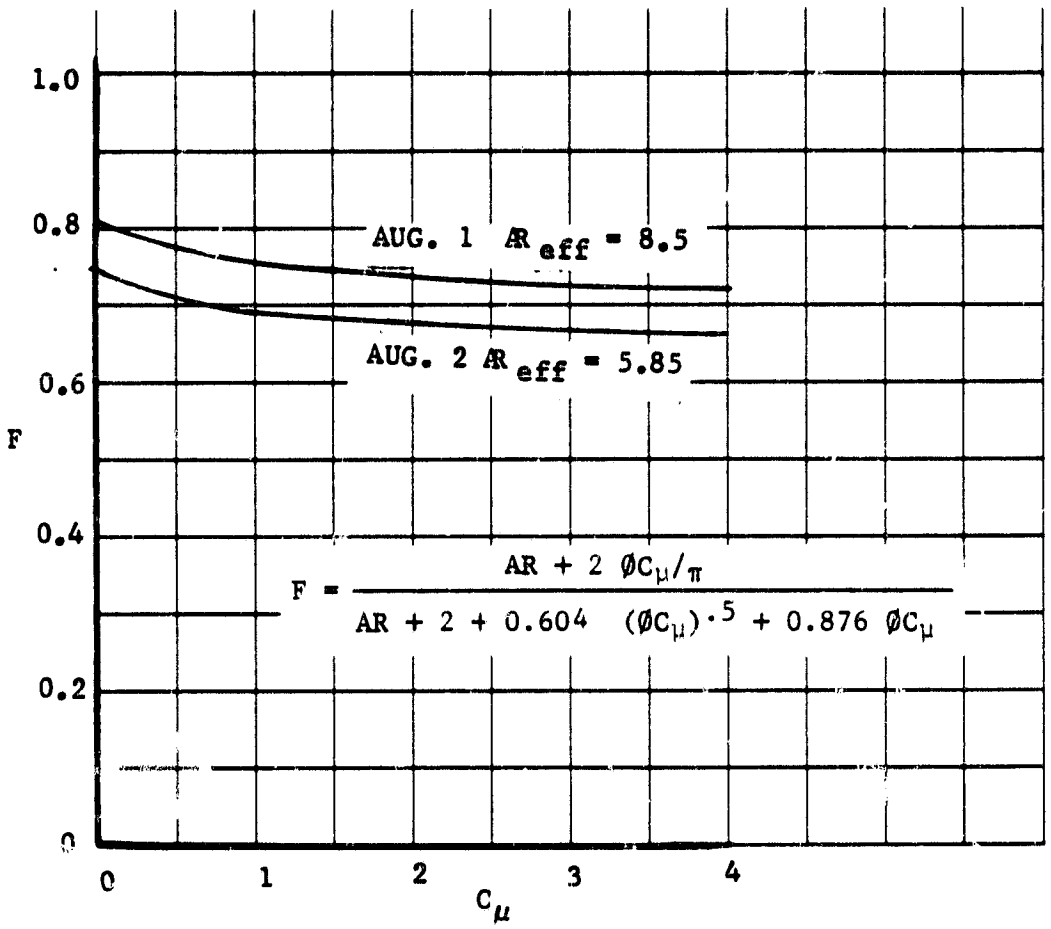

Figure 60. Correction Factor for 3-D Effects

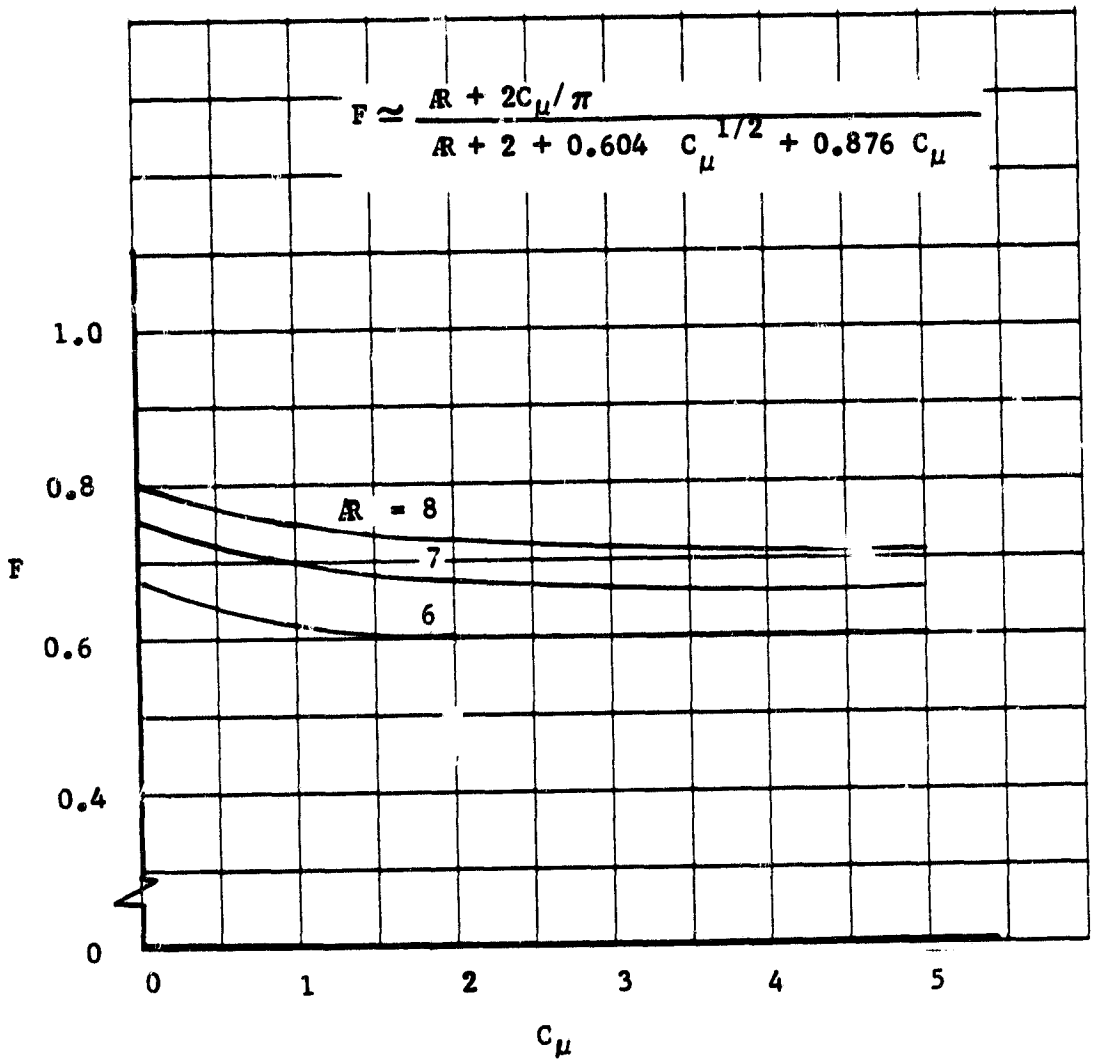

Figure 61 Basic 3-D Correction Factors

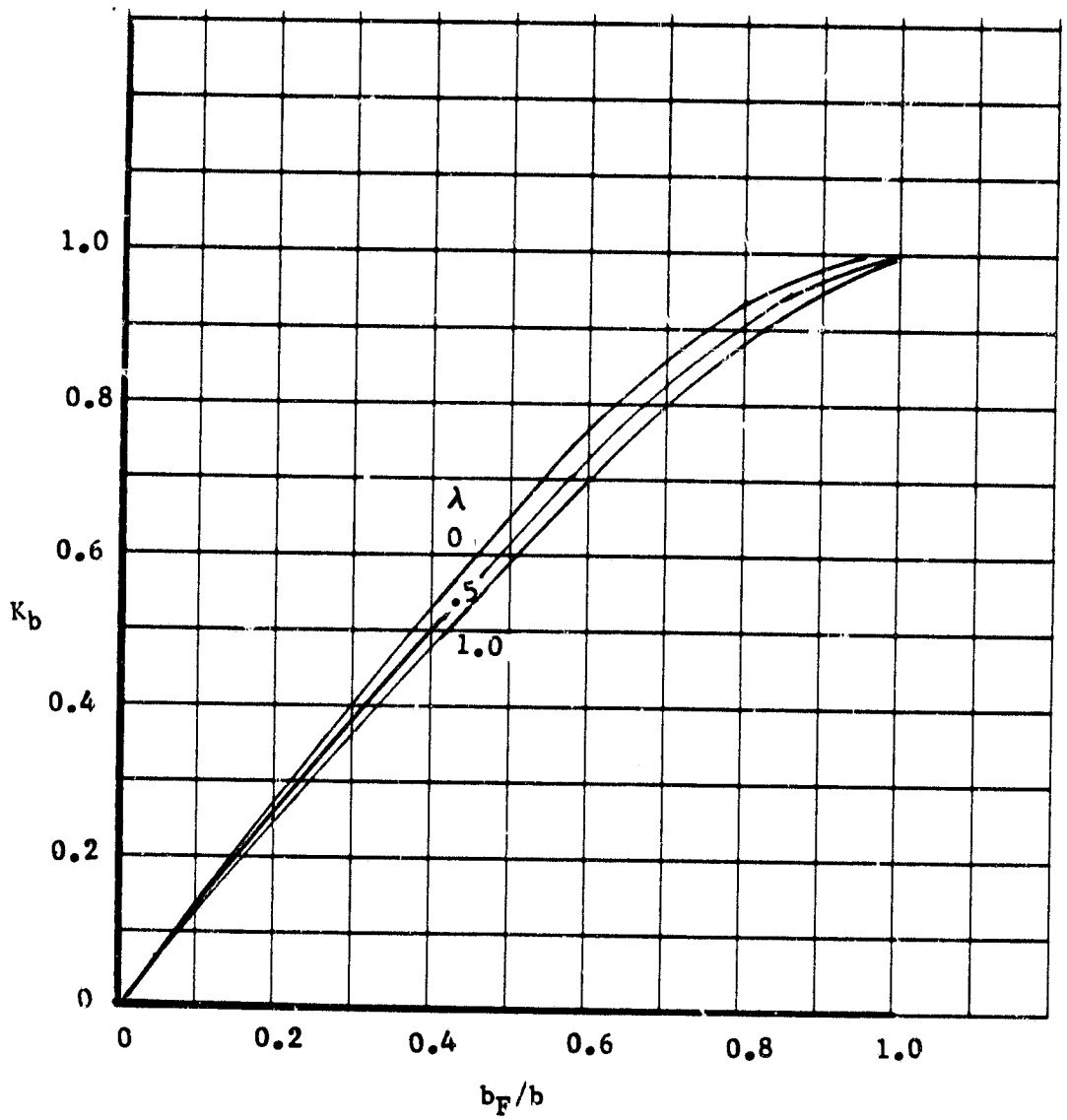

Figure 62 Lift Correction Factor for Flap Span

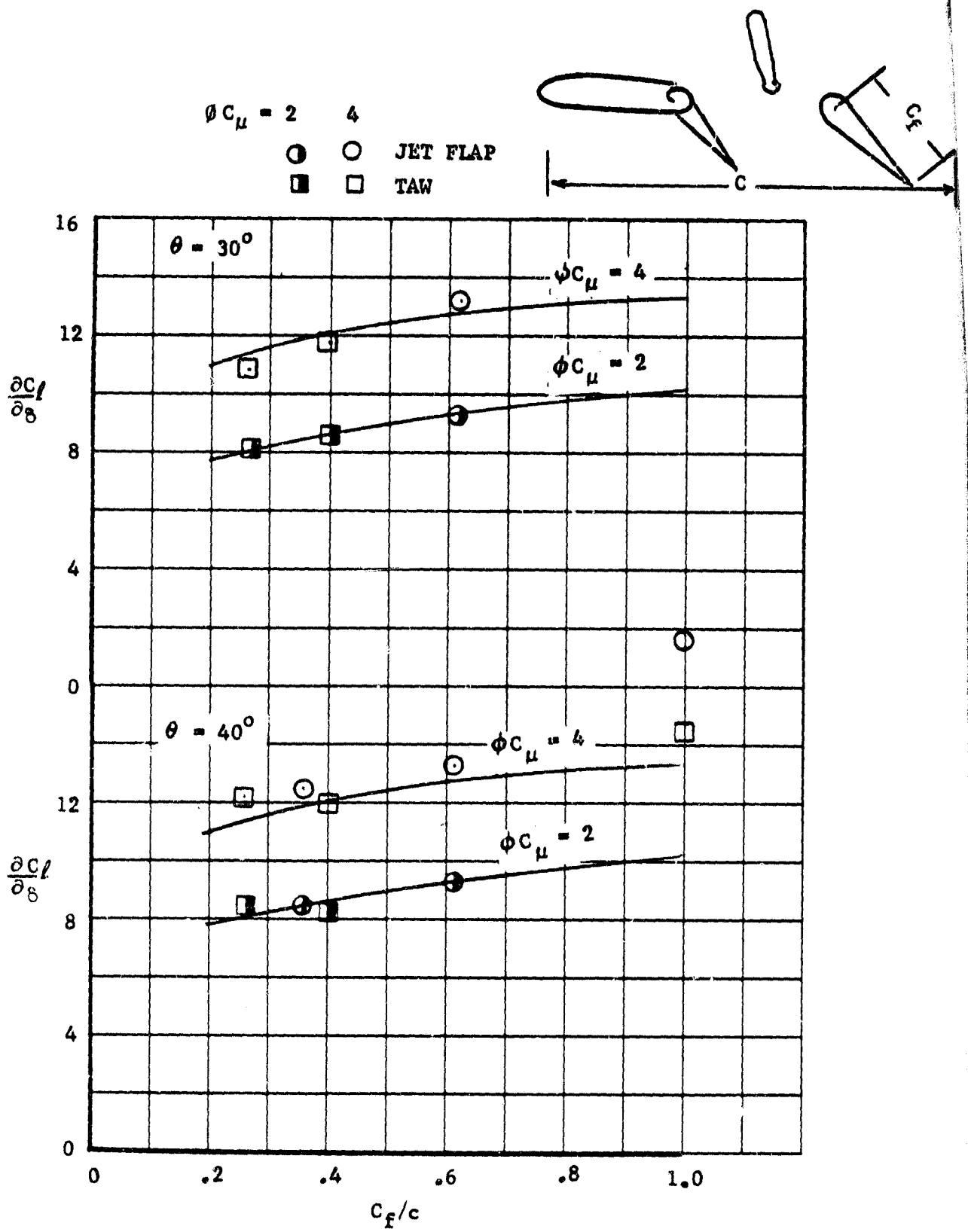

Figure 63. Variation of Flap Lift with Blowing Momentum Coefficient

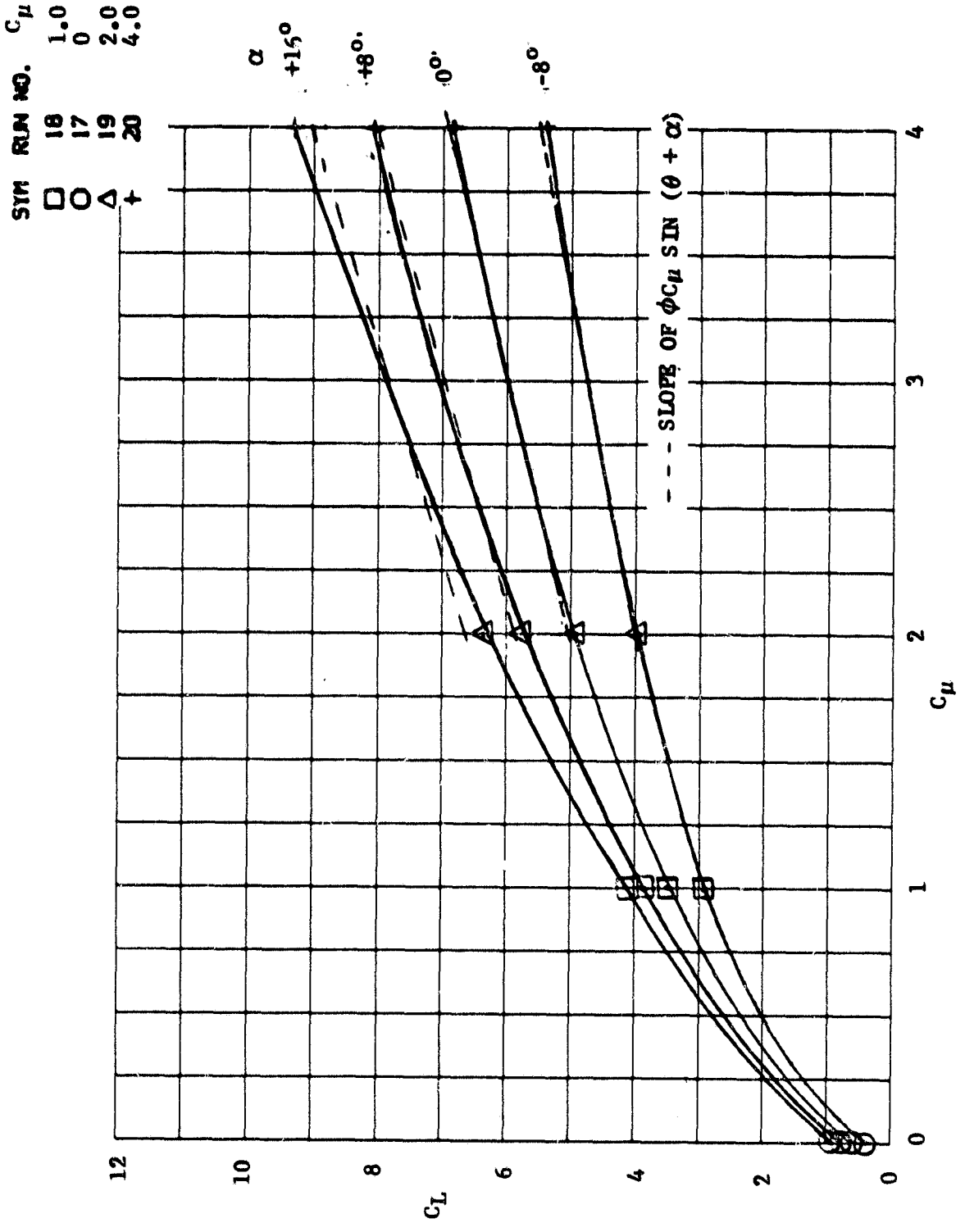

Figure 64 Variation of Augmenter 1 Lift with Blowing Coefficient

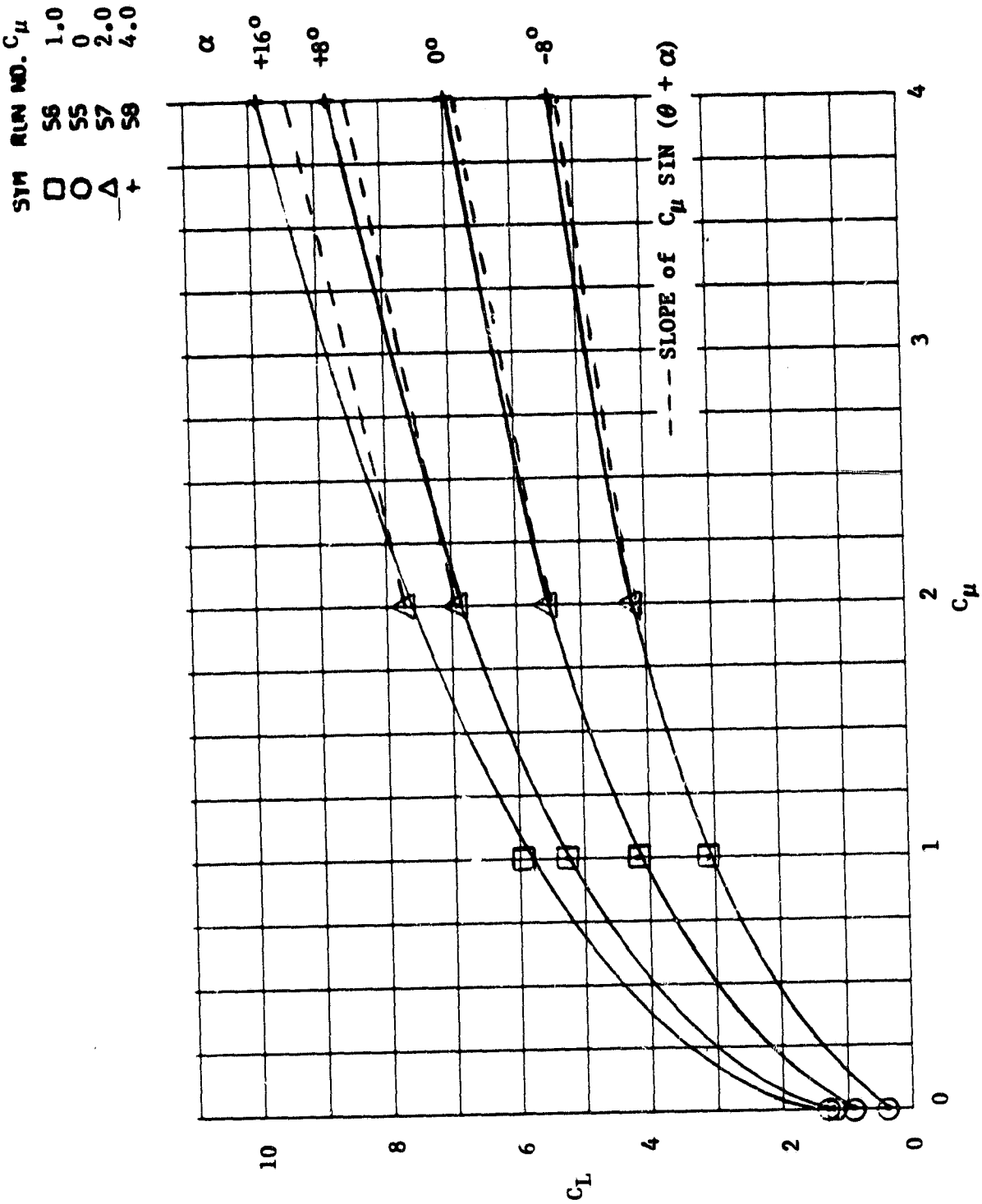

Figure 65 Variation of Jet Flap 1 Lift with Blowing Coefficient

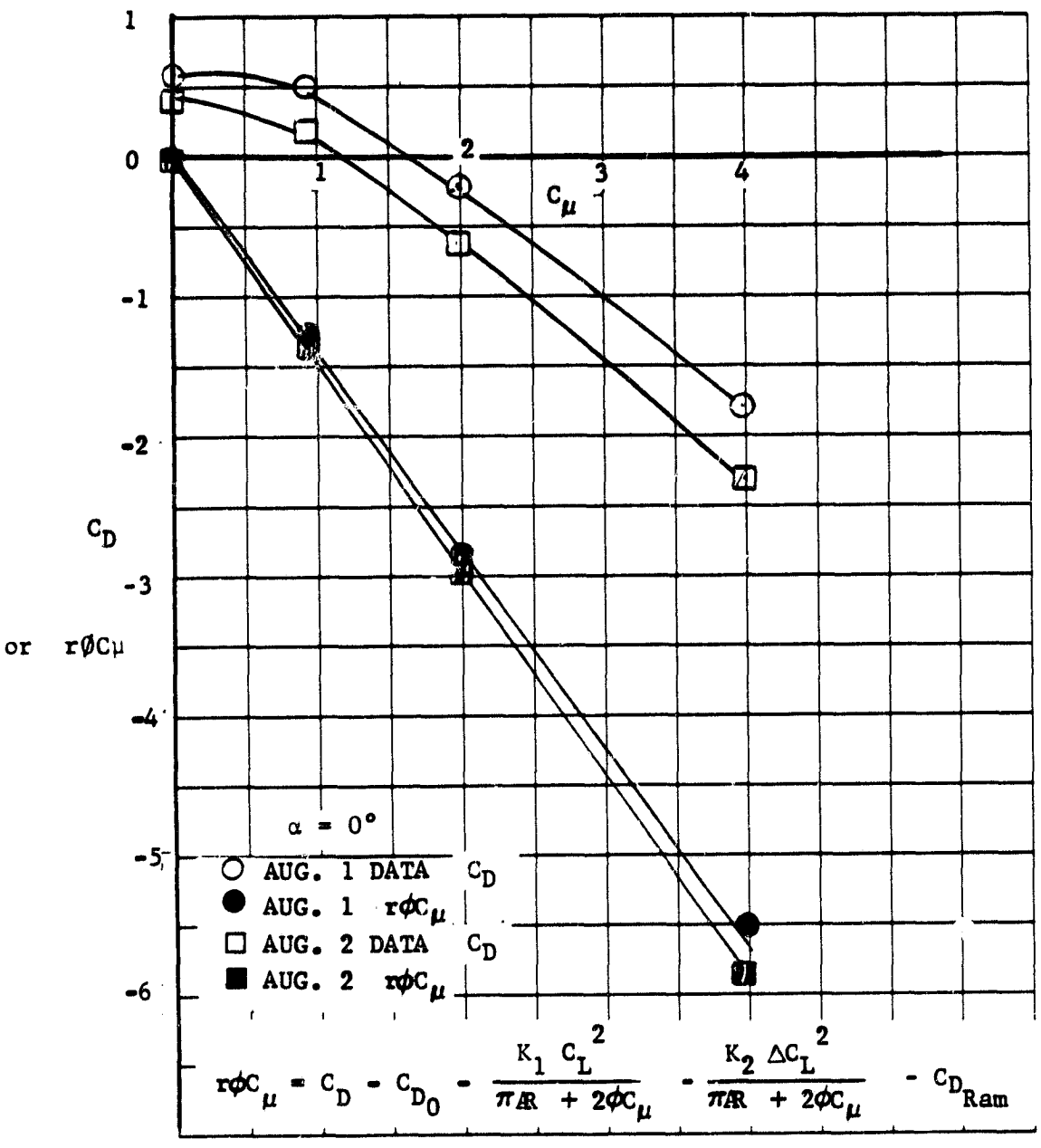

Figure 66 Variation of Augmenter 1 Drag with Blowing Coefficient

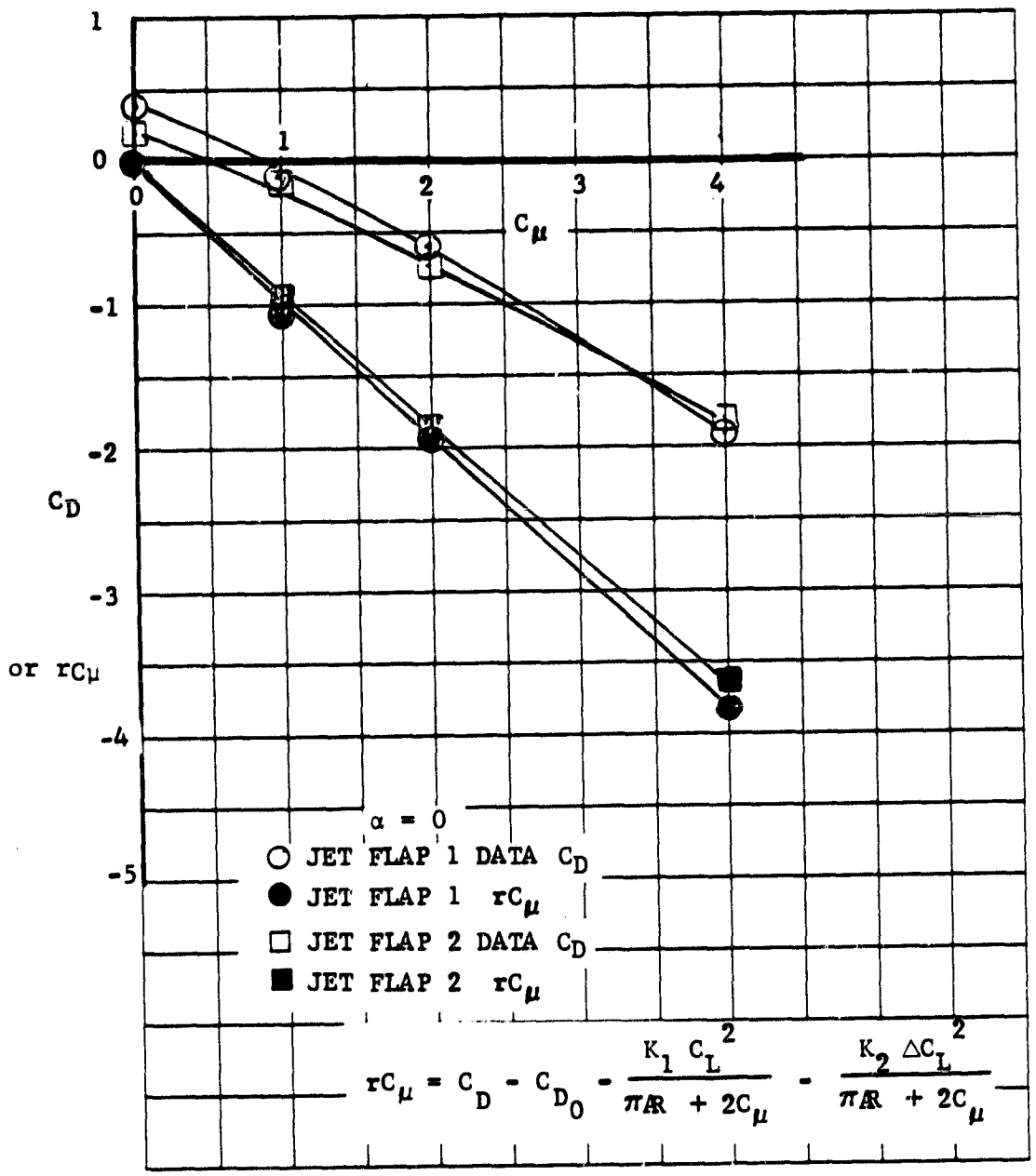

Figure 67 Variation of Jet Flap 1 Drag with Blowing Coefficient

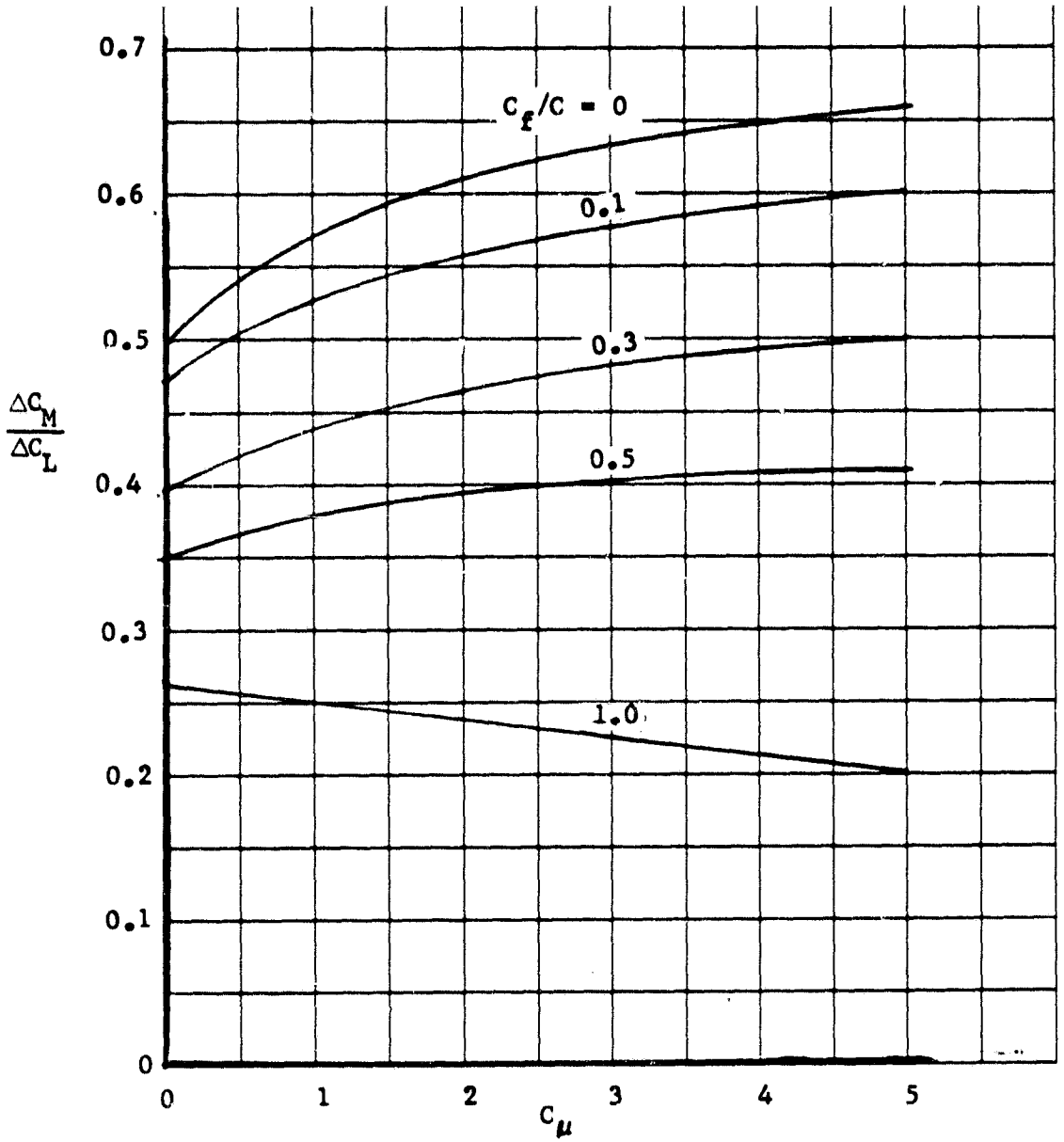

Figure 68 Variation of a.c. Location with Blowing Coefficient Theory

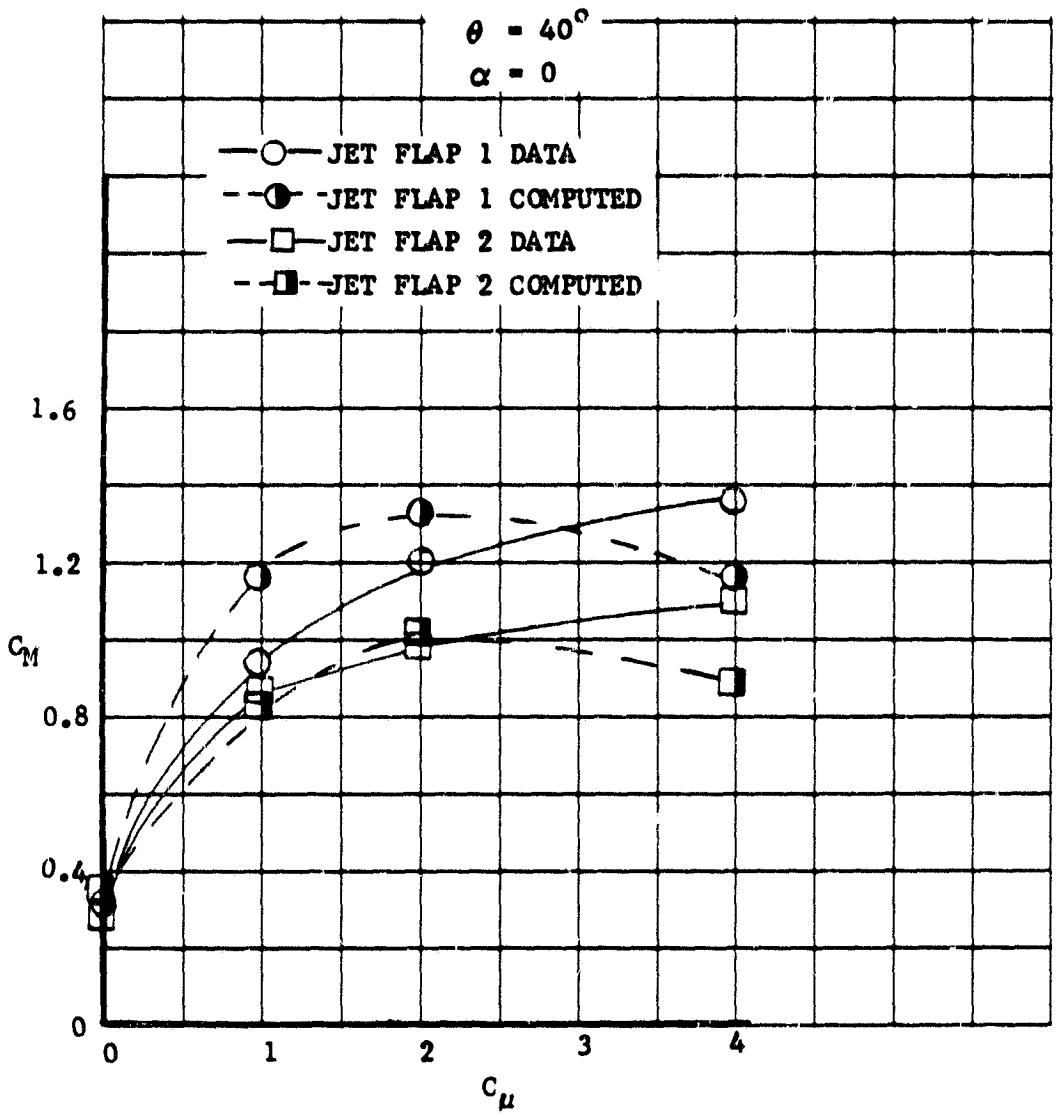

Figure 69 Variation of Jet Flap Pitching Moment Coefficient with Blowing Moment Coefficient

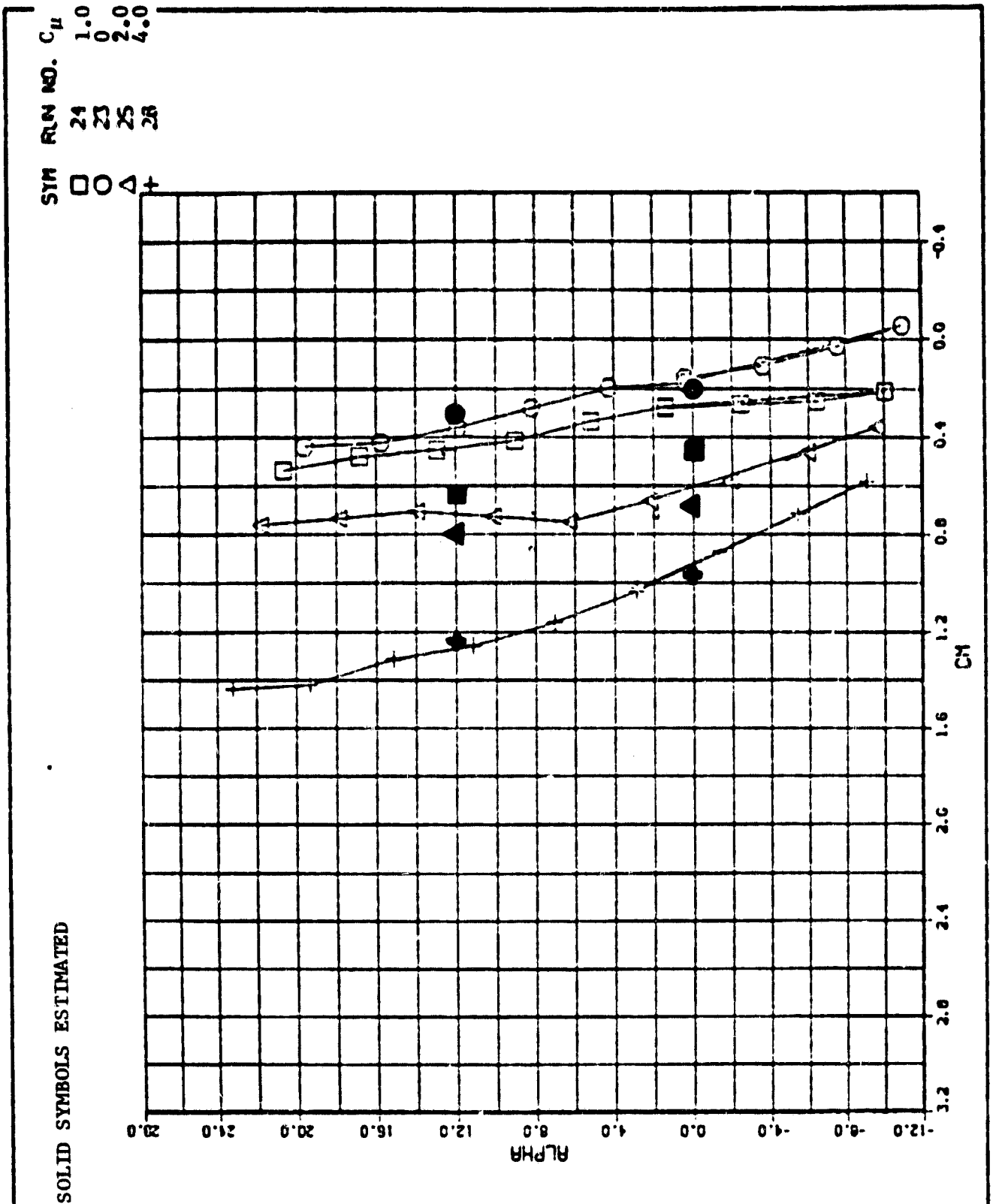

Figure 70 Comparison of Test and Calculated Pitching Moment Coefficient, Augmenter Number 1; $\theta = 40^{\circ}$, $\delta_D = 8^{\circ}$

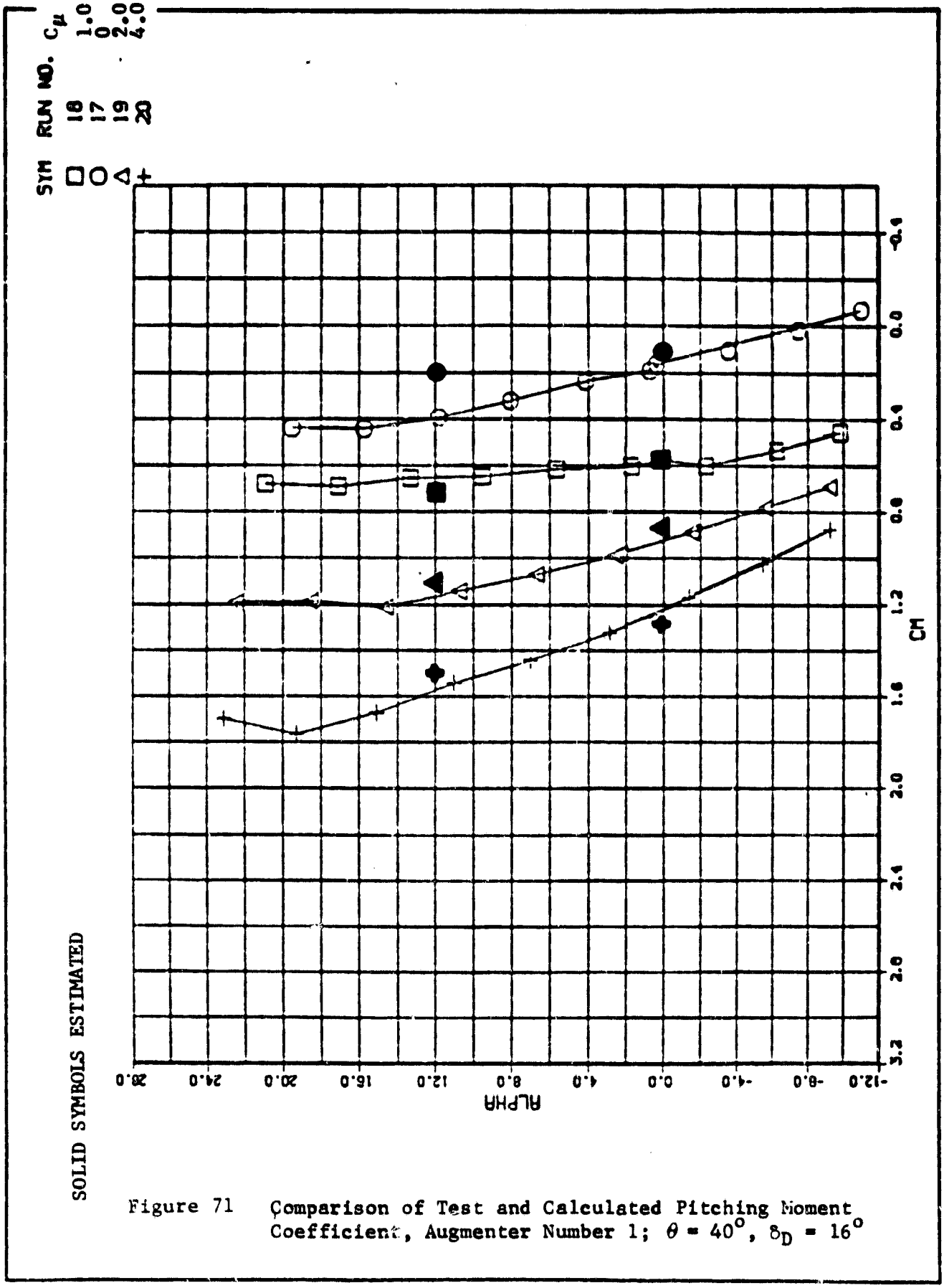

Figure 71 Comparison of Test and Calculated Pitching Moment Coefficient, Augmenter Number 1; $\theta = 40^{\circ}$, $\delta_D = 16^{\circ}$

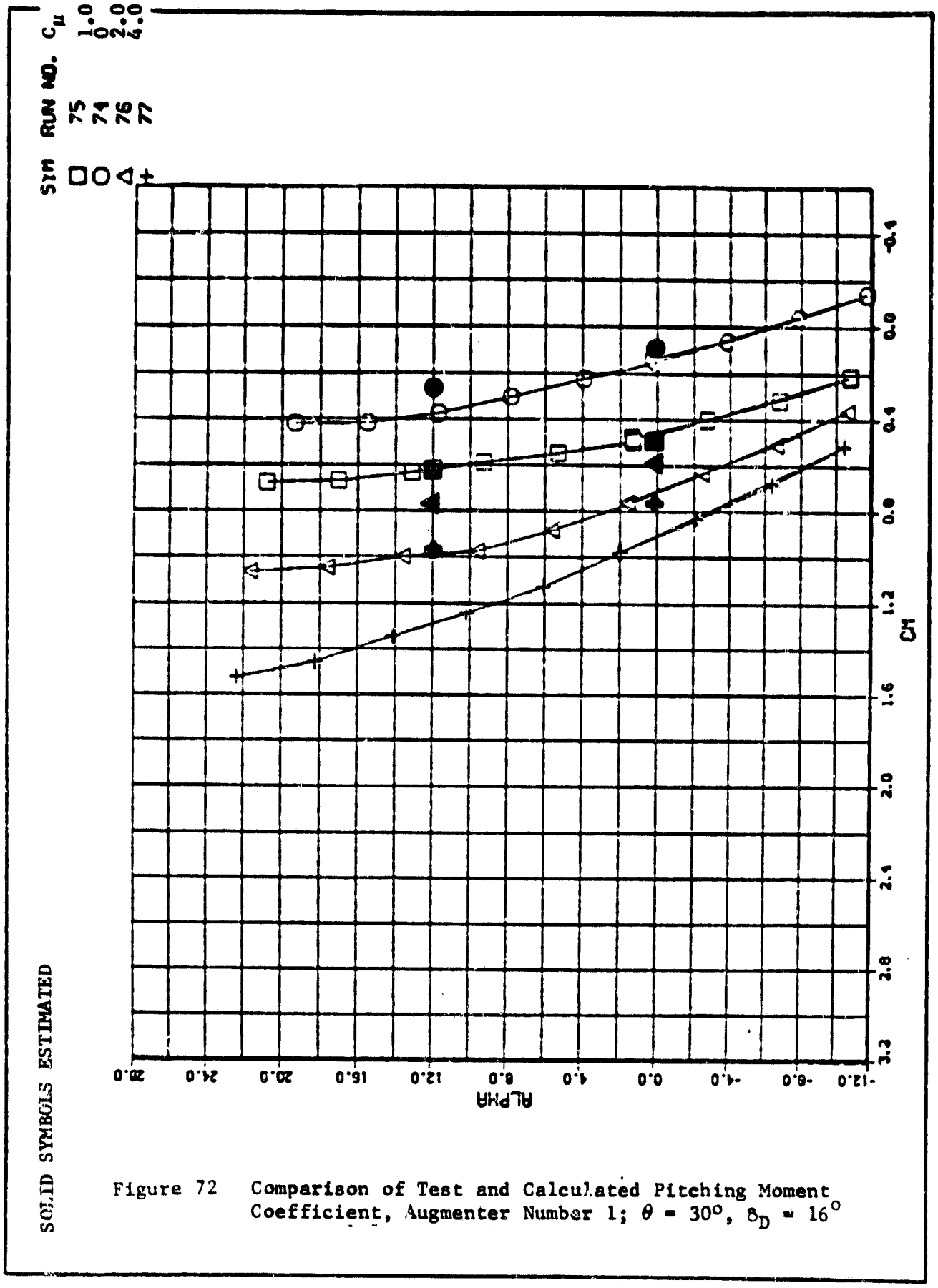

Figure 72 Comparison of Test and Calculated Pitching Moment Coefficient, Augmenter Number 1; $\theta = 30^{o}$, $\delta_D = 16^{o}$

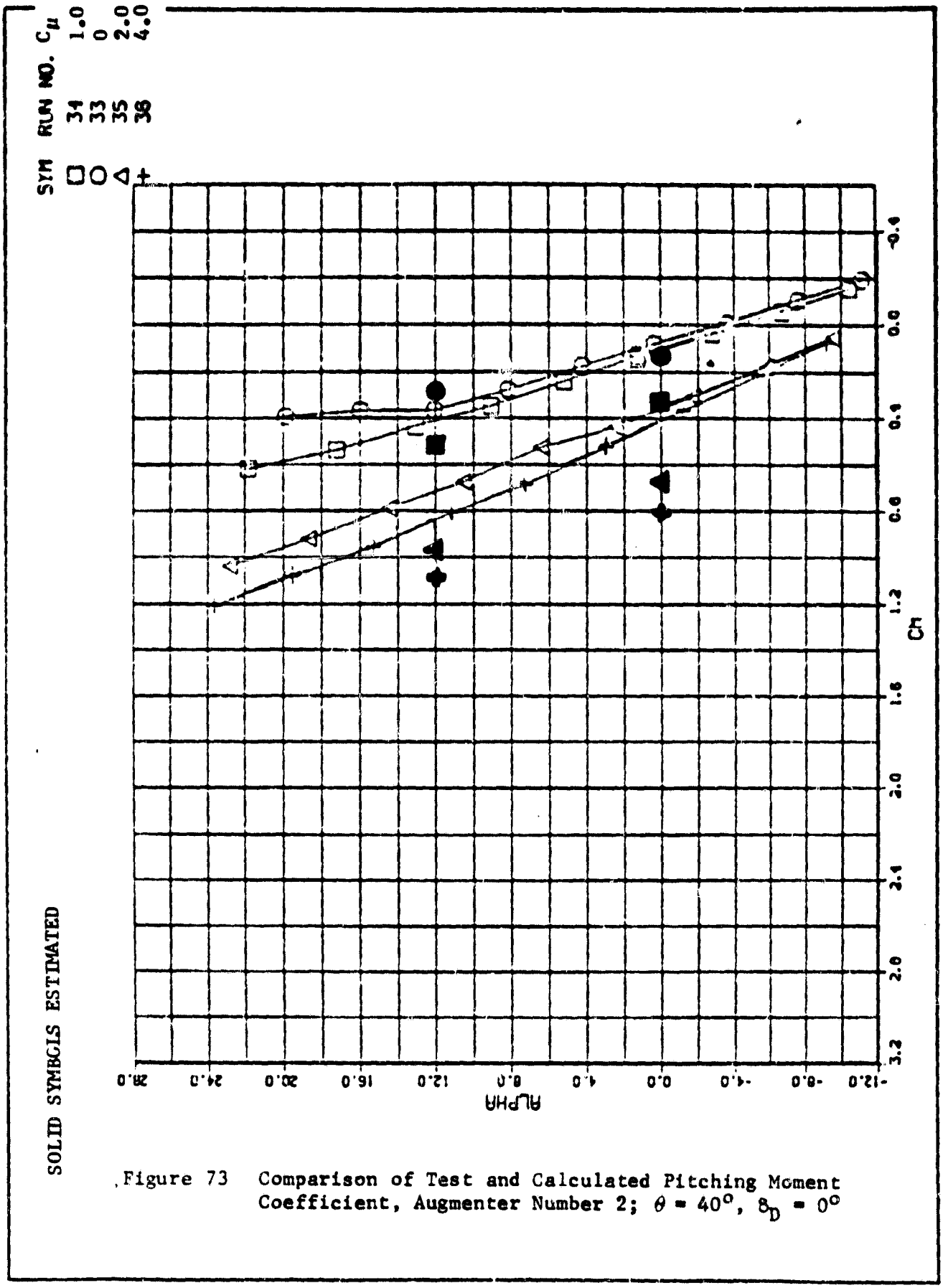

Figure 73 Comparison of Test and Calculated Pitching Moment Coefficient, Augmenter Number 2; $\theta = 40^{\circ}$, $\delta_D = 0^{\circ}$

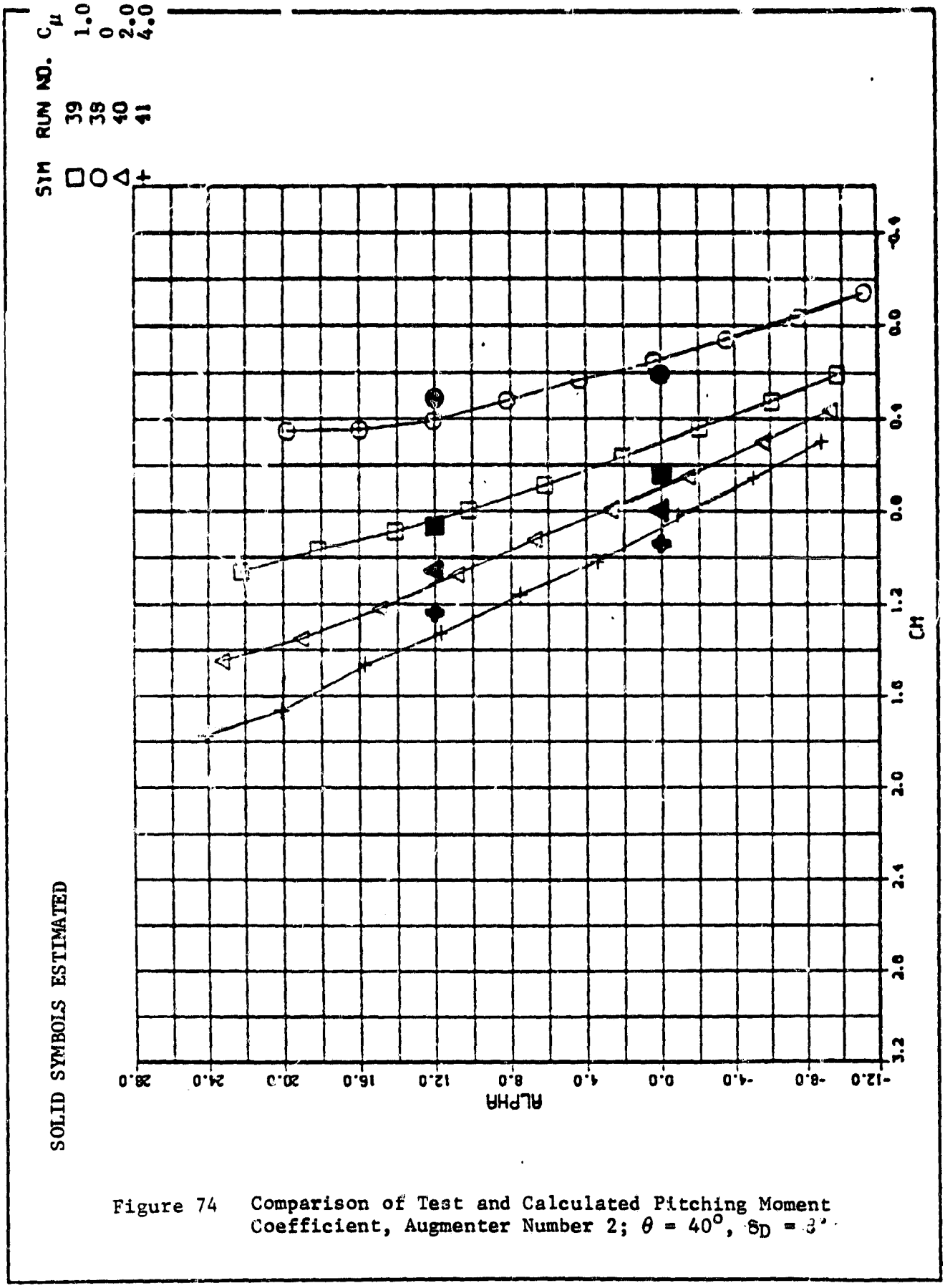

Figure 74 Comparison of Test and Calculated Pitching Moment Coefficient, Augmenter Number 2; $\theta = 40^{\circ}$, $\delta_D = 3^{\circ}$

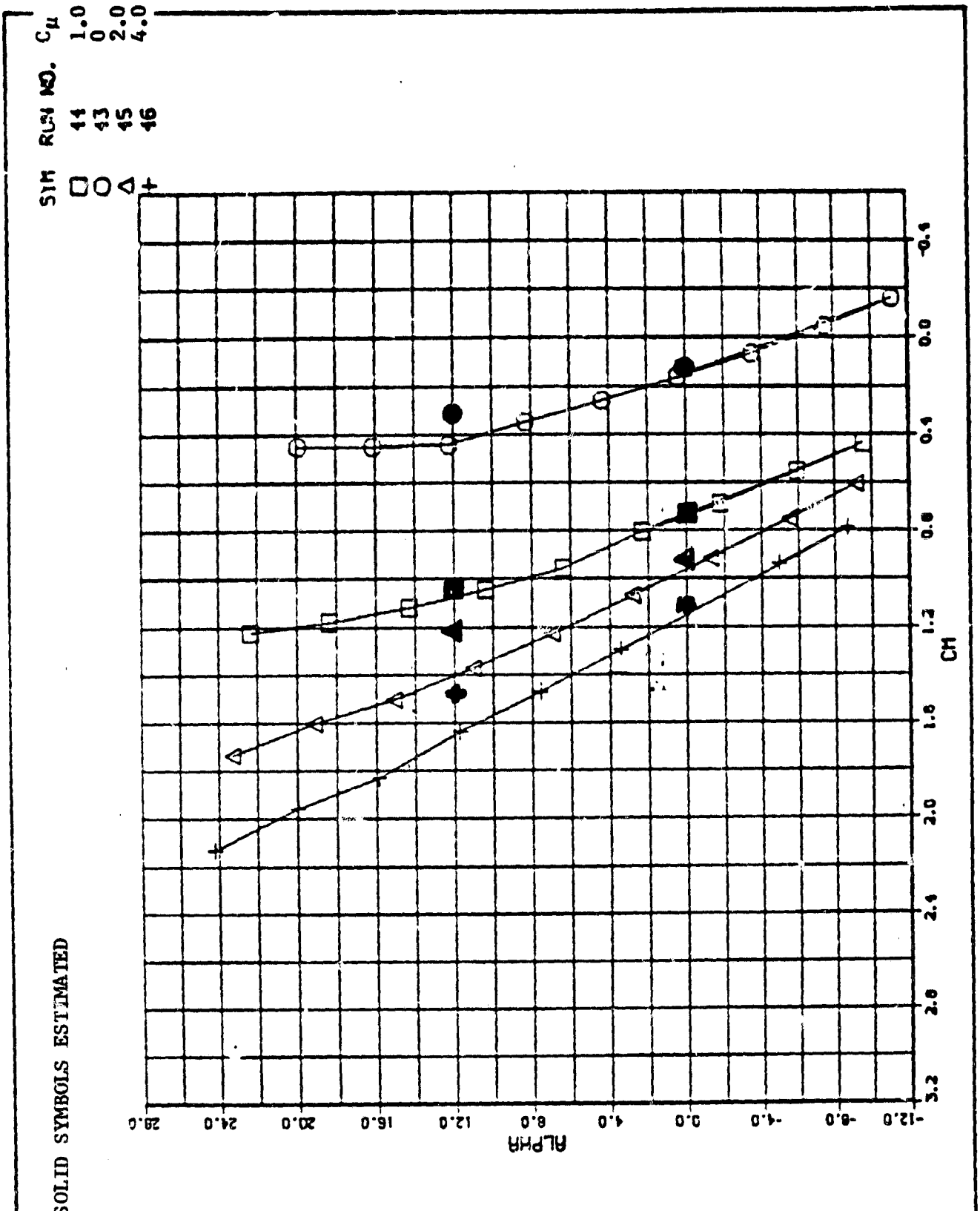

Figure 75 Comparison of Test and Calculated Pitching Moment Coefficient, Augmenter Number 2; $\theta = 40^\circ$, $\delta_D = 16^\circ$

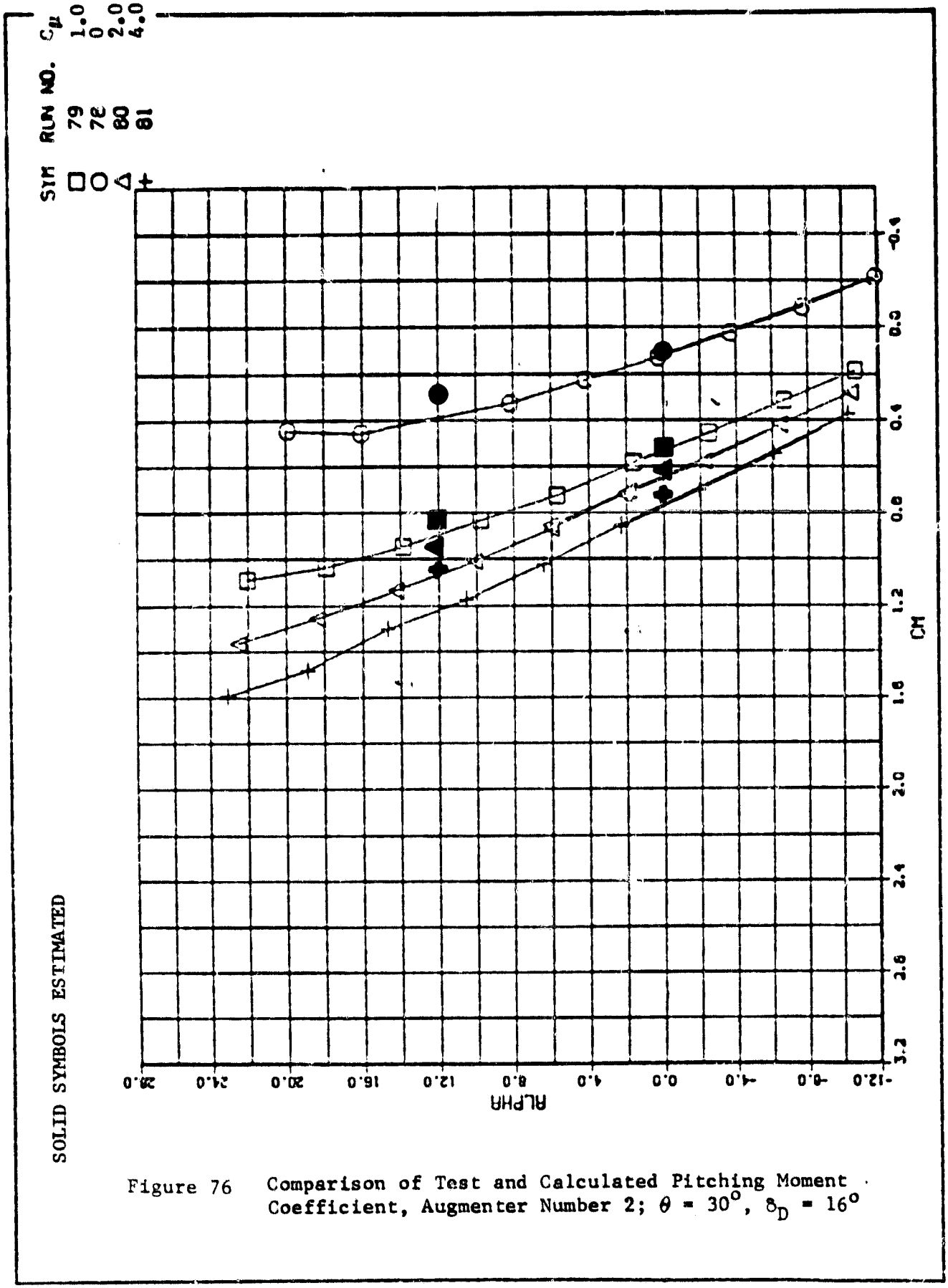

Figure 76 Comparison of Test and Calculated Pitching Moment Coefficient, Augmenter Number 2; $\theta = 30^{\circ}$, $\delta_D = 16^{\circ}$

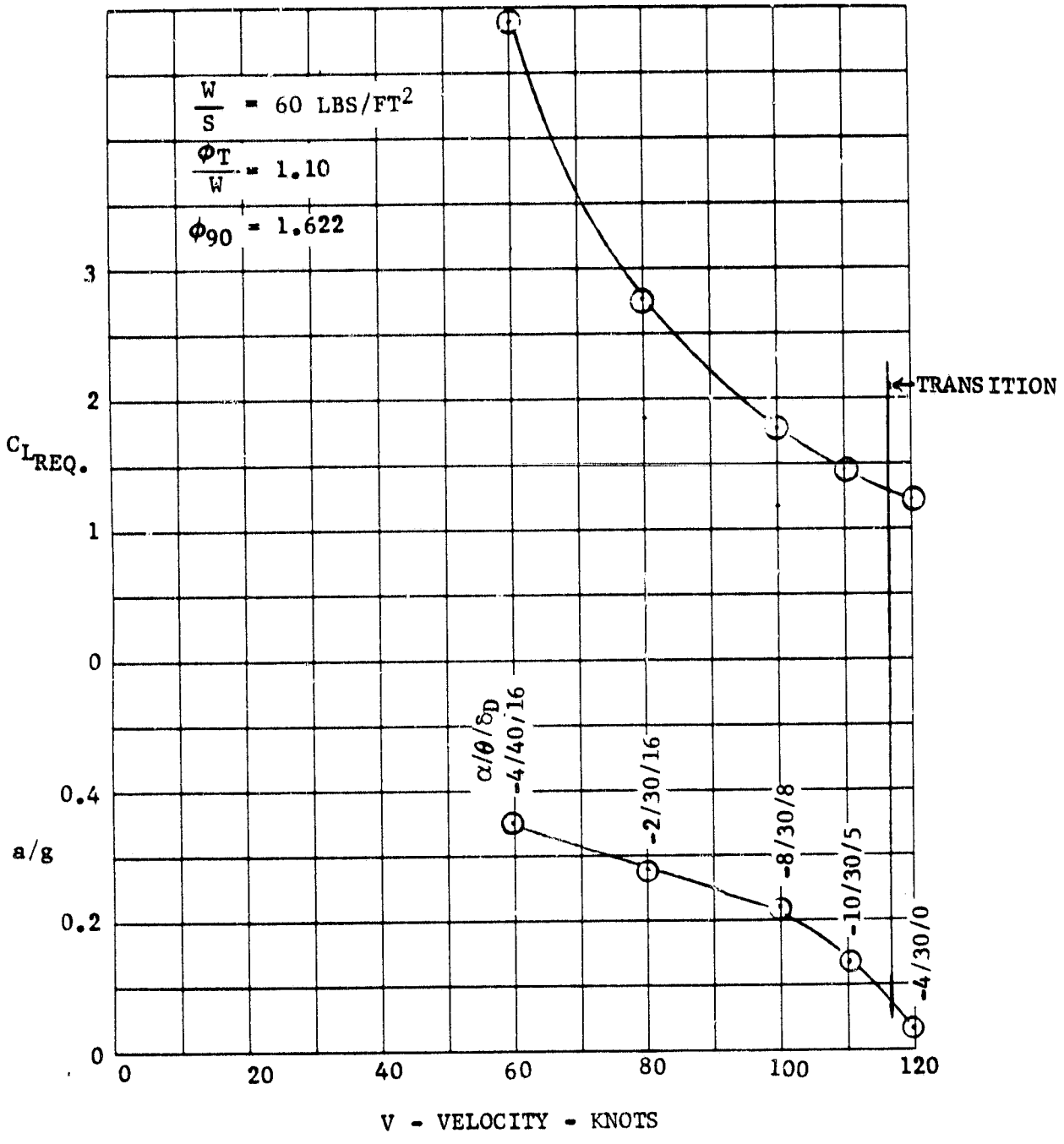

Figure 77. Transition Performance, Augmenter Number 1